Characterization of reservoir quality and supply chains for critical raw materials

Zur Erlangung des akademischen Grades einer

DOKTORIN DER NATURWISSENSCHAFTEN (Dr. rer. nat.)

von der KIT Fakultät für
Bauingenieur-, Geo- und Umweltwissenschaften

des Karlsruher Instituts für Technologie (KIT)

genehmigte

DISSERTATION

von

Jasemin Ayse Ölmez

aus Hanau

Tag der mündlichen Prüfung: 25. Juli 2025

Referent: Prof. Dr. Christoph Hilgers
Korreferent: Prof. Dr. Matthias Hinderer

Karlsruhe (2025)

Acknowledgements

I am deeply indebted to my supervisor Christoph Hilgers for discussions on several topics like science, economics, and beyond. I am encouraged by his enthusiasm for science and his willingness to embrace new ideas and methods. I would like to express my deepest gratitude to you for countless discussions and for the opportunity to gain experience in different scientific fields, several lectures, field schools, and to contribute to industrial projects. Thank you for always asking about "what I want to do, and why I want to do it".

Matthias Hinderer is thankfully acknowledged for serving as a co-supervisor for this thesis. Thank you for always offering time for discussions and for supporting the process. Your constructive comments and tips contributed to improving the thesis.

I am sincerely grateful to Benjamin Busch for countless hours in discussing ideas, models, and research questions. Your optimistic, motivating, and supportive manner has always helped me to improve the studies. I am incredibly grateful for our pleasant field schools with students, for improving lectures and exercises together, and your support during field work and lab work.

Phoenix Zementwerke Krogbeumker GmbH & Co. KG in Beckum (Germany), especially Patrick Pottmeier & Wolfgang Schnieders, are thanked for granting access to the quarry for field work and an OGV field trip, safe working conditions, permission to collect samples and to publish the data.

Sämann Stein- und Kieswerke GmbH in Knittlingen (Germany), especially Ulrich Sämann, Jochen Sämann & Sebastian Martsch are thanked for access to the Knittlingen quarry and the opportunity for field work, safe working conditions, permission to collect samples and publish the data. I am also thankful for the access to the quarry with our students during field schools.

OMV Exploration & Production GmbH in Vienna (Austria) is thankfully acknowledged for funding, providing sample material, and the permission to publish the research data. A special thanks is due to Rolf Möbius, Kanchan Dasgupta, Albert Gauer, and Filippo Tosoratti for several discussions, your inputs, comments and ideas which improved the manuscript, and discussions during our stay in Gänserndorf.

I would like to thank the Think Tank Industrial Resource Strategies (TT IRS), especially Christian Kühne, for funding, the opportunity to work on raw material topics, and to present and publish the data.

Special thanks to my colleagues from Structural Geology at KIT, Agnes Kontny, Dennis Quandt, Katharina Steiger, Felix Allgaier, Olajide Jonathan Adamolekun, Melike Yildirim Ayyildiz, Dorina Juhász, Yonghui Chen, Luis Baumgartner, Johanna Berckhan, and Bruno Daniel Leite Mendes, for inspirational discussions. Felix Allgaier is additionally acknowledged for acquiring drone images in the quarries in Beckum and Knittlingen. Thanks to Dennis Quandt for the time we spent together in teaching and on field schools with students.

I would like to extend my sincere thanks to my colleague Chaojie Cheng for his support and several hours of discussion about project ideas and beyond in our office. Special thanks to Ulrike Brecht and Oxana Sobko for support in any bureaucracy and organization topic at KIT.

Petrographic studies are not possible without thin sections, and I am obliged to Martin von Dollen for sample and thin section preparation, hours of discussion about minerals, rocks and fossils, and assistance during field work.

Our bachelor and master students, with whom I was working in the field and those who wrote their final thesis co-supervised by me, are thankfully acknowledged for fracture measurements, help during sample collection and sample preparation, and thus contribution to this work.

Thanks to Nevena Tomašević, Lucas Eskens, Paul Baville, Giridas Maiti, Robert Šamarija, Agnes Kontny, Johanna Berckhan, Benjamin Busch, Martin von Dollen and Dorina Juhász for support during two GirlsDay's.

Many thanks to Christian Masurenko, Prof. Thierry Bineli-Betsi, Antje Wittenberg & Mario Schmidt for discussions on resource topics in different countries.

Thanks to Frank Schultmann, Uwe Langenmayr (both KIT IIP) and Luis Baumgartner for the cooperation on a project on raw material demand for hydrogen electrolyser.

Jochen Kolb is thankfully acknowledged for discussion about resources and mining.

Thanks to Armin Zeh and Antonin Bilau for their introduction and first test runs on U-Pb dating of carbonate minerals using LA-ICP-MS.

Rafael Ferreiro Mählmann is thankfully acknowledged for discussion about resources, minerals and beyond.

Thanks to Jens Hornung for discussion about reservoir characterization and petrophysics.

I am grateful for the possibility to do joint research with our Moroccan colleagues. Thank you for your warm welcome, the insights into geology and respectful mining in Morocco. Thanks to Moha Ikenne, Nourissaid Icame, Mohamed Bensaou, and Fatiha Askkour for our joined field school with our bachelor and master students and the insights into the Moroccan geology and traditions. Groupe Managem & Akka Gold Mining, especially Atman Madi, is thankfully acknowledged for permission for field work, safe working conditions, and daily care in the Ouansimi mine (Anti-Atlas region).

My special thanks are due to my family for their love & continuous support.

Abstract

Understanding reservoir quality is essential for subsurface use and exploration as it determines economic viability and reduces uncertainty, risk, and cost. In part I reservoir quality for e.g., geothermal brines, CO_2 storage, and hydrocarbons are assessed for three different areas. In part II the impact of the Russia-Ukraine conflict on global raw material supply chains is evaluated and furthermore the role of selected African countries in raw material supply is assessed. This study contributes with case studies on reservoir rocks and global supply chains, to the optimal utilization of the subsurface for fluid and solid raw materials.

The Campanian lithologies in Beckum are studied as outcrop analog to understand petrophysical and petrographic heterogeneity and the presence on possible fluid migration pathways from underlying Upper Carboniferous strata. He-pycnometry, Klinkenberg-corrected air permeabilities, p-wave velocities, transmitted and reflected light analyses, point-counting, and cathodoluminescence were used. Results show low matrix porosity (1.0–18.7%) and permeability (<0.0001–0.2 mD), due to compaction, early (ferroan) calcite cementation, and formation of compaction bands in the vicinity to ductile clay mineral laminae. P-wave velocities range from 2089 to 5843 m/s. The introduced "Compactable Depositional Volume" (CDV) helps evaluate the timing of cementation relative to compaction, and the effect of compactional volume loss on reservoir properties can be obtained. NW-SE oriented, partially sealed veins with (ferroan) calcite and strontianite likely formed during Late Cretaceous inversion and fault reactivation. Due to poor reservoir quality, these lithologies may act as barriers to rising mine water from abandoned coal mines, unless disrupted by faults or fault-related damage zones.

An outcrop analog study evaluates diagenesis, fractures, and vein cementation in tight, fractured limestones of the Upper Muschelkalk-Lower Keuper transition on the eastern Upper Rhine Graben shoulder (SW Germany). Fracture occurrence, spacing, and clustering are critical for reservoir performance, especially in tight formations. Early and burial diagenetic cementation with (ferroan) calcite and dolomite reduces matrix porosity (0.16–10.58%) and permeability (<0.0001–9.7 mD). Samples with stylolites and partially sealed fractures show highest permeability (up to 9.7 mD at 1.2 MPa) and retain up to 41% of the initial permeability measured at 30 MPa. Fracture orientations were recorded manually and analyzed using the normalized correlation count method. Clustering around a breached kink band fault plane is not symmetrically arranged and contains fracture sets of different strike. Fracture clusters are also recorded away from the fault. Slip and dilation tendencies reveal, that fracture sets striking NNE-SSW, WNW-ESE, and NW-SE are more likely to contribute to fluid flow as they are suitably oriented in the present-day stress field. The

(breached) reverse kink bands are the first reported in this region (~180–200 km N-NE of the Alpine front) and are likely related to compression by far field stresses induced by the Alpine orogeny during the Eocene.

The Flysch play in the Vienna Basin is composed of several nappes, forming complex reservoir compartments and hosts several sandstone-mudrock interbeds. This study focuses on reservoir assessment using drill cuttings from two wells covering ~ 400 m of stratigraphy targeting the Paleocene-Eocene Greifenstein Fm. (Glauconite Sandstone, 1.–3. GLS). The samples are analyzed for petrographic properties using transmitted light microscopy and cathodoluminescence, and compared to well sections with known production data. The sandstones are cemented by mostly ferroan calcite, resulting in low optical porosity (<5%). Individually elevated porosity is related to partially dissolved K-feldspar. The highest glauconite content is observed in the 3. GLS. The paragenetic sequence indicate that reservoir quality is independent of compaction. Depth accuracy of cuttings is improved using handheld X-ray fluorescence (pXRF) based on Si/Al ratio, and gamma ray logs to distinguish sandstone- and mudrock-rich intervals. Diagenetic variations and the geochemical fingerprint are linked to reservoir quality and known production performance of individual well sections. The reservoir quality is restricted to fractures and partially sealed veins, and areas of known production are related to lower optical porosity in finer-grained sandstones, higher carbonate vein cement contents, and lower Fe+Mg contents. While fracture orientations cannot be derived from cuttings, vein presence and internal textures can be identified. Drill cuttings are the first sample obtained while drilling a well and thus the first opportunity to analyze the subsurface on-site. However, cuttings are often underutilized.

The Russia-Ukraine conflict disrupted global supply chains for oil, gas, metals, and other raw materials. Both countries are resource-rich and had strong economic ties to the EU and Germany. The EU27 lists currently 34 critical and 17 strategic raw materials. Individual raw materials show a high market concentration in individual countries, often over 90%. Russia plays a major role in mining and refining, using available and inexpensive energy. Ukraine was a key alumina producer, and supplied ~50% of the global neon market before production came to halt. The conflict's impact on bauxite, alumina, titanium, lithium, noble gases, nickel, palladium, platinum, and vanadium is assessed. Responses from countries like South Korea and China show how infrastructure and affordable energy help offset shortages. South Korea's steelworks mitigated neon shortages, while China increased titanium sponge production by ~1.6 in three years due to existing capacity and energy availability.

The mining potential of Botswana, Morocco, Namibia, and Zimbabwe in mining, processing of mining products and participation in smelters, are highlighted which are to date barely recognized by German investors. China e.g., directly invests in mining projects in Africa, and Russia, and is also actively involved in the mining sector, some of which are

accompanied by a military presence. Botswana shows comparatively good WGI indicators and emphasizes the need for investment, which is to date not perceived from e.g., German companies. For many African nations, mining and raw material exports are vital for economic growth.

Kurzfassung

Das Verständnis von Reservoirqualität ist für die Nutzung und Erkundung des Untergrunds von entscheidender Bedeutung, da sie die wirtschaftliche Durchführbarkeit bestimmt und Unsicherheiten, Risiken und Kosten verringert. In Teil I werden Reservoirqualitäten, z. B. für geothermische Solen, CO_2-Speicherung und Produktion von Kohlenwasserstoffen, für drei verschiedene Regionen bewertet. In Teil II werden die Auswirkungen des Russland-Ukraine-Konflikts auf die globalen Lieferketten von Rohstoffen analysiert und die Rolle ausgewählter afrikanischer Länder bei der Rohstoffversorgung untersucht. Die Studie trägt mit Fallstudien zu Reservoirgesteinen und globalen Lieferketten zu einer Nutzung des Untergrundes für flüssige und feste Rohstoffe bei.

Die Lithologien des Campanium in Beckum werden als Aufschlussanaloge untersucht, um die petrophysikalische und petrographische Heterogenität und mögliche Fluidmigrationspfade aus den darunter liegenden Schichten des Oberkarbons zu verstehen. Die Ergebnisse zeigen niedrige Matrixporositäten (1,0–18,7 %) und Permeabilitäten (<0,0001–0,2 mD), die auf Kompaktion, frühe Zementation mit (Eisen-) Kalzit und die Bildung von Kompaktionsbänder am Übergang zu duktilen Tonmineralschichten zurückzuführen sind. Die P-Wellen-Geschwindigkeiten reichen von 2089 bis 5843 m/s. Der eingeführte Parameter „Compactable Depositional Volume“ (CDV) hilft den Zeitpunkt der Zementation im Zusammenhang zur Kompaktion zu bewerten, und die Auswirkung auf die Reservoireigenschaften zu ermitteln. NW-SE orientierte, teilweise versiegelte Adern mit (Eisen-) Kalzit und Strontianit bildeten sich wahrscheinlich während der spätkreidezeitlichen Inversion und Reaktivierung von Verwerfungen. Aufgrund der abdichtenden Lagerstättenqualität können diese Lithologien als Barrieren für aufsteigendes Grubenwasser aus stillgelegten Kohlebergwerken wirken, sofern sie nicht durch Verwerfungen oder verwerfungsbedingte Störungszonen unterbrochen werden.

Die Aufschlussanalogstudie bewertet Diagenese, Brüche und Aderzementierung in dichten, geklüfteten Kalksteinen des Übergangs vom Oberen Muschelkalk zum Unteren Keuper auf der östlichen Schulter des Oberrheingrabens (SW Deutschland). Das Auftreten, die Abstände und die Orientierung von Klüften sind entscheidend für die Qualität des Reservoirs, speziell in dichten Formationen. Frühe- und versenkungsdiagenetische Zementation mit (Eisen-) Kalzit und Dolomit reduziert die Matrixporositäten (0,16–10,58%) und Permeabilitäten (<0,0001–9,7 mD). Proben mit Stylolithen und partiell versiegelten Klüften zeigen die höchste Permeabilität (bis zu 9,7 mD bei 1,2 MPa) und erhalten bei 30 MPa Umschließungsdruck bis zu 41 % der ursprünglichen Permeabilität. Die Orientierungen der Klüfte wurden manuell aufgenommen und mit der normalisierten Korrelationszählung

analysiert. Die Clusterbildung um eine durchbrochene Knickbandverwerfungsebene ist nicht symmetrisch angeordnet und enthält Klüfte mit unterschiedlichem Streichen. Kluftcluster werden auch abseits der Verwerfung aufgezeichnet. Gleit- und Dilatationstendenzen zeigen, dass NNE-SSW, WNW-ESE und NW-SE streichende Kluftorientierungen, mit größerer Wahrscheinlichkeit zum Fluidtransport beitragen, da sie im gegenwärtigen Spannungsfeld entsprechend ausgerichtet sind. Die (durchbrochenen) umgekehrten Knickbänder sind die ersten, die in dieser Region (~180–200 km N-NE der alpinen Deformationsfront) beschrieben wurden, und stehen wahrscheinlich im Zusammenhang mit Kompression durch Fernfeldspannungen während des Eozäns.

Die Flysch-Reservoire im Wiener Becken bestehen aus mehreren Deckenüberschiebungen mit komplexen Lagerstättenkompartimenten aus Sandstein-Tonstein-Wechselfolgen. Bohrklein aus zwei Bohrungen (ca. 400 m Stratigraphie der paläozän-eozänen Greifenstein-Fm., Glaukonitsandstein, 1.–3. GLS) dient zur Ableitung von Kontrollfaktoren auf die Lagerstättenproduktivität. Die Proben werden mikroskopisch untersucht und mit Abschnitten bekannter Produktionsdaten verglichen. Die Sandsteine sind meist durch eisenhaltigen Kalzit zementiert, was zu geringer optischer Porosität (<5 %) führt. Erhöhte Porosität tritt bei teilweiser Lösung von K-Feldspat auf. Der höchste Glaukonitgehalt findet sich im 3. GLS. Die Reservoirqualität ist unabhängig von der Kompaktion. Die Tiefengenauigkeit des Bohrkleins wird durch Vergleich von pXRF (Si/Al-Verhältnis) und Gamma-Ray-Logs verbessert. Die Reservoirqualität beschränkt sich auf Klüfte und partiell versiegelte Adern; produktive Bereiche zeigen geringere Gesteinsporosität, höhere Karbonatzementierung und niedrigere Fe+Mg-Gehalte. Kluftrichtungen sind nicht ableitbar, das Vorhandensein von Kluftmineralisation und ihre interne Mikrostrukturen jedoch erkennbar.

Der Russland-Ukraine-Konflikt hat globale Lieferketten für Öl, Gas, Metalle und andere Rohstoffe unterbrochen. Beide Länder sind rohstoffreich und wirtschaftlich mit der EU und Deutschland verbunden. Die EU27 listet aktuell 34 kritische und 17 strategische Rohstoffe. Einige Rohstoffe zeigen Marktkonzentration von über 90 % in einzelnen Ländern. Russland ist bedeutend im Bergbau und in der Raffination aufgrund verfügbarer, günstiger Energie. Die Ukraine war ein wichtiger Tonerdeproduzent und belieferte ~50 % des globalen Neonmarkts vor Produktionsstopp. Untersucht werden Auswirkungen auf Lieferketten von Bauxit, Tonerde, Titan, Lithium, Edelgase, Nickel, Palladium, Platin und Vanadium. Reaktionen Südkoreas und Chinas zeigen, wie eine vorhandene Infrastruktur und Energieverfügbarkeit Engpässe ausgleichen kann: Südkoreas Stahlwerke kompensierten Neonmangel, China steigerte die Titanschwammproduktion in drei Jahren um Faktor 1,6.

Die Bergbaupotenziale von Botswana, Marokko, Namibia und Simbabwe in den Bereichen Bergbau, Verarbeitung von Bergbauprodukten und Beteiligung an Hüttenwerken werden beleuchtet, die von deutschen Investoren bisher kaum wahrgenommen werden. China

beispielsweise investiert direkt in Bergbauprojekte in Afrika, und auch Russland ist im Bergbausektor aktiv, zum Teil begleitet von militärischer Präsenz. Botswana weist vergleichsweise gute WGI-Indikatoren auf und betont den Bedarf an Investitionen, der zum Beispiel von deutschen Unternehmen bisher nicht wahrgenommen wird. Für viele afrikanische Staaten sind Bergbau und Rohstoffexporte entscheidend für das Wirtschaftswachstum.

Contents

Declaration of originality

Chapter 2: As first author Jasemin A. Ölmez extended and re-evaluated a dataset which was prepared during her graduate project. She wrote the article with inputs from Dr. Benjamin Busch and Prof. Dr. Christoph Hilgers. Discussions with both co-authors contributed to this manuscript.

Chapter 3: As first author, Jasemin A. Ölmez performed the data analysis and evaluation. Parts of the manual fracture measurements in the field were performed by students for a student field project, and a Bachelor thesis. Both were quality-controlled by the author and Dr. Benjamin Busch. She wrote the entire article with inputs from Dr. Benjamin Busch and Prof. Dr. Christoph Hilgers. Discussions with both co-authors contributed to this manuscript.

Chapter 4: As first author Jasemin A. Ölmez performed the data analysis and evaluation. Co-Author Dr. Benjamin Busch assisted during point-count analyses and evaluation. She wrote the article with inputs from Dr. Benjamin Busch, Rolf Möbius, Kanchan Dasgupta, Albert Gauer, Filippo Tosoratti, and Prof. Dr. Christoph Hilgers. The discussions with all co-authors contributed to this manuscript.

Chapter 5: As first author, Jasemin A. Ölmez performed the data analysis and evaluation. She wrote the entire article with input from Prof. Dr. Christoph Hilgers.

Chapter 6: As first author, Jasemin A. Ölmez performed the data analysis and evaluation. She wrote the entire article with input from Prof. Dr. Christoph Hilgers.

1 Introduction

For geological subsurface utilization of sedimentary rocks, the understanding of reservoir quality is crucial. It is influenced by the depositional system, fluid-rock interactions, and structural geological overprint by faults and fractures, including cementation of fractures. Understanding reservoir quality is key for successful exploration, helps to understand the economic viability of natural resources, and limits uncertainties such as exploration risks and costs in storage and production scenarios (e.g., Ozkan et al., 2011; Camp et al., 2018; Worden et al., 2018; Ciriaco et al., 2020). Reservoir quality highly depends on the use case whether a lithology should be porous and permeable or sealing. A reservoir rock for exploitation of hydrocarbons, geothermal energy or for CO_2 storage from CCS (carbon capture and storage) should be porous and permeable. Top seals and lateral seals of tight rocks are important to constrain the migration of such fluids. Furthermore, impermeable lithologies are required for nuclear waste disposal or rising mine water levels. The combined structural and diagenetic alteration are a function of basin history and fluid-rock interaction. As a result, petrophysical properties such as porosity and permeability vary between sedimentary basin, across basins and within reservoirs in a basin (e.g., Quandt et al., 2022). Besides the interconnected pore space in sedimentary rocks, natural fractures play an important role. Especially for reservoir exploitation in tight formations, fractures act as the main fluid conduit besides faults (e.g., Narr, 1996; Olson et al., 2009; Bahrami et al., 2012; Lamarche et al., 2012; Lavenu et al., 2013; Khelifa et al., 2014; Becker et al., 2018; Busch et al., 2019).

Furthermore, with a geological perspective, the value chains from mines to smelters are explored in two chapters, which summarize a more extensive study for the Think Tank Industrial Resources Strategies (TTirs). Growing world population and increasing prosperity demands for more raw materials and energy, which are essential for modern life, and further improve the developed standard which has had to be built up over decades (BMWi, 2021). Technologies are constantly evolving; digitalization and the energy and mobility transition are causing an increase in demand and variability for raw materials. Additionally, industrially driven countries such as Germany want to increase the proportion of recycled materials in all areas at the same time. The International Energy Agency estimates that the demand for critical metals and industrial metals will triple by 2050 for the “net zero scenario” (IEA, 2023). Not every material including metals can be recycled and provided as secondary raw material, as suitable technologies are missing or technically not possible (e.g., Tercero Espinoza, 2012; UNEP, 2013; Reuter et al., 2019). For many critical raw materials the recycling rate is low, as e.g., less than 1% of rare earth elements are recycled (Eurostat, 2022; Geng et al., 2023). Resilient access to and resilient supply chains for raw

materials are essential for an industrialized country like Germany, but also for other countries with a high share of GDP in the manufacturing industry such as China, Japan, the USA and South Korea, in order to remain competitive. This is jeopardized by price and supply risks of raw materials and energy. There are currently no large, internationally active mining companies in the field of metallic raw materials based in Germany and EU27. To avoid supply bottlenecks the source of raw materials must be diversified.

1.1 Motivation

In this work, rock properties from sedimentary reservoir rocks are studied to derive reservoir-specific diagenetic and structural controls affecting reservoir quality. These are addressed in three chapters in part I of this thesis.

The second part (part II) of this thesis addresses the critical raw material supply chain. This covers an analysis of the interaction of supply and demand of selected raw materials and how they are affected by the Russia-Ukraine conflict, and how selected African countries may contribute to global raw material supply.

Addressing both the STEEL-PEG (social, technological, ecological, economic, legal, political, ethical, geological) may aid in defining required future developments, and result in more resilient supply chains for geoenergy applications and georesources.

1.2 Research questions

Part I – Reservoir quality assessment

Part I of this thesis evaluates the location specific influences of faults, fractures, fracture cementation, and (structural) diagenetic overprint on fluid flow behaviour in the subsurface in three different use cases in Central Europe. The main questions that will be answered are:

- Are Upper Cretaceous limestones in the Münsterland Cretaceous Basin, which are unconformably overlying coal-bearing Upper Carboniferous lithologies, baffles for rising mine water levels? Are fractures affecting fluid pathways in the studied lithology, or are they pervasively sealed? How can compaction be classified in intraporous bioclastic carbonate rocks?

- Which controlling factors affect fluid migration in fractured Middle Triassic Upper Muschelkalk lithologies? What is the influence of partially sealed veins and stylolites on fluid flow? Are higher fracture intensities (i.e. fracture clusters) only restricted to the vicinity of faults? Are all fracture clusters likely to contribute to fluid flow?
- Can cuttings be used to perform structural diagenetic studies and for fingerprinting of producing and non-producing intervals? Can cuttings deliver supporting arguments to clearly define the studied sections of Vienna Basin Flysch play as a fractured reservoir and highlight the main fluid conduits? Can cuttings be used to define paragenetic sequences, as cuttings are so far underutilized samples, but the most abundant sample type from the subsurface.

Part II – Raw materials

Part II of this thesis evaluates the effect of geopolitical conflicts on global raw material supply chains based on a literature study published as booklets (in German) in the publication series of the Think Tank Industrial Resources Strategies (TTirs), and the mining potential in African nations in relation to country-specific resource availability and current developments. The main questions that will be answered are:

- Does the Russia-Ukraine conflict affect global raw material supply?
- What are the strategic plans of the EU to secure the supply with critical and strategic raw materials?
- Which options are available to diversify raw material supply chains? What factors are limiting the extension of domestic raw material processing?
- What is the mining potential of selected African countries at different stages in terms of ethical, societal, political, and economical situations? What are common cultural differences that previously limited the extension of European raw material cooperation's with African countries?
- Did specific business models, that have been successfully established in African countries, lead to increased prosperity and well-being? What is the ongoing research and development cooperation between European and African partners?

1.3 Aims

Part I – Reservoir quality assessment

The aim of part I of this study is to enhance the understanding of diagenetic and structural controls on reservoir quality in naturally fractured tight carbonate and clastic lithologies using outcrop analogs and drill cuttings. The understanding is relevant for geothermal applications, reservoir utilization, gas storage scenarios, and the assessment of the influence of rising mine water levels. Therefore, three study locations in different settings, the Münsterland Cretaceous Basin, the southern Germanic Basin (now exposed on the eastern shoulder of the Cenozoic Upper Rhine Graben), and the Vienna Basin are studied in detail.

Especially in tight lithologies the understanding of fractures on fluid flow needs to be considered. To assess the influence of natural fractures on reservoir quality two outcrop analogs from the Münsterland Cretaceous Basin and the southern Germanic Basin are studied, the rocks are furthermore petrographically analyzed and linked with petrophysical laboratory data. Additionally, for the Muschelkalk lithologies from the southern Germanic Basin, fracture cluster and their relation to the vicinity of a fault are analysed, as well as the potential influence of the present-day stress field. The formation of a compressive conjugate reverse kink-band north of the alpine deformation front is discussed. In addition, the analysis of petrophysical and petrographic data in relation to early and burial diagenetic alteration enables reservoir rock typing.

Cuttings are provided during drilling of every well and are only macroscopically assessed as a standard workflow. To enhance the information gain in reservoir scenarios, cuttings are also petrographically analyzed to study detrital and authigenic rock compositions, the (structural) diagenetic sequence and to derive geochemical fingerprints using portable X-ray fluorescence (pXRF). No published data on the (structural) diagenetic overprint for the studied glauconite sandstone (1. to 3. GLS, Greifenstein Fm.-equivalent) from the Flysch play in the Vienna Basin is available and strict reservoir quality controls are poorly defined. The current working hypothesis is that the studied lithologies act as fractured reservoirs. Hence, based on cuttings from two wells, a detailed paragenetic sequence is established and microstructural observations linking production behaviour to partially sealed microfractures are evaluated.

Part II – Raw materials

The aim of the second part of this study is to analyze the current critical and strategic raw material supply chains, benchmarks of the EU's critical raw materials act, and mining potentials. As the global raw material supply is affected by geopolitical actors, conflicts, global pandemics, the geological distribution of resources, and variable market prices, state

or region-specific guidelines or policies, successfully achieving the set goals may become challenging. Georesources including geofluids are still the basis of modern-day life and will become increasingly more important in achieving the UN's 17 sustainable development goals. In light of these goals, the mining potential in e.g., African countries should also try to fulfill the benchmarks during resource exploitation. The second part therefore address STEEPLE and geological aspects (STEEL-PEG), as the societal, ethical, political, and economical aspects of georesources. The EU defined 34 critical and 17 strategic raw materials, and four benchmarks for strategic raw materials set for 2030 as (1) a minimum of 10% of the EU's annual consumption of strategic raw materials has to originate from EU mines, (2) a minimum of 40% of the EU's annual consumption of strategic raw materials has to originate from EU processing, (3) a minimum of 25% of the EU's annual consumption of strategic raw materials has to originate from domestic recycling and (4) a maximum of 65% of the EU's annual consumption of a strategic raw material at any relevant stage of processing is allowed to originate from a single third country as written in the "Regulation (EU) 2024/1252" of the European Parliament and Council of April 11, 2024 (European Union, 2024).

Russia and the Ukraine host large amount of natural resources, mining and refinery capacities, and both had economic ties with Germany. The Russia-Ukraine conflict has heightened geopolitical tensions, and impacted the supply of raw materials for industries relying on oil and gas but also metals. The Ukraine was one of the largest exporters of neon globally, which is needed e.g., for semiconductor manufacturing. Russia's inexpensive energy is used to refine metals such as aluminium, which are than exported. However, it is shown that, if stockpiling and heavy industry infrastructure such as existing steelworks are present, shortages can be counterbalanced. Countries that not only hosts natural resources but are also socially and politically stable may be considered in order to build a resilient supply chain. African countries such as Botswana, Morocco, Namibia, and Zimbabwe offer various opportunities to secure raw materials through mining, the processing of mining products and participation in smelters. However, these opportunities are hardly being taken up by German investors today, meaning that investments are coming from other countries that are thus generating secure access to raw materials.

1.4 Objectives

Part I – Reservoir quality assessment

The Upper Cretaceous and Middle Triassic Upper Muschelkalk to Lower Keuper limestones are studied petrophysically for porosity and permeability using He-pycnometry and an air permeameter, and petrographically using a transmitted light microscope, reflected

light microscope and cold cathodoluminesence to assess the (structural) diagenetic history. Fracture orientation for both outcrop analogs are assessed using a manual compass, and for the Upper Cretaceous additionally drone images.

For the Upper Cretaceous, one quarry in the Münsterland Cretaceous Basin was studied. In total, 49 thin sections, and 74 porosity and permeability measurements on plugs are carried out. Fracture orientation is measured including veins (N=499). This study focusses mainly on porosity and permeability variations in comparison to the structural and diagenetic history (incl. cementation, compaction, and fracture orientation).

For the Middle Triassic Upper Muschelkalk to Lower Keuper porosity and permeability values of 109 plug samples from a quarry on the eastern Upper Rhine Graben shoulder are studied. In total, 30 thin and thick sections are analyzed petrographically. Fracture orientations including veins (N=576) are measured with respect to the recorded vertical lithological columns, as well as on scan lines where one scan line was placed parallel to a wall with a breached compressional conjugate reverse kink band and the other scan line was placed on a perpendicular wall without heterogeneities as faults to investigate if clustering is only restricted to faults and their fault damage zone. In this work, the focus is on petrophysical and petrographic analyses to understand the (structural) diagenetic history, and structural analysis to understand the paleo-stress influence with respect to future application, if the same fracture sets are available in the subsurface.

Drill cuttings have a high potential to be used for rock characterization where drill cores are missing. Petrographic analyses of cuttings using thin sections allows the determination of grain sizes and sorting, but also the determination of the (structural) diagenetic history. With regard to the Paleocene-Eocene Greifenstein Fm. equivalent (Glauconite Sandstone, GLS) from the Vienna Basin in Austria 83 cutting samples from two wells, covering ~400 m of stratigraphy are studied. For the 1.–3. GLS series, the detrital composition and thus rock composition (QRF) varies between subarkose to sublitharenites to feldspathic litharenites and subordinary litharenites and one lithic arkose. Samples from well 1 shows higher quartz content than samples from well 2. Petrographic analyses reveal the impact of (structural) diagenetic processes and thus cementation, dissolution, and compaction on reservoir quality.

All investigated samples either from outcrop or the cuttings from two wells are mostly pervasively cemented by mostly ferroan calcite and calcite. Analyzing vein material under the microscope and using cold cathodoluminescence, the cross-cutting relationships and therefore the paragenetic sequence of vein composition and growth is constrained.

Part II – Raw materials

The current supply of raw materials is examined using selected examples (alumina, bauxite, titanium, nickel, noble gases, palladium and platinum, vanadium) using open access data as e.g., reports, data platforms, articles and trading websites. Stable supply chains are important for a resilient supply, especially for industrialized nations such as Germany, where the storage of critical raw materials is not politically secured. Information about global and EU needs on raw materials are combined from reports by e.g., DERA, BGR or OECD. Political statements are mostly based on Government announcements and reports. Using the example of the Russia-Ukraine conflict, the production countries for mining and smelting products are shown for selected raw materials using data from USGS mineral commodities and trading data as e.g., from UN Comtrade.

The supply chains are examined and how nations with different strategies compensate for possible shortages or shortfall, as shown for the example of neon from Ukraine, where a steel manufacturer in South Korea started to produce their own neon and now develops a recycling process for neon to reduce dependencies. At the same time, the importance of countries with unexploited mining potential is growing in the search for strategic partnerships to diversify the supply of raw materials, as also addressed by the EU in the Critical Raw Materials Act and its benchmarks. For this, selected African countries (Botswana, Morocco, Namibia, and Zimbabwe) are selected to illustrate the role of China and Russia in the mining industry. For example, Botswana is a country rich in raw materials with a stable political situation, but direct investments in mining from Germany or the EU27 is lacking. To illustrate social and political factors the Worldwide Governance Indicator from the World Bank is used.

1.5 Summary

Part I – Reservoir quality assessment

Carbonate rocks in the German Münsterland Cretaceous Basin

Sedimentary Cretaceous rocks in the Münsterland Cretaceous intracratonic basin (Fig. 1.1) unconformably overly folded Upper Carboniferous formations, the latter was mined over decades for hard coal. The Cretaceous sedimentary basin composed of marly claystone, marls and limestones is discussed to have a sealing character on the northernmost extent of the former coal mining district of the Ruhr area. The rocks are interpreted to decouple rising mine-water levels or gas seepages from ground water horizons (Rudolph et al., 2010; Coldewey and Wesche, 2017). The sedimentary rocks of the Upper Cretaceous in the Münsterland Cretaceous Basin have so far been studied regarding lithological, stratigraphic, and paleontological questions (e.g., Giers, 1958; Arnold et al., 1960; Voigt and Häntzschel, 1964; Wolf, 1995; Kappel, 2002; Kaplan, 2004; Wilmsen et al., 2019; Püttmann and Mutterlose, 2021). Furthermore, previous mineralogical analyses focused on identifying mineable formations for the cement industry. Therefore, data on the impact of diagenesis and compaction on fluid flow properties are not available. An outcrop analog was selected to provide data on the fracture network, the diagenetic alteration, and the effect of diagenesis and compaction on hydraulic properties of the exposed Campanian lithologies. The Campanian limestones show a diagenetic overprint, resulting in low porosity and permeability values (Fig. 1.2). Therefore, only fractures might enhance reservoir quality by providing fluid pathways (Fig. 1.3). The studied fractures are mostly pervasively sealed by (Fe-)calcite and strontianite.

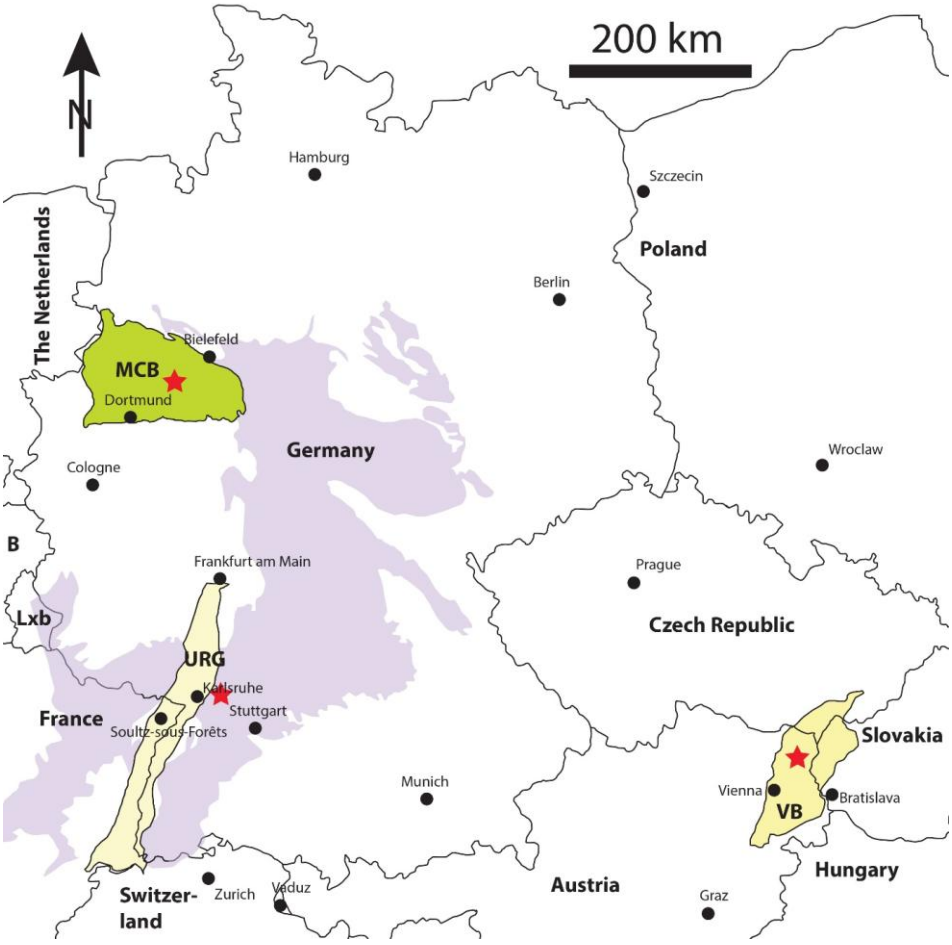

Figure 1.1 Overview map of study locations and basins. The Münsterland Cretaceous Basin (MCB, green fill for Cretaceous) is located in NW Germany, the star marks the Beckum quarry. The Upper Rhine Graben (URG, yellow for Quaternary) is located in SW Germany, France and Switzerland, the study location is situated on the eastern graben shoulder. The Knittlingen quarry is marked with a red star next to Karlsruhe. The distribution of Triassic lithologies in outcrops is given in purple. The Vienna Basin (VB, yellow for Tertiary) is located in NE Austria and parts of Czech Republic and Slovakia, the two investigated wells are located north of Vienna (red star). The map is redrawn and modified after BGR (2025) „Geoportal der Bundesanstalt für Geowissenschaften und Rohstoffe“. Lxb – Luxemburg.

Carbonate rocks in the SW-Germanic Basin: Middle Triassic Upper Muschelkalk and Lower Keuper

The Eocene to recent Upper Rhine Graben (Fig. 1.1) rift basin was traditionally of interest for hydrocarbon exploration and exploitation (e.g., Reinhold et al., 2016; Böcker et al., 2017). In recent years, the Upper Rhine Graben is increasingly becoming the focus for geothermal exploration (Kushnir et al., 2018; Harlé et al., 2019; Heap et al., 2019), as the graben hosts the largest geothermal anomaly in Germany (Clauser and Villinger, 1990; Pribnow and Schellschmidt, 2000). High geothermal gradients exceed 100 K/km in certain areas atop the Triassic sedimentary rocks, such as at Soultz-sous-Forêts in France (Pribnow and Schellschmidt, 2000) or ~90 K/km in Landau (Vidal et al., 2018). In the pre-Jurassic Mesozoic and Palaeozoic sedimentary succession and underlying hydrothermally altered granites geothermal gradients in the active hydrothermal system reduce to approximately 10 K/km, before reaching 30 K/km in the deep granitic basement (Vidal et al., 2018). Fluid migration pathways are related to faults and fractures, with elevated fracture permeability in active fault zones (Frey et al., 2022) while convection cells are expected to also rely on fractures in the Triassic lithologies below the Keuper claystones (Vidal et al., 2015). Although the Middle Triassic Muschelkalk rocks are located at sufficient depths within the Upper Rhine Graben and are expected to host relevant temperatures for geothermal usage (Stober and Bucher, 2015), geothermal projects so far mostly focused on the deeper crystalline basement, Permian Rotliegend, or Triassic Bunter formations (Vidal and Genter, 2018; Frey et al., 2022).

The petrography, facies or sequence stratigraphy for Upper Muschelkalk lithologies in the southern part of the Germanic Basin (Fig. 1.1) are well constrained but highlight some heterogeneity in the amounts of cements (Vollrath, 1938; Brüderlin, 1970; Mehl, 1982; Seufert, 1984; Aigner, 1985; Brunner and Simon, 1985; Seufert and Schweizer, 1985; Aigner, 1986; Aigner and Bachmann, 1992; Geng and Zeeh, 1995; Geng, 1996; Zeeh and Geng, 2001; Hagdorn and Simon, 2021). The Germanic intracontinental basin formed due to thermal relaxation from the Rotliegend to the Muschelkalk, after a post-Variscan rifting phase in the late Carboniferous to earliest Permian (Scheck and Bayer, 1999). At the Soultz-sous-Forêts geothermal site (Fig. 1.1), Lower and Middle Muschelkalk lithologies were studied for their petrophysical, thermal, and geomechanical properties (Heap et al., 2019). Diagenetic studies on the Upper Muschelkalk exposed on the Eastern Upper Rhine Graben shoulder mainly focused on dolomite formation during burial and uplift (Geng and Zeeh, 1995; Geng, 1996; Zeeh and Geng, 2001). However, the understanding of the influence of diagenetic processes on reservoir quality for Upper Muschelkalk lithologies in this region is limited. Developing a carbonate reservoir is often challenging, as they are often heterogenous, making predictions difficult (e.g., Burchette, 2012; Garland et al., 2012).

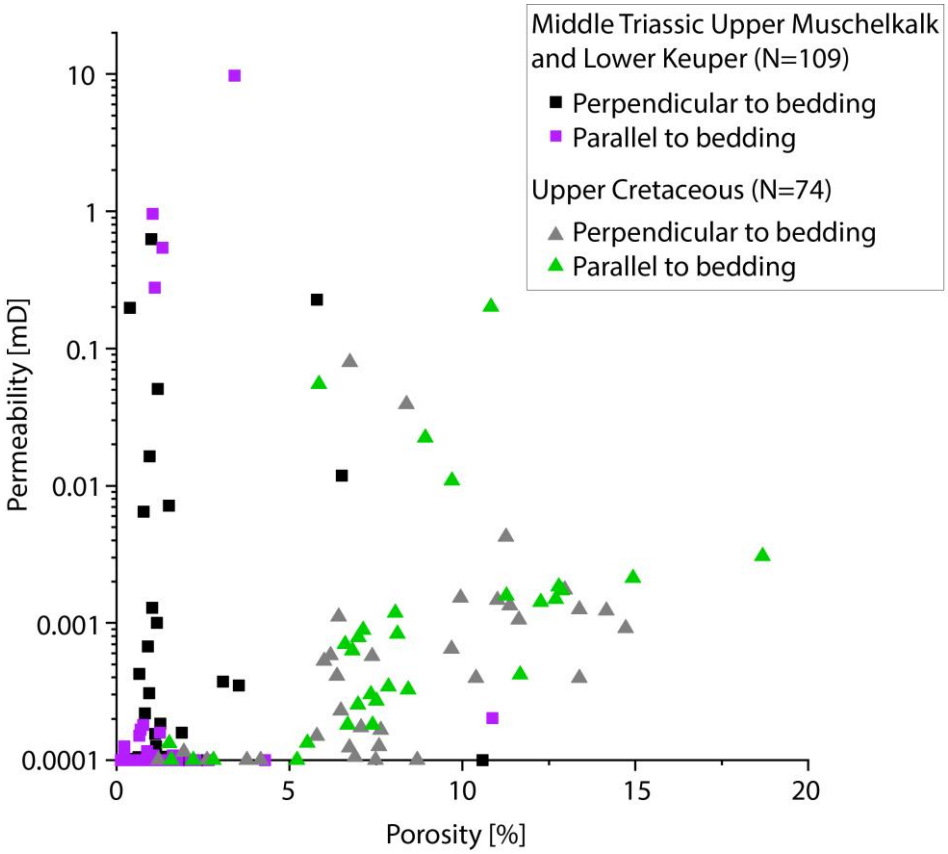

Figure 1.2 He-porosity and permeability (1.2 MPa confining pressure, Klinkenberg-corrected, 1-inch diameter plugs) cross-plot of Upper Cretaceous, Middle Triassic Upper Muschelkalk and Lower Keuper limestone samples.

Most carbonate reservoirs are naturally fractured reservoirs (Lamarche et al., 2012), but the understanding about fracture orientation and clustering within the Upper Muschelkalk in Germany is sparse. Open fractures are given as the preferred fluid pathways in tight rocks such as the studied Upper Muschelkalk lithologies. Therefore, fracture networks are of interest in e.g., geothermal energy production, hydrocarbon recovery, gas storage, and groundwater reservoir assessment, as they improve the reservoir quality (Narr, 1996; Laubach et al., 2004; Bahrami et al., 2012; Lamarche et al., 2012; Khelifa et al., 2014; Carlos de Dios et al., 2017). Although previous studies highlight fracture corridors to be important in Mesozoic lithologies in the Upper Rhine Graben area (Reinhold et al., 2016), reliable data on fracture spacing and clustering are not available. However, fracture clusters have been shown to be important for the success of reservoir development (Narr, 1996; Li

et al., 2018; Marrett et al., 2018). Furthermore, the ability of faults and fractures to transmit fluids is governed by the current stress field (e.g., Barton et al., 1995; Finkbeiner et al., 1997; Mattila and Tammisto, 2012) and has been shown to be effective in controlling fluid migration pathways in the Upper Rhine Graben (Allgaier et al., 2023a).

In an outcrop analog on the eastern graben shoulder Upper Muschelkalk and Lower Keuper limestones are studied to derive controlling factors on host rock and partially sealed fracture permeability, the fracture intensity of the five most frequent fracture sets (based on strike orientation) in association to faults and in the undisturbed host rock, the dilation and slip tendency of fracture sets in the present day stress field, and to deliver first measurements on the permeability preservation of partially sealed fractures, and stylolites at up to 30 MPa confining stresses. The Upper Muschelkalk and Lower Keuper limestones illustrate a diagenetic overprint mostly by cementation with (ferroan) calcite and/or dolomite which reduces porosity and permeability (Fig. 1.2). Fracture strike is studied as fractures may enhance reservoir quality by providing fluid pathways, if oriented suitable in the present-day stress field (Fig. 1.3).

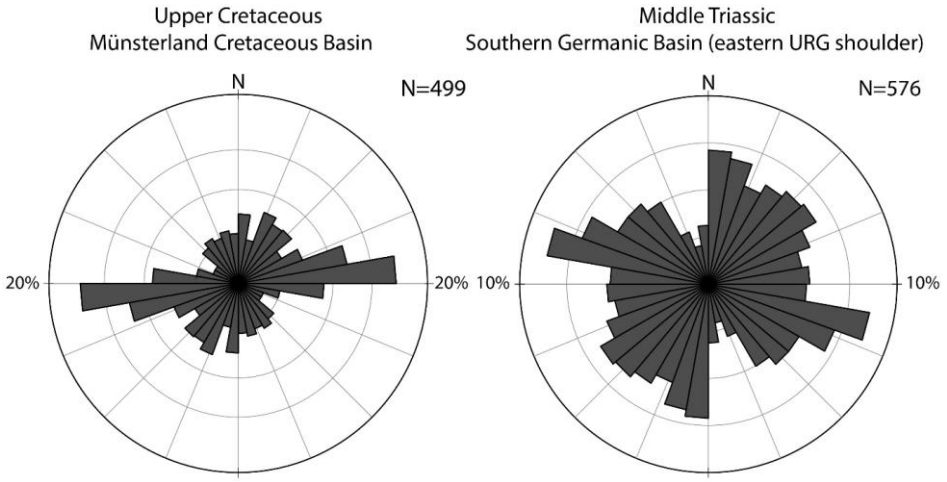

Figure 1.3 Fracture strike of Upper Cretaceous (chapter 2, Beckum quarry) and Middle Triassic (chapter 3, Knittlingen quarry) Upper Muschelkalk to Lower Keuper lithologies plotted as rose diagrams.

Clastic turbidite rocks of the Flysch play in the Austrian Vienna Basin

The Vienna Basin is a strike-slip pull apart basin and a major hydrocarbon province in Central Europe (Fig. 1.1), with exploration starting 150 years ago, and first economically producible discoveries of conventional oil and gas fields were made in the early 1930s

(Arzmüller et al., 2006; Rupprecht et al., 2017; Möbius et al., 2023). Since the 20th century, about 6000 wells have been drilled (Arzmüller et al., 2006), making the Vienna Basin a well-studied area in terms of the stratigraphic history and depositional settings (see Harzhauser et al., 2020 and references therein). However, the understanding of reservoir rock properties in sandstone reservoirs in the flysch is challenging due to small scale reservoir compartmentalization and the lack of comprehensive data within the flysch. The primary composition of sandstones is controlled by several factors e.g., the provenance, the depositional system, transport energy and distance, grain size and sorting, which can affect reservoir properties (e.g., Dickinson and Suczek, 1979; Coskun et al., 1993; Johnsson, 1993; Bjørrlykke, 1998; Griffiths et al., 2019; Lupin and Hampson, 2020). Diagenetic alteration due to compaction, cementation and dissolution can overprint the primary sedimentary controls, resulting in improvement or reduction of given matrix permeability and porosity (e.g., Bjørlykke, 1988; Coskun et al., 1993; Dutton and Loucks, 2010; Morad et al., 2010; Busch et al., 2024). Predictive and reliable controls on reservoir quality for the Flysch play in the Vienna Basin are not established so far, which leads to a challenge for well planning, as finding high reservoir quality intervals with open or partially sealed fractures is complex and can only partially be resolved by seismic data (Möbius et al., 2023).

Although fracture or vein orientations cannot be reconstructed from drill cuttings, the presence of partially sealed veins in specific formation sections can be identified and used for reservoir quality assessments. Core runs typically do not exceed 20 m, while drill cuttings are often continuously sampled along the whole well, covering the up to 750 m thick glauconitic sandstone series which, due to alpine nappe stacking, appears twice or thrice in certain areas (Wessely, 2006). Cuttings are generally used to better understand the reservoir performance based on optical assessment (Rupprecht et al., 2017). Drill cuttings can be used to classify the rocks and distinguish different rock types in formations (Fig. 1.4). Fractures are commonly present in the two investigated well sections (Möbius et al., 2023), therefore fracture and vein characteristics are interpreted to influence reservoir quality and thus productivity. Additionally, using a portable X-ray fluorescence device to analyze the geochemical compositions, a depth correction between cuttings and gamma ray well logs can be achieved. This improves the understanding of reservoirs, controlled by fractures and partially sealed veins. However, this research approach is not only applicable to hydrocarbon production, but also to the future development in the Vienna Basin towards deep geothermal energy, for which high flow rates are required and therefore an understanding of fractures or partially sealed veins.

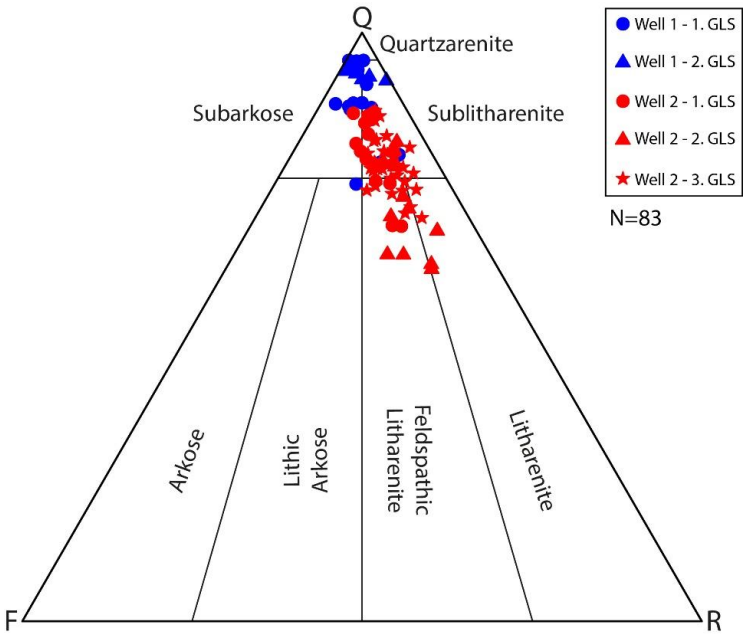

Figure 1.4 Detrital composition for sandstone drill cuttings derived from thin section analyses (Q=quartz, F=feldspar, R=rock fragments, in %).

Part II – Raw materials

In addition to geofluids such as geothermal brine, hydrocarbons, sequestered CO_2, among others, raw materials such as metals, and their availability in a geopolitical context are important for e.g., the planned energy transition. Frequently reservoir rocks and metals precipitates are related. The previously studied Münsterland Cretaceous Basin lithologies are not only relevant as cap rocks for potential rising mining water, but were also the host lithology for strontianite veins, which were mined from 1871 onwards. At that time, strontianite was extracted in around 700 mines in the region, the last mine extracted the last 70 tons of strontianite from the Münsterland in 1945 (Börnchen, 2007). Today, strontium is a critical raw material according to the EU27 Critical Raw Materials Act (CRMA) list (European Union, 2024).

In the Upper Rhine Graben, Vulcan Energy Resources Ltd. are pursuing the approach of using the extracted thermal water to additionally produce battery grade lithium (Vulcan Energy, 2025). Lithium is a critical and strategic raw material, and the company's "Zero Carbon Lithiumproject" is one of the 47 strategic projects supported by the EU to secure the supply of strategic raw materials from domestic sources (European Commission, 2025). Critical raw materials have an increased supply risk but are essential for the implementation

of the EU's economic goals with its most relevant industrial sectors renewables, e-mobility, energy industry, information & communication technology (ICT), and aerospace & defense (Europäische Kommission, 2021; European Commission, 2023). The currently funded 47 strategic projects are a possible step towards diversification and enhancement of recycling within the EU countries. But imports from third countries still remain essential and the recent as well as future enhanced demand cannot be supplied by recycling and circular economy alone.

The production of individual critical raw materials and thus the market concentration are often over 90% in individual countries (Europäische Kommission, 2023b). However, most of the raw materials with a high market concentration originate from countries that do not adhere to German or EU regulations regarding human rights, environmental protection or safety aspects. A high market concentration is particularly at risk during supply bottlenecks or shortfall (Europäische Kommission, 2023b). Countries as e.g., South Korea demonstrate the importance of hosting domestic heavy industry, as the production capacities of domestic steel mills were able to establish the production of the missing noble gases for the chip industry. Additionally, the stockpiling of critical raw materials can ensure against supply bottlenecks or failures, where feasible. An energy-intensive smelting and refining industry is required for recycling, which requires sufficient amounts of recyclable materials from high-quality waste and primary raw materials. For this, the access to reliable and affordable energy is required. In light of this, countries like China were able to significantly increase their titanium sponge production in three years (2021–2024) by a factor of c. 1.6 (USGS, 2023, 2025), when Russian and Ukrainian supply was reduced. Due to the EU's inability to mine and refine the full demand of the critical raw materials domestically, foreign trade will remain necessary (Europäische Kommission, 2023b). Diversifying EU imports, reducing market concentrations, and improving the European value chain for strategic and critical raw materials are the objectives of the European regulation on critical raw materials (Europäische Kommission, 2023b). The EU is supporting bilateral agreements with third countries and local supply chains to reduce reliance on market concentrations, which calls for both short and long-term actions (Europäische Kommission, 2023c). Direct partnerships or direct investments in mining, also in third countries not only within the EU member states, could also be formed with countries that have undeveloped mining potential. Botswana, for example, might play a crucial role here, as this country is rich in raw materials, and shows a relatively stable political and social environment. Therefore, assessing the effect of current geopolitical conflicts on raw material supply chains and the possibilities for mining collaborations in African countries may outline future potentials for a more resilient and reliable supply chain regarding critical and strategic raw materials. None of the raw materials are considered to run short in supply due to adaptation strategies, based on alternative mines, smelters and refineries, and associated industries.

1.6 Overview of the thesis

1.6.1 Reservoir quality of Upper Cretaceous limestones (Ahlen-Fm., Beckum Member, Münsterland Cretaceous Basin): Effects of cementation and compaction on the compactable depositional volume

In this chapter the reservoir quality of Upper Cretaceous limestones (Campanian) is studied, as the Upper Cretaceous lithologies in the Münsterland Cretaceous Basin in NW Germany unconformably overlie folded Carboniferous lithologies, currently affected by rising mine water levels. Petrophysical and petrographic heterogeneity and their effect on possible fluid migration pathways for e.g., rising mine water is analyzed. Early diagenetic cementation, compaction and the individual formation of compaction bands of deformed and cemented calcispheres around ductile clay mineral laminae result in low matrix porosity (1.0% to 18.7%) and permeability (<0.0001 mD to 0.2 mD). Using cold cathodoluminescence, host rock and vein cementation is analyzed for cross-cuttings relationship and textures. The compaction of bioclasts derived from petrographic analyses with original intraparticle porosity are described using the compactable depositional volume (CDV) for carbonate rocks, which may be a useful tool to assess the timing of cementation in relation to compaction and to assess the effect of compactional volume loss on reservoir properties. Partially sealed fractures sealed by (ferroan) calcite and strontianite are preferentially NW-SE oriented, and are discussed to originate most likely due to Late Cretaceous inversion and reactivation of fault systems. The Upper Cretaceous limestones may act as baffle against increasing mine-water levels from dismantled, post-mining subsurface hard coal mines in the region, if not faulted and containing fractured damage zones.

1.6.2 Structural and diagenetic controls on fluid pathways in fractured Triassic Muschelkalk and Keuper limestones, southern Germany

This chapter combines petrographic and petrophysical data with fracture analysis in a quarry on the eastern Upper Rhine Graben shoulder which exposes Middle Triassic Upper Muschelkalk to Lower Keuper limestones in SW Germany. The outcrop analog is studied to understand the diagenetic and structural interactions in formations that are also found at depth in the Upper Rhine Graben, which is of interest for geo-energy production (geothermal and hydrocarbons). Cementation and compaction occurred during early and burial diagenesis and reduced the matrix porosity (0.16% to 10.58%) and permeability (<0.0001 mD to 9.7 mD). As partially sealed veins are interpreted to maintain fracture

porosity, the impact of increasing confining stress on the permeability of undisturbed limestones, as well as limestones containing stylolites, and partially sealed veins are analyzed. Cross-cutting relationships and textures on host rock and vein cementation is analyzed using cold cathodoluminescence. It is shown, that a sample with a partially sealed vein preserve higher permeability at 30 MPa confining stress (41% of initial value, compared to 16% for stylolite and 11% for an undisturbed host rock of the initial value). Fracture orientation is analyzed using the normalized correlation count method (NCC) and shows, that fracture clustering does not only occur in fracture sets striking parallel to fault strike or only in the vicinity of faults, but also in a wall without a fault. Slip and dilation tendencies indicate that clustered fracture sets striking NNE-SSW, WNW-ESE, and NW-SE are more likely to contribute to fluid flow under present-day stress. (Breached) conjugate reverse kink bands are interpreted to be caused by compression by far field stresses induced by the Alpine orogeny during the Eocene. Microstructural analysis on thin section from veins of the breached kink band show cemented fault planes, and euhedral crystal facets, indicating locally persevered pore space.

1.6.3 Reservoir characterization and well production proxy analyses on drill cuttings: Case study from the Flysch play in the Vienna Basin (NE Austria)

In this chapter drill cuttings from two hydrocarbon wells in the Vienna Basin in Austria are analyzed for petrographic properties and compared to sections of the wells with known production data. The wells target the Paleocene-Eocene Greifenstein-Fm. equivalent (Glauconite Sandstone, GLS) and cover ~400 m of stratigraphy covering sections from three different reservoir sections (1. to 3. GLS). Cuttings are continuously available during drilling, unlike core material, and they still allow a semi-quantitative determination of rock properties from the subsurface but are often underutilized. Fracture and vein orientation cannot be reconstructed from drill cuttings, but their presence and their internal texture (open, partially sealed, sealed) and some cross-cutting relationships in specific formation sections can be identified and analyzed, e.g., using combined transmitted light microscopy and cathodoluminescence. Vein texture and composition can be linked to known areas of production for petrographic reservoir quality assessments. Borehole gamma ray logs in combination with handheld portable X-ray fluorescence (pXRF) analyses on cleaned and dried drill cuttings is used to improve the depth accuracy of the cutting samples and to geochemically fingerprint the samples based on the Si/Al ratio, which is a proxy for sandstone-rich and mudrock-rich sections. The diagenetic variation and the geochemical fingerprint by pXRF from cuttings are linked to reservoir quality and production performance of individual well perforations and can thus provide additional information on reservoir quality where core material is unavailable. The reservoir quality in the studied section is

discussed to be independent of the detrital and authigenic mineralogy of the studied sandstone cuttings and only related to fractures and partially sealed veins. Productive intervals in this study are related to lower Fe+Mg ratios obtained from pXRF.

1.6.4 Effects of the Russia-Ukraine conflict on the supply of selected raw materials

This chapter presents the effects of the Russia-Ukraine conflict on the supply of selected raw materials (bauxite and alumina, titanium, lithium, noble gases, nickel, palladium and platinum, vanadium). In 2022, the Russia-Ukraine conflict has heightened geopolitical tensions, resulted in war, and influenced global supply chains of raw materials such as oil, gas, and metals. Russia and the Ukraine are resource-rich countries, both with long-standing economic ties to Germany and important exporter of raw materials to the EU. Russia has a large global share in mining and refining of nickel and vanadium, while aluminium ore (bauxite), alumina, and titanium ore are imported to Russia, and are refined and exported using the available and inexpensive energy. Ukraine was a large producer of alumina, and exporter of the noble gas neon with a global market share of around 50%, which came to a halt. The example of South Korea's steel industry reveals, that if existing stockpiling and infrastructure construction at existing steelworks are present, shortages can be counterbalanced, as shown for the noble gas neon. The EU27 member states requests to reduce reliance on third nations, increasing mining awareness among EU countries and signing strategic agreements for critical and strategic raw materials, which is possibly accelerated by the Russia-Ukraine conflict. China shows, that if production capacities are present and reliable and cheap energy can be ensured, the production of titanium sponge could be increased by a factor of c. 1.6 within three years.

1.6.5 Resilient supply of critical and strategic raw materials for Germany – Potentials in Africa

This chapter highlights the potential of selected African countries Botswana, Morocco, Namibia, and Zimbabwe on mining, processing of mining products and participation in smelters, which are to date barely recognized by German investors. China directly operates and invests in mining projects in African countries. Russia is also actively involved in the mining sector in African countries. However, some of which are accompanied by a military presence. The share of German imports of over 10% of industrial metals and metal alloys from African counties, and mining/processing data from USGS mineral commodities highlights the importance and potential of individual countries. The Worldwide Governance Indicator data from the World Bank and the Mining Contribution Index map gives information about the current evolution stage of the selected countries and how important the

mining sector is for the country's economy. African countries host large volume of resources, of which some that are still unknown but could be developed through responsible mining.

1.7 Parts of this thesis which have been published

Articles

Ölmez, J.A., Busch, B., Möbius, R., Dasgupta, K., Gauer, A.L., Tosoratti, F., Hilgers, C., 2025, Reservoir characterization and well production proxy analyses on drill cuttings: Case study from the Flysch play in the Vienna Basin (NE Austria), Energy Geoscience 6, 100461, doi: 10.1016/j.engeos.2025.100461.

Ölmez, J.A., Busch, B. & Hilgers, C., 2024, Reservoir quality of Upper Cretaceous limestones (Ahlen-Fm., Beckum Member, Münsterland Cretaceous Basin): Effects of cementation and compaction on the compactable depositional volume. International Journal of Earth Sciences (Geol Rundsch) 113, pp. 2207–2232, doi: 10.1007/s00531-024-02411-z.

Ölmez, J.A., Hilgers, C., 2024, Resiliente Versorgung Deutschlands mit kritischen und strategischen Rohstoffen – Potentiale aus Afrika / Resilient supply of critical and strategic raw materials for Germany – potentials in Africa, GDMB, World of Mining – Surface & Underground 76 No. 2, pp. 101–107.

Ölmez, J.A., Hilgers, C., 2024, Resilient supply of critical and strategic raw materials for Germany – potentials in Africa, GDMB, World of Metallurgy – ERZMETALL 77 No. 2, pp. 113–120.

Manuscripts in review

Ölmez, J.A., Busch, B., Hilgers, C., Structural and diagenetic controls on fluid pathways in fractured Triassic Muschelkalk and Keuper limestones, southern Germany.

Additional articles

Ölmez, J.A., Busch B., Hilgers, C., 2024, Sedimentologie, Petrographie und Strukturgeologie der Beckum-Sfm. (Campanium, Ahlen-Fm.) im südöstlichen zentralen Münsterländer Kreidebecken (Exkursion A am 3. September 2024) (Sedimentology, petrography and structural geology of the Beckum member (Campanian, Ahlen Fm.) in the

Southeastern Central Münsterland Cretaceous Basin), Jahresberichte und Mitteilungen des Oberrheinischen Geologischen Vereins, N.F. 106: pp. 1–15, 7 Fig.; Stuttgart, doi: 10.1127/jmogv/106/0001.

Ölmez, J.A., Hilgers, C., 2024, Resiliente Rohstoffversorgung Deutschlands – Bergbaupotentiale in ausgewählten Ländern Afrikas und die Rolle Chinas, ThinkTank IRS, p. 49, doi: 10.5445/IR/1000168179.

Ölmez, J.A., Hilgers, C., 2023. Rohstoffe für Deutschland und Auswirkungen des Russland-Ukraine Konflikts, ThinkTank IRS, p. 55, doi: 10.5445/IR/1000166052.

Contributions to other published articles

Busch B., Pistor F., Ölmez, J.A., Quandt, D., Müller, B., Niederhuber, T., Enukidze, O., Schneider, J.C., Stutz, H.H., Hilgers, C., 2025, Petrographic, petrophysical, and geochemical characteristics of Barremian carbonate rocks from the Enguri High Arch Dam area (Georgia). Zeitschrift der Deutschen Gesellschaft für Geowissenschaften, doi: 10.1127/zdgg/2025/0509.

Baumgartner, L., Langenmayr, U., Ölmez J.A., Schultmann, F., Hilgers, C., 2025, Wasserstoffwirtschaft – Rohstoffbedarf und Kosten für die Elektrolyse: Eine regionale Analyse für Baden-Württemberg, ThinkTank IRS, p. 46, doi: 10.5445/IR/1000179523.

Busch, B., Ölmez, J.A., 2024, Geologische Traverse von der Ibbenbürener Karbonscholle in das Münsterländer Kreidebecken (Exkursion C am 5. und 6. September 2024.), Jahresberichte und Mitteilungen des Oberrheinischen Geologischen Vereins, N.F. 106: pp. 39–65, 13 Fig.; Stuttgart, doi: 10.1127/jmogv/106/0003.

Hilgers, C., Busch, B., Ölmez, J.A., 2023, Klima, Rohstoffverfügbarkeit und Energiewende – Deutschland in der Krise. Leibniz-Sozietät der Wissenschaften zu Berlin e.V., Berlin, Haßler G. (Hrsg.), Band 159 Jahrgang 2023, pp. 21–70.

Conference contributions related to parts of this thesis

Ölmez, J.A., Hilgers, C., 2024, Potentiale aus Afrika für eine resiliente Rohstoffversorgung mit kritischen und strategischen Rohstoffen für Deutschland, at GeoSaxonia, Dresden.

Ölmez, J.A., Busch B., von Dollen, M., Kuroczik, J., Hilgers, C., 2024, Reservoir quality of Middle and Upper Triassic carbonate rocks of the Kraichgau area (SW Germany), at GeoSaxonia, Dresden.

Ölmez, J.A., Busch B., Möbius R., Dasgupta K., Gauer A.L., Tosoratti F., Hilgers C., 2024, Petrography-based workflow on drill cuttings in combination with borehole gamma ray

data and pXRF on reservoir rocks from the Vienna Basin Flysch Play, at DGMK Frühjahrstagung, Celle.

Ölmez, J.A., Hilgers, C., 2023, Metallic raw materials for Germany – Unexploited mining potentials of African developing countries based on the examples Botswana, Morocco, and Zimbabwe, at transforming towards a sustainable society – challenges and solutions Scientific Conference at KIT, Karlsruhe.

Ölmez, J.A., Hilgers, C., 2023, The German industrial and economic market is adapting – Impact of the Russia-Ukraine conflict on the supply of metallic raw materials for Germany, at transforming towards a sustainable society – challenges and solutions Scientific Conference at KIT, Karlsruhe.

Ölmez, J.A., Busch, B., Hilgers, C., 2023, Reservoir quality and diagenesis of limestones from the Upper Cretaceous (Beckum-Fm.) of the Münsterland Cretaceous Basin, at Geo-Berlin, Berlin.

Ölmez, J.A., Busch, B., Hilgers, C., 2023, Diagenetic controls and reservoir quality of tight limestones from the Upper Cretaceous, at DGMK Frühjahrstagung, Celle.

Ölmez, J.A., Busch, B., Hilgers, C., 2022, Controlling factors of petrophysical parameters in Upper Cretaceous limestones (Beckum-Fm.) of the Münsterland Cretaceous Basin (North Rhine-Westphalia, Germany), at DMG Sektionstreffen Petrologie und Geochemie, Mainz.

Ölmez, J.A., Busch, B., Hilgers, C., 2022, Reservoir quality heterogeneity in Upper Cretaceous limestones of the Münsterland Basin (Beckum-Fm., Münsterland Basin), at DGMK Frühjahrstagung, Celle.

Ölmez, J.A., Busch, B., Hilgers, C., 2021, Reservoir quality in Upper Cretaceous limestones of the Münsterland Basin, at German Section of the Society of Petroleum Engineers and its Student Chapters, online.

Additional conference contributions and conference contributions to other published works

Yildirim Ayyildiz, M., Ölmez J.A., Hilgers, C., 2025, Assessing the feasibility of EU27 critical raw materials act and Germany's green energy goals – Case study on rare earth elements, at International Symposium on Magmatism, Metamorphism, and Associated Mineralization, Errachidia, Morocco.

Frenzel, M., Fuchs, S., Graupner, T., Hector, S., Ölmez, J.A., 2024, Mineral Exploration, Economic and Ore Deposit Geology, Session at GeoSaxonia, Dresden.

Juhász, D.R., Busch, B., Ölmez, J.A., Cheng, C., Hilgers, C., 2024, Permeability measurements of possible CO_2 cap rocks – effect of confining stresses and time, at GeoSaxonia, Dresden.

Möckel, I.M., Ölmez, J.A., Askkour, F., Ikenne, M., Madi, A., Hilgers, C., 2024, Regional and structural geology of Neoproterozoic to Lower Cambrian rocks in the Ouansimi copper mine, Western Anti-Atlas of Morocco, at TSK conference, Freiburg im Breisgau.

Ölmez, J.A., Möckel, I.M., Askkour, F., Ikenne, M., Madi, A., Hilgers, C., 2023, Regional geology and structural control of copper-bearing vein formation in the Western Anti-Atlas of Morocco, at GeoBerlin, Berlin.

Hilgers, C., Ölmez, J.A., 2023, Geopolitische Rahmenbedingungen und Rohstoffverfügbarkeit, at Kongress BW, Stuttgart.

Busch, B., Ölmez, J.A., Hilgers, C., 2023, Diagenetic reservoir quality prediction modelling for CCS, underground gas storage, and geothermal applications, at transforming towards a sustainable society – challenges and solutions Scientific Conference at KIT, Karlsruhe.

Cheng, C., Busch, B., von Dollen, M, Ölmez, J.A., Hilgers, C., 2023, Using the subsurface for green energy transition and net-zero emissions: potential and risks, at transforming towards a sustainable society – challenges and solutions Scientific Conference at KIT, Karlsruhe.

Cheng, C., Busch B., Ölmez, J.A, Hilgers, C., 2023, Understanding micro-processes of reservoir and cap rocks for sustainable and secure geological carbon sequestration, at Workshop Negative Emissions Technologies at KIT (NET@KIT), Karlsruhe.

Cheng, C., Busch, B., von Dollen, M., Ölmez, J.A., Hilgers, C., 2023, Visualisation of microbial activities in reservoirs during UHS based on real-rock micromodels, at DGMK Frühjahrstagung, Celle.

2 Reservoir quality of Upper Cretaceous limestones (Ahlen-Fm., Beckum Member, Münsterland Cretaceous Basin): Effects of cementation and compaction on the compactable depositional volume

2.1 Abstract

The Upper Cretaceous limestones unconformably overlie Upper Carboniferous coal-bearing lithologies and are studied to assess their effect on rising mine-water levels in the Ruhr mining district. Upper Cretaceous sedimentary rocks from the Münsterland Cretaceous Basin have previously been studied regarding their sedimentary structures and fossil content. However, understanding the petrophysical and petrographic heterogeneity in regard to sedimentary properties and their effect on fluid migration pathways is yet missing. Utilizing He-pycnometry, Klinkenberg-corrected air permeabilities, p-wave velocities, transmitted and reflected light analyses, point-counting and cathodoluminescence, we assess the petrophysical, geomechanical and mineralogical properties. Porosity ranges from 1.0 to 18.7% and permeability ranges from <0.0001 to 0.2 mD, while p-wave velocity ranges between 2089 and 5843 m/s. Mechanical compaction leads to grain rearrangement, deformation of calcispheres, foraminifera and ductile clay mineral laminae. Above and below clay laminae, compaction bands of deformed calcispheres develop. Early diagenetic mineral precipitation of ferroan calcite in inter- and intragranular pores reduces porosity and permeability and influences geomechanical properties. An underestimated aspect of limestone petrography is the relationship of the original primary compactable depositional volume and the influence of compaction, deformation and cementation during early and late diagenesis on reservoir properties. The detrital dominated limestones show an originally high compactable depositional volume (CDV). Overall, reservoir qualities are poor and indicate the sealing potential of the studied lithologies. The Upper Cretaceous (Campanian) limestones thus may act as a barrier for increasing mine-water levels from dismantled, post-mining subsurface hard coal mines in the region.

2.2 Introduction

Carbonate rocks have very heterogeneous reservoir properties from bed to reservoir scale (Lucia et al., 2003; Ehrenberg and Nadeau, 2005; Rashid et al., 2017). The reservoir properties rely on depositional, diagenetic and structural modification (Worden et al., 2018). Usually, the reservoir quality of a formation is determined to identify porous and permeable lithologies, e.g., for oil and gas exploration, carbon capture and storage (CCS) or geothermal use-cases (Choquette and Pray, 1970; Amthor et al., 1994; Ehrenberg, 2006; Ehrenberg et al., 2006; Ahr, 2008; Armitage et al., 2013; Abuamarah and Nabawy, 2021). Since the reservoir quality is influenced by diagenetic modification (compaction, mineral precipitation, alteration, and dissolution) and the fracture network, an understanding of controlling factors and anisotropies is important. Understanding the diagenetic overprints in Cretaceous sediments as sandstones and limestones are important for the successful exploration of a reservoir or storage potential for gas sequestration and were studied e.g., in Abu Dhabi (Morad et al., 2019), the Amposta offshore oil reservoir in Spain (Playà et al., 2010), and China (Xi et al., 2015). However, macro- and microscale natural fractures additionally influence the reservoir or sealing potential of carbonate rocks (La Bruna et al., 2020). Although carbonate turbidite systems are heterogeneous, fractured carbonate turbiditic deposits can be of interest for e.g., oil and gas production (Coffa et al., 2015).

This study aims to determine the porosity and permeability as well as their controlling factors as the studied Upper Cretaceous limestones unconformably overly Upper Carboniferous coal-bearing strata. The Upper Cretaceous deposits are discussed to be sealing lithologies on top of the northernmost extent of the former coal mining district (Fig. 2.1a), which are discussed to decouple the rising mine-water levels or gas seepages from the ground water since the cessation of coal mining in Germany (Rudolph et al., 2010; Coldewey and Wesche, 2017). The sedimentary rocks of the Upper Cretaceous in the Münsterland Cretaceous Basin have so far mainly been studied in lithological and paleontological terms (e.g., Giers, 1958; Arnold et al., 1960; Voigt and Häntzschel, 1964; Kappel, 2002; Wilmsen et al., 2019; Püttmann and Mutterlose, 2021). The stratigraphic sequences of the Campanian rocks were determined by e.g., Giers (1958), Wolf (1995), Kaplan (2004), and Kappel (2002) using detailed regional designations. Prior mineralogical analyses have mainly been carried out to determine mineable formations for the cement industry. However, limited research has focused on the diagenetic parasequence and petrophysical properties of the studied lithologies. An underresearched aspect in this region is therefore the small-scale distribution of petrographic and petrophysical heterogeneities and their influence on the reservoir rock as well as the relation to the fracture network. Since compaction and diagenesis influence porosity and permeability, a detailed investigation of the petrographic and petrophysical properties can identify controlling factors for reservoir

properties. Here, we determine the reservoir quality and the diagenetic parasequence to assess the impact of diagenesis and compaction on the compactable depositional volume. For this purpose, outcrop analogues were studied and sampled. Outcrop analogues also provide information on lateral layer continuity, the fracture network and their influence on the fluid flow on the basin scale. Results can be applicable to assess the interaction of rising mine-water and outline future potential for regional geothermal use of the formation.

2.3 Geological setting

The study location is in the opencast mine of Phoenix Zementwerke Krogbeumker GmbH & Co. KG in Beckum, NW Germany. Beckum is located in the southeast of the Central Münsterland Cretaceous Basin and exposes Upper Cretaceous (Campanian) marlstones, claystones/shales and limestones of the Beckum Member. The Münsterland Cretaceous Basin itself contains Lower Cretaceous to Upper Cretaceous deposits and is surrounded by the Osning fault in the north/northeast, the Egge mountains to the east and the Haarstrang to the south. The basin opens towards the Lower Rhine Embayment in the west/northwest (Fig. 2.1a, b).

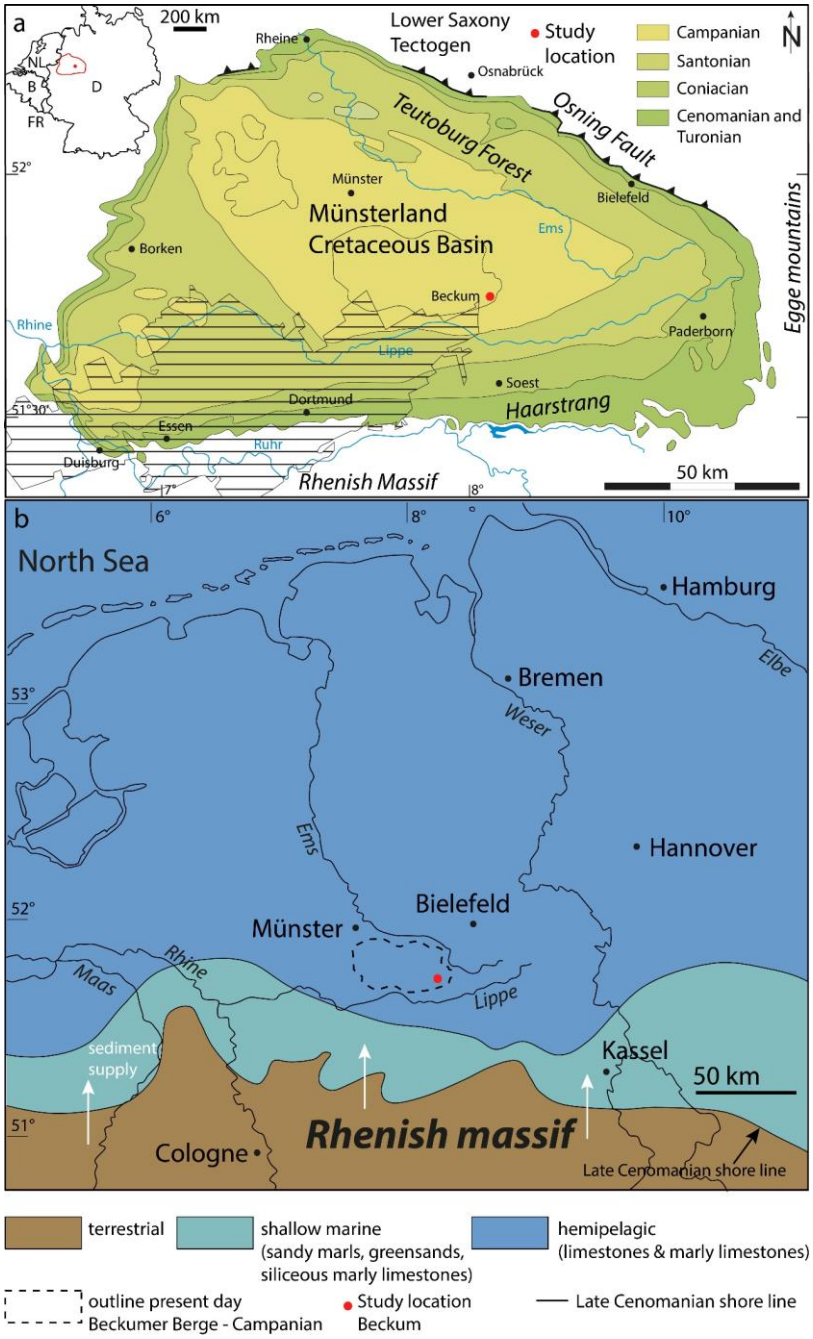

Figure 2.1 (Figure caption on next page)

Figure 2.1 (previous page) a) Simplified stratigraphic overview of the Münsterland Cretaceous Basin, the study location Beckum is marked in red. Limestones, claystones/shales and marlstones are exposed and mined for the cement industry (modified after Hiss and Mutterlose, 2010; Janetschke and Wilmsen, 2013 and references therein; Drozdzewski and Dölling, 2018). The red box displays the Münsterland Cretaceous Basin, the red dot marks the approximate location of the study area in Germany (Beckum), and the hatched area marks the distribution of former hard coal mines. (Wirges and Dodenhoff, 2019; Geologischer Dienst NRW, 2020), D: Germany, B: Belgium, FR: France, NL: Netherlands, b) Paleogeographic map of the North German Basin area and present day outline of the approximate study location (red dot) in the Beckumer Berge with possible terrestrial sediment supply (white arrows) from the Rhenish massif during the late Cenomanian, modified after Hiss (1995) & Erbacher et al. (2020).

During the late Cretaceous, Europe was influenced by compression and deformation events of the Central European Basement, resulting in basement shortening and anticline uplift and folding and inversion of normal faults (Voigt et al., 2021 and references therein). The North Atlantic rift in conjunction with a tectonically induced regression at the transition from the Upper Jurassic to the Lower Cretaceous, based on the subsidence of the Lower Saxony Basin during transtensional tectonics, led to a change in sedimentation in Northwestern and Central Europe (Vejbæk et al., 2010).

During the Cretaceous, smaller transgression and regression events occurred, and NW-SE to W-E compressional directions affected NW Europe (Kley and Voigt, 2008). The long-term sea level during the Cretaceous had a maximum at 100 ± 50 m (Miller et al., 2005). Increased crustal extension of the Atlantic leads to intensive rifting and subsidence in the Central European Basin System, e.g., in the Lower Saxony Basin until the end of the Aptian (ca. 125-115 Ma) (Mazur and Scheck-Wenderoth, 2005; Vejbæk et al., 2010). The South Atlantic ocean opening resulted in a drift of the African Plate northward and compression transfer due to the Iberian-Peninsula to Europe (Voigt et al., 2021). Furthermore, Africa shifted relatively ESE to Europe (ca. 120 Ma), which caused a sinistral strike-slip movement along the plate boundary (Kley and Voigt, 2008). During the Santonian (ca. 84 Ma) Africa drifted in a NE direction (Kley and Voigt, 2008) and lead to a compression towards the NE in Central Europe, which caused the inversions of NW-SE striking basins and increased subsidence (cf. Dölling et al., 2017). The southern edge of the inverted Lower Saxony Basin is represented by the Münsterland Cretaceous Basin (Voigt et al., 2021). As a result, the Late Cretaceous basement thrusts and inversion basins are formed as intraplate structures due to the weak lithosphere resulting from the Variscan orogeny and the overlying Palaeozoic to Mesozoic extensional basins (Kley and Voigt, 2008). The NW-SE striking uplift and overthrust in the intraplate area is the result of the beginning of the Africa-Iberia-Europe convergence (Kley and Voigt, 2008). NW-SE oriented overthrusting of the

Lower Saxony Tectogen onto the Münsterland Cretaceous Basin led to curvature and partial overthrusting of the Cretaceous formations in the Teutoburg Forest (Wulff et al., 2017).

Upper Cretaceous clastic and carbonate sediments were deposited into a shallow basin north of the Rhenish Massif (Fig. 2.1b) (Wilmsen et al., 2019; Erbacher et al., 2020). In general, the thickness of the Upper Cretaceous sediments reaches up to 2,000 m in the north of the basin, and 500 m at the southern margin due to low sedimentation rates and formation gaps (Scheck-Wenderoth et al., 2008; Voigt et al., 2021). The thickness distribution of the Upper Cretaceous in the Central European Basin System shows a dominance of NW-SE striking structural pattern, e.g., reactivation of faults due to inversion with local WNW-ESE striking folds and thrusts (Scheck-Wenderoth et al., 2008). From the western margin of the Ruhr area in Duisburg to the Paderborn Plateau in the east (Fig. 2.1a), the shallowly north-dipping rocks of the Münsterland Cretaceous Basin uncomfortably overlie the folded Upper Carboniferous of the Ruhr and Sauerland regions. The youngest deposits are present in the center of the Münsterland Cretaceous Basin (Beckumer Berge and Baumberge) and are exposed from old to young from Stromberg, Beckum and Vorhelm Member, which are to date combined in the Ahlen-Formation (Ahlen-Fm.) (STD, 2016). The Lower Campanian consists of the Stromberg Member, comprising bioturbated grey limestones and marls with a mottled background. Slightly pronounced gradations indicate turbiditic fillings. Parallel to the strata, horizontally to obliquely bedded glauconitic, sandy limestones may occur (cf. Giers, 1958; Kappel, 2002; Wilmsen et al., 2019). The Upper Campanian starts with the Beckum Member, consisting of alternating limestone-marly shale sequences with a thickness of up to 25 m (Giers, 1958). The limestone banks are deposits of debrite and turbidite flows and separated by thin (<0.2 m) claystone/marlstone to marly shale layer (Wolf, 1995; Kaplan et al., 1996; Kappel, 2002; Kaplan, 2004). The overlying Vorhelm Member consists of a limestone-marlstone or marly shale alternation sequence with a total thickness up to 80 m (Giers, 1958), showing no marker horizons and lateral inhomogeneities (Kappel, 2002). In general, the Campanian lithologies in the Münsterland Cretaceous Basin are described as allochthonous sediments, resulting from debris flows, turbidites or submarine slumping (Giers, 1958; Wolf, 1995; Kaplan et al., 1996; Kappel, 2002).

2.4 Materials and methods

In the Phoenix quarry in Beckum, a total of ~ 17.5 m limestone–marly shale alternations were recorded on successive vertical walls. Samples were taken from each limestone layer. In addition, samples were also taken from the vicinity of a fault zone to assess the influence on petrophysical and petrographic properties. Rock classification in the field was performed according to (Dunham, 1962) and is supplemented by microscopic classification

after Folk (1959) and Dunham (1962). For the fracture strike orientation, images were taken with a Mavic 2 Enterprise drone on a plane surface on the highest strata of the quarry. The fracture pattern was analysed and plotted with FracPaQ using the workflow from (Healy et al., 2017). For the petrophysical analysis, a total of 74 plug samples were drilled parallel and perpendicular to stratification from a hand specimen using a water-cooled 1-inch (~ 2.54 cm) core drill. The trim ends of the plugs drilled parallel to the stratification were used for thin section preparation. The plugs were dried at 40 °C in a drying oven for one week until weight constancy. Helium porosity and grain density were determined using a Micrometrics AccuPyc II 1340 pycnometer (e.g., Monsees et al., 2021). The Klinkenbergcorrected intrinsic permeability measurements were carried out with an air permeameter from Westphal Mechanic using dry, oil-free laboratory air (80% N_2, 20% O_2) as permeant at 1.2 MPa confining pressure to avoid sample bypassing (e.g., Klinkenberg, 1941; Rieckmann, 1970; Schmidt et al., 2021). The measurement range for the device is between 0.0001 and 10,000 mD (1 mD ≙ $9.869*10^{-16}$ m^2). Ultrasonic pulse velocity measurements were carried out using a Proceq Pundit 200 ultrasound system with two 54 kHz transducers at 200 V pulse voltage and 50 × receiver gain. The longitudinal wave (p-wave) was determined by measuring the transit time t_0 (µs) via the longitudinal axis of the plugs and converted into the wave velocity (v_p; m/s). A coupling gel was used for direct and soft contact with the plugs. The measurement frequency depends on the sample diameter. For samples with a diameter of 2.54 cm, the frequency has to be below 1 MHz to secure physical consistency (Kummerow, 2006).

A total of 49 samples were embedded in blue dyed epoxy resin to highlight porosity and were used to prepare thin sections with a thickness of 30 µm. Thirty-five of these thin sections were stained with a combined solution of alizarin red S and potassium ferricyanide (Dickson, 1965) in 0.3% HCl on one half of the thin section to distinguish different carbonate phases and covered with a glass cover slip. Calcite will stain reddish (pink, orange) and ferroan calcite will stain blue, while dolomite remains unstained (Dickson, 1965). The remaining 14 thin sections were polished for further microscopic analyses. A Leica DMLP and a Progres Gryphax camera system were used for petrographic examination. Polished thin sections were also examined using cold cathode cathodoluminescence (CITL CL8200 Mk5-2 Optical Cathodoluminescence System mounted on a Leica DIALUX 20 ES) (e.g., Monsees et al., 2020) in a low vacuum <0.001 mbar, at an acceleration voltage of 10.3 kV and a current of 325 µA to distinguish different cement phases and zonations. Opaque minerals were analysed by reflected light microscopy on polished thin sections with a Leitz OrthoplanP and a Progres Gryphax camera system using oil immersion. For the grain size determination of the calcispheres, at least 100 grains were measured in each thin section with ImageJ on a grid adjusted to the largest observed grain size to gain area weighted results (e.g., Becker et al., 2017). The width of clay laminae, compaction bands and veins were also measured using ImageJ. For micrite (≤4 µm) and microsparite (5–10 µm), grain

size values by Folk (1959) and Folk (1974) were used. As the grain size could not be determined during point-counting, the distinction between micrite and microsparite was not possible; therefore, the term micrite is used. Point counts were performed on 300 points using a Pelcon semi-automatic point counter installed on a Leica DMLP microscope using a step-length adjusted to the maximum observed particle size (e.g., Busch et al., 2019) of 100 µm. The porosity types were determined according to (Choquette and Pray, 1970). The compaction of the calcispheres was further determined following Fry's method (Fry, 1979) using ImageJ. To determine the compaction ratio, horizontal (long) and vertical (short) lengths of the calcispheres were measured, but were only recorded in the vicinity of the clay mineral laminae.

2.4.1 Compactable depositional volume

The concept of 'compactable depositional volume (CDV)' was introduced to determine the volume loss as a function of compaction prior to cementation. The CDV is the volume that is potentially compactable after deposition and before the formation of authigenic cements similar to the intergranular volume (IGV) commonly used in sandstones (Houseknecht, 1987; Paxton et al., 2002). The CDV is the sum of interparticle porosity, intraparticle porosity, microporous clay and micrite and all authigenic phases, which precipitated in primary pores (including intraparticle pores) (Eq. 2.1). Just as the IGV, it measures the amount of intergranular porosity and pore-filling cements. In contrast to IGV, however, carbonate rocks often contain porous fossils, which may break or compact. Thus, the CDV also considers intraparticle porosity. This may aid in further assessing the degree of compaction in carbonate rocks within samples of the same lithology, especially when distinguishing inter- and intraparticle porosity, while also capturing the stabilizing effects of authigenic phases. As this indicator calculation also includes microporous micrite and clay mineral laminae, it is possible that the value does not reach 0%, but samples rich in micrite or clay mineral laminae will show high CDV, which can still be correlated to high microporosity contents. Similarly, sandstone samples containing abundant depositional clay mineral matrix will also show high IGV values (Paxton et al., 2002). In samples which contain abundant porous particles (e.g., calcispheres), the presented approach can aid in comparing the effect of compaction, as uncompacted samples will have higher CDV than compacted samples. However, just as the IGV, the CDV is not directly comparable to the petrophysically measured Heporosity, as intraparticle cements can fill cavities within porous particles, reducing the porosity, while stabilizing the particle itself against compaction. Therefore, this point-count-based calculation enables the comparison of the state of compaction within a lithology and its relation to assessed reservoir properties.

Eq. 2.1

$$CDV\ (\%) = (\Sigma Interparticle\ porosity\ (\%) + \Sigma Intraparticle\ porosity\ (\%) + \Sigma Interparticle\ cement\ (\%) + \Sigma Intraparticle\ cement\ (\%) + \Sigma Micrite\ (\%) + \Sigma Clay\ laminae\ (\%))$$

2.5 Results

2.5.1 Lithology

The lithological profile contains alternating, layered argillaceous limestones to calcareous marlstone and marlstone to claystone or marly shale deposits of varying thicknesses (Fig. 2.2). The total recorded lithological thickness is ~ 17.5 m. Due to further simplification, the terminologies limestone and marly shales are used. The marly shale layers are dark grey, finely bedded and up to 1.6 m thick at the upper level, but generally are <0.2 m thick. Overall, a fining-upwards trend is recognizable; the marly shale bed thickness increases towards the top, while the limestone beds recede (Fig. 2.2 and Fig. 2.3a, b). The limestones and marly shales are both fine-grained and the limestones are classified as mudstones to wackestones after Dunham (1962). Firm, dark, claystone to marly shale layers (approx. 5 cm thick), which occur at irregular intervals between the limestones and marly shales, are apparent. The observed fault (Fig. 2.3c) was characterized as a normal fault using slickensides. Some of the fracture surfaces show a brownish to yellowish coating, which is due to iron hydroxide precipitation associated with alteration of idiomorphic pyrite and marcasite in the formation. One well-preserved belemnite was found at about 2.6 m (Fig. 2.2), which was determined as belemnite mucronate due to its slenderness. In higher strata (Fig. 2.2), two belemnite fragments were found, but could not be classified because of missing morphology information.

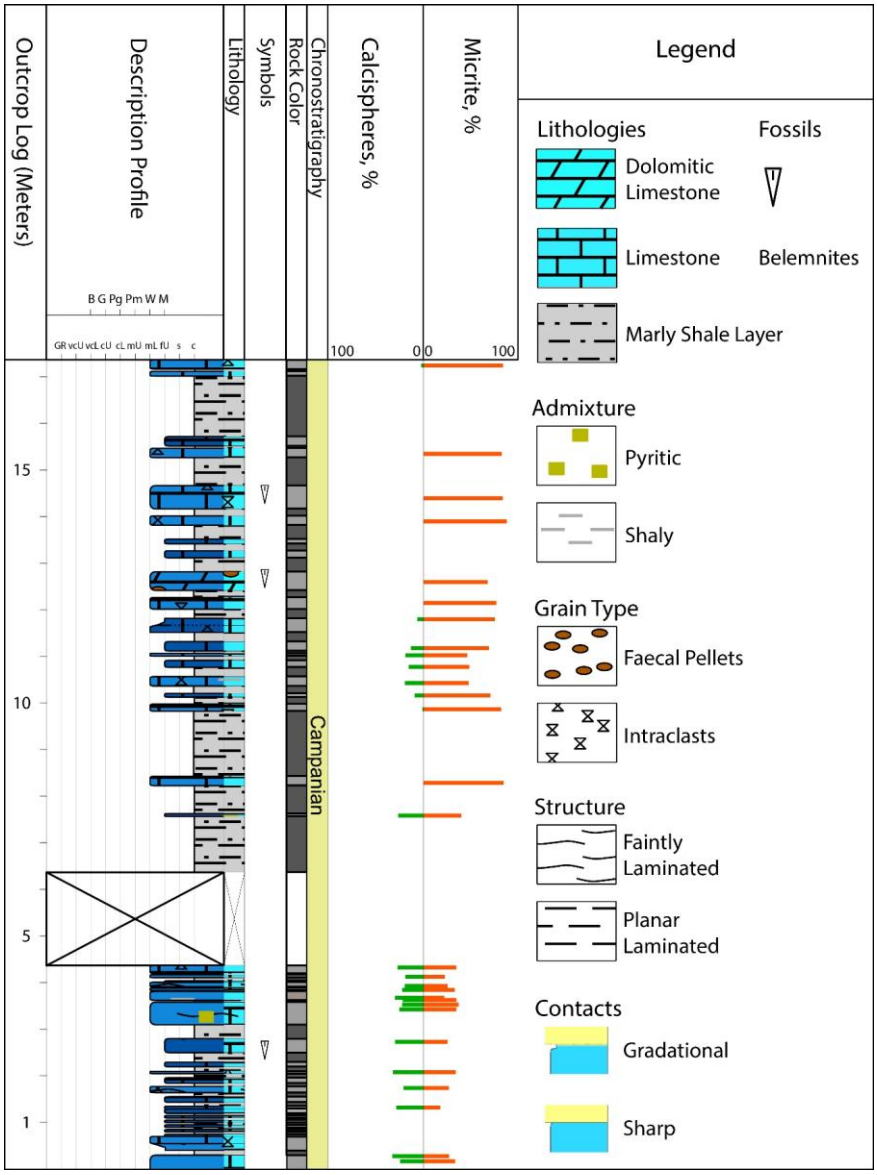

Figure 2.2 Stratigraphic column including grain size distribution and petrographic data (point counting data for calcispheres and micrite content). Faintly laminated limestones are in the lower studied part, interbedded with marly shale layers. A fining-up trend is noted towards the top. In addition, faintly laminated limestones are predominant in the lower section. Missing part is marked by a white box.

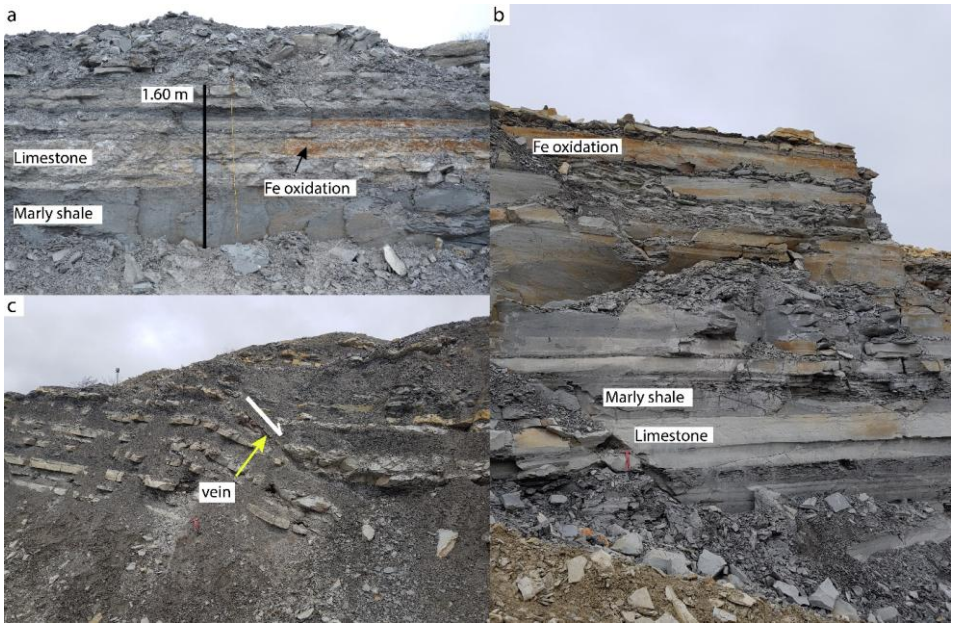

Figure 2.3 Overview parts of the studied outcrop with different wall sections. a) The lower part of the studied lithologies hosts limestone-marly shale alternations. The faintly laminated limestone surfaces are rough, the interbedded marly shales are of varying thickness and occur as thinner or thicker beds (e.g., in the lower part of the Fig. 2.3a). The limestone surface is partly coated with pyrite/marcasite and thus brownish to yellowish due to iron hydroxide precipitation. The wall strikes W-E. b) In strata above, the thickness of interbedded marly shale is increasing, and the limestones are no longer faintly laminated, but massive with even surface. The wall strikes NNW-SSE to NW-SE. c) Fault zone with normal fault (white arrow) and (ferroan) calcite/strontianite vein (yellow arrow). The wall strikes NNE-SSW to NE-SW. Hammer for scale.

2.5.2 Structure

Three main fracture orientations were obtained from the drone imagery evaluation, showing three main sets striking WSW-ENE, NNE-SSW and NW-SE (Fig. 2.4). Fractures are partly continuous, penetrate limestone and marly shale layers or are interrupted during layer changes, but open fractures (mm range aperture) are only rarely found.

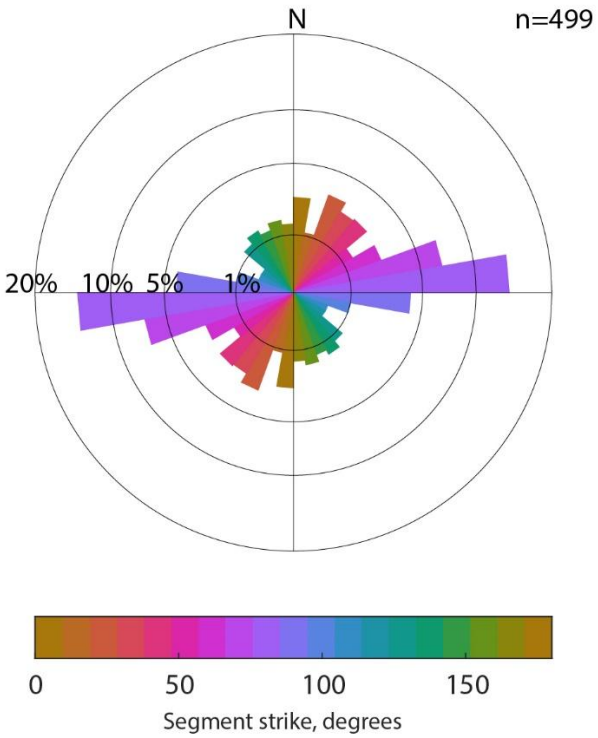

Figure 2.4 Fracture data from drone imagery plotted as rose diagram (strike plot). Fracture data were generated using the FraqPaQ workflow from Healy et al. (2017). Main striking sets from WSW-ENE, NNE-SSW and NW-SE.

2.5.3 Petrography: texture

The average size of the calcispheres is 0.042 mm (avg. range 0.038 to 0.044 mm). For micrite-dominated layers, the average grain size is limited by the maximum grain size (0.004 mm) per definition after Folk (1959, 1974). The well-rounded calcispheres with a calcitic test appear evenly distributed (Fig. 2.5a) and as elongated rock fragments within the micritic matrix (Fig. 2.5b). The calcispheres (stained red) are partly deformed around clay laminae (Fig. 2.5c, d), and rarely broken (Fig. 2.5e). By microscopical analyses, the limestones are classified as wackestone to packstone according to Dunham (1962). Grains as detrital quartz, glauconite and some unstained carbonate grains have a rounded to elliptical shape, but are not aligned parallel to bedding.

2.5.4 Detrital composition

The most abundant detrital component is micrite with an average content of 51.5% (min.: 17.7%, max.: 88.0%). The second most abundant are calcispheres with an average content of 16.4% (min.: 0.0%, max.: 34.7%). The third most abundant are clay minerals in laminae (avg.: 4.8%, min.: 0.0%, max.: 22.7%). In addition, different foraminifera types (avg.: 1.2%, min.: 0.0%, max.: 4.0%), detrital quartz and chert grains (avg.: 0.2%, min.: 0.0%, max.: 2.7%), test or shell fragments (avg.: 0.8%, min.: 0.0%, max.: 3.3%), unidentified carbonate grains (avg.: 0.2%, min.: 0.0%, max.: 2.7%), phosphate grains (avg.: 0.3% min.: 0.0%, max.: 1.0%), glauconite (avg.: 0.4%, min: 0.0%, max.: 2.0%), micrite in calcispheres (avg.: 0.1%, min.: 0.0%, max.: 2.0%), dolomite rhombs (avg.: 0.0%, min.: 0.0%, max.: 1.0%), bivalves (avg.: 0.0%, min.: 0.0%, max.: 0.3%), undifferentiated fossils (avg.: 0.0%, min.: 0.0%, max.: 0.3%) and micrite in foraminifera (avg.: 0.0%, min.: 0.0%, max.: 0.3%) are recorded (full sample table in digital appendix – chapter 2). In total, the detrital composition varies between 51.7% and 94.0% (avg.: 76.3%). Micrite, calcispheres, tests and shell fragments, foraminifera and other microfossils in this study are primarily composed of calcite, as indicated by the red stain (Fig. 2.5a, e), while only individual foraminifera have a dolomitic composition and remain unstained (Fig. 2.5f). Dolomite occurs rarely as single rhombic crystal within the micrite matrix. Chert occurs as yellow grains or as silicified shell fragments and show small microcrystalline spheroids with crossing extinction. Glauconite is found occasional in thin sections as rounded grains (Fig. 2.5c). The detrital composition in limestones varies with the calcisphere content and the position along the lithological profile. If the calcisphere content decreases, the micrite content increases (cf. Fig. 2.2). In younger strata, where clay laminae are mostly missing, the micrite matrix is densely packed and individual calcispheres are deformed both in aductile way and locally crushed. In general, the calcispherecontent decreases towards the top of the studied section (cf. Fig. 2.2). Calcispheres are also found as parts of densely packed clasts, which are partially aligned to the bedding direction (Fig. 2.5b). Surrounding clay laminae, calcispheres often appear deformed in a ductile way (Fig. 2.5c, d). The clay laminae thickness varies between 0.04 and 0.37 mm (avg.: 0.16 mm). Cemented calcisphere clasts occur occasional with an average length of 1.08 mm (min.: 0.24 mm, max.: 2.09 mm).

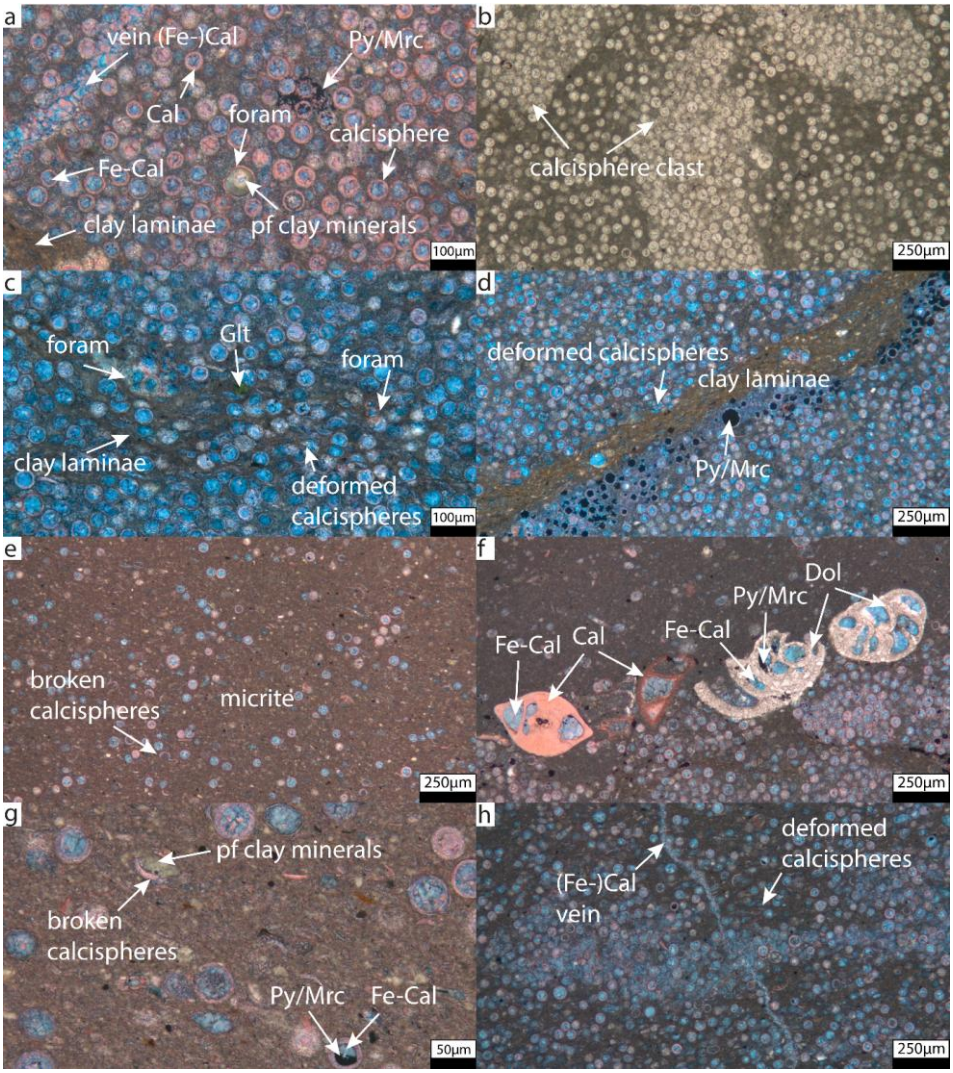

Figure 2.5 (Figure caption on next page)

Figure 2.5 (previous page) Photomicrographs showing a) former hollow calcispheres which are cemented by ferroan calcite and also smaller veins are completely sealed by (ferroan) calcite (sample PHX34). Calcite is stained red und ferroan calcite is stained blue. However, also green clay minerals occur as filling in calcispheres or foraminifera. b) Some thin sections showing clasts of reworked former calcisphere packstones (sample PHX30). Without staining, the distinction between calcite and ferroan calcite is not possible. c) Calcispheres are deformed elliptical in areas where clay laminae are present, glauconite occurs occasional (sample PHX27). d) The appearance of pyrite/marcasite framboids is mostly limited to the vicinity of clay laminae or high clay content within the micritic matrix (sample PHX33). The opaque minerals occur either pore filling in fossils or dispersed in the clay laminae or the micritic matrix. e) The upper lithologies consist mostly of micrite and clay (sample PHX12). f) Dolomite or dolomitization of former fossils occur sporadically (sample PHX19). g) Reworked and broken fossils and tests are occurring within a more clay dominated matrix (sample PHX12). h) Deformed calcispheres also occur at the transition to cemented calcisphere packstone clasts (sample PHX16). Cal: calcite, Fe-Cal: ferroan calcite, (Fe-)Cal: (ferroan) calcite, foram: foraminifera, pf: pore filling, Py/Mrc: pyrite/marcasite, Glt: glauconite, Dol: dolomite.

In a single layer at ~ 12.5 m (Fig. 2.6) consisting mainly of clay and micrite, partially or completely dissolved peloids/pellets with an average size of 0.35 mm (min.: 0.2 mm, max.: 0.49 mm) occur frequently. They contain fossil fragments or pyrite and are crosscut by most likely (ferroan) calcite veins (Fig. 2.6a, b). In stained thin sections, the remnants of the peloids/pellets remain unstained, indicating a dolomitic composition.

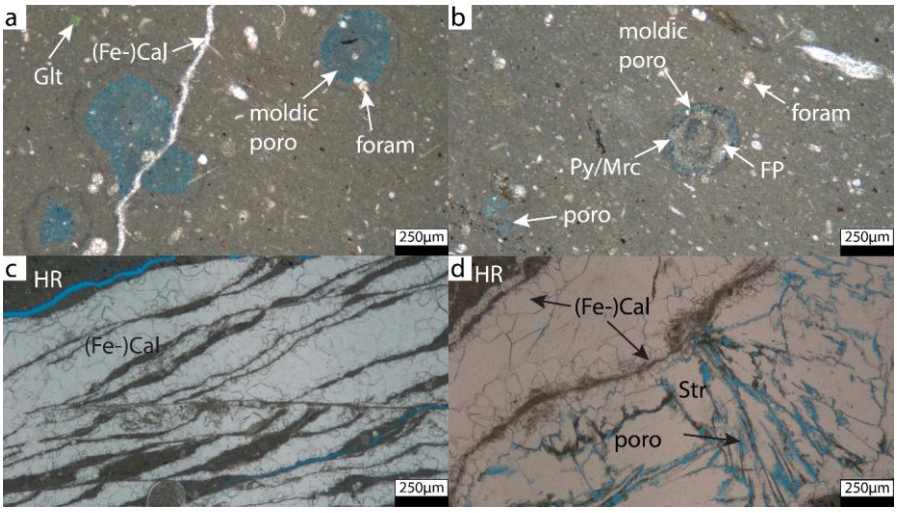

Figure 2.6 (Figure caption on next page)

Figure 2.6 (previous page) a) Photomicrographs showing micrite to clay matrix, containing smaller test or shell fragments, foraminifera, and glauconite. Former pellets are completely or partially dissolved and therefore causes moldic porosity. A carbonate vein, most likely (ferroan) calcite crosscuts the former pellet. b) The pellets are roundish, and dissolution is more pronounced at the outline of the pellet. c) Sheared carbonate (likely ferroan calcite) vein, which includes host rock material. d) The syntaxial (ferroan) calcite vein is completely sealed and shows growth competition, whereas bladed to fibrous strontianite veins retain intercrystalline porosity (sample PHX10). foram: foraminifera, Glt: glauconite, moldic poro: moldic porosity, poro: porosity, (Fe-)Cal: (ferroan) calcite, HR: host rock, FP: faecal pellet; Py/Mrc: pyrite/marcasite, Str: strontianite.

2.5.5 Authigenic phases

The most abundant authigenic phase is sparry ferroan calcite, which precipitated in the calcispheres (stained blue, avg.: 10.4% min.: 0.0%, max.: 23.3%). The second most common authigenic phase is pore-filling ferroan calcite, e.g., within the micrite matrix (avg.: 6.9%, min.: 0.0%, max.: 27.0%), while the third most abundant are unstained porefilling carbonates (avg.: 1.7%, min.: 0.0%, max.: 10.3%). Other authigenic minerals include porefilling calcite (avg.: 1.3%, min.: 0.0%, max.: 6.7%), sparry ferroan calcite in foraminifera chambers (avg.: 0.5%, min.: 0.0%, max.: 2.3%), (ferroan) calcite and strontianite vein cements (avg.: 0.4%, min.: 0.0%, max.: 10.0%), pyrite/marcasite in calcispheres (avg.: 0.3%, min.: 0.0%, max.: 5.3%) and in clay laminae (avg.: 0.2%, min.: 0.0%, max.: 1.3%). Porefilling green clay minerals (avg.: 0.7%, min.: 0.0%, max.: 2.7%), sparry ferroan calcite in bivalves (avg.: 0.0%, min.: 0.0%, max.: 0.3%), clay minerals in calcispheres (avg.: 0.0%, min.: 0.0%, max.: 0.3%) and clay minerals in foraminifera (avg.: 0.0%, min.: 0.0%, max.: 0.3%) reflect minor authigenic minerals. In total, the authigenic composition varies between 6.0 and 48.3% (avg.: 23.4%). Blue-stained sparry ferroan calcite fills the inner part of calcispheres or other fossils and most veins (Fig. 2.5a). Porefilling green clay minerals and green clay minerals in fossils most often coat the inside of individual fossil tests (Fig. 2.5a). Where the fossils or calcispheres are broken, further sparry ferroan calcite cements are also encasing the broken fragments (Fig. 2.5g).

Pervasively sealed veins (Fig. 2.5a, h) are composed of an intergrowth of ferroan calcite (stained blue) and calcite (stained red, Fig. 2.5a). This mineral paragenesis will be abbreviated as (ferroan) calcite. Narrow veins show a width from 0.012 to 0.05 mm (avg.: 0.026 mm), while wide veins around the fault show widths between 0.25 and 0.63 mm (avg.: 0.42 mm). Composite veins composed of (ferroan) calcite and strontianite were observed around the fault and within the undisturbed lithology (Fig. 2.6c, d). Composite veins of (ferroan) calcite and strontianite still retain open intercrystalline porosity between the strontianite

crystals (Fig. 2.6d). Depending on the crystal section, strontianite can be fibrous to radiating spherulitic, bladed or botryoidal (Fig. 2.6d). They partly fill the remaining inner fracture porosity, which is outlined by euhedral crystal terminations of elongate blocky (ferroan) calcite crystals (Fig. 2.6d). In these composite veins, pyrite/marcasite is often present at the host rock-vein interface and encased in (ferroan) calcite. Also, a sheared (ferroan) calcite vein contains elongated host rock inclusions and remaining fracture porosity is filled by strontianite, where strontianite again retains intercrystalline porosity within the vein (Fig. 2.6d, Fig. 2.8). Larger strontianite or (ferroan) calcite/strontianite veins are found in samples from the fault zone and in samples PHX10, PHX26 and PHX27. Pyrite and marcasite are mostly found surrounding or within clay laminae as framboids, within calcispheres and other fossils (Fig. 2.5d).

The framboidal pyrite present in intraparticle pores of calcispheres and foraminifera is additionally encased in ferroan calcite in some samples (Fig. 2.5a, f, g). Cathodoluminescence analyses show that the calcitic calcispheres show a bright orange luminescence and a dull luminescing centre, where they are filled by ferroan calcite. Narrow authigenic, syntaxial (ferroan) calcite veins (avg. 0.01 to 0.05 mm wide) show no consistent zonation but a rather dull orange luminescence or non-luminescence with individual areas of brighter luminescence (Fig. 2.7a, b). In wider veins (0.25 to 0.63 mm wide), the brightest orange zones occur at calcite crystal boundaries showing euhedral terminations, while the centre mostly exhibits a dull orange luminescence indicating the presence of ferroan calcite. At the transition from host rock to vein, the (ferroan) calcite crystals show syntaxial growth and growth competition (Fig. 2.7b, c). In sample PHX10, the (ferroan) calcite vein cements precipitate syntaxially on the host rock inclusions, and their crystal size increases towards the centre of the vein (Fig. 2.7b). In addition, the host rock inclusions appear to be cut again and are overgrown by an even larger syntaxial (ferroan) calcite phase (top of Fig. 2.7b). The euhedral terminations of these crystals are again encased in strontianite (Fig. 2.7b). Strontianite shows a turquoise-bluish luminescence and zones of brighter and duller luminescence or non-luminescence in larger crystals (Fig. 2.7b, c, d). The micritic matrix generally shows a pale orange luminescence (Fig. 2.7 a, c, f), while only the sample containing a sheared vein shows a purple luminescence of the micrite both at the host rock-vein interface (Fig. 2.7d) and in the narrowly spaced (20–100 μm) host rock inclusions inside the vein (Fig. 2.7b, e). The peloids/pellets (interpreted as faecal pellets) encased in a micritic matrix show a reddish luminescence (Fig. 2.7f).

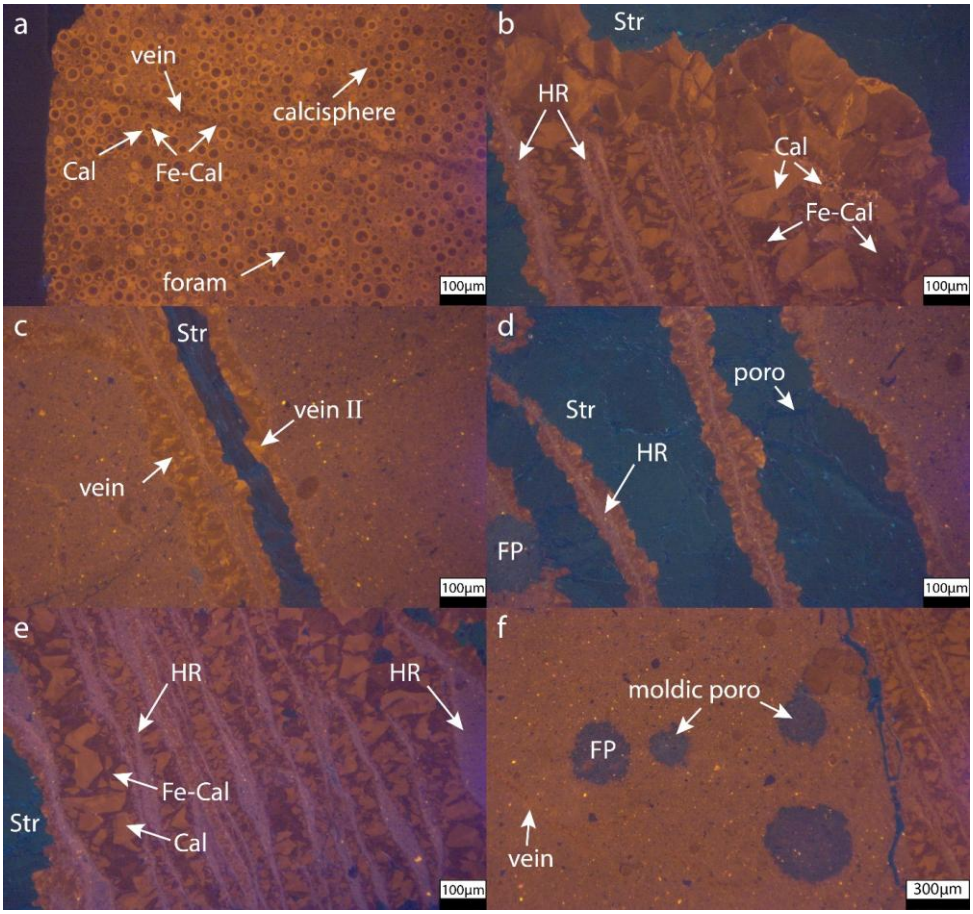

Figure 2.7 Photomicrographs of cold cathodoluminescence showing different luminescence properties of calcite (Cal), ferroan calcite (Fe-Cal), and strontianite (Str). a) Calcite shows bright orange luminescence color, while ferroan calcite is dull (sample PHX34). Calcite occurs in the test of calcispheres or other fossils, while ferroan calcite cements occur as pore filling cement or vein. The luminescence of micrite between the fossils is not as bright as pure calcite. b), c) The wide veins contain zones of both bright and dull luminescence up to non-luminescence calcite to Ferroan calcite, while reactivated veins (vein II) also contain strontianite which shows a bluish luminescence (sample PHX10). Multiple parallel veins also contain host rock fragments (HR). d) Larger strontianite veins also show zonation within the crystals with brighter and darker zones (sample PHX10). Faecal pellets (FP) are partially dissolved. e) Host rock inclusions in (ferroan) calcite veins show a purple luminescence (sample PHX10). f) Remaining faecal pellets show a reddish luminescence (sample PHX10).

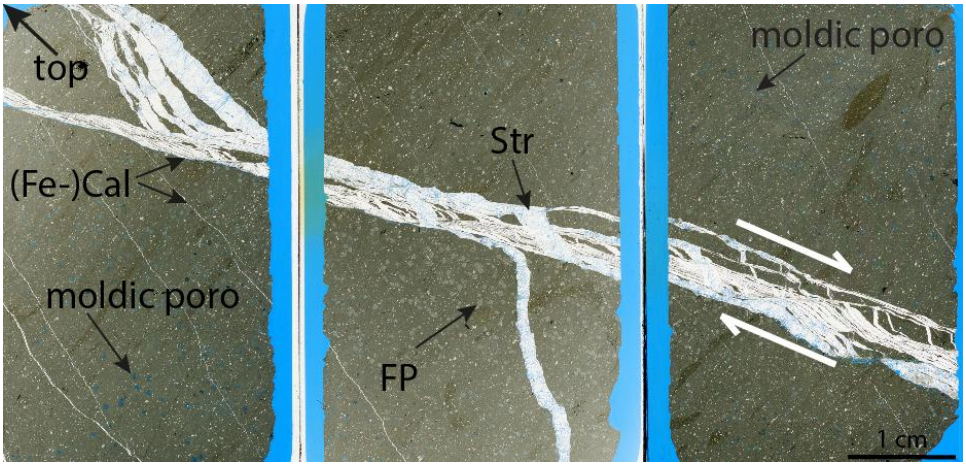

Figure 2.8 Thin section scans (layer PHX10), the top of the layer is marked with an arrow on the upper left corner. Wider (ferroan) calcite veins precipitate syntaxially and include host rock fragments. Smaller (ferroan) calcite veins are parallel to each other. Faecal pellets are locally dissolved (moldic porosity, left side) or preserved (e.g., in the center). White arrows highlight normal fault displacement and associated extensional fracturing, resulting in a sheared (ferroan) calcite vein and vein reactivation with strontianite precipitation. (Fe)-Cal: (ferroan) calcite, moldic poro: moldic porosity, FP: faecal pellet, Str: strontianite.

2.5.6 Optical porosity

Optical porosity is low with an average of 0.32% (min.: 0.0%, max.: 3.0%) and includes intergranular porosity (min.: 0.0%, max.: 1.0%) mostly between calcispheres and micrite, vuggy porosity in micrite (min.: 0.0%, max.: 1.0%), porosity in clay laminae (min.: 0.0%, max.: 0.7%), intraparticle porosity in foraminifera (min.: 0.0%, max.: 0.3%) and intercrystalline porosity in veins (min.: 0.0%, max.: 3.0%). Secondary porosity is visible in PHX10, due to (partial) faecal pellet dissolution. Due to the low content, no point-counting data on secondary porosity of faecal pellets are available.

2.5.7 Compaction and deformation

Compaction is recorded mainly by deformed calcispheres in contact with clay laminae and an absence of intergranular porosity. The calcispheres are partially pressed into the clay laminae and thereby elliptically deformed or even broke (Fig. 2.5c, d). This elliptical deformation allows the calculation of the degree of compaction with the Fry method (Fry, 1979). The average ratio for undeformed calcispheres in areas lacking clay laminae 1.03

(min.: 0.97, max.: 1.14) and for deformed calcispheres within clay laminae is 1.82 (min.: 1.30, max.: 4.24) (PHX21–PHX34). Using ImageJ, the average thickness of the compaction bands formed by deformed calcispheres and clay laminae is 0.35 mm (min.: 0.26 mm, max.: 0.52 mm) (PHX24, PHX 26, PHX27, PHX33 and PHX34). The average vertical shortening measured on calcispheres around clay laminae is therefore 38.5% (min.: 4.5%, max.: 73.6%) and is restricted to the compaction bands formed by deformed calcispheres and clay laminae. No chemical compaction (e.g., stylolitization) was observed in the thin sections.

2.5.8 Compactable depositional volume

The compactable depositional volume (CDV) is the sum of potentially compactable volume after deposition and before diagenetic processes (which can cause the formation of cements in former pore spaces) and compaction (which can cause porosity and therefore volume loss due to grain rearrangement and fracturing of porous (micro)fossils). High CDV values thus represent samples, which retained most of this volume and could be less compacted than samples having lower CDV values. In this study, the CDV includes compacted (detrital) micrite, clay laminae, authigenic sparry ferroan calcite cements in calcispheres and foraminifera, pore-filling and intergranular calcite and ferroan calcite, calcite and unstained carbonate cements, clay minerals in calcispheres and foraminifera, pore-filling clay minerals in micrite, pyrite and marcasite in clay laminae, calcispheres or foraminifera, microcrystalline cement in calcispheres, and all visible porosity in thin sections. In this study, the average CDV is 79.3% and ranges from 63.7% to 96.0%.

2.5.9 Petrophysical data

The He-porosity of the plugs drilled parallel to the stratification ranges from 1.0% to 18.7% (avg.: 8.1%). The grain density is 2.69 g/cm^3 to 2.85 g/cm^3 (avg.: 2.74 g/cm^3). The He-porosity of the plugs drilled perpendicular to the stratification ranges from 1.2% to 14.7% (avg.: 7.7%). The grain density range is 2.68 g/cm^3 to 2.78 g/cm^3 (avg.: 2.74 g/cm^3). For the fault zone, the He-porosities range from 4.1% to 9.9% (avg.: 6.0%) and grain densities from 2.73 g/cm^3 to 2.78 g/cm^3 (avg.: 2.74 g/cm^3). For plugs drilled parallel to stratification, permeability ranges from <0.0001 mD (technical measurement limit) to 0.201 mD (avg.: 0.0038 mD). For plugs drilled perpendicular to the stratification, the permeability ranges from <0.0001 mD to 0.079 mD (avg.: 0.0097 mD). The maximum values measured parallel to stratification are thus up to one order of magnitude higher than the plugs measured perpendicular to the stratification. For the fault zone, the permeability ranges from <0.0001 mD to 0.0003 mD (avg.: 0.0002 mD). The p-wave velocity (v_p) of the plugs drilled parallel

to the stratification ranges from 3333 to 5659 m/s (avg.: 4662 m/s). The v_p of the plugs drilled perpendicular to the stratification ranges from 2089 to 5843 m/s (avg.: 4230 m/s).

2.5.10 Correlations of petrophysical and petrographic properties

He-porosity and permeability values show no consistent correlation to each other (Fig. 2.9a). The correlation of grain density and He-porosity (Fig. 2.9b) indicates that porosity generally increases with higher grain density (parallel: R^2=0.63, perpendicular: R^2=0.54). Grain density (parallel: R^2=0.52, perpendicular: R^2=0.45) and porosity (parallel: R^2=0.91, perpendicular: R^2=0.81) both show a negative correlation with v_p (Fig. 2.9c, d).

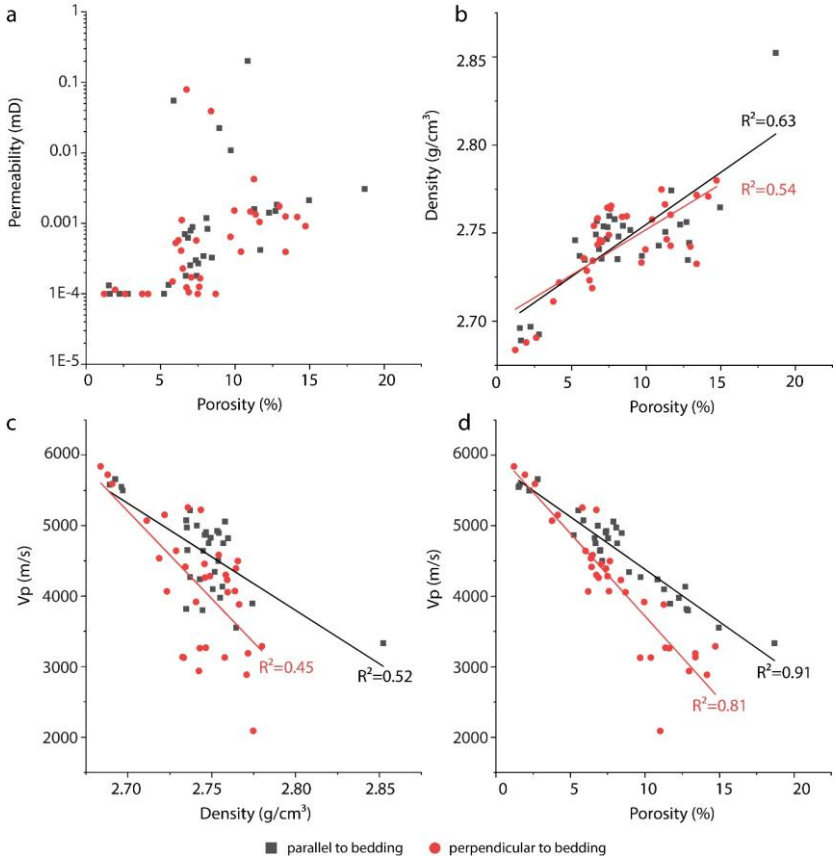

Figure 2.9 Cross-plots of petrophysical data, a) porosity (%) and permeability (mD), b) porosity (%) and grain density (g/cm³), c) density (g/cm³) and v_p (m/s), d) porosity (%) and v_p (m/s).

In addition, porosity decreases with higher amounts of authigenic components (parallel: R^2=0.30, perpendicular: R^2=0.59) (Fig. 2.10a), while this correlation is more robust in samples prepared perpendicular to bedding. Porosity furthermore decreases with higher amounts of detrital calcispheres (parallel: R^2=0.38, perpendicular: R^2=0.54) (Fig. 2.10d), but increases with higher amount of total detrital components (parallel: R^2=0.28, perpendicular: R^2=0.58) and micrite (parallel: R^2=0.43, perpendicular: R^2=0.67) (Fig. 2.10b, c). Samples containing more than 4% clay laminae show a slightly positive trend with porosity and grain density (Fig. 2.11a, b), whereas the v_p decreases with a higher amount of clay laminae (Fig. 2.11c).

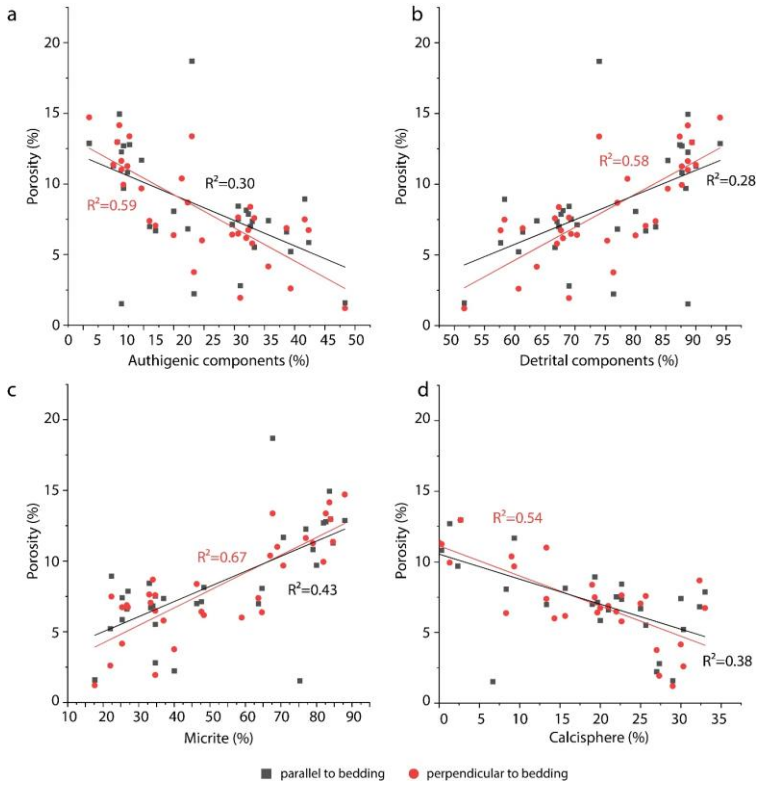

Figure 2.10 Cross-plots of petrophysical and petrographic data, all given in (%), a) authigenic components and He-porosity, b) detrital components and He-porosity, c) micrite and He-porosity, and d) calcispheres and He-porosity. The cross-plots indicates lower porosities in samples containing higher amounts of authigenic components and higher porosities in samples containing higher amounts of detrital components. Since micrite and calcispheres are the main detrital parts, higher micrite content results in higher porosity, while samples containing higher amounts of calcispheres show lower porosities.

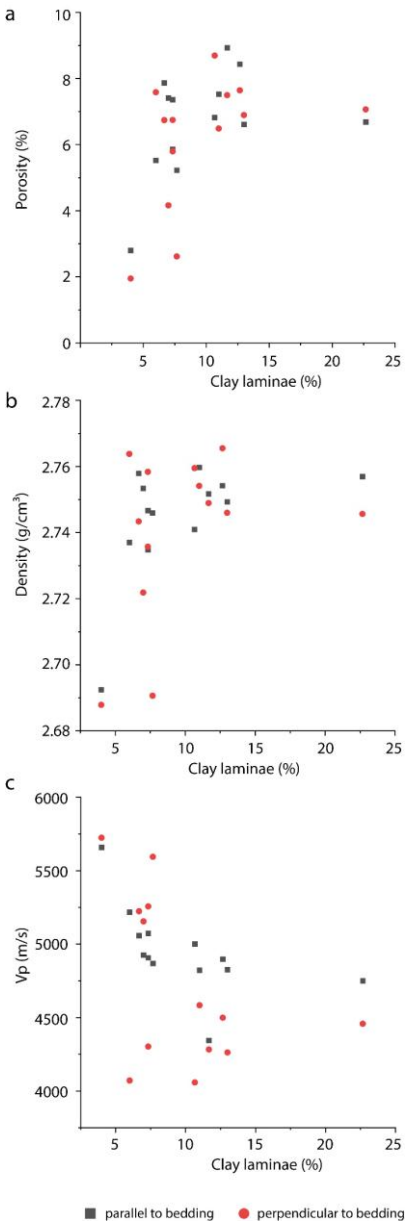

Figure 2.11 Cross-plot for He-porosity (%) and grain density (g/cm³) with an amount of clay laminae (%) from point counting for samples containing at minimum 4% clay laminae, a) higher porosity shows a slightly positive trend with higher amount of clay laminae, b) higher amount of clay laminae (minimum 4%) shows a slightly positive trend with (b) density and a slightly negative trend with (c) $v_{p.}$

The CDV shows a negative correlation with the sum of authigenic components (Fig. 2.12a; R^2=0.42), a positive correlation with sum of the detrital components (Fig. 2.12b; R^2=0.45) and also a positive correlation with the amount of micrite (Fig. 2.12c; R^2=0.79). The correlation of CDV and He-porosity indicates a generally positive correlation (Fig. 2.12d; parallel: R^2=0.40, perpendicular: R^2=0.60). Samples having lower present-day CDV values thus have lost more porosity and volume during compaction and thus have lower present-day porosity.

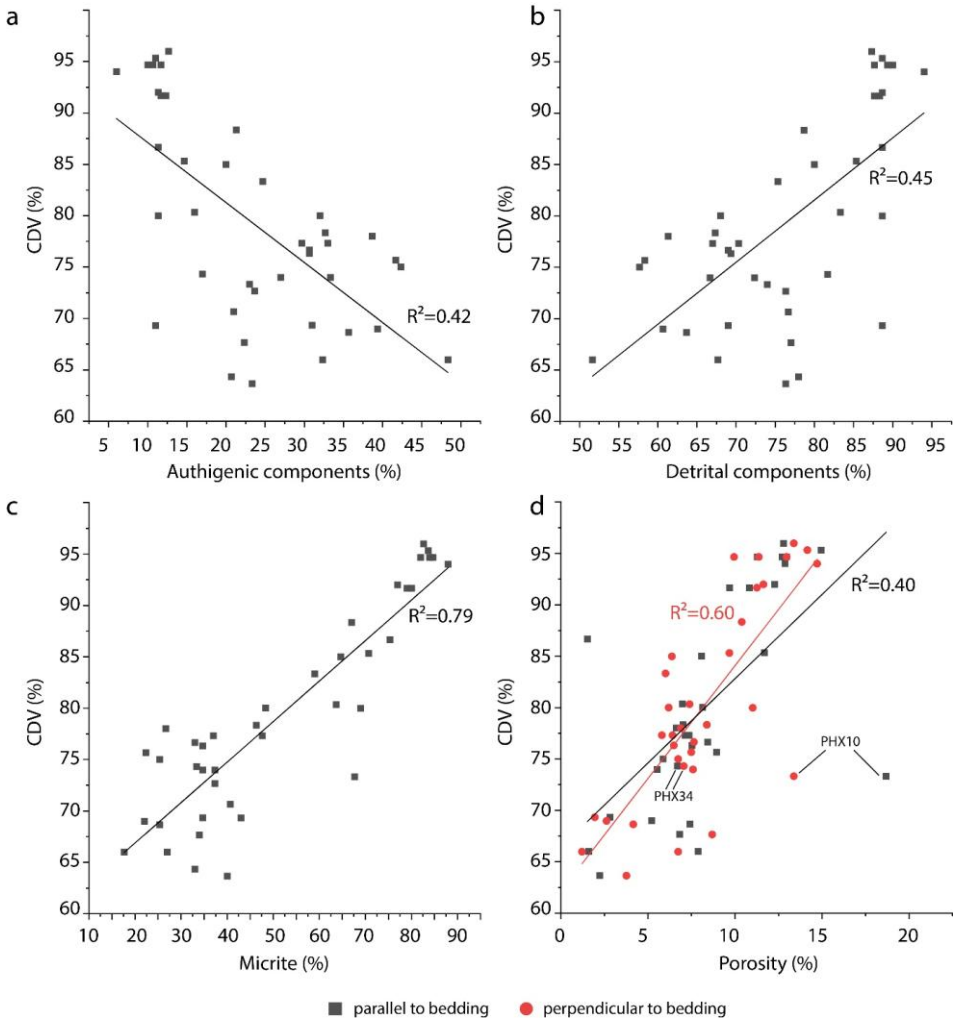

Figure 2.12 (Figure caption on next page)

Figure 2.12 (previous page) Cross-plot for compactable depositional volume (CDV) with petrophysical and petrographic data, all given in (%). CDV versus a) authigenic components, b) detrital components, c) micrite and d) He-porosity. Higher CDV thus correlates negatively with the amount of authigenic components, but positively with detrital components, while micrite shows the best correlation. Higher CDV also correlate with higher measured porosity. PHX10 marks the value for a sample with a CDV of 73.33%, containing no calcispheres but 67.67% micrite (porosity parallel and perpendicular to stratification of 18.69%, 13.38%) (Fig. 2.6). PHX34 marks a sample with a CDV of 74.33% containing 25% calcispheres and 33.33% micrite (porosity parallel and perpendicular to stratification of 6.69%, 7.07%) (Fig. 2.5a).

2.6 Discussion

2.6.1 Lithology and petrographic analyses

The alternation of pelagic, allochthonous limestone beds (argillaceous limestones to calcareous marlstone) with marly shale layers (claystone to marlstone) and an overall fining upward trend indicate turbiditic or debris flow deposits as also previously described by Kappel (2002). Turbidites and debrites often originate due to overload at slopes and slope failure or due to tectonic triggers, e.g., basin inversion, earthquakes or gravity driven flow (e.g., Dott, 1963; Bouma, 1964; Lowe and Guy, 2000 and references therein; Bouma, 2004). The presence of clasts composed of individual densely packed calcispheres could represent erosion and re-deposition by turbidity currents. As typical turbiditic sequence lithologies are not recognized in the studied lithologies, the layers can also be interpreted as debris flows with silt grain sizes. Due to the small grain size and high micrite content towards the top of the studied interval, the layers can also be interpreted as suspension flow in general (cf. Voigt and Häntzschel, 1964). The visible fining upward trend in thin sections and field observations (Fig. 2.2, 2.3) may thus represent a combination of smaller sea-level fluctuations in combination with suspension flow. Furthermore, the absence of calcispheres at the top of the studied interval may be an indication for sea-level or environmental changes (e.g., Masters and Scott, 1979; Vodrazkova and Munnecke, 2010). In this case, the sedimentation rate may be controlled by the Late Cretaceous inversion (e.g., Voigt et al., 2021) and thus slumping (cf. Wolf, 1995). The origin and transformation of carbonate muds and micrite is still an ongoing discussion (e.g., Munnecke et al., 2023), and detrital micrite can be classified as allomicrite (e.g., Wolf, 1965; Munnecke et al., 2023). Micrite observed in this study was classified as detrital, as the lithologies are described as redeposited. But also, autochthonous micrite could be part of the lithologies, after redeposition, and thus the term allomicrite was not applied. Also, glauconite, phosphate and dolomite

are classified as detrital due to the redeposition. Additional authigenic occurrence cannot be excluded.

Textures observed in thin sections and hand specimen from higher strata indicate rapid deposition, since fossils, e.g., foraminifera or test and shell fragments, are broken and do not show any preferential orientation (cf. Fig. 2.5e, g). The macroscopic fossil content is low; apart from three preserved belemnites, other macroscopic fossils are rarely present at the studied wall sections (Fig. 2.2). One belemnite was completely preserved and described as belemnite mucronate, due to its slenderness (Giers, 1958; Kappel, 2002). Based on the limestone-marly shale alternation, the calcispheres and foraminifera content, the identified belemnite and the overall rarely found macrofossils, the deposits can be interpreted to belong to the Beckum Member, in the transitional area of the Stromberg to the Beckum Member (c.f., Giers, 1958; Kappel, 2002). The transition to the Vorhelm Member in the hanging wall cannot be excluded.

The most abundant detrital components are micrite and calcispheres. They indicate deposition on a shelf in shallow to deep marine environment (e.g., Wilson, 1975; Grobe and Machel, 2002). Calcispheres are described as oligostegines (e.g., Giers, 1958; Voigt and Häntzschel, 1964; Kappel, 2002) or calcareous dinoflagellate cysts in previous publications (e.g., Wendler and Willems, 2004; Wiese et al., 2004). Also, the term calcisphere is described as ‘problematic’ by Versteegh et al. (2009), since the terminology and grouping is not clearly defined. In general, the abundance of calcispheres in Cretaceous lithologies worldwide (Albian to Upper Campanian) is well known (e.g., Vodrazkova and Munnecke, 2010; Wendler and Bown, 2013). As Cretaceous calcispheres are common between shallow-water and shelfmargin to slope deposits (e.g., Masters and Scott, 1979), the depositional environment cannot be clearly classified by the calcispheres as an indicator. However, the association with mostly planktic foraminifera indicates a shelf-margin to slope deposit (Masters and Scott, 1979).

The observed roundish to elliptical peloids/pellets exhibiting dissolution porosity along their margins (Fig. 2.6b) were interpreted as non-skeletal grains and because of the average grain size of 0.35 mm as peloids, which are partly or completely dissolved. Since they are not stained, a dolomitic composition is derived. Since some of the peloids also contain round structures, small opaque components or foraminifera fragments, the peloids are further interpreted as lithified faecal pellets (cf. Fig. 2.6a, b). Generally, faecal pellets preferentially occur in slope or shelf/ramp facies as well as deep water environments (Deik et al., 2019), and are therefore not considered as depositional indicators. Rarely occurring green clay minerals, filling intraparticle pores in foraminifera or calcispheres, and individual glauconite grains are interpreted to be redeposited, since all former pore spaces from microfossils are filled by either ferroan calcite cement, pyrite/marcasite, micrite or green clay

minerals. Both green clay minerals (berthierine, odinite or verdine facies) and glauconite indicate a shallow marine origin (Odin, 1990; Ryan and Hillier, 2002; Huggett, 2013) prior to redeposition. Since aragonite, the main component of other faecal pellets, is metastable and would be converted into calcite at shallow burial depths (e.g., Deik et al., 2019; Reuning et al., 2022), a recrystallization to dolomite is interpreted. However, as the partially dissolved pellets are crosscut by a ferroan calcite veins (Fig. 2.6a) and the intragranular porosity of the pellets remains uncemented, we interpret the formation of intragranular porosity to occur after fracturing and ferroan calcite vein formation, most likely during late diagenesis and exposure at the surface.

2.6.2 Paragenesis

2.6.2.1 Early diagenesis

Early diagenesis begins instantly after deposition and in conjunction with mechanical compaction of detrital components during overall shallow to intermediate burial (Fig. 2.13a). Based on regional reconstructions, the maximum burial depth likely did not exceed 1.5 km depth (Uffmann, 2014). The compaction also allowed dehydration of the clay laminae, which additionally release elements (e.g., Fe^{2+} and Ca^{2+}) into solution, which is also described in the transformation of smectite to illite (Boles and Franks, 1979). Furthermore, this initial compaction due to overburden resulted in the elliptical deformation and occasional fracturing of calcispheres close to clay laminae (Fig. 2.13c).

The observed pyrite and marcasite as framboids in clay laminae and calcispheres likely incorporated iron deliberated from clay mineral dehydration during initial compaction formed by bacterial sulphate reduction (BSR) in a shallow burial environment (Berner, 1970; Coleman, 1985). The BSR onset is often spontaneous, if organic-rich sediments and lower oxygen penetration are present (Machel and Grobe, 2001 and references therein). The main process of BSR is the microbial reduction of sulphate to hydrogen sulphide to form iron sulphide, aragonite dissolution, and an increase of alkalinity is the consequence (Biehl et al., 2016; Deik et al., 2019 and references therein). This leads to precipitation of calcite cements (e.g., Friis, 1995; Reuning et al., 2006; Deik et al., 2019) or dolomite and therefore to the lithification of the interpreted faecal pellets. However, incipient sulphate reduction can lead to carbonate dissolution due to a drop in pH (Reuning et al., 2022). The authors show that for specific cases a slightly higher concentration of organic matter allows an increased aragonite dissolution during sulphate reduction in the same depth, where dolomite cementation starts in a shallow burial environment (Reuning et al., 2022). The dolomitic composition of the pellets is supported by the pellets remaining unstained and showing a reddish luminescence in CL (Fig. 2.7f) (e.g., Götze, 2012). Also, further microbial mediated processes such as iron reduction and methanogenesis could lead to diagenetic

dolomite formation (Petrash et al., 2017, and references therein). Iron is a redox-sensitive element, and therefore the reduction by Fe(III)-respiring microorganisms leads to incorporation of iron in dolomite or newly formed carbonate overgrowths (Petrash et al., 2017, and references therein). The latter is depending on the occurrence of biologically produced sulphide anions, which could also lead to pyrite formation (Petrash et al. 2017, and references therein). As the calcispheres (both, deformed and intact) and also other fossils are filled with iron sulphides in the vicinity of clay laminae (Fig. 2.5a, d, f, g), a contemporaneous process of clay mineral dehydration and BSR (additional processes cannot be excluded) is interpreted. Furthermore, ferroan calcite precipitation is interpreted to postdate framboidal pyrite/marcasite formation and compaction as it encases iron sulphides and fills intraparticle pores in deformed and undeformed calcispheres and foraminifera. The precipitation of ferroan calcite likely was enhanced by the release of Fe and Ca into solution by the clay mineral dehydration. The formation of ferroan carbonates by elemental uptake from intraformational claystones is also observed in sandstones (cf. Miocic et al., 2020), where Fe- and Mg-rich carbonates are present in close proximity to clay layers. Also, the early burial release of Ca-ions by carbonate dissolution coupled to BSR could be feasible. However, the origin of early diagenetic calcite cements is debated as shown by Munnecke et al. (2023). Further mechanical compaction and fracturing of these initially hollow calcispheres (Voigt and Häntzschel, 1964), which are now filled by ferroan calcite, is inhibited, while uncemented foraminifera or calcispheres would likely crush under further mechanical stresses as derived from geomechanical laboratory tests on calcisphere-containing calcarenites (cf. Leuthold et al., 2021).

2.6.2.2 Late diagenesis

As (ferroan) calcite veins are following the outline of calcispheres filled by ferroan calcite (Fig. 2.5a, b), it is interpreted that they formed following the precipitation of intraparticle ferroan calcite, as thehollow calcispheres would have likely fractured. Within these veins, cathodoluminescence indicates areas with higher amount of Fe or Mn, or REE, based on its luminescence (Fig. 2.7a) (Budd et al., 2000), and may indicate slight changes in fluid compositions during vein precipitation. Most of the ferroan calcite cements present a dull orange luminescence up to non-luminescence representing Fe enrichment relative to Mn (cf. Budd et al., 2000). The assessment of a variability in the Fe content during vein cement precipitation is also supported by carbonate staining showing calcitic (red) and ferroan calcitic (blue) zones in stained thin sections (Fig. 2.5a). As (ferroan) calcite in the wider composite veins often encases pyrite/marcasite in contact with the host rock, the initial precipitate in the fracture is interpreted to be pyrite/marcasite.

Fault controlled, late diagenetic fluid interactions can also precipitate iron sulphides (pyrite and marcasite) at the transition of the rock before the fractures are filled by (ferroan) calcite

or strontianite (Grobe and Machel, 2002). The elongate blocky (ferroan) calcite crystals with euhedral crystal terminations (Fig. 2.7b) indicate a large open fracture aperture in which crystal facets could form (Prajapati et al. 2018). The remaining fracture porosity was then filled by strontianite precipitating on the euhedral crystal facets (Fig. 2.7c, d) (cf. Giers, 1958; Grobe and Machel, 2002). Since the veins in general contain strontianite, (ferroan) calcite and sulphides, the paleo-fluid is interpreted as sodium chloride rich, probably influenced by Zechstein salts from Northern Germany (e.g., Harder, 1964; Grobe and Machel, 2002). Alternatively, the strontium content in mineralized deep water of the Ruhr area is up to 1530 mg Sr/l, which would be high enough for the formation of strontianite deposits in the central Münsterland (Dölling and Juch, 2009, and references therein). These mineralized fluids may precipitate strontianite in contact with lower salinity formation waters in Cretaceous limestones, at lower pressures and temperatures of near-surface conditions (Dölling and Juch, 2009, and references therein). Although no correlation between the regional concentrations of Sr in mineralized fluids from the Ruhr area and the presence of strontianite veins could be established, it is the more likely source for strontianite veins (Dölling and Juch, 2009, and references therein). Earlier assumptions of lateral secretion from Upper Cretaceous limestones and marls (Kramm, 1985) based on similar Sr isotope signatures have mostly been discarded, as the Sr content in these limestones does not change with increasing distance from the veins (Dölling and Juch, 2009, and references therein). However, the formation of strontianite veins due to lateral secretion would also result in a more homogeneous occurrence of strontianite veins in joints. In this study, as well as described by Bauch et al. (2003), strontianite veins are mostly restricted to NW-SE striking veins, and (subordinate) in NE-SW. As the strontianite veins are dominantly found in areas surrounding faults within the Upper Cretaceous limestones of the region and mainly in NW-SE and only subordinately in NE-SW orientation, a relation with the Upper Cretaceous compressional event and inversion (e.g., Osning thrust) as a result of stress field change is interpreted (e.g., Drozdzewski, 1988; Kley and Voigt, 2008; Dölling et al., 2017; Voigt et al., 2021). Fault-controlled movement of warm and saline strontiumrich formation fluids from fractured and deformed Palaeozoic bedrocks could be an additional source (Grobe and Machel, 2002). As the host rock surrounding the sheared vein (Fig. 2.7e) also shows a purple luminescence of the micritic host rock, it is likely that in the vicinity to this sheared vein, the host rock was altered prior to (ferroan) calcite vein precipitation. Alternatively, a violet-blue luminescence in carbonates has previously been assigned to intrinsic lattice deformation in calcites (Toffolo et al., 2019). However, this cannot be linked to the shear displacement, as other host rock inclusions in the same sample still show an orange luminescence (Fig. 2.7b-d).

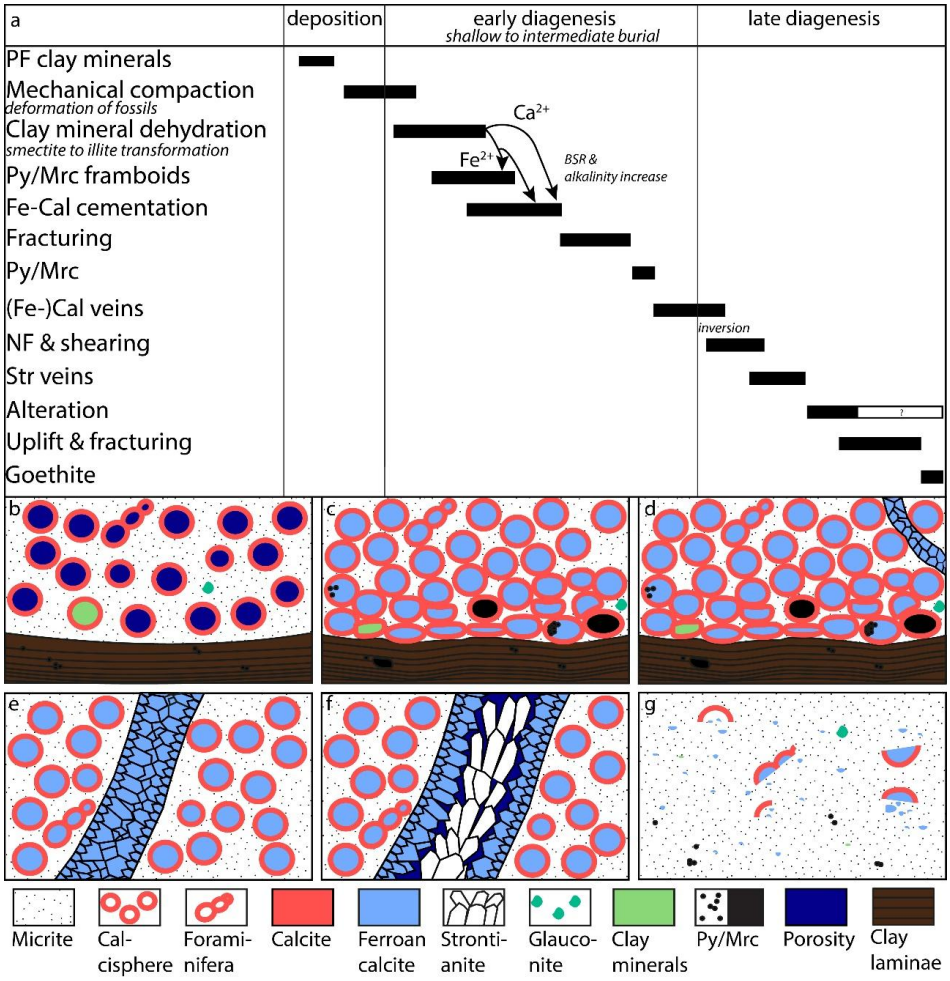

Figure 2.13 (Figure caption on next page)

Figure 2.13 (previous page) Schematic illustration of the studied sections, a) paragenetic sequence from deposition to late diagenesis of the studied carbonate rocks. Combination of rock and mineral composition, compaction and tectonic influence. b) Calcispheres, foraminifera and other fossils, clay laminae, and micrite are the main detrital components. Following (re-)deposition, calcispheres and other cavities within fossils are on occasion filled by green clay minerals and micrite or retain primary porosity. c) Intermediate burial compaction due to overburden stress leads to grain rearrangement and deformation. The still hollow calcispheres are elliptically deformed and rarely broken, especially at the transition to ductile clay laminae, forming compaction bands. Simultaneously, BSR enables the formation of pyrite/marcasite framboids and ferroan calcite cements. d) (Ferroan) calcite veins following the outlines of cemented fossils are completely sealed. e) Larger syntaxial euhedral (ferroan) calcite veins showing growth competition of elongate blocky crystals are also completely sealed. f) Fault controlled re-opening of (ferroan) calcite veins and late diagenetic fluid interaction leads to the formation of strontianite encasing euhedral calcite and ferroan calcite facets. g) The upper part of the studied lithologies shows less fossils in general and a high micrite/clay content. Clay laminae are mostly missing. The fossils are broken and mainly ferroan calcite cement precipitates in intraparticle pores. Framboidal pyrite/marcasite is found within the clay-rich micritic matrix. PF: pore filling, BSR: bacterial sulphate reduction, Py/Mrc: pyrite/marcasite, Fe-Cal: ferroan calcite, (Fe-)Cal: (ferroan) calcite, NF: normal fault (or normal fault reactivation), Str: strontianite.

Shearing of the studied vein in sample PHX10 syndates the precipitation of (ferroan) calcite veins, as the displaced and cut host rock inclusions, which are stabilized by (ferroan) calcite veins, are again overgrown by calcite and ferroan calcite (Fig. 2.6b and 2.7). The shearing furthermore predates the precipitation of strontianite, as the (ferroan) calcite overgrowing cut host rock inclusions is encased in strontianite (Fig. 2.6c). As the partially dissolved faecal pellets are crosscut by narrow (ferroan) calcite veins (Fig. 2.6a), their dissolution is interpreted to postdate the latest phase of (shear) fracturing, (ferroan) calcite and strontianite precipitation. The most likely interpretation is dissolution due to exposure to meteoric water. However, the presence of faecal pellets is only restricted to this individual layer showing dissolution, resulting in moldic porosity, which enhances the porosity but not the permeability. As the fracture surfaces of the few observed open fractures contain brownish iron residue (Fig. 2.3a, b), most likely goethite stains, it is suggested that the open fractures formed near to the present-day surface in a humid, oxidizing climate (e.g., Burgess et al., 2016), likely during uplift and stress release.

2.6.3 Compaction and CDV

The average optical porosity derived from point counting is 0.32%. A lack of visible porosity, including macroporosity, may be caused by compaction. Macroporosity is only

visible in samples containing dissolved pellets or within wider veins containing strontianite. Also, mechanical compaction is indicated by well-defined laminae interpreted as compaction bands, where elliptically deformed calcispheres and clay laminae are in contact. Initial mechanical compaction after (re)deposition causes grain rearrangement, while ductile clay laminae form boundaries, where the calcispheres deformed elliptically and even break. The average vertical compaction is 38.5%, but since the determination of compaction by Fry (1979) is in this case related to calcispheres at the transition to clay laminae, no overall correlation could be done, since not every thin section contains calcispheres and clay laminae. The elliptical deformation of calcispheres in the Münsterland Cretaceous Basin was already recognized by Giers (1958), but not quantified. As the combination of compacted calcispheres and clay laminae forms compaction bands parallel to bedding, direction-dependent hydraulic properties, e.g., permeability perpendicular to the compaction band, are decreased by on avg. 0.4 orders of magnitude. This effect is also observed for compaction bands formed during geomechanical lab experiments (c.f. Stanchits et al., 2009; Baud et al., 2012; Leuthold et al., 2021). Similar to the use of palynomorphs (cf. Pliocene of Great Bahama Bank or Silurian of Gotland, Westphal and Munnecke, 1997) as a compaction indicator in fine-grained carbonates, calcispheres and also other intraporosity bearing fossils can record localized compaction.

To further assess the impact of compaction based on petrographic parameters, similar to the IGV calculations in sandstones (Houseknecht, 1987; Paxton et al., 2002), the concept of the 'compactable depositional volume' was evaluated. As both compaction and cementation influence the volume and porosity loss during diagenesis and one process may limit the other, we chose the CDV to assess controlling factors on volume and porosity. Samples with higher measured He-porosity show higher CDV, which means that depositional porosity and volume is retained and can be assessed using the CDV. However, a higher proportion of authigenic cements shows lower CDV and porosity values (Fig. 2.10a and 2.12a), indicating that the cementation reduces porosity but does not effectively inhibit compaction, supporting the assessment that the cements formed after initial compaction. Furthermore, the CDV shows a positive correlation with detrital minerals (Fig. 2.12b). This is related to the large proportion of micritic matrix, which preserves microporosity (Zhang and Lu, 2019) which enhances the CDV. As micrite has a high intercrystalline porosity at deposition of up to ~ 80% (Bathurst, 1970; Shinn et al., 1977; Moshier, 1989; Goldhammer, 1997; Zhang and Lu, 2019), it is included in this assessment, just as depositional clay mineral matrix is included in IGV assessments in sandstones (Paxton et al., 2002). After Lee et al. (2021), the initial porosity of Miocene to Holocene wackestones of the west coast of Australia starts at ~ 60%. Although the composition or texture of some samples, as well as the measured He-porosity varies, the CDV can show similar values, as shown in Fig. 2.12d. The sample PHX10 (Fig. 2.7b-f) shows a CDV of 73.33% and a porosity of 18.69% parallel

to the stratification and 13.38% perpendicular to the stratification, whereas the sample PHX34 (Fig. 2.7a, 2.5a) shows a CDV of 74.33%, but a porosity of 6.69% parallel to the stratification and 7.07% perpendicular to the stratification. The sample PHX10 is composed mostly of micrite (67.67%) and no calcispheres, whereas the sample PHX34 contains 25% calcispheres and 33.33% micrite. High CDV values (e.g., 96% in sample PHX05) are an effect of overrepresentation of micrite. The same effect, however, can be observed in IGV calculations of sandstone samples rich in depositional clay minerals (c.f. Paxton et al., 2002). However, the optical porosity in the thin sections is determined by point counting and does not include microporosity in micrite and clay minerals or clay minerals in laminae because of the limited magnification of the microscope. Also, just as with depositional clay mineral matrix in sandstones and their effect on compaction (i.e. IGV in Paxton et al., 2002), the initial microporosity of micrite is not included in the calculation of the CDV. In contrast, sandstones do not necessarily contain grains with primary intraparticle porosity apart from fossils, which can be reduced by compaction. As the primary porosity in carbonate rocks is influenced by pre-depositional and depositional processes (Choquette and Pray, 1970), both have to be considered to analyse the CDV. If applicable in similar lithologies, the CDV may be a suitable indicator for post-depositional compaction in limestones containing components or fossils with intraparticle porosity and may capture the compactional effect on reservoir properties. The CDV should be a basis to compare samples within the same stratigraphy and to relate the effect of compaction on petrophysical parameters as measured porosity and permeability. Also, as described by Lee et al. (2021), the compaction behaviour of carbonate rocks varies, as well as the early stage of porosity.

2.6.4 Reservoir quality controlling factors

The reservoir quality controlling factors for the analysed lithology are (1) mechanical compaction, which leads to grain rearrangement, (micro)porosity loss and formation of compaction bands at ductile clay laminae boundaries; (2) cementation of former pore spaces with mainly ferroan calcite and (3) vein formation of (ferroan) calcite and strontianite, overall reducing the porosity and permeability. The subordinate dissolution of faecal pellets slightly enhances porosity but not permeability, since the moldic pores are not connected (Fig. 2.6b, 2.7f, 2.8). Also, particle sizes influence porosity, as micrite and clay laminae still contain microporosity, whereas calcispheres are fully cemented. Tests are most likely not cemented, which contributes to the microporosity (e.g., Abouelresh and Mahmoud, 2022). However, a higher amount of calcispheres causes lower He-porosities and higher v_p values, likely related to larger volumes of ferroan calcite cements precipitating in the intraparticle pores. Also, compaction and a decrease of porosity enhance v_p values (e.g., Anselmetti and Eberli, 1993).

The recorded sonic matrix compressional velocity range is typical for limestones with an average porosity of 5–20% (Rider and Kennedy, 2011). Slightly better correlating v_p and porosity values parallel to bedding are related to clay laminae and compacted calcispheres or calcisphere clasts aligned to the bedding. Also, the mineralogical composition as well as fabric can influence the sonic matrix compressional velocity (Kenter et al., 2007). In this study, the amount of clay laminae in samples with a minimum content of 4% shows a slightly negative correlation with v_p (Fig. 2.11c). Another influencing factor are pore types, as carbonate rocks can include various pore sizes and types (e.g., Weger et al., 2009). Positive deviations of a porosity-velocity trend and therefore higher velocity values can be caused by the pore type and the depositional and diagenetic overprint, which is shown by Anselmetti and Eberli (1999). However, macroporosity within the thin sections in this study is poor, except for layer PHX10 due to dissolution processes. Porosity and permeability values are generally low and show no log-linear correlation (Fig. 2.9a). For samples drilled parallel to the stratification, higher grain density correlates with higher He-porosity (Fig. 2.9b), which also correlates with higher amounts of clay laminae (Fig. 2.11a, b) and the presence of compaction bands in samples containing clay laminae (Fig. 2.5d).

Micrite, clay laminae and fossil tests contain microporosity, which is not visible in the thin sections using transmitted light microscopy, but can influence petrophysical properties, which is known from clays in sandstones (e.g., Nadeau and Hurst, 1991). In general, the influence of micrite and clay laminae depends on their texture, pore space geometry and sizes (e.g., Volery et al., 2010; Deville de Periere et al., 2011; Regnet et al., 2015; Smodej et al., 2019). Samples containing more than 4% clay laminae show a slightly positive trend with higher porosity and grain density (Fig. 2.11a, b). Plugs drilled parallel to the stratification are of factor 1.4 higher for the maximum permeability than that of samples drilled perpendicularly to the stratification. This is largely related to the anisotropy related to compacted calcispheres and clay laminae (Fig. 2.5d), since clay layers and compaction bands are known to act as fluid flow barriers (cf. Kayser, 2006). But in average, the permeability is in the same order. In addition, mechanical compaction decreases porosity and permeability in general (e.g., Halley and Schmoker, 1983; David et al., 2001; Croizé et al., 2013), since grain rearrangement and calcisphere deformation reduce the inter- and intragranular pore space and pore throat sizes. Smaller amounts of calcispheres in higher strata of the lithological column can thus be related to slightly higher permeabilities, which is interpreted to be related to a higher amount of micrite (Fig. 2.2) and a lower degree of compaction. As the lower measurement limit of the permeameter is 0.0001 mD, the permeability of samples given as 0.0001 mD will likely be lower, enhancing the sealing potential of the host rock.

The effect of diagenesis in the studied samples reduces the reservoir quality in general, since carbonate cements filled former pore spaces and fractures. Large-scale, near-surface

fluid flow is thus likely restricted to faults and fractures (e.g., Grobe and Machel, 2002), as also observed in injection tests in the area of Münster (Mohrdieck, 1996). Veins are mostly sealed with (ferroan) calcite, rarely strontianite or both, and only a few open fractures were observed in the quarry. However, they may also be an effect of carbonate vein dissolution during weathering and quarry operation or an effect of stress release during uplift (e.g.Wyrick and Borchers, 1981). Goethite was formed likely by the alteration of pyrite in the host rock and stained the surface (cf. Burgess et al., 2016). Otherwise, the fractures would have likely been sealed by (ferroan) calcite or strontianite, as documented for the veins, and do not contribute to fluid flow in the subsurface. As the studied samples originate directly from and further away from the fault zone (Fig. 2.3c), and petrophysical data do not vary distinctly around the fault (digital appendix – chapter 2), the fault zone is interpreted to not influence porosity and permeability in the host rock. Dissolution is limited to one layer (PHX10), which increases porosity, but not the permeability. Due to the presence of (ferroan) calcite and strontianite as vein precipitates, the reservoir quality is low and the studied lithologies are therefore tight. Therefore, the studied lithologies in the Central Münsterland Cretaceous Basin, overlying the northernmost extent of subsurface coal mining, are likely acting as sealing lithologies. Although vertical variations in the composition of limestones and marly shales and thicknesses are known, the lithologies show a continuous lateral extent on up to 150 km^2 (Giers, 1958). Only at the transition to the basin border, inhomogeneities can be expected (Giers, 1958). However, the studied lithologies are partially overlying the northern extend of former coal-mining districts, and thus may not be representative for the whole coal-mining district. The facies with its deposited sediments will vary towards the south (c.f. Fig. 2.1a).

2.7 Conclusions

The study of Upper Campanian limestones (Beckum Member) illustrates the impact of early and late diagenetic processes in former high porosity, mostly detrital rocks. Low matrix porosity (1.0 to 18.7%) and permeability (<0.0001 to 0.2 mD) is related to mechanical compaction, resulting in compaction bands and early cementation of former pore spaces with mainly ferroan calcite. Only marginal dissolution of faecal pellets slightly improves porosity but not permeability, which is seen only in one layer. Fractures are cemented and sealed by (ferroan) calcite and mostly preferred NW-SE orientated strontianite, due to the Late Cretaceous inversion and reactivation of fault systems. The precipitation of (ferroan) calcite and strontianite veins further diminished large-scale fluid pathways. The rocks around the studied fault do not show different petrophysical properties or diagenetic alteration as surrounding rocks in the quarry. Open and brownish coated fractures are most likely uplifted related. Due to the low matrix permeability below 0.2 mD, lithologies can be considered as seals. This also indicates that a geothermal utilization of this formation at

depth may be limited. Overall, the up to 25-m-thick Beckum Member limestone and marly shale alternation from the Upper Cretaceous acts as a regional seal, if not faulted with associated fractured damage zones. Only open fractures and faults, if present in the subsurface, could enhance fluid pathways. Therefore, fault-related fluid flow may have been limited. The compactable depositional volume (CDV) for carbonate rocks, derived from petrographic thin section analyses, may be a useful tool to assess the timing of cementation in relation to compaction if components with intraparticle porosity are present and to assess the effect of compactional volume loss on reservoir properties. The effect of overrepresentation by micrite and therefore high CDV values is comparable to the effect from IGV calculations of sandstone samples rich in depositional clay minerals.

3 Structural and diagenetic controls on fluid pathways in fractured Triassic Muschelkalk and Keuper limestones, southern Germany

3.1 Abstract

Understanding structural and diagenetic interactions is key in analyzing reservoir quality (i.e. fluid pathways) in tight lithologies in the focus of geo-energy production as e.g., geothermal energy. Fracture spacing and clustering is crucial for reservoir production success and reduces uncertainty in reservoir exploration and utilization. This outcrop analog study evaluates diagenesis, fractures, and vein cement generations in tight fractured limestones of the Upper Muschelkalk-Lower Keuper transition on the eastern Upper Rhine Graben shoulder in SW Germany. Early and burial diagenesis led to cementation of former pore spaces and therefore drastically reduced the matrix porosity and permeability (porosity: 0.16 to 10.58%, permeability: <0.0001 mD to 9.7 mD). Highest permeabilities are recorded in samples containing partially sealed veins and stylolites (up to 9.7 mD) at 1.2 MPa confining stress. The impact of increasing confining stress on the permeability of undisturbed limestones, as well as limestones containing stylolites and partially sealed veins, indicate that besides an undisturbed host rock sample and a sample containing stylolites, partially sealed veins preserve higher permeability at 30 MPa confining stress (41% of initial value, compared to 16 and 11% of the initial value).

Fracture cluster analyses using the normalized correlation count method indicates that clustering around the fault is not symmetrically arranged and contains fracture sets of different strike. Fracture clusters also exist away from the fault. Slip and dilation tendencies indicate that clustered fracture sets striking NNE-SSW parallel to the Rhine graben rift, WNW-ESE, and NW-SE parallel to the in-situ maximum principal horizontal stress are more likely to contribute to fluid flow as they are suitably oriented in the present-day stress field. Breached, decameter-scale reverse kink bands are the first reported in the region, c. 180-200 km N-NNE of the Alpine deformation front. Kink bands are most likely related to compression by far field stresses induced by the Alpine orogeny during the Eocene, and show partially cemented fault planes indicating locally persevered pore space.

The applied methods of structural and diagenetic reservoir quality assessment and obtained outcomes aid in the understanding of fluid migration pathways for geoenergy applications in the Upper Rhine Graben area and are transferrable to other fractured tight reservoirs worldwide, which can help to solve problems for energy or heat supply that are of societal importance.

3.2 Introduction

Most carbonate reservoirs are naturally fractured (Garland et al., 2012; Lamarche et al., 2012). Fractures in reservoirs can enhance the local permeability and thus positively influence production, but can thus also result in increased uncertainty during reservoir development (e.g., Almansour et al., 2020), as sealed fractures can result in reservoir compartmentalization (Moore and Wade, 2013). However, fractured carbonates host a large amount of conventional reserves globally (Harbaugh, 1967; Burchette and Britton, 1985; Burchette, 2012), such as giant fields producing hydrocarbons as the Ghawar oil field in Saudi Arabia (Kosari et al., 2017), the Gachsaran Oil Field in Iran, Kirkuk in Iraq (Tavakoli, 2020) or pre-salt carbonate reservoirs of the Santos Basin at the Brazilian Atlantic margin (e.g., Wagner Moreira et al., 2023). Fractured carbonates are also relevant as energy storage sites such as Europe's largest gas storage site Rehden, Germany, with 3.95 bcm working gas at 1.9–2.3 km depth (LBEG, 2023), and supply drinking water for approximately 25% of the world population worldwide, where the reservoir is found at 10s of meters depth (Suski et al., 2008; Medici et al., 2021). Furthermore, carbonate reservoirs are of recent interest for geothermal energy production. For example, deep geothermal exploration in the NW European Carboniferous Basin in the Netherlands and the Molasse Basin in Germany target fractures, faults and karstification (Kaminskaite-Baranauskiene et al., 2023; Gutteridge et al., 2025).

Fluid flow and surface area for heat exchange depend on permeable host rock porosity and the size and abundance of naturally occurring or engineered fractures. These in turn depend on several factors such as the depositional environment and facies, rock-fabric, and the diagenetic overprint (Burchette and Britton, 1985; Ahr, 2008; Burchette, 2012; Worden et al., 2018). Diagenetic processes can cause cementation, calcification/dolomitization, but also dissolution of minerals, and/or compaction and formation of stylolites (Schoenherr et al., 2018; Humphrey et al., 2019; Gomez-Rivas et al., 2022; Ölmez et al., 2024), which increases the complexity in predicting petrophysical properties. Therefore, when assessing carbonate reservoirs, a combination of rock classification, diagenetic analysis, petrophysical analysis (e.g., Machel, 2005) and the assessment of the structural inventory provide

constraints on reservoir properties and thus limit exploration risks (e.g., Becker et al., 2019b).

Open fractures (joints) in tight rocks may be preferred fluid pathways in the subsurface, and are therefore of increasing interest in research related to geothermal energy production, hydrocarbon recovery, gas storage, and groundwater reservoir assessment (Laubach et al., 2004; Bahrami et al., 2012; Khelifa et al., 2014; Carlos de Dios et al., 2017; Elliott et al., 2025). Although the ability of fractures to transmit fluids is widely considered to be principally governed by the current stress field (e.g., Barton et al., 1995; Finkbeiner et al., 1997; Mattila and Tammisto, 2012) in some cases the openness of fractures is relatively insensitive to small differences in confining pressures in the subsurface (Laubach et al., 2004) and mineral deposits in the fractures may be determinative of the capacity of fractures to support flow (Olson et al., 2009; Almansour et al., 2020). Furthermore, the understanding of fracture spacing and clustering are important for the success or failure of production of reservoirs (Narr, 1996; Li et al., 2018; Marrett et al., 2018). Especially in tight formations (low matrix porosity and permeability), the reservoir is dominantly controlled by its fracture network (Agosta et al., 2010; Becker et al., 2018; Becker et al., 2019a; Rashid et al., 2023; Elliott et al., 2025). A combination of fracture data from outcrop studies and subsurface help understand fracture pattern and can be used for fractured reservoir modelling, and thus reduce uncertainties for geoenergy applications (Becker et al., 2018; Allgaier et al., 2023a).

Because data from the subsurface is scarce and mostly only allows the delineation of properties from a point source (i.e. individual plugs) or line-source (e.g., geophysical logs) in wells, outcrop analog studies can aid in understanding lateral variations (Becker et al., 2019a). Assuming that fractures formed as different generations over time to have different strike orientations per generation, care has to be taken to only assess fractures with the same strike orientation (e.g., Li et al., 2018) when assessing fracture clustering and intensity. Tectonic processes such as lateral compression, extension, fluid overpressure or uplift can cause fracturing and enhance flow properties (e.g., Moore and Wade, 2013) or affect pre-existing fractures by dilation or shearing in a present-day stress field (Morris et al., 1996; Ferrill et al., 2020), which can adjust fluid pathways in open and partially sealed veins. Especially partially sealed veins, occasionally preserving bridging textures, are interpreted to preserve permeability at depth (Gale et al., 2010; Lander and Laubach, 2015). However, the analysis especially of barren fractures in quarries does not necessarily reflect fracture intensities at depths (e.g., Becker et al., 2018; Li et al., 2018).

The Upper Rhine Graben hosts the largest geothermal anomaly in Germany (Clauser and Villinger, 1990; Pribnow and Schellschmidt, 2000) and is in the focus of geothermal exploration (Kushnir et al., 2018; Harlé et al., 2019; Heap et al., 2019). At the Soultz-sous-Forêts geothermal site in France, Lower and Middle Muschelkalk lithologies were studied

with a focus on petrophysical, thermal, and geomechanical properties (Heap et al., 2019). So far, the Upper Muschelkalk lithologies were of interest in terms of facies and sequence stratigraphy (Vollrath, 1938; Brüderlin, 1970; Mehl, 1982; Seufert, 1984; Aigner, 1985; Brunner and Simon, 1985; Seufert and Schweizer, 1985; Aigner, 1986; Aigner and Bachmann, 1992; Geng and Zeeh, 1995; Geng, 1996; Zeeh and Geng, 2001; Hagdorn and Simon, 2021). Structural analysis of the Triassic Muschelkalk focused on fracture intensity related to near normal, strike-slip and reverse faults (Meier et al., 2015). The understanding of the interplay of rock properties (e.g., porosity and permeability), diagenetic processes, structural overprint, and the influences on reservoir quality is not established yet. However, successfully assessing the reservoir quality of fractured limestones may be key in unlocking geothermal and hydrocarbon reservoir potential in the Upper Rhine Graben.

The Upper Muschelkalk carbonate platform in southern Germany has been described as a reservoir which can be related to carbonate reservoirs in the Middle East due to conceptually comparable characteristics (Kostic and Aigner, 2004; Koehrer et al., 2012; Warnecke and Aigner, 2019). The petrophysical values can vary within microfacies types, therefore a grouping for petrophysical values with respect to facies types is not applicable in all regions (Kostic and Aigner, 2004).

In this study, we evaluate compressional and tensional deformation structures in form of (breached) conjugate reverse kink bands, different fractures and vein cement generations, in combination with lithological, petrographic, and petrophysical analyses to assess reservoir quality in fractured limestones of the Upper Muschelkalk to Lower Keuper transition. Kink bands are tabular fold zones cutting foliation as e.g., bedding, where foliation is rotated as result from shear couple and commonly occur as conjugate sets (box fold like conjugate system) (Dewey, 1965) and are used as paleo-stress indicator in rocks (Srivastava et al., 1998). The studied quarry is located on the eastern Upper Rhine Graben shoulder in SW Germany highlights breached, decameter conjugate kink bands. We also determine the effect of increases in confining stress on the permeability of undisturbed limestones, and limestones containing stylolites and partially sealed veins. In combination with structural and diagenetic assessments, fracture cluster analyses using the NCC method, and T_d and T_s evaluations, we evaluate the controlling factors on fluid pathways in carbonates. The applied workflows and derived results contribute to the understanding of migration pathways of fluids for e.g., geothermal energy or hydrocarbons in the Upper Rhine Graben and other fractured carbonate platforms elsewhere.

3.3 Geological setting

The Muschelkalk was deposited in the southern Germanic Basin, following a northwards marine ingression into the basin (Fig 3.1d), which was separated from the open-marine Tethys by the Vindelician/Bohemian Massif in the south (Aigner, 1985; Aigner, 1986; Kostic and Aigner, 2004). Following the opening of the Burgundy gate, the East Carpathian gate and the Silesian-Moravian gate (Fig. 1d), the transgression during the Muschelkalk formed a gently inclined carbonate ramp comprising limestone, dolostone, claystone, and evaporite deposits (Kostic and Aigner, 2004). The transition to the Vindelician-Bohemian Massif during the Muschelkalk is characterized by coast-parallel deposition of terrestrial sediments (Aigner, 1985; Kostic and Aigner, 2004 and references therein). The Muschelkalk limestones has been being replaced by a dolomitic limestone facies towards the terrestrial sediments (Kostic and Aigner, 2004). The studied top part of the Upper Muschelkalk (Meißner Fm., LGRB, 2022) is characterized by an overall shallowing up sequence of a highstand systems tract at the end of the Muschelkalk and comprises an increasing amount of bioclastic, oolitic and oncolitic beds and shows increasing and more intense dolomitization (Aigner and Bachmann, 1992). This regressive trend during the uppermost Muschelkalk continues into the Lower Keuper (Aigner and Bachmann, 1992). The overlying Keuper (Early Ladinian to Rhaetian) is characterized by transgressive and regressive deposits, which lead to the formation of clastic to transitional marine and evaporitic deposits (Ziegler, 1982). The lowermost Keuper (Erfurt Fm.) is present as claystone/dolomite intercalations, which may contain fine- to medium-grained sandstone beds. Furthermore, coaly layers and limey and phosphatic bonebeds can occur marking the lithostratigraphic boundary between the Muschelkalk and Keuper (Etzold and Franz, 2005). The general evolution is described as subsidence and deposition from the Triassic to the Cretaceous, followed by uplift and erosion throughout the Cretaceous to Eocene, while remaining Mesozoic and newly deposited Cenozoic lithologies in the Upper Rhine Graben experience another phase of subsidence from the Eocene onwards (Bossennec et al., 2021 and references therein). In contrast to the Upper Rhine Graben, the Mesozoic lithologies on the graben shoulders did not experience an additional burial since the Eocene but were uplifted and are now exposed in outcrop. The studied Knittlingen quarry is located on the eastern Upper Rhine Graben shoulder, approximately 30 km east of the city of Karlsruhe, Germany (Fig. 3.1a, b, c) and exposes Middle Triassic Muschelkalk and Keuper lithologies (Early Anisian to Early Ladinian).

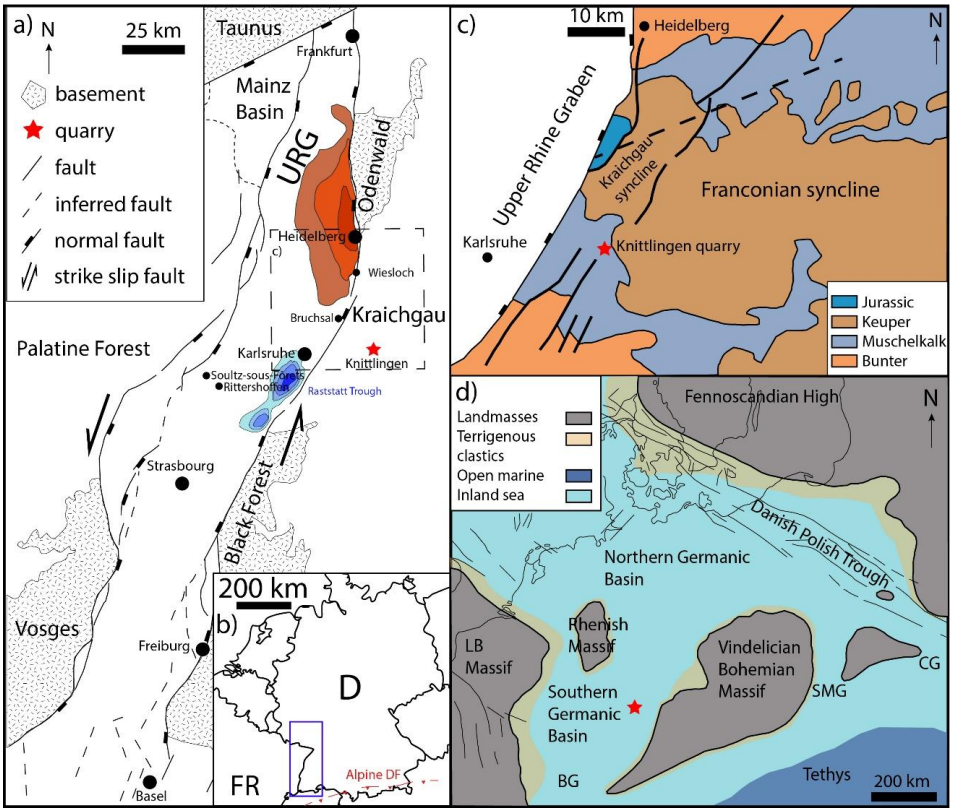

Figure 3.1 Overview of the study location and the Upper Rhine Graben. a) The study location is around 30 km east of the city of Karlsruhe in Knittlingen, isolines for the Heidelberg pull apart basin (red) and Rastatt trough outlining the depocenters (blue) (modified after Schumacher, 2002; Gabriel et al., 2013; Böcker et al., 2017; Busch et al., 2024). b) Marked location of the Upper Rhine Graben in blue box and Kraichgau area in SW Germany (modified after Busch et al., 2022b). Alpine deformation front (Alpine DF, dashed red line) adapted from Käßner et al. (2024). c) Simplified geological and tectonically map, the approximal location of the Knittlingen quarry is marked with a red star (redrawn and modified after Meier et al., 2015). d) Study location (red star) with paleogeographic distribution of landmasses during the middle Triassic Upper Muschelkalk, redrawn and modified after (redrawn and modified after Franz et al., 2015; Warnecke and Aigner, 2019, and references therein). BG: Burgundy Gate, CG: East-Carpathian Gate, SMG: Silesian-Moravian Gate, LB: London Brabant Massif.

The Upper Rhine Graben is an about 300 km long (Basel to Frankfurt/Main), approximately 30 to 40 km wide intracontinental rift basin with an overall NNE-SSW strike

direction (Fig. 3.1a), and was formed as part of the European Cenozoic Rift System (Ziegler, 1992; Schumacher, 2002). The region and location of the Upper Rhine Graben rift is linked to changing stress fields (Fig. 3.2) and reactivation of Permo-Carboniferous NNE-SSW oriented fault systems (Ziegler, 1992; Schumacher, 2002). During the Permian and Early Triassic, the region experienced N-S and NNE-SSW extension in a normal faulting regime (Dezayes and Lerouge, 2019).

For Central Europe, the σ_1-axis is reconstructed as NW-SE during the Early Cretaceous and NE-SW compression during the Late Cretaceous, persisting into the Paleocene (Kley and Voigt, 2008), leading to uplift in the area of the southern Germanic Basin (Böcker, 2015 and references therein) (Fig. 3.2).

During the Middle Eocene W-E directed extension resulted in reactivation of Permo-Carboniferous NNE-SSW oriented fault systems and initiated the Upper Rhine Graben rift formation (Ziegler, 1992; Schumacher, 2002). Subsequently, the maximum principal stress rotated clockwise towards a NNE-SSW oriented compression around the Middle to Late Eocene (Schumacher, 2002). In the late Eocene, extension and subsidence of the southern part of the graben occurred due to NNE trending Alpine compression (Rotstein and Schaming, 2011 and references therein).

During the Oligocene, rifting of the Upper Rhine Graben was characterized by W-E to WNW-ESE extension, leading to the development of NNE-SSW striking graben-parallel faults (Schumacher, 2002). The NNE-SSW striking faults are abundant in the Cenozoic sequence, whereas the NNW-SSE oriented faults mostly abut against these large faults (Reinhold et al., 2016).

Reorientation of the stress field during the Miocene resulted in a sinistral strike-slip movement along the boundary faults of the Upper Rhine Graben, leading to a direction of the maximum principal stress to NNW-SSE to NW-SE and development of minor faults with a predominant NNW-SSE strike (Schumacher, 2002). Consequently, NNE-SSW trending faults have been reactivated in the same shear direction (Ahorner, 1975; Schumacher, 2002).

The current stress field (principal stress directions and magnitudes) for the central region of the Upper Rhine Graben derived from well data from the Bruchsal geothermal site matches with σ_{Hmax} oriented approximately NW-SE (Meixner et al., 2014).

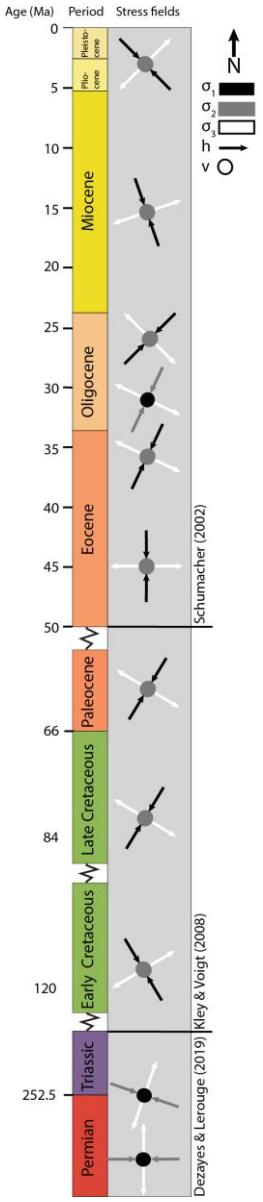

Figure 3.2 Changes in stress field over time in Central Europe. For the Permian and Triassic, a normal faulting regime with $\sigma_1=\sigma_V$ is given (modified and redrawn from Dezayes and Lerouge, 2019). For Early Cretaceous to Late Eocene the stress field was dominantly compressional with $\sigma_1=\sigma_{Hmax}$ (modified and redrawn from Schumacher, 2002; Kley and Voigt, 2008).

The continental Upper Rhine Graben rift basin accumulated Paleogene and Neogene marine and terrestrial deposits, which unconformably overly the Mesozoic sequence. Burial depths of Mesozoic units partly exceeding 5000 m (Anders et al., 2013), related to pull-apart basins (Rastatt trough, south of Karlsruhe, Fig. 3.1a) forming in releasing bends. The structural configuration of the Upper Rhine Graben is characterized by intricate horst and graben formations, anticlines, monoclines, faulted anticlines and roll over-structures (Durst, 1991).

The Upper Rhine Graben is of primary focus for deep geothermal exploration in Central Europe, owing to high geothermal gradients exceeding 100 °C/km in certain areas, recorded for Tertiary, Jurassic and Upper Triassic (Keuper) sediments and sedimentary rocks from drill holes (Pribnow and Schellschmidt, 2000; Vidal et al., 2015), e.g., at the Soultz-sous-Forêts site (Fig. 3.1a). High temperature gradients are generally related to conduction-dominated heat transfer, and low temperature gradients are indicative for convective fluid flow (Pribnow and Schellschmidt, 2000). Main fluid conduits are interpreted to be permeable fault damage zones and fractures, hosting convection cells in the Permo-Carboniferous basement and Permian to Middle Triassic sedimentary rocks (Vidal et al., 2015; Vidal and Genter, 2018).

3.4 Materials and methods

In the Knittlingen quarry a total of 32.3 m stacked vertical lithological profiles were recorded using the carbonate rock classification after Dunham (1962). The quarry has an overall north-south extension of ~ 440 m, a west-east extension of ~ 450 m while the main investigated southern part of the quarry has a north-south extension of ~ 275 m and a west-east extension of ~ 280 m. Measurements of spectral gamma ray (sGR) were conducted with a hand-held gamma ray spectrometer RS-230 BGO Super-SPEC detecting natural gamma radiation of ^{40}Th, ^{232}K and ^{238}U (cf. Schmidt et al., 2021). The measuring time was 60 s per spot with a distance of 20 cm between individual measurement spots. Measured sGR values were converted to API units using the following multipliers 1 ppm U=8.09 API units, 1 ppm Th=3.93 API units and 1 % K=16.32 API units following Rider and Kennedy (2011). During lithological profile acquisition, individual limestone layers were sampled for petrophysical measurements and petrographic characterization. In addition, vein samples and samples of the slickensides in the breached kink band planes were collected to assess their microstructure.

In total 109 plugs were drilled parallel (N=45) and perpendicular (N=64) to stratification using a water-cooled core drill with ~ 2.54 cm diameter (one-inch) from hand specimen for petrophysical analysis. Trim ends of individual plugs oriented parallel to the

stratification were used for thin section preparation. The plugs were dried in a vacuum-oven until weight constancy at 40 °C for one week. Grain density and porosity were measured using a micrometrics AccuPycII 1340 pycnometer using helium (cf. Becker et al., 2017). Klinkenberg-corrected (Klinkenberg, 1941; Rieckmann, 1970) intrinsic permeability was measured with an air permeameter manufactured by Westphal Mechanic, with a measurement range between 0.0001 mD and 10,000 mD, using dry, oil-free laboratory air as permeant at a confining pressure of 1.2 MPa to avoid sample bypass under steady-state flow conditions (Busch et al., 2022a).

The assessment of permeability of undisturbed host rock samples and samples with partially sealed veins or stylolites at elevated confining pressures (30, 20, 10, 1.2 MPa) was assessed on three plug samples in an isostatic flow cell using helium as a permeant at room temperature (22 ± 1 °C) (cf. Monsees et al., 2020). Permeabilities were measured during the unloading cycle after all samples were loaded up to a maximum confining pressure of 30 MPa. The cell is fitted with a HPLC pump (high-performance liquid chromatography pump) using water to regulate confining pressures. As the results are apparent permeabilities, the Klinkenberg correction was used to correct possible slip flow (Klinkenberg, 1941; Amann-Hildenbrand et al., 2016). Pressure sensitivity coefficients of permeability (γ) were calculated after David et al. (1994) to compare the results. Since the reference effective confining pressure P_0 in David et al. (1994) is 1.25 MPa, the respective measurements at elevated confining pressures are plotted at 8.75, 18.75, and 28.75 MPa.

For petrographic analysis a total of 30 thin (~ 28 µm) and thick sections (100 µm) were prepared. All samples were embedded in blue dyed epoxy resin to visualize optical porosity. In total, 24 thin sections were stained with a combined solution of alizarin red S and potassium ferricyanide to distinguish different carbonate phases after Dickson (1965) and covered with a glass cover slip. Dolomite remains unstained, whereas calcite will stain reddish (pink to orange), ferroan calcite will stain blueish (purple to blue), and ferroan dolomite will stain pale blue (cf. Ölmez et al., 2024). Additionally, six samples were prepared as thick sections with a thickness of 100 µm and were polished for cathodoluminescence (CL) analysis. Furthermore, eight trim ends of plugs were fine ground with 4000 grit sand paper to assess fracture cements in CL.

For petrographic analysis a Leica DMLP fitted with a Progres Gryphax camera system was used, and polished thin sections were additionally examined using cold cathode cathodoluminescence (CITL CL8200 Mk5-2 Optical Cathodoluminescence System mounted on a Leica DIALUX 20 ES) in a vacuum to assess zonation or possible cross cutting relationships of individual vein and cement generations. Point counting was performed to link detrital or diagenetic cement phases to reservoir quality. Therefore, point counts were performed on 300 points on 24 thin sections using a Pelcon semi-automatic point count stage

using a step-length of 250 µm to account for the variety of grain size (from micrite to mm sized shells) installed on a Leica DMLP microscope (as also shown in Busch et al., 2019). Optical porosity types were determined using the classification of Choquette and Pray (1970). As the grain size of micrite (≤4 µm) and microsparite (5–10 µm) by Folk (1959) and Folk (1974) could not be determined during point-counting, the term micrite is used (cf. Ölmez et al., 2024). Grain size of dolomite was measured on the long axis of each crystal (at minimum 20 measurements per thin section) on microphotographs using ImageJ.

Drone image acquisition for orthomosaic generation to document the kink bands was performed using a DJI Phantom 4 Advanced Plus. The photogrammetric point-cloud and orthomosaic generation was done using Agisoft PhotoScan (now Metashape) (Cawood et al., 2017; Allgaier et al., 2023b). Fracture dip direction and dip angle were recorded using a manual compass (N=576) and processed using OpenStereo (Grohmann and Campanha, 2010). We prepared two scan lines, recording fracture orientations once subperpendicular to the exposed breached kink band (striking NNW-SSE, 26.7 m length, N=346) and along a perpendicular wall (striking ENE-WSW, 11.88 m long, N=133) in order to analyze fracture set intensities and clustering. Manual fracture detection (dip direction, dip angle) of the northern kink bands are based on point clouds in CloudCompare (Girardeau-Montaut, 2017) using the compass tool (e.g., see Allgaier et al., 2023b).

To assess fracture set intensities and gain information about spatial arrangement, we use the normalized correlation count (NCC) method (Marrett et al., 2018). This method distinguishes random fracture arrangements from clustered and periodic arrangements using the two-point correlation function or correlation sum (Bonnet et al., 2001; Wang et al., 2019). As fracture strike is not always perpendicular to the scan line, the recorded apparent distances between the fractures require correction using the Terzaghi method (Terzaghi, 1965; Li et al., 2018). For this purpose, sub-parallel sets of five main fracture strike orientations were grouped into sets (striking 10°, 50°, 70°, 110°, 140°), resulting in corresponding 338 fractures in total for these analyses. The sets were differentiated based on strike rose and polar plot density clusters. The respective angle between the strike of the fracture set and the scan line was used to obtain corrected distances (Terzaghi, 1965; Li et al., 2018). The generated data was analysed using CorrCount in Matlab (cf. Marrett et al., 2018). Pattern morphology of normalized correlation counts were described after Marrett et al. (2018) and Li et al. (2018). As no bedding planes were accessible in the quarry, no data on fracture length and connectivity can be obtained.

To assess the relation of present fracture orientations and present-day stress orientation, we also performed dilation and slip tendency analyses (Morris et al., 1996; Ferrill et al., 2020; Allgaier et al., 2023b) in FracTend (Healy, 2023). Dilation and shear tendency analyses identifies fractures in which the ratio of shear stress (τ) to effective normal stress (σ_n) exceeds the frictional strength (μ) of the fracture, they are therefore critically stressed and

show a higher probability of being hydraulically conductive (Barton et al., 1995; Ferrill et al., 2020). The slip tendency T_s (Eq. 3.1) reflects the likelihood of fracture reactivation in shear mode assuming no cohesion (Morris et al. 1996) and the dilation tendency T_d (Eq. 3.2) reflects the likelihood of a plane to dilate (to open) in tensile mode (Ferrill et al., 1999):

Eq. 3.1

$$T_s = \frac{\tau}{\sigma_n} \geq \mu$$

Eq. 3.2

$$T_d = \frac{(\sigma_1 - \sigma_n)}{(\sigma_1 - \sigma_3)}$$

Using the trend and plunge of the poles of recorded fractures from the two scanlines and the reconstructed present-day stress orientation and magnitude in the Upper Rhine Graben (Meixner et al., 2014; Allgaier et al., 2023a) at 1000 m depth using stress gradients $\sigma_2=\sigma_V$=23.8 MPa/km, $\sigma_1=\sigma_{Hmax}$=28.8 MPa/km, $\sigma_3=\sigma_{hmin}$=15.3 MPa/km and pore pressure of 10.2 MPa/km allows the assessment which fracture orientations are more likely to contribute to fluid flow.

3.5 Results

3.5.1 Lithological description and gamma ray signature

3.5.1.1 Overview

The Knittlingen quarry exposes Upper Muschelkalk to Lower Keuper lithologies, fractures, veins and faults. In both quarry parts (northern and southern part, Fig. 3.3a), kink bands are present, and in one wall a breached kink band with mineralization is exposed. This study focuses on the southern part of the quarry (red box in Fig. 3.3a).

In the studied area (Fig. 3.3b) stacked vertical lithological profiles were recorded (red lines in Fig. 3.3b, d). Manual compass measurements were taken along the lithological profiles, and on scan lines (orange lines in Fig. 3.3b).

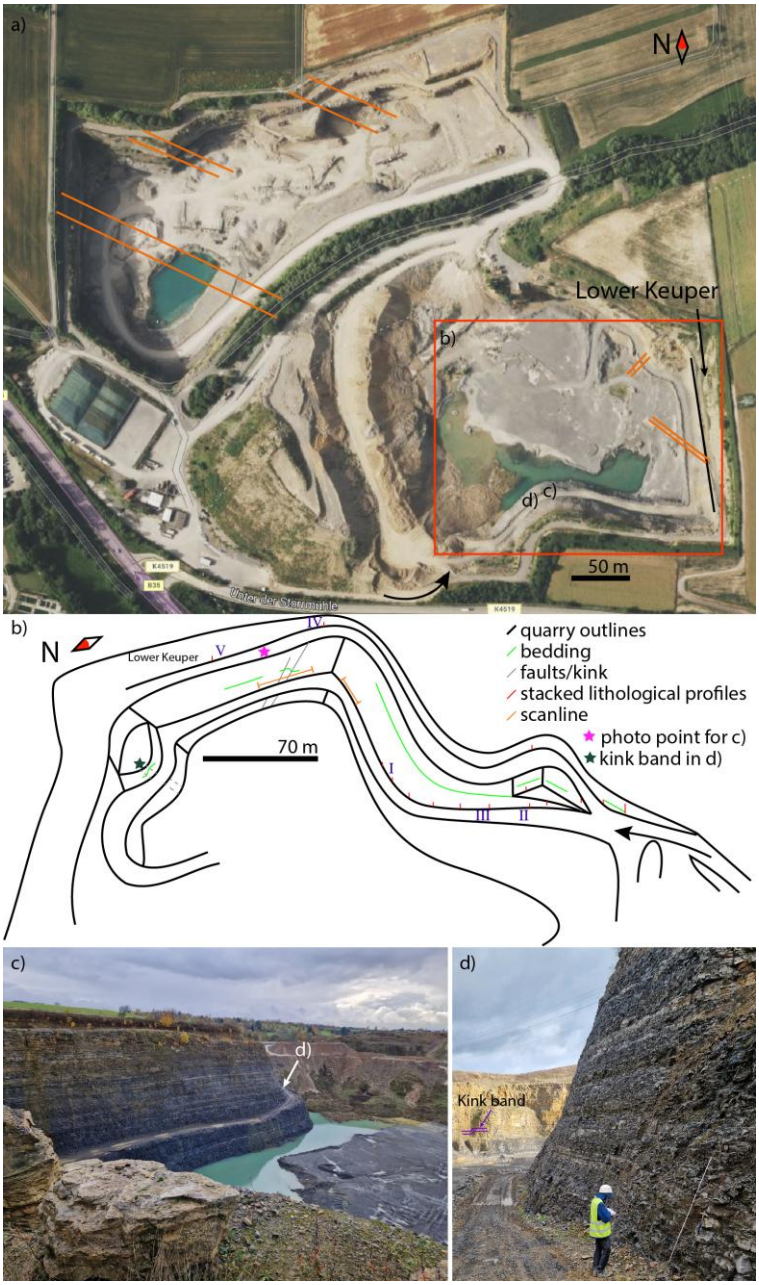

Figure 3.3 (Figure caption on next page)

Figure 3.3 (previous page) Overview of the quarry. a) Aerial image of the quarry, the NE part is currently mined, the study location is marked with a red box and redrawn as schematic map in b). Orange lines indicate location and strike of kink band planes (Bing maps, 2025). b) Schematic map of the study area and locations of sampling and stacked vertical lithology descriptions (red lines), roman numbers are shown in Fig. 3.4 (I, II, III) and 3.5 (IV and V). c) View from top into the quarry, where Upper Muschelkalk lithologies are exposed. d) Record of vertically stacked lithologies profiles, and one kink band in the background, location is marked with a dark green star in b).

3.5.1.2 Upper Muschelkalk

In total, 25.8 m of limestone to marly claystone alternations for the Upper Muschelkalk is recorded (Fig. 3.4, 3.5, 3.6). The studied Upper Muschelkalk lithologies are composed of dark grey to very dark grey, mostly calcitic, mudstones, wackestones, and packstones (further called limestones) classified after Dunham (1962) and very dark grey marly claystone intercalations (Fig. 3.4, 3.6).

The number of intercalated marly claystones decrease toward the top of the studied lithology (Fig. 3.4a, b). The recorded wacke- or packstones include (recrystallized) shell fragments (Fig. 3.4b), showing a dark grey or white color. Some of the shells are non-reactive to HCl indicating a dolomitic or silicic composition. The limestone texture is mostly massive. Toward the younger strata, wacke- and packstones are more abundant than mudstones (Fig. 3.4a (older strata), b (younger strata), 6). Subordinately, erosional surfaces and bioturbation between underlying mudstones and overlying wacke-/packstones can be observed (Fig. 3.4c, d). Both, decreasing marly claystone contents and the increasing amount of shells within the limestones indicate a general shallowing upward trend. Calcitic veins (mm-thick) are present perpendicular to bedding, mostly strata-bound and rarely crosscutting multiple limestone beds.

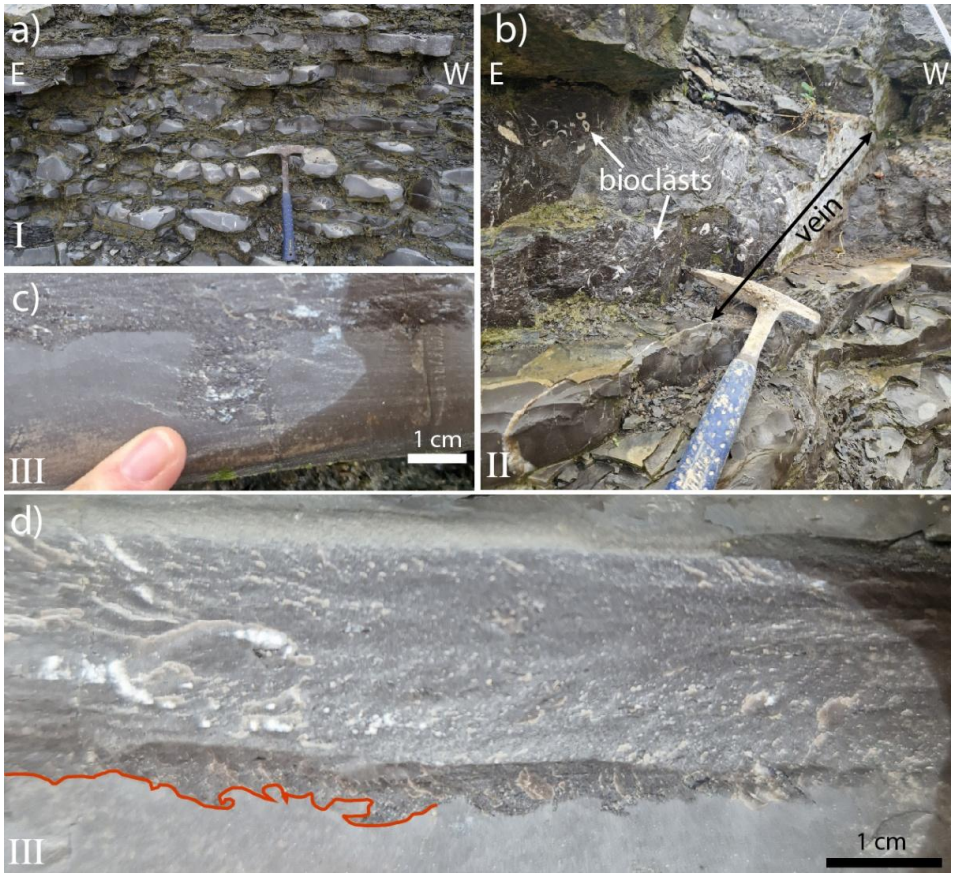

Figure 3.4 Overview of the Upper Muschelkalk, locations in the quarry are marked in Fig. 3.3b as roman numbers. a) Lower part of the studied succession with more marly claystone interbeds. b) Upper Muschelkalk, alternation of marly claystones, mudstones and packstones with bioclasts (bivalves and brachiopods), and a calcite vein penetrating several banks. c) Upper Muschelkalk, bioturbation trace, maybe glossifungites or similar. d) Upper Muschelkalk, erosion (some parts outlined in red) of underlying mudstone.

3.5.1.3 Lower Keuper

For the Lower Keuper, a total of 6.5 m of limestone to marly claystone alternation is recorded. The limestones are mostly massive mudstones. At the base of a dark grey marly claystone layer (Vitriolschiefer), an approximately 2 cm thick bonebed layer can be found (Fig. 3.5a). This is followed by a thicker limestone layer (Blaubank) with brachiopod impressions, bioturbation, and cavities at the base indicating dissolution (Fig. 3.5b). Toward

younger strata, the claystone content increases and only thinner calcitic limestone beds are exposed (Fig. 3.5c, 3.6).

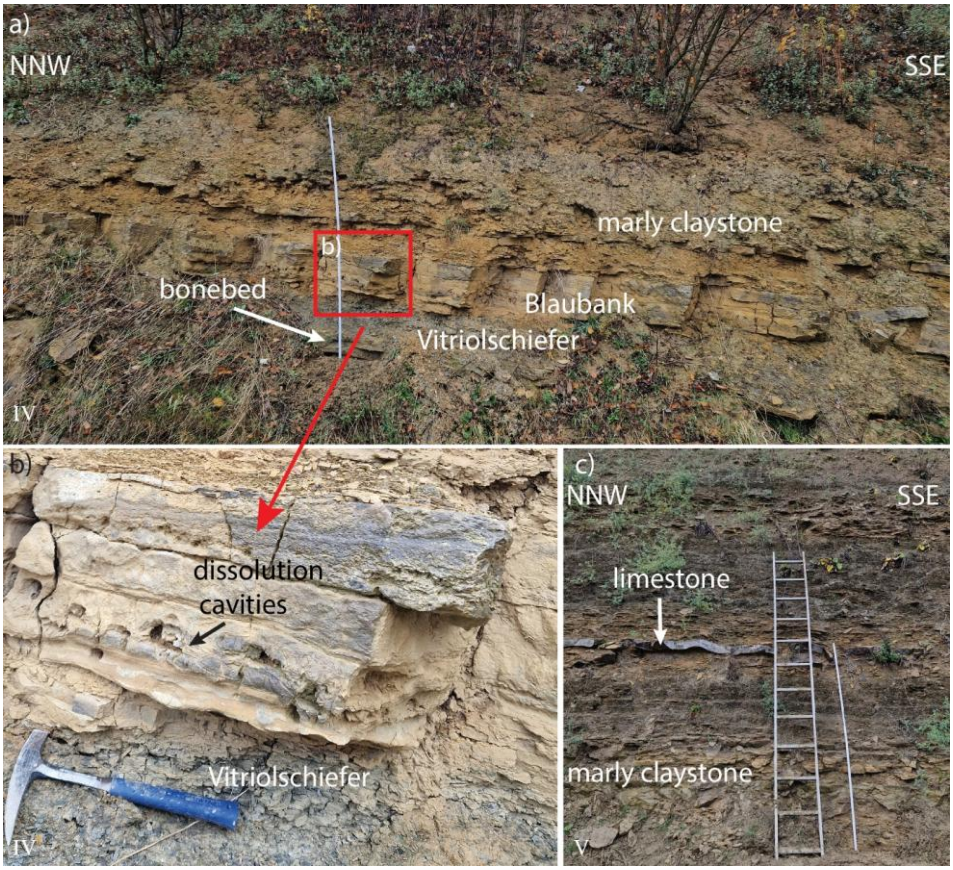

Figure 3.5 Overview of the Lower Keuper, locations in the quarry are marked in Fig. 3.3b as roman numbers. a) Succession of bonebed containing fish teeth, phosphatic pellets, bone fragments, ostracods and dark grey Vitriolschiefer, Blaubank and marly claystone. b) The calcitic Blaubank show layer of ostracods and dissolution cavities. c) The topmost studied section is dominantly composed of marly claystone and only thinner limestone beds (mudstones) occur.

3.5.2 Lithological column and spectral gamma ray (sGR)

The calculated sGR for the Upper Muschelkalk profiles (N=135) varies between 16 and 86 API and generally decreases from the base of the studied Upper Muschelkalk section

toward the top, reflecting the recorded decrease in marly claystone layers throughout the lithological column (Fig. 3.6). The calculated sGR for the Lower Keuper profiles (N=30) ranges from 48 to 151 API (Fig. 3.6). The base of the Keuper is indicated by increasing gamma ray values, related to the sudden increase in marly claystone content.

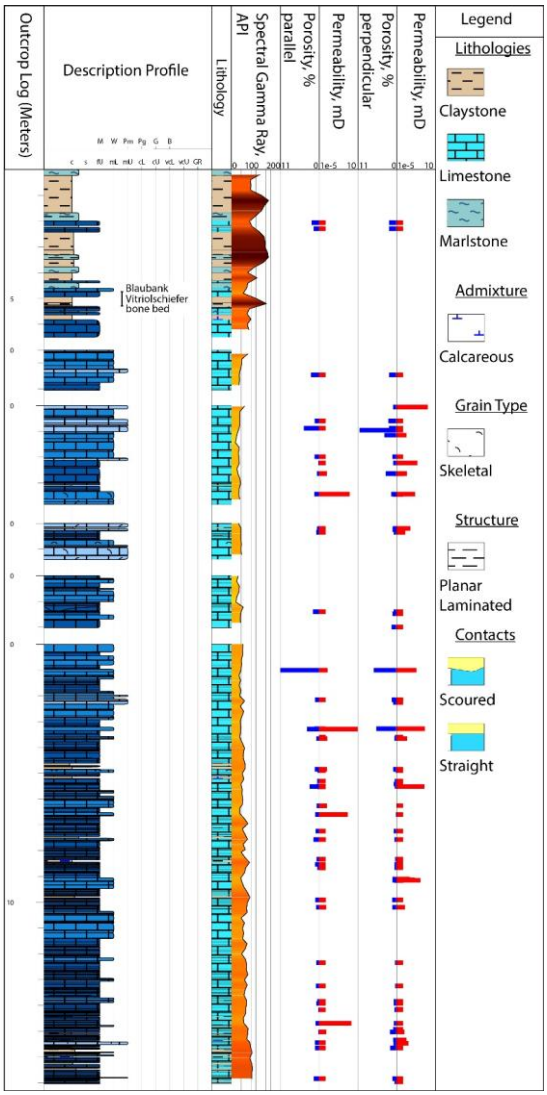

Figure 3.6 Lithological column of stacked vertical logs from topmost Lower Keuper (6.5 m in total) to Upper Muschelkalk (25.8 m in total), sGR in API, helium porosity (%, blue) and permeability (mD, red) of plug samples from limestone beds drilled parallel or perpendicular to bedding.

3.6 Petrography

The stained thin sections confirm the macroscopic classification as limestones. A detailed point-count table is found in the digital appendix – chapter 3, and all contents are given as vol% of the bulk sample. As most of the point-counted thin sections are limestones from the Upper Muschelkalk and only one is from the Lower Keuper, samples are not classified based on their stratigraphy. The fine-grained, calcitic, matrix is summarized as micrite.

3.6.1 Detrital components

The samples are dominantly composed of calcitic micrite (crystal sizes between <4 and ~ 13 µm), biodetritus (e.g., shells, crinoids, gastropods, teeth, or fish scales), or peloids. The most abundant detrital components are micrite (Fig. 3.7a), ranging from 0.0% to 93%, peloids (Fig. 3.7a, 0.0%–21.7%) which are distributed without any orientation and mostly composed of calcitic micrite and crinoid fragments (0.0%–6.7%). Intercrystalline clay between dolomite spar (0.0%–6.0%) is present in three samples. Phosphatic peloids, bone fragments, scales, and teeth are summarized as phosphates (0.0%–1.3%) and occur in most of the samples (Fig. 3.7f), but were not always encountered during point counting. Individual samples show mostly undeformed ooids (up to 12%, Fig. 3.7c) with mostly bioclastic centers. Quartz grains (0.0%–0.3%) occur rarely, whereas shell fragments showing primary textures and calcitic composition (0.0%–9.3%) are present in most of the samples. Gastropods (0.0%–0.3%) were observed in different samples, but were only point counted twice. Ostracods (0.0%–4.7%) are only encountered in one sample, but are highly concentrated in individual layers (Fig. 3.7d).

3.6.2 Authigenic components

The main authigenic phases are calcite spar (0.0%–48.7%, Fig. 3.7c) that occurs distributed in the samples, replacive chert in shell fragments (0.0%–41.0%), and neomorphic replacements of shells with calcite spar (0.0%–31.3%, Fig. 3.7f) growing from the rim into the center of the shell. Micritic envelopes are mostly seen on recrystallized shells and only subordinately on crinoid fragments, and make up between 0.0% and 19.7% (Fig. 3.7e). Some of the recrystallized shells additionally show both, the replacement with calcite spar at the shell rim, and Fe-calcite (Fe-Cal) in the center (Fig. 3.7f), the latter ranging between 0.0%–15.0%. Individual shells are additionally replaced by not only chert but also macrocrystalline quartz (0.0%–9.3%). Where chert replaces bioclasts, it often transitions into macrocrystalline quartz, which is again encased in Fe-calcite replacements of bioclasts (Fig. 3.7l). Individual shells also show additional replacement by dolomite (Dol, 0.0%–

10.0%), of which some additionally show a Fe-dolomite (Fe-Dol) rim (0.0%–2.0%) (Fig. 3.7k). Dolomite and Fe-dolomite replacements often show curved crystal facets, pleochroism, and undulose extinction, typical of saddle dolomite. Dolomite spar (Fig. 3.7c, e) also replaces peloids and ooids in individual samples (0.0%–21.7%), as well as micrite (0.0%–31.3%, Fig. 3.7b) mostly as planar-e to planar-s rhombs, where few of the dolomite spars also show a Fe-dolomite rim (0.0%–3.0%). These dolomite rhombs show almost no pleochroism in plane-polarized light. In some samples, only the peloidal shape remains, whereas the detritus is fully dolomitized. Where dolomite spar in e.g., bioclasts is (partially) dissolved, FeO/FeOOH outlines (0.0%–4.3%) are often observed. Because of different optical properties of the dolomite, the crystal size was additionally measured, to distinguish three dolomite types:

- Dolomite type I crystals (Fig. 3.7c), observed as fabric-selective dolomitization of ooids/peloids (almost no pleochroism, dusty appearance, normal extinction) with crystal sizes from 0.03–0.30 mm (avg.: 0.11 mm).
- Dolomite type II crystals (Fig. 3.7b), replacing the matrix (no pleochroism, dusty appearance in the center) with smaller crystal sizes from 0.01–0.14 mm (avg.: 0.05 mm), often associated to intercrystalline clay minerals.
- Dolomite type III crystals (Fig. 3.7i, k) replacing bioclasts, matrix and vein cements (strong pleochroism, dusty appearance, undulose extinction) with larger crystal sizes from 0.04–1.30 mm (avg.: 0.27 mm).

Detrital components show an isopachous fibrous to bladed radial calcitic rim cement (0.0%–31.7%) which is the dominant cement in two samples (Fig. 3.7c, e), and is less frequent in samples containing higher micritic matrix contents. Additionally, one sample also shows parts of calcitic rim cements replaced by SiO_2 (0.7%), where the detrital component is also (partly) replaced by chert. Pore filling cements are Fe-calcite (0.0%–10.3%), dolomite (0.0%–2.3%), and chert (0.0%–1.3%), which are observed in between biodetritus, occasionally also encasing rim cements where present (Fig. 3.7c). Pyrite (0.0%–7.0%) is present within the majority of the samples, and mostly present in the matrix and in bioclasts, and rarely occurs as geopetal pyrite in bioclasts in individual samples. Additionally, pyrite is also present in one sample at the interface between the host rock and a composite dolomite and Fe-calcite vein. One sample shows a druse, which is filled by chert, which transitions into macro quartz, and some of the remaining pore space is filled with calcite

and/or Fe-calcite, with some areas of the thin section showing non-pervasive quartz pseudomorphs after sulphates (up to 4.3%, Fig. 3.7g), indicated by bladed crystal morphologies filled by quartz. Additionally, one sample with a larger recrystallized shell also shows quartz pseudomorphs after sulphate evaporites (0.7%). Authigenic quartz is present as laths with euhedral outlines within the matrix (Fig. 3.7c), containing solid inclusions of the replaced material, in some thin sections, but where only point counted once (0.3%).

Clay mineral-rich stylolites are not always encountered during point-counting and vary between 0.0% and 4.3%. In one sample, the stylolite shows defined sutured boundaries (Fig. 3.7i), whereas this effect is less pronounced in other samples (Fig. 3.7j). Stylolites are characterized by enrichment of e.g., clay minerals along pressure dissolution fronts. The columnar side of the stylolites show thinner clay mineral accumulations. Some stylolites are associated to veins and displace them (Fig. 3.7j). Wispy, discontinuous dissolution seams, not yet forming a stylolite (i.e. lacking the columnar features), were not encountered during point counting, but are present in individual samples.

Vein cements are of calcitic composition (0.0%–10.7%), Fe-calcite (0.0%–17.7%) or occur as veins showing internal zonation of these. Dolomite vein cements (0.0%–7.0%) show pleochroism and undulose extinction typical for saddle dolomite, which is on occasion encased by Fe-calcite and subordinately Fe-dolomite (0.3%).

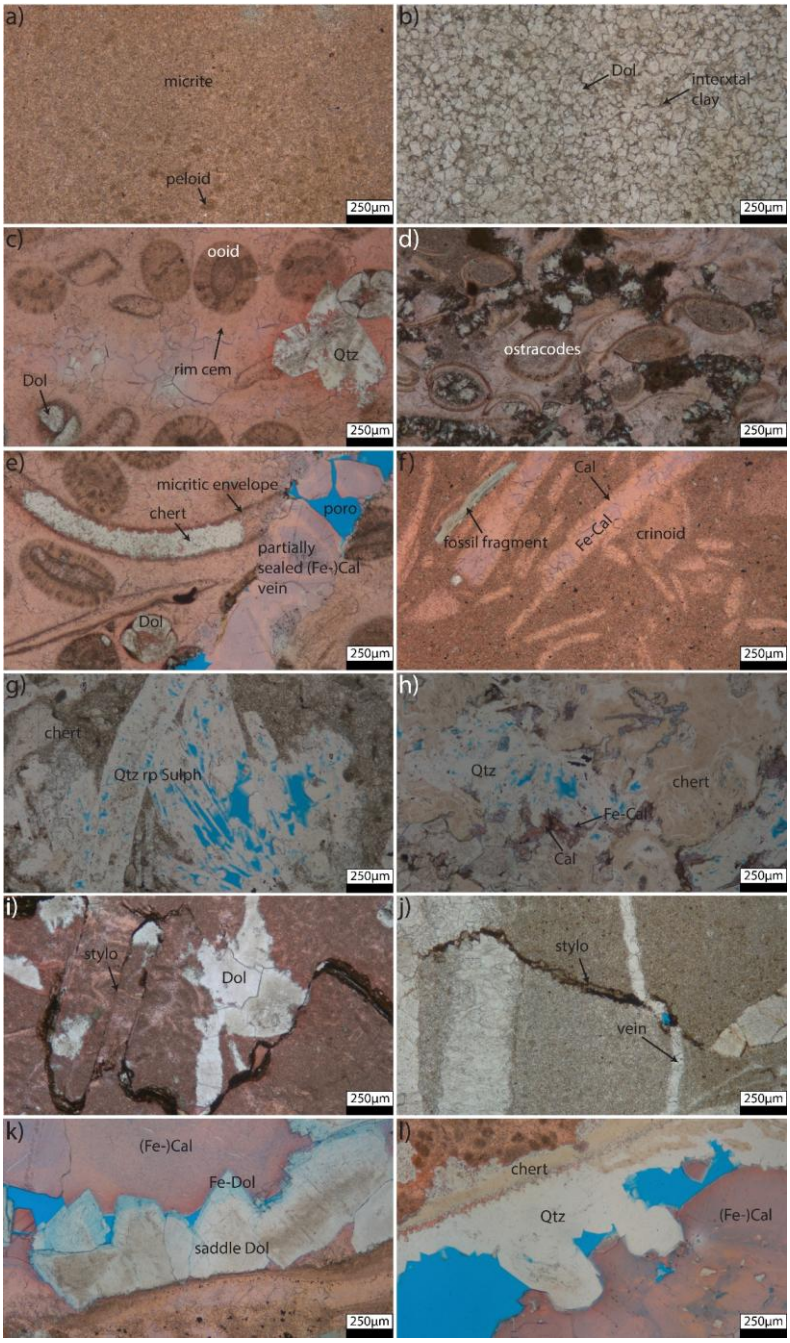

Figure 3.7 (Figure caption on next page)

Figure 3.7 (previous page) Photomicrographs of detrital components and authigenic phases of Upper Muschelkalk and one Keuper sample. a) calcitic micrite and micritic peloids. b) Sparitic dolomite (planar-s) with cloudy centers, clear rims and intercrystalline clay (interxtal clay) between the spars. c) calcitic ooids of which some are replaced by dolomite spar show a calcitic isopachous fibrous rim cement and authigenic quartz laths. d) Keuper sample, ostracods are aligned parallel to bedding, dolomite spars are distributed between bioclasts and calcite spar cements or in bioclasts. e) Partially sealed vein with internal zonation of ferroan calcite and calcite, one shell fragment is replaced by chert, ooids are either dolomitized or not and one show one dolomite rhomb in the ooid rim. f) Shell fragments with elongate blocky to euhedral calcite cement, and sparitic Fe-calcite (Fe-Cal) cement in the center, and a calcitic crinoid fragment. g) In former shells, chert and replacive quartz are abundant, in some areas overgrown by macroquartz (h), and some of the remaining porosity is filled with calcite or ferroan calcite. i) Columnar stylolites and dolomite cement. j) Stylolite displaces a vein (unstained section). k) Saddle dolomite overgrown a shell shows a ferroan dolomite rim and is encased in ferroan calcite and calcite. l) Macroquartz overgrows chert and is encased by ferroan calcite and calcite.

3.6.3 Optical porosity

Optical porosity was differentiated into intraparticle porosity (0.0%–14.7%), fracture porosity (0.0%–2.0%) in partially sealed veins and in one sample mouldic porosity (0.3%). Intraparticle porosity is mostly restricted to areas where bioclasts are dissolved or replaced, e.g., in dolomitized peloids or ooids.

3.6.4 Cathodoluminesence

Cathodoluminescence (CL) analyses were performed to gain additional insight into the structural and diagenetic development based on characteristic luminescence behavior of components and cements. Furthermore, CL analyses may allow a more detailed assessment of fracture cement paragenesis, based on cross-cutting relationships. Slight differences in luminescence intensity between samples are due to different surface qualities of polished thin sections and fine ground trim ends.

In the studied samples calcite mostly shows an orange luminescence, Fe-calcite and Fe-dolomite are dull to non-luminescent and dolomite shows a purple-reddish luminescence (Fig. 3.8a). Veins or recrystallized shells often show internal sector zoning of calcite and Fe-calcite and are combined as (Fe-)calcite cements (Fig. 3.8b).

Some veins show partially sealing cements with sector zoned crystals bridging the fracture (Fig. 3.8c), other veins are pervasively sealed and cross-cut and displaced by a younger vein generation. Individual micritic peloids cannot be accurately distinguished from cements or micrite forming the matrix based on different luminescence colors. Crystal boundaries or the boundary between peloid/ooid and the rim cement only occasionally show a slightly brighter luminescence (Fig. 3.8c). In individual samples larger shells are also overgrown by saddle dolomite with reddish-purple luminescence and a non-luminescent Fe-dolomite rim, encased by (Fe-)calcite (Fig. 3.8d).

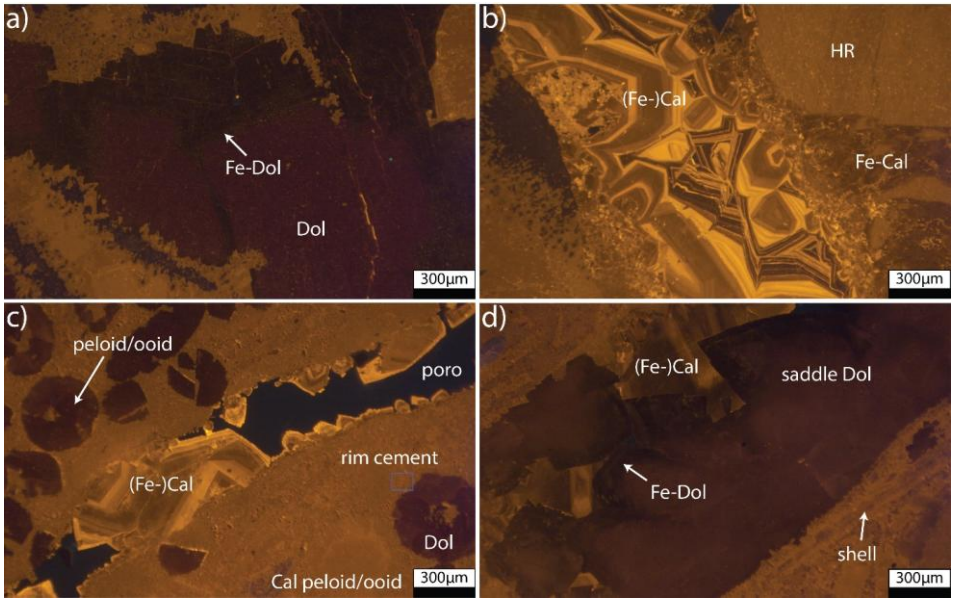

Figure 3.8 Cathodoluminescence on thin sections and plug trim ends. a) Reddish-purple luminescence of dolomite and non-luminescence Fe-dolomite rim with surrounding calcite spar with orange luminescence and some calcite spar with dolomite cementer (M15). b) Euhedral (Fe-)calcite crystal facets with internal zonation of calcite and non-luminescent Fe-calcite in a vein (M15). c) Dolomitized former ooids or peloids with purple luminescence, whereas calcitic ooids/peloids with calcitic rim cements (blue box) show (dull) orange luminesce, but not as bright as calcitic zones in the vein (M16). Partially sealed (Fe-)calcite vein with bridging crystals. d) Larger shell replaced by saddle dolomite with Fe-dolomite rim and (Fe-)calcite (M43).

3.6.5 Relation of fracture cementation

In addition to cathodoluminescence analyses on host rocks, three vein samples and two samples of the cemented slickensides from the breached kink band were studied. Partially fracture filling saddle dolomite shows a reddish-purple luminescence and pyrite at the host rock-vein interface (1, Fig. 3.9a, b). This vein also includes (Fe-)calcite cements encasing euhedral dolomite crystal facets (2, Fig. 3.9b). This composite vein is crosscut by a dull to non-luminescent (Fe-)calcite vein (3, Fig. 3.9a, b). These mostly pervasively sealed blocky (Fe-)calcite veins show weak internal sector zoning in dull orange luminescing cements in CL analyses (3, Fig. 3.9c). These are crosscut by a brighter (Fe-)calcite vein, showing internal sector zoning in bright and dull orange luminescing cements (4, Fig. 3.9c). A vein generation composed of mostly dull luminescing Fe-calcite cement, which in some samples shows slightly brighter luminescence, is only found in a sample from the fault zone (5, Fig. 3.9g) and is crosscut by brighter cement phases (6, 7, Fig. 3.9g). One of those brighter vein cements is also only found in samples from the fault area and shows a heterogeneous luminescence without distinct zoning (6, Fig. 3.9f, g). A partially fracture-filling (Fe-)calcite phase showing internal zonation of more dull or bright zones and euhedral crystal facets (7, Fig. 3.9d, f-h). This vein phase is crosscut other vein cement generations if present in host rock and fault samples. This zoned luminescence cement phase (7) is additionally enclosed by a dull-non-luminescent Fe-calcite phase forming the rim of a partially sealed vein in the fault core (8, Fig. 3.9h). Additionally, some veins include host rock inclusions in both host rock samples and fault samples, which are in some cases arranged parallel to the host rock-vein interface (Fig. 3.9d), and imply fracturing following initial fracture cementation.

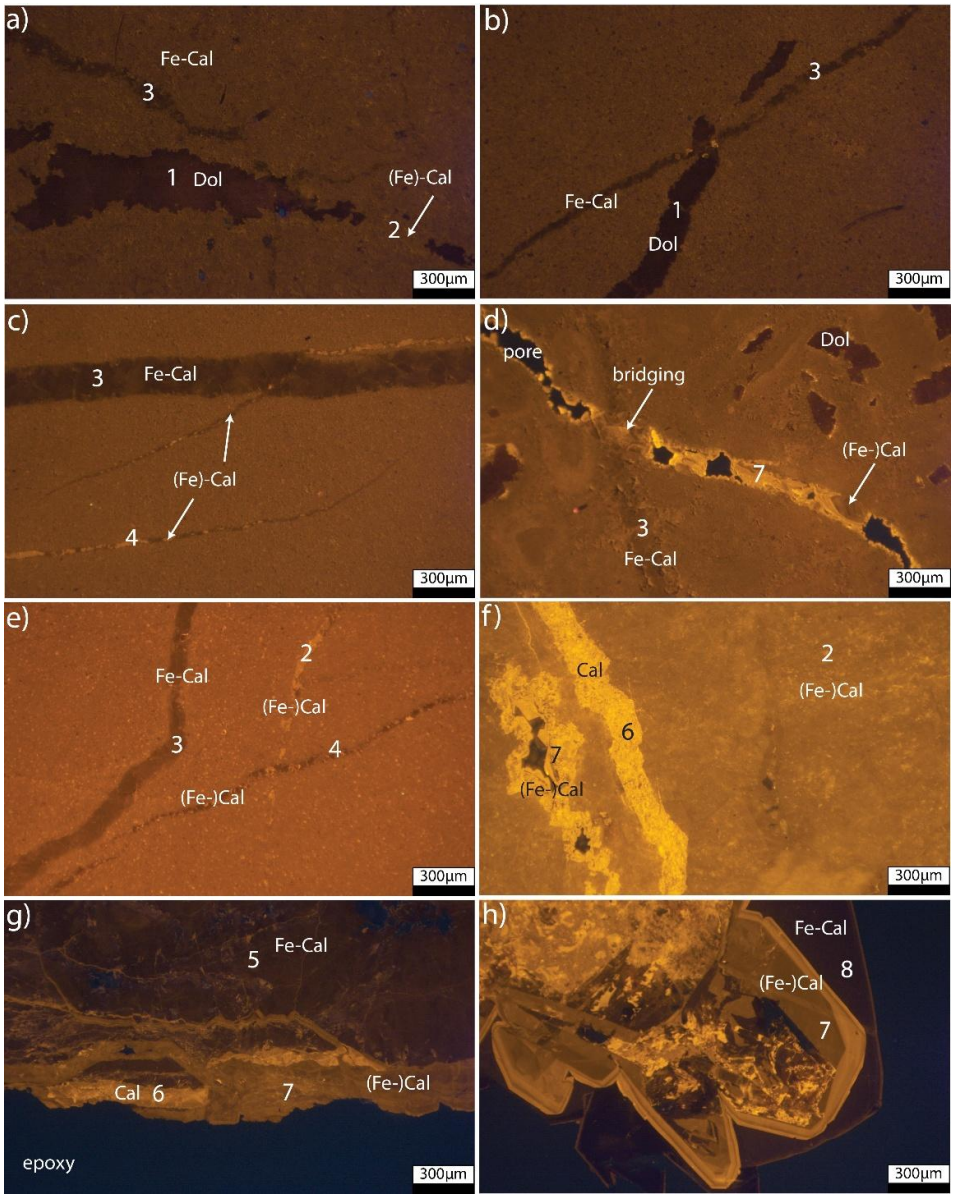

Figure 3.9 (Figure caption on next page)

Figure 3.9 (previous page) Cathodoluminescence on vein thin sections from host rocks and fault area. a), b) Dolomite vein show some patches of (Fe-)calcite cement and is crosscut by a Fe-calcite vein (M25). c) Dull to non-luminescent Fe-calcite vein is crosscut by a (Fe-)calcite vein with internal zonation (M27). d) Partially sealed (Fe-)calcite vein with bridging crystals and internal zonation. Dolomite in ooids/peloids show reddish-purple luminescence (M14). e) Darker and brighter Fe- calcite veins are crosscut by a darker, partially non-luminescent (Fe-)calcite vein (KB_vein). f) Perversely sealed bright vein crosscut a darker luminescent (Fe-)calcite vein. A younger phase shows remaining pore space and cementation with (Fe-)calcite and euhedral crystals (KB_FL). g) Non-luminescent Fe-calcite vein and a brighter cement phase with is displayed by a (Fe-)calcite phase (KB_VB). e) Larger euhedral (Fe-)calcite and Fe-calcite cement in partially sealed vein (KB_FL).

3.7 Porosity, Permeability, Density

For Muschelkalk samples drilled parallel to stratification, He-porosity ranges between 0.13% to 10.87% (avg.: 1.33%), grain density ranges between 2.68 g/cm³ and 2.73 g/cm³ (avg.: 2.73 g/cm³), and bulk density ranges between 2.41 g/cm³ and 2.72 g/cm³ (avg.: 2.67 g/cm³), while the permeability ranges between <0.0001 mD and 9.7 mD (avg.: 0.27 mD). Two Keuper samples show He-porosity of 1.53% and 2.13%, permeabilities of <0.0001 mD, grain density for both of 2.7 g/cm³ and bulk density of 2.65 g/cm³ and 2.66 g/cm³.

The measured He-porosities for Upper Muschelkalk samples drilled perpendicular to bedding range from 0.16% to 10.58% (avg.: 1.33%), while grain density ranges from 2.67 g/cm³ to 2.75 g/cm³ (avg.: 2.71 g/cm³), and bulk density ranges from 2.44 g/cm³ and 2.74 g/cm³ (avg.: 2.67 g/cm³). Gas permeability varies between <0.0001 mD and 0.6283 mD (avg.: 0.0186 mD). He-porosity for two Keuper samples are 2.16% and 2.18%, permeability is <0.0001 mD, grain density is 2.69 g/cm³ and 2.70 g/cm³, and bulk density is 2.63 g/cm³ and 2.64 g/cm³. The highest porosity values are measured in samples showing druses.

Due to the measurement limit of the device, samples measured below the limit are given as 0.0001 mD for further rock typing. He-porosity and gas permeability show no correlation (Fig. 3.10a). Rock types (mudstone, wackestones and packstone) show no correlation with porosity or permeability (Fig. 3.10b). The highest permeability is measured in samples showing (partially sealed) veins (Fig. 3.10b).

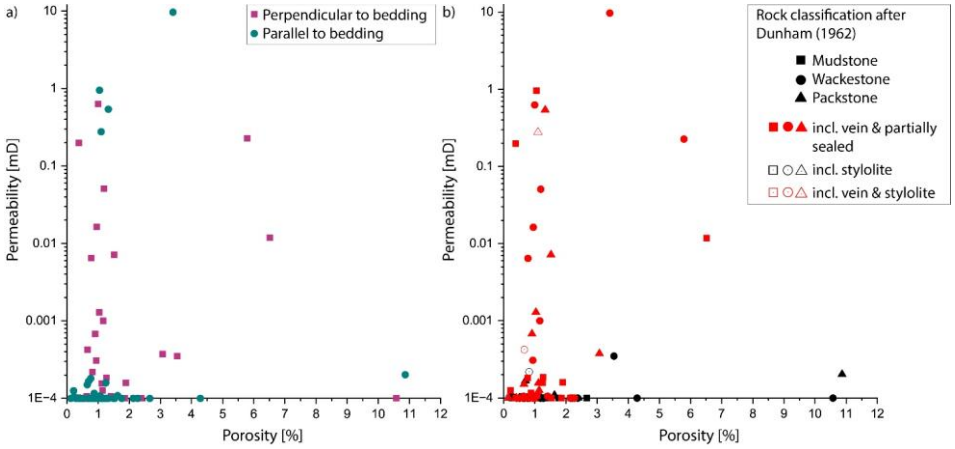

Figure 3.10 He-porosity and gas permeability plots. a) Porosity and permeability show no correlation; green dots are samples drilled parallel to bedding and purple squares are samples drilled perpendicular to bedding. b) Rock type after Dunham (1962) (shape of symbols) show no correlation with porosity and permeability. Only samples which include either (partially sealed) veins or stylolites, or both, can enhance the permeability. The samples showing the highest permeability value shows a fracture oriented parallel to measurement direction, which is only marginal sealed and thus enhances the fluid flow in measurement direction. Samples with stylolites are shown as unfilled symbols with black outline, samples with (partially sealed) vein and stylolite are displayed as unfilled symbols wirh red outline.

Three samples were additionally measured under elevated confining stress (Fig. 3.11). Sample I contains a partially sealed vein, axially crossing the whole plug, sample II contains stylolites parallel to stratification and the axis of the plug, and sample III is a host rock sample without any special features and is described as a massive wackestone (Fig. 3.11). At 30 MPa confining pressure permeabilities are 0.13 mD for sample I, 0.05 mD for sample II and $3.0*10^{-6}$ mD for sample III. At 1.25 MPa confining pressure, permeabilities are 0.32 mD for sample I, 0.27 mD for sample II and $2.7*10^{-5}$ mD for sample III. The calculated pressure sensitivity coefficients of permeability γ are 0.03 for sample I, 0.06 for sample II and 0.071 MPa^{-1} for sample III (digital appendix – chapter 3) and are at lowest for the sample containing the partially sealed vein. When normalizing the permeability measurements to the highest measured value of each sample (1.0), the sample containing the partially sealed vein retains 41% of the initial permeability, whereas the sample containing the stylolite only retains 16% and the undisturbed host rock only retains 11% of the initial permeability at 1.25 MPa confining pressure.

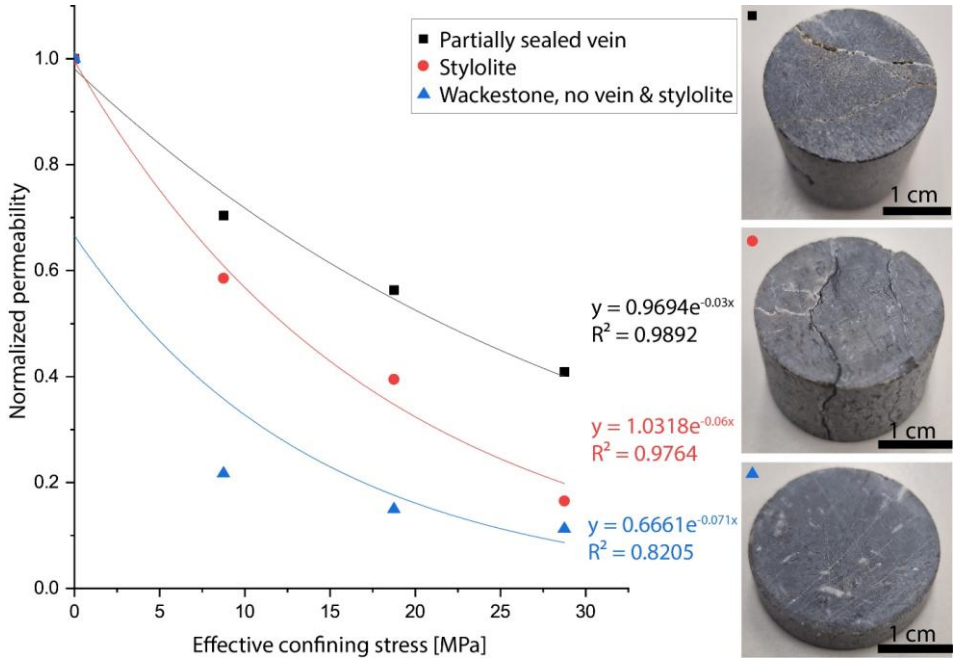

Figure 3.11 Normalized permeability measured with decreasing effective confining stresses of 30 to 1.25 MPa and exponential trend lines. The permeabilities are normalized to initial permeabilities measured at 1.25 MPa. Thus, the permeability of a partially sealed vein sample at 30 MPa is c. 41% lower than the permeability at 1.25 MPa.

3.8 Rock typing

Rock typing links the porosity and permeability measurements with petrographic properties and enables the assessment of reservoir quality controls (Fig. 3.12). As not every plug has a corresponding thin section, the plots only represent a part of the petrophysical measured samples shown in Fig. 3.10. The micrite content does not correlate to differences in reservoir quality (Fig. 3.12a), only one sample with higher amount of micrite shows comparatively higher permeability but not enhanced porosity. The content of shells (with primary features) and recrystallized shells does not correlate to enhanced porosity or permeability (Fig. 3.12b), since samples with shell contents between 20% and 30% show among the lowest and highest permeabilities. The fracture porosity and vein cements (Fig. 3.12c) and stylolite content (Fig. 3.12d) appear to affect permeability of individual samples, since individual samples with higher permeability show higher stylolite contents or preserved fracture porosity in partially cemented veins. Where veins are pervasively sealed,

permeability remains low (~ 0.0001 mD). One sample displaying a stylolite which is oriented parallel to the plug's long axis and bedding and enhances the fluid flow at 1.2 MPa confining pressure (Fig. 3.12d, blue square). Because the matrix permeability of the studied limestones is low (max. 9.7 mD for one sample with a fracture sealed only marginal and parallel to the measurement direction, else max. ~ 1 mD), and thus only fractures and partially sealed veins enhance permeability if oriented suitable parallel to measurement direction (Fig. 3.10, 3.11, 3.12), reservoir quality seems to be mostly related to structural elements in the studied lithology.

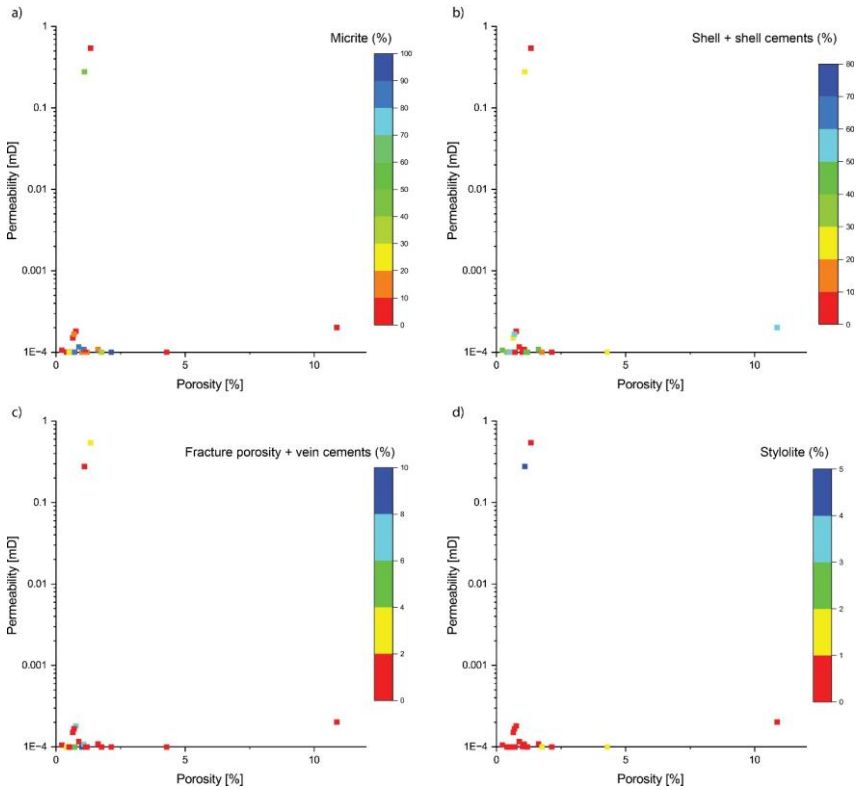

Figure 3.12 Color-coded porosity-permeability plots linked with petrographic analyses. a) Micrite content, b) shells and recrystallized shells and their cements, c) fracture porosity + vein cements, permeability is higher in one sample containing fracture porosity + vein cements, d) stylolite, permeability is higher one the sample containing stylolites. Point counting data given in in volume percent. Only individual samples show elevated permeability with occurring fracture porosity + vein cements and stylolites.

3.9 Structures and fractures

Fractures recorded along the lithological column and the two scanlines (N=576) show three main strike orientations (NNE-SSW, WNW-ESE, NW-SE) and subordinate sets (NE-SW, ENE-WSW, W-E and NNW-SSE) (Fig. 3.13). The highest frequency is observed in WNW-ESE and NNE-SSW strike.

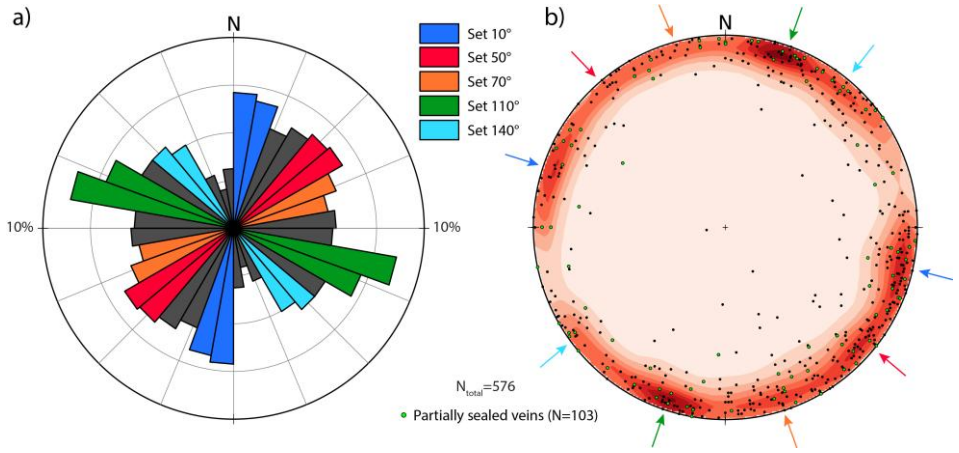

Figure 3.13 Rose and pole point contour plot. a) Fracture strike of compass measurements for the Upper Muschelkalk and Lower Keuper from lithological columns and two scan lines (N=576). Fracture sets were selected to represent the most prominent strike orientations (set 1 (10°), set 2 (50°), set 4 (110°)), strike orientations that are most suitably oriented in the present day stress field (set 1 (10°), set 4 (110°), set 5 (140°)), or to showcase that clustering analyses still require assessment of the stress field (set 3 (70°)). b) Fracture data plotted as poles to planes (lower hemisphere), arrows highlight highest pole densities, colors are related to facture sets in a). Partially sealed veins are highlighted as green poles (N=103).

Several deca-meter scale reverse kink bands are exposed in the southern (Fig. 3.3a, 3.14a-c) and northern quarry parts (Fig. 3.3, Fig. 3.14d). While the four kink bands in the northern quarry part consistently dip toward 021° to 034° with dips ranging from 49° to 67° (Fig. 3.15, blue great circles and poles), the decameter-scale conjugate reverse kink-band with a breached kink-band boundary in the SSE show a dip direction/dip of 024/65 and 018/55 in the SSE part and of 157/59 and 160/66 in the NNW part (Fig. 3.14, 3.15).

The calcite cementation on the breached kink band boundary show slickensides, which indicate reverse, strike-slip, and normal faulting, but clear cross-cutting relationships are

absent. The conjugate kink band itself indicates compression with the maximum principal stress σ_1 in N-S direction (179/01), the intermediate principal stresses σ_2 is located in the intersection of the kink planes (088/33), minimum principal stress σ_3 (271/56) is normal to σ_2. In addition, normal faulting is observed at the topmost part of the quarry wall, at the transition to the Lower Keuper (Fig. 3.14a, red arrow at topmost part).

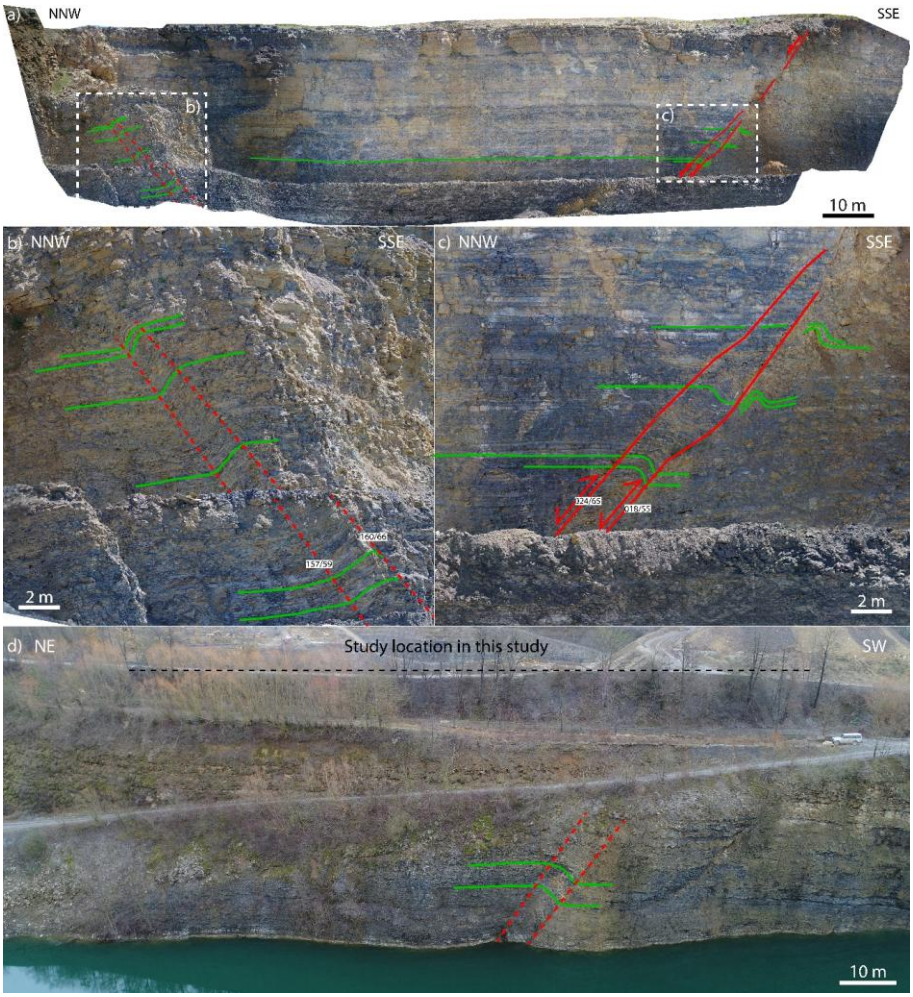

Figure 3.14 Wall panel in the quarry with kink band recorded with drone. a) Overview of the wall striking NNW-SSE with kink band in the NNW part. b) Breached kink band in SSE part of the quarry. c) On top, of the Upper Muschelkalk in a layer (a), red arrow) a normal fault is observed. d) Overview of a kink band occurring in the northern part of the quarry (Fig. 3.3a).

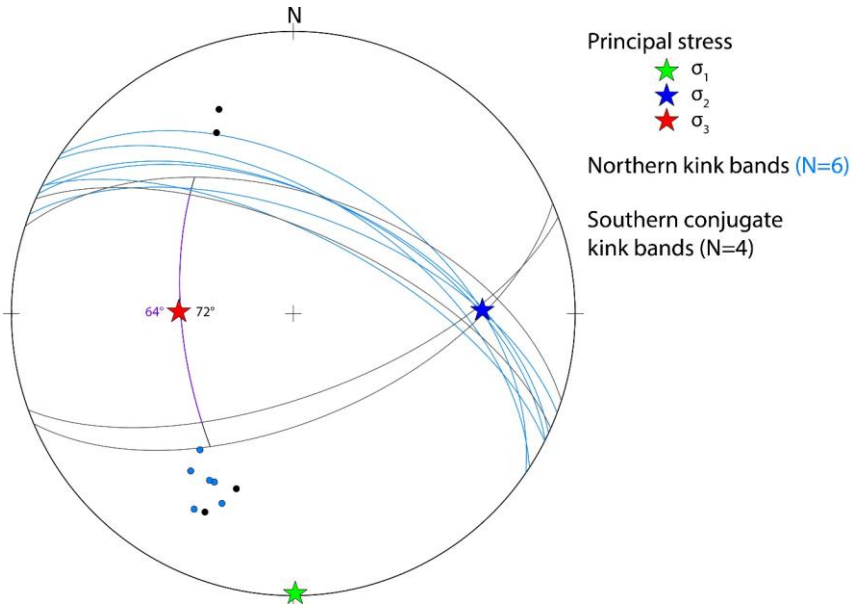

Figure 3.15 Stereonet projection of kink bands in the northern quarry part (cf. Fig. 3.3a) in blue, and conjugate kink band planes as great circle and poles in black using OpenStereo. The opening angle for the conjugate kink band is 64° to 72°, and the maximum principal stress σ_1 (green) is oriented N-S.

To analyze if fracture intensities are affected by the presence of faults of the breached kink band, fracture intensity and clustering analyses are performed on a scanline parallel to the wall strike (348°). Clustering would imply that more fractures are encountered than can be expected in a random fracture arrangement, whereas anti-clusters would imply that fewer fractures are encountered than can be expected in a random fracture arrangement.

For the scanline parallel to the NNW striking quarry wall with a fault zone of 2 m width (Fig. 3.14c), statistically significantly higher fracture intensities are observed in fracture sets (cf. Fig. 3.13) of all strike orientations (Kink 10°, 50°, 70°, 110° and 140° in Fig. 3.16), where major and minor peaks occur in different fracture sets (Fig. 3.16, 3.17). However, for sets with strike orientations of 10°, 50°, 110°, and 140°, the higher fracture intensity is found in the hanging wall of the fault zone, while higher fracture intensities in the fracture set striking to 70° are found in the footwall of the breached kink band (to the right of the breached kink band in Fig. 3.16). Assessing the normalized correlation count, all fracture sets show significantly higher and lower peaks than a random fracture arrangement, except for set 70°, where only subordinary higher peaks than in a random arrangement can be determined. Sets 10° and 50° are mostly indistinguishable from random with only small

peaks indicating clusters at 10s of cm length scales above the 95% confidence limit. Sets 10° and 50°, however, show anti-clustering, indicating length scales, where fewer fractures than in a random arrangement are observed at length scales of three to eight meters. Set 70° is mostly indistinguishable from random. Set 110° aligns subparallel to the main faults of the breached kink band (kink band planes strike 114° and 108°). It shows regularly-spaced fractal clusters up to one meter length scales and three to five meter length scales, but also anti-clustering at length scales of one to two meters and between five and 20 m. Set 140° is mostly indistinguishable from random with only weak clusters at the meter scale and anti-clusters at length scales of four to six meters.

Fracture intensities in the quarry wall perpendicular to the previous one, striking E to ENE (084°), for the same fracture set orientations striking 10° to 140° (Base 10°, 50°, 70°, 110° and 140° in Fig. 3.17), show statistically significant clusters of higher fracture intensity in four of five scanlines, although no fault is present in the direct vicinity. Set 10° shows two minor and one larger peak, set 50° three larger peaks, set 70° show no statistically relevant intensity clusters, set 110° one interval with high fracture intensities and nine subsidiary peaks and set 140° show four larger peaks. Due to the shorter length of the scanlines, and fewer recorded fractures, the normalized correlation counts cannot be accurately assessed for all length scales. The normalized correlation count for set 10° is indistinguishable from random with only weak peaks above the confidence limit at 10s of centimeter and six to seven meters length scales. Set 50° show contains too few fracture data to accurately assess the correlation count. Set 70° is indistinguishable from random with no indication for clusters at any recorded length scales. Set 110° is indistinguishable from random with minor weak clusters at 0.5 m to one meter length scales. Set 140° is mostly indistinguishable from random with weak clustering at 10 centimeters length scales and weak anti-clustering at seven to eight meters length scales.

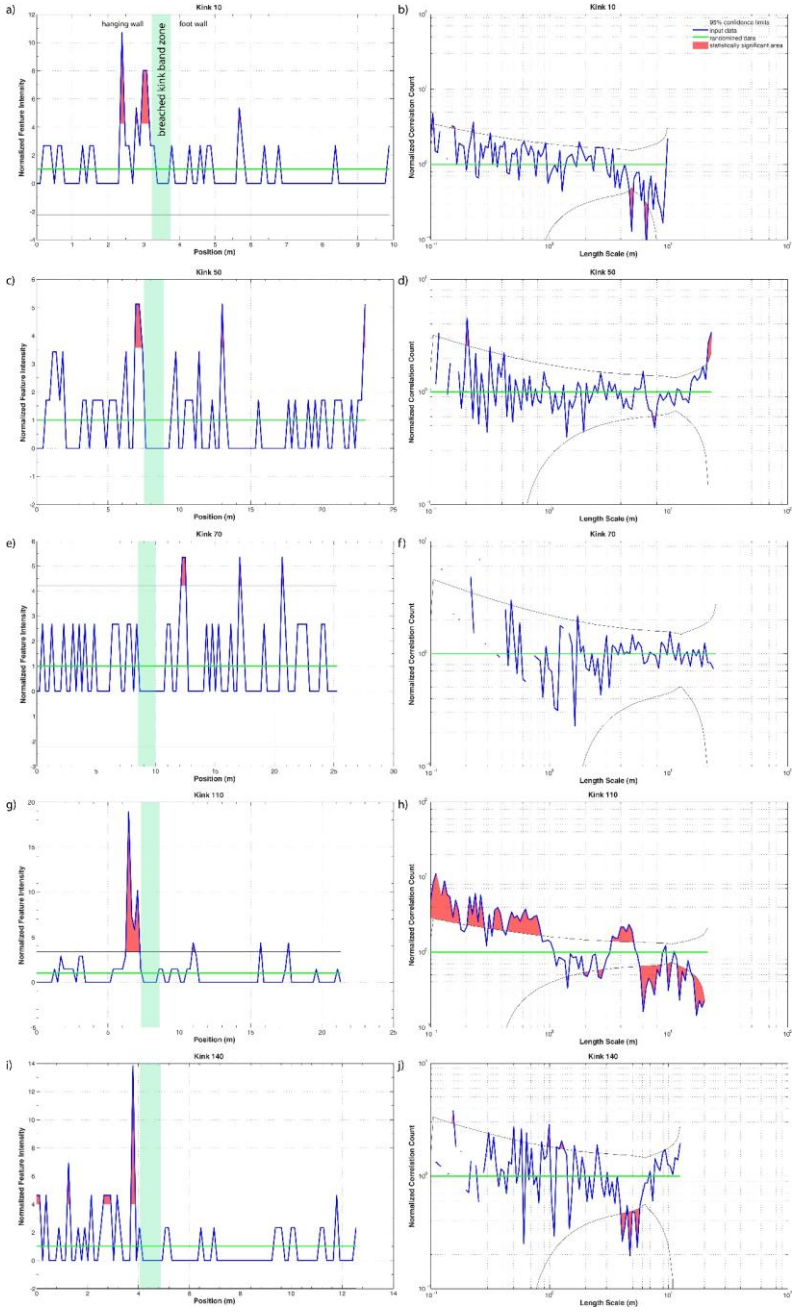

Figure 3.16 (Figure caption on next page)

Figure 3.16 (previous page) CorrCount results for normalized fracture intensities (left column) and normalized correlation count (right column) for the wall striking 348° (NNE-SSW). Green areal marks the position of the breached kink band. Black lines indicate the boundaries of the 95% confidence interval. Red highlighted areas (peaks) are exceeding the 95% confidence interval and are therefore statistically significant. Green line is random value given by the program, values in this area are not classified as clustered and thus indistinguishable. a) Statistically significant fractures of strike orientation 10° (red colored peaks) are limited to the footwall of the breached kink band, the values are (b) indistinguishable from random with only weak clusters above and beneath the lower confidence limit (N=38). c) One peak is present at foot wall, and two on hanging wall, which are (d) are indistinguishable from random, as they do not clearly exceed the 95% confidence interval (N=59). e) Three peaks occur at hanging wall, which are (f) indistinguishable from random (N=38). g) Main peak is present at foot wall and minor at hanging wall, which can be classified as (h) regularly-spaced fractal clusters with peaks and troughs over larger length scales (N=69). i) Peaks occur at the foot wall, but are (j) indistinguishable from random with only weak clusters (N=44).

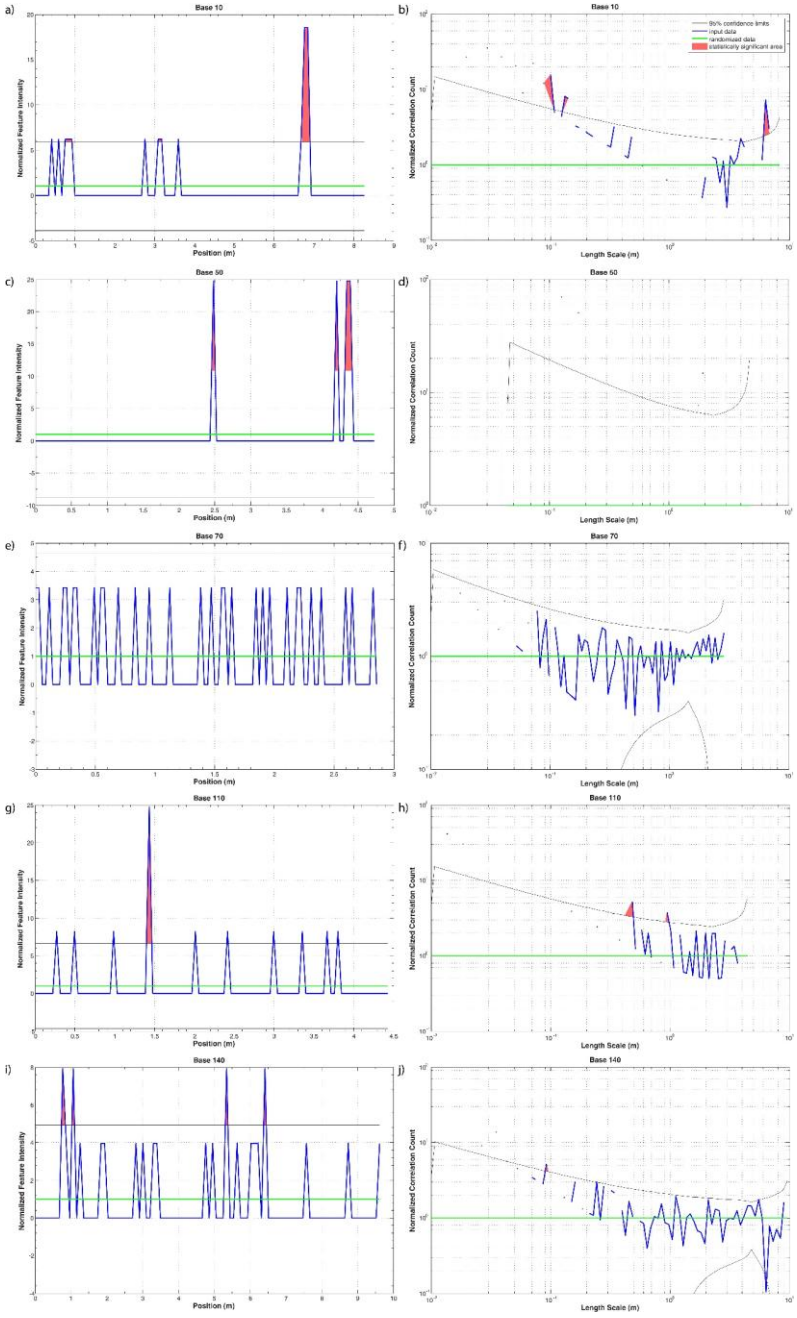

Figure 3.17 (Figure caption on next page)

Figure 3.17 (previous page) CorrCount results for normalized fracture intensities and normalized correlation count for the undisturbed wall striking 084° (W-E). The 95% confidence interval is given as black lines. Peaks are highlighted with red filling and exceeding the 95% confidence interval and are thus statistically significant. The green line is what is classified as random value given by the program, thus, values plotting this area are not classified as clustered and thus indistinguishable from random. a) One Major and two minor peaks occur, which are (b) indistinguishable from random with only weak clusters above the confidence limit (N=17). c) Three peaks occur, and the only (d) five points but are above the confidence limit, but cannot clearly be classified as cluster, because of the small amount of fracture values (N=5). e) No statistically significant peaks occur; thus, the fractures are (f) indistinguishable from random (N=30). g) One major and nine minor peaks are present, which are (h) indistinguishable from random with minor weak clusters above the confidence (N=13). i) Four peaks are present which are (j) indistinguishable from random with weak clusters above and below the confidence limit (N=26).

3.9.1 Dilation and slip tendency

While the presence of fracture clusters in the vicinity of faults and the undisturbed lithology is promising to possibly enhance the fluid flow, the assessment of fracture orientation in relation to the present-day stress field is required to assess their influence on subsurface fluid flow. Therefore, we also assess dilation (T_d) and slip (T_s) tendencies.

T_d and T_s analyses are performed for all measured fractures (Fig. 3.18a, b) and separately for the fracture strike sets included in the clustering analyses (Fig. 3.18c, d). For the present-day stress field, values from Meixner et al. (2014) derived for the nearby Bruchsal geothermal well (15 km NE of the studied quarry) were used. Low to medium T_d are observed for strike set 10°, medium T_d for strike set 110° and high T_d for strike set 140°. For slip tendencies, low to medium T_s for strike set 50°, 70°, 140° and high for strike set 110° and 10°.

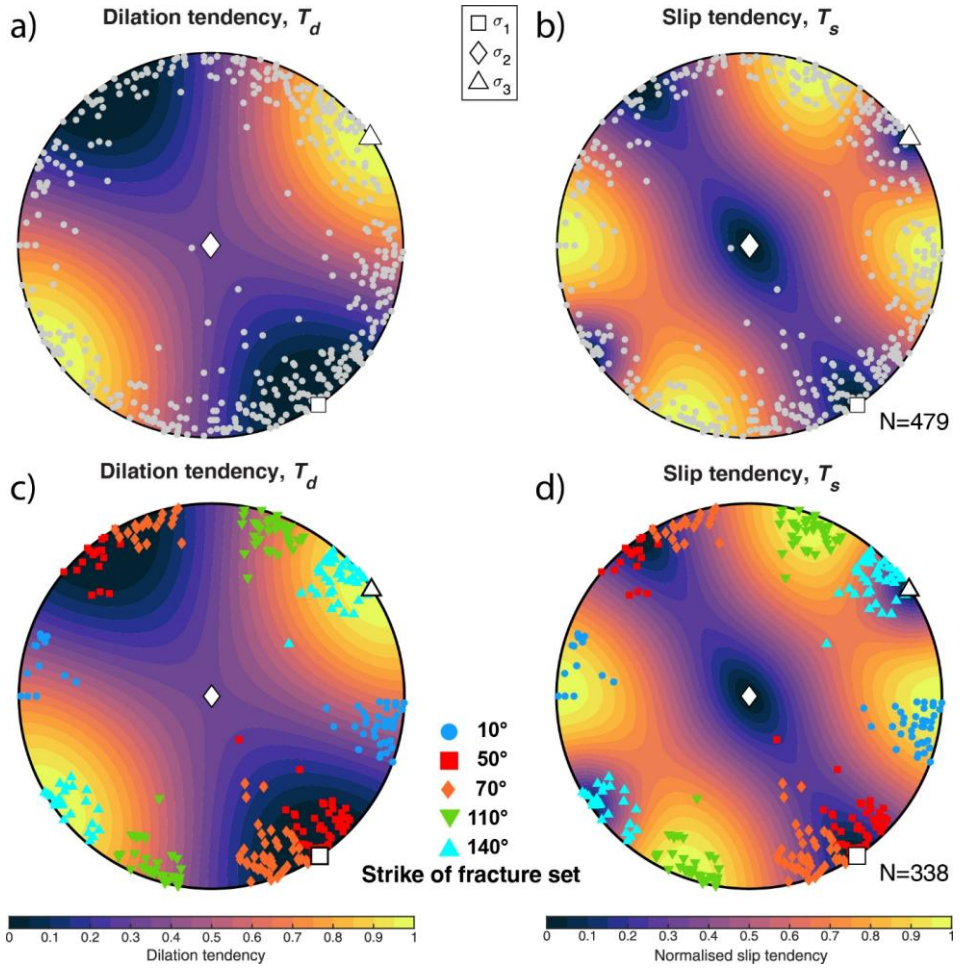

Figure 3.18 Dilation (T_d) and slip (T_s) tendency for clustered fracture strike sets (cf. Fig. 3.13). a), b) Dilation and slip tendency for all fractures of both scan lines. Fracture data for c) and d) are filtered in set classes as used for normalized correlation count. c), d) Dilation tendency for grouped striking sets in both scan lines, low to medium T_d for strike set 10°, medium T_d for strike set 110° and high for strike set 140°. d) Slip tendency for grouped striking sets in both scan lines, low to medium T_s for strike set 50°, 70°, 140° and high for strike set 110° and 10°.

3.10 Discussion

3.10.1 Lithology

The studied lithologies are composed of limestones and (marly) claystones from the Upper Muschelkalk from the base, to the Lower Keuper at the top. The elevated marly claystone content and limited dolomite content aligns with the description of the basin facies (Hagdorn and Simon, 2021) (Fig. 3.1b), located toward the depositional center of the southern Germanic Basin. Upper Muschelkalk shoals in Germany indicate the transition from an open ramp towards sheltered backshoal lagoon (Aigner, 1985; Adams and Diamond, 2019). Shoals are expected between the London Brabant Massif to the west and the Vindelician-Bavarian Massif to the east (Franz et al., 2015; Adams and Diamond, 2019). The topward decrease in marly claystone intercalations and relative increase in wacke- and packstones toward the top of the studied Upper Muschelkalk section and accompanying generally decreasing sGR response (Fig. 3.6) is in agreement with gamma-log measurements and lithology descriptions from boreholes in the studied area (Brunner and Simon, 1985). The data suggest a general shallowing upward trend, which is also described by e.g., Aigner (1985) and Aigner and Bachmann (1992) for the Germanic Basin and by Vollrath (1938) in the studied area. The uppermost part of the studied lithologies show some quartz pseudomorphs after sulphates, which may indicate a short period of brackish environment which lead to formation of evaporitic minerals, as e.g., described for authigenic euhedral quartz replacements after sulphates described by Friedman and Shukla (1980) for middle Silurian rocks.

Mud- and wackestones are interpreted to be deposited in low energy regimes, likely indicating an off-shoal environment. Wackestones show some shell debris, which might results from occasional input from storm events as is also described for other Upper Muschelkalk lithologies in the Germanic Basin (Kostic and Aigner, 2004). In the upper part of the studied Upper Muschelkalk succession, rarely packstones are exposed, mostly composed of shell debris. Ooids occur in some of the layer, which suggests a more storm wave dominated environment, which is also described for off-shoal areas and tempestites by Kostic and Aigner (2004). Tempestites are classified as storm flood rhythmites and where described for the Triassic Muschelkalk and Jurassic storm deposits (Ager, 1974; Mehl, 1982). The interpretation of storm dominated deposition is furthermore supported by the chaotic arrangement of skeletal components. Only few shells show a convex up alignment within the bed, which is describes as a common feature during less energetic phases of tempestite sequence (Ager, 1974).

One layer from the uppermost part additionally shows dominantly skeletal components as shell debris with a micritic envelope and dolomitized shell fragments, which is described

for a more shoal margin environments with episodic input from the shoal complex (Kostic and Aigner, 2004). The presence of likely stenohaline crinoid fragments (Hagdorn and Simon, 2021) in combination with shell fragments and other skeletal components, and alternating micritic layers are interpreted as multiphase storm events (multiphase tempestites) (Hagdorn and Simon, 2021). The crinoid content in the formation is reduced as a result of a clayey facies encroaches from the north, occasionally introducing brackish water (Hagdorn and Simon, 2021).

The observed transition from micritic to shell-bearing layers is either sharp or undulating/bioturbated (Fig. 3.4), as also described by Mehl (1982) for tempestites in the southern Germanic Basin. The skeletal layer however always transitions into a micritic layer or marly claystone on top. Mehl (1982) described vertically aligned bioturbation traces caused by glossifungites in the Upper Muschelkalk. Furthermore, the occurrence of an erosive contact between a wackestones with the underlying mudstone (Fig. 3.4d) is also described by (Ager, 1974). The observed contact types (Fig. 3.4c, d) are therefore either formed by greater bottom currents or bioturbation during quieter periods.

The transition from the Upper Muschelkalk to Lower Keuper in the quarry is marked not only by a color change of the lithologies to beige claystones following the last grey claystone of the Vitriolschiefer (Fig. 3.5), but also by an increase in the sGR signal (Fig. 3.6). This increase was also described for borehole gamma ray logs in the northern part of the southern Germanic Basin (Brunner and Simon, 1985; Etzold and Franz, 2005). In addition, the interpretation of the lithostratigraphic boundary is supported by the observed phosphatic bonebed layer (Grenzbonebed), and the thick-bedded blueish-grey limestones ("Blaubank", Fig. 3.5, 3.6). The base of the bone bed overlays the upper boundary of the Muschelkalk unconformity in southwest Germany (Hagdorn and Simon, 2021). The bone bed is a thin layer (approx. 2-3 cm) and contains higher contents of phosphatic components as small bone fragments, scales, teeth, coprolites, some ostracods, and inorganic phosphorite pellets than lithologies above and below (Parrish, 1978; Reif, 1982). Due to their high lateral persistence and thickness up to 20 cm (incl. their subseries, Reif, 1982 and references therein) they are the dominant lithostratigraphic marker horizon at the transition of the Upper Muschelkalk to the Lower Keuper. Bone beds generally form in shallow water during the early part of a transgression cycle or near the end of a regressive cycle. For the studied Muschelkalk/Keuper transition their formation is related to an alternation of low sedimentation phases below the normal wave base on an open shelf and phases influenced by strong currents and turbulence (Reif, 1982 and references therein). The Grenzbonebed is interpreted as depositional sequence boundary and subsequent transgressive flooding (Warnecke and Aigner, 2019). The Blaubank additionally contains layers composed of ostracods, teeth, bone fragments, and other phosphatic grains. The occurrence of ostracods is linked to brackish environments, which is also described by Hagdorn and Simon (2021).

The described lithological section therefore matches previous descriptions and can be assigned to the Meißner Fm. of the Upper Muschelkalk (moM) and the base of the Erfurt Fm. (ku1) from the Lower Keuper.

3.10.2 Paragenetic sequence

As no absolute ages are known, the paragenetic sequence is subdivided in early and burial diagenesis and based on cement parageneses and cross-cutting relationships. Peloids or pellets, combined as peloids in this study as this term describes ovoid particles of micro- or cryptocrystalline appearance (McKee and Gutschick, 1969), are overall composed of calcitic micritic. In general, the origin of these allochems could be faecel pellets, algae, reworking of mud grains, recrystallization of bioclasts, or they can be formed in situ (Folk, 1959; Macintyre, 1985; Chafetz, 1986; Kazmierczak et al., 1996). Most of the crinoid fragments show a dusty appearance, which is due to micrite-filled intraparticle pores. However, the primary porous stereo of crinoids can also be filled with other diagenetic cements, which can occur before or after burial, which favors the crinoid components to sink in the water column (Savarese et al., 2007).

3.10.2.1 Early diagenesis of carbonate sediments

As some bioclasts (shells and crinoids) and peloids show either micritic envelopes or are completely composed of micrite the earliest interpreted alteration is likely the recrystallization/micritization of peloids and bioclasts. Micritization of ooids and the loss of former structures are also described by Brüderlin (1970) for Upper Muschelkalk biosparites in the southwestern part of the southern Germanic Basin. The formation of micritic envelopes, prominently observed on shells and crinoid fragments, is possibly due to algae or cyanobacteria (Bathurst, 1966). However, different mechanisms on micritization have been reported e.g., recrystallisation, dissolution and reprecipitation as well as borings by e.g., algae and micrite precipitation in those borings (Bathurst, 1966). Especially the later (boring and precipitation) is often used to define the term micritic envelope, forming a cryptocrystalline isopachous rim on clasts which preserves these from alteration (Bathurst, 1966). Micritic envelopes were part of most of the biosparitic samples, which is aligned with the assumption that micrite envelopes are common in biosparites (Alexandersson, 1972 and references therein). Furthermore, micritic envelopes may indicate a former composition of high Mg-calcite or aragonite, as micritic envelopes form on skeletal particles composed of high Mg-calcite or aragonite in modern environments (Buchbinder and Friedman, 1970 and references therein).

The previous presence of sulphates is indicated by bladed crystal mouldic morphologies which are now partially occluded by chert and clear macro quartz. The precipitation of

sulphates is interpreted to occur during early diagenesis. Furthermore, former dissolution pores at the margin of sulphate molds are filled by calcite and Fe-calcite, indicating a formation of sulphates prior to carbonate cement precipitation.

Pyrite is found in e.g., shells or gastropods and encased in calcitic intraparticle cements. The formation of pyrite is interpreted to be early diagenetic likely due to bacterial sulphate reduction (BSR) (Berner, 1970), shortly after the deposition of bioclasts. This is a typical early diagenetic cement formation, also recorded in fine grained Jurassic limestones (Honjo et al., 1965). However, redeposition of pyrite cannot be excluded.

Sparry replacive calcite cement grows from the rim of bioclasts into their center, which is encased by sparry ferroan calcite, where the crystal size also increases away from the test of the former shells. The occurrence of two generation of calcite spar is also described in e.g., Bathurst (1975), where the first generation is described to be caused by neomorphism in subaerial to submarine environments, leading to remaining preserved pore space. Changes of pore fluid composition may lead to a cementation with Fe-calcite in the remaining pore space.

Based on the different optical properties of dolomite, two phases of dolomitization of former fossils or components as e.g., shells, ooids and peloids are observed in the samples (Fig. 3.7). The first phase (crystal size: 0.03–0.30 mm, avg.: 0.11 mm, dusty appearance mostly in center, non-pleochroitic) predominantly replaces ooids and peloids, whereas the intraparticle cements remain mostly unaltered by this phase. As only parts of the matrix in individual samples are dolomitized, the dolomitization process was limited. Active marine phreatic environments in shallow marine settings, especially in the mixing zone, are liable to form post-depositional dolomite by reflux down to 200 m below the surface or 300 m in marine dominated mixing zones (Cander, 1994; Budd, 1997; Gaswirth et al., 2007; Read et al., 2016). Furthermore, active marine phreatic environments are often characterized by high Mg-calcite precipitation, implying Mg availability in fluids (Longman, 1980). In some samples, ooids/peloids are partly or completely dolomitized, whereas the cements and matrix are unaltered, indicating selective dolomitization, which does not necessarily pre-date the formation of rim and pore-filling cements. The dolomitization of individual ooids is in agreement with observations by Brüderlin (1970) for Upper Muschelkalk lithologies in the southern Germanic Basin. The onset of dolomitization of ooids and peloids is interpreted to pre-date the formation of cement phases filling interparticle porosity. The dolomitization of the matrix in individual samples (type II, crystal site 0.01–0.14 mm, avg.: 0.05 mm) (Fig. 3.7b) is interpreted to be related to temporarily hypersaline/evaporative or occasionally supratidal conditions, also affecting the sediments during early diagenesis, as also observed in samples from supratidal environment from the Jurassic (Rameil, 2008). The described early diagenetic dolomite which may have formed under evaporitic conditions are

also described by Zeeh and Geng (2001) for the top part of the Meißner Fm. in the Upper Muschelkalk in southwestern Germany.

We distinguish between three types of dolomite: 1) selective in ooid/peloids, 2) matrix replacive and 3) saddle dolomite in shells, matrix replacive or as vein cement. The dolomite types are, distinguished by petrographic properties as pleochroism or extinction pattern, while Zeeh and Geng (2001) distinguish Trigonodus-dolomite I-III, compaction dolomites and saddle dolomite in matrix. The presence of some stylolites, and co-existence of dolomite within these stylolites are not interpreted as individual dolomite phase in our study, as the grain size does not differ from matrix replacement dolomite. However, the observed crystal size of our three dolomite types are in alignment with measured sizes by Zeeh and Geng (2001), where the crystal size of Trigonodus-dolomites vary between <0.0 to 0.3 mm, classified as very fine crystalline dolomite type I, recrystallized dolomite type II and dolomite type III of subhedral to anhedral crystals with nonplanar texture. The observed dusty appearance in dolomite centers and clear rims also match the description by Zeeh and Geng (2001).

The presence of isopachous/bladed fibrous calcite rim cement encasing partially replaced peloids/ooids (Fig. 3.7) and other skeletal fossil fragments, implies a formation during early diagenesis prior to mechanical compaction and following dolomitization. As the rim cements are interlocked in some samples, most interparticle porosity is occluded by this process. Generally, rim cements form in active marine phreatic environments (Longman, 1980) during early diagenesis. An isopachous fibrous/bladed calcite rim cement was also described by Geng and Zeeh (1995) for Muschelkalk samples from the Upper Rhine Graben and nearby areas and assigned to early diagenesis. The rim cements showed an orange to dull orange luminescence (Fig. 3.8), whereas Geng and Zeeh (1995) described rim cements as dull orange or non-luminescent. The relative age constraint to isopachous fibrous/bladed calcite rim cement and low degree of compaction prior to cementation implies that all preceding alteration occurred in shallow water depth, potentially including short-lived supratidal conditions with limited evaporative alteration. Calcite and subordinary Fe-calcite cements encase isopachous fibrous/bladed calcite rim cement on particles and occlude either all or most of the remaining interparticle pore space following very minor mechanical compaction (Fig. 3.7e, f). They therefore have to post-date formation of rim cements and form during early diagenesis (cp. Immenhauser, 2022). As the calcite and Fe-calcite cements are partially replaced by chert and quartz laths, they have to pre-date the formation of quartz and chert replacements. The orange luminescence of the (Fe-)cal cement (Fig. 3.8), however, does not match the described non-luminescence with only individual bright orange subzones or outer rims in slightly ferroan calcite cements encasing earlier generations as described by Geng and Zeeh (1995).

Some bioclasts are also replaced by chert, partially replacing the rim cements on neighboring grains as well, the replacement by chert is interpreted to post-date calcite rim cement precipitation. Silicification (incl. chert replacement) is a prominent early diagenetic alteration in the mixing zone of active marine phreatic systems (Knauth, 1979). Silicification of shells is also described as early diagenetic to syn-sedimentary process in Muschelkalk deposits by Geng (1996). As chert and quartz are observed to fill bladed crystal molds, they are interpreted to have replaced sulphate in nodules. Similar replacements are described in evaporitic settings in the US, forming at temperatures below 40 °C (Chowns and Elkins, 1974; Milliken, 1979). Possible dissolution of gypsum is also described by (Geng, 1996) for Muschelkalk deposits in and around the Upper Rhine Graben during early diagenesis. However, remaining intracrystalline pore space is visible in former sulphate molds lined by chert and quartz, indicating that the replacement was not pervasive and some sulphate may have been preserved, or that chert and quartz replacements stabilized the molds against compaction (Fig. 3.7). As quartz laths are also observed to replace intraparticle calcite cement, as well as fibrous/bladed rims cements and margins of bioclasts (Fig. 3.7e), and contain inclusions of the cement phases, they are interpreted to post-date the formation of these cement phases and contemporaneously to the initial replacement of bioclasts by chert and macroquartz.

3.10.2.2 Burial diagenesis of carbonate sediments

The overall low preserved optical porosity (0.0% to 14.7%, the latter in particles) indicates that most burial diagenetic alteration is restricted to cementation of remaining pore spaces prior to further mechanical and chemical compaction, formation of fractures and (partial) cementation of these. Individual samples show stylolitization and formation of dissolution seams, which are an effect of increasing vertical effective stresses during burial.

The third phase of dolomite (type III) is the replacement of bioclasts and matrix which is characterized by larger crystal sizes (0.04–1.30 µm, avg.: 0.27 µm), curved crystal outlines, undulose extinction, and are in some cases outlined by a phase of Fe-dolomite, and therefore classified as saddle dolomite (Fig. 3.19). Saddle dolomite is characterized by subordinately curved crystal facets and undulose extinction under crossed polarizers. These features are also observed in shallow-water, mixed siliciclastic-carbonate sequences in Lower Triassic ramp succession in western Hungary (Győri et al., 2020). The undulose or sweeping extinction is caused by distorted crystal lattice structure (Warren, 2000). To form saddle dolomite, elevated temperatures of 60 °C to 150 °C during burial are needed (Warren, 2000), indicating a burial depth of at least 2 km for a geothermal gradient of 30 °C/km. Saddle dolomite rhombs in shell fragments show a bright reddish luminescence and a non-luminescent rim using CL and a blue stain around some rims of saddle dolomite, indicating an increase of iron incorporated into dolomite, leading to non-luminescence behavior

(Pierson, 2006). As clay minerals de-water during mechanical compaction and provide Fe in solution (Miocic et al., 2020), iron could be incorporated during further cementation of dolomite or calcite in the studied limestone-marly claystone section. The burial diagenetic dolomitization of shell fragments by saddle dolomite, was also interpreted by Geng and Zeeh (1995). As saddle dolomite and Fe-dolomite rims are encased in Fe-calcite, the saddle dolomite precipitation is pre-dating the last phase of Fe-calcite cementation in bioclasts. The enrichment of iron in calcite during burial, may be caused by pressure solution from relatively iron-rich lithologies was also described by Bathurst (1975). Matrix replacive, undulose dolomite (type III) pre-date the formation of stylolites, as replacive dolomite is dissolved along them (Fig. 3.7j). In individual samples veins are displaced along stylolites, indicating that the formation of some veins predates the formation of stylolites (Toussaint et al., 2018).

3.10.2.3 Burial diagenesis of carbonate veins

As most veins in host rock samples and from a breached kink band crosscut all other diagenetic products, they are interpreted to post-date diagenetic alteration of the host rock. The paragenetic sequence (Fig. 3.19) of fracture filling carbonate cements is color coded with the observed colors from cathodoluminescence analyses (Fig. 3.8, 3.6). Pyrite at vein boundaries pre-dates or syn-dates the formation of the saddle dolomite vein (1, first vein generation). The occurrence of dolomite and pyrite in veins are also described in the Muschelkalk e.g., from the Mississippi-Valley-Type (MVT) Pb-Zn-Ag deposit near Wiesloch (see Fig. 3.1a) approximately 40 km north of our study area (Pfaff et al., 2010). The MVT deposits emplaced due to fluid mixing of ascending fluids in a releasing bend along the eastern Upper Rhine Graben fault in the Miocene (Pfaff et al., 2010). However, in this study pyrite most likely coprecipitates with saddle dolomite, as pyrite is not always present at the host rock-vein interface. The occurrence of saddle dolomite as fracture mineralization is also described by Geng and Zeeh (1995). Since saddle dolomite veins (generation 1) in a host rock sample also include (Fe-)calcite cements (generation 2), the formation of the latter is interpreted to postdate the formation of saddle dolomite (Fig. 3.19).

The earliest vein cement generation in a breached kink band sample includes (Fe-)calcite cements with similar luminescence characteristics as the vein cement generation 2 of the host rock samples. This composite vein and the generation 2 veins in the breached kink band samples are crosscut by a dull to non-luminescent (Fe-)calcite vein, which is interpreted to be vein generation 3. These are crosscut by a brighter (Fe-)calcite vein (generation 4) (Fig. 3.9). Veins from generation 5 are only found in a breached kink band sample (mostly dull Fe-calcite, Fig. 3.19) and are crosscut by very bright orange luminescing vein cement generation 6 and bright orange luminescing vein cement generation 7, which is found in both host rock and breached kink band samples. The partially fracture filling (Fe-)calcite generation 7 crosscutts generation 6 and always shows euhedral crystal facets in

contact with fracture porosity. Vein generation 7 is furthermore encased by a dull to non-luminescent Fe-calcite vein cement (generation 8) in a breached kink band sample. Due to the observed paragenesis, generation 8 is likely the latest vein cement generation in the studied samples. Overall, luminescence colors similar to vein cement generations 1–4 and 7 are found in host rock samples. Generations 2–8 (based on luminescence) are also found in the veins in the breached kink band boundary, highlighting a complex interplay of interacting vein sets.

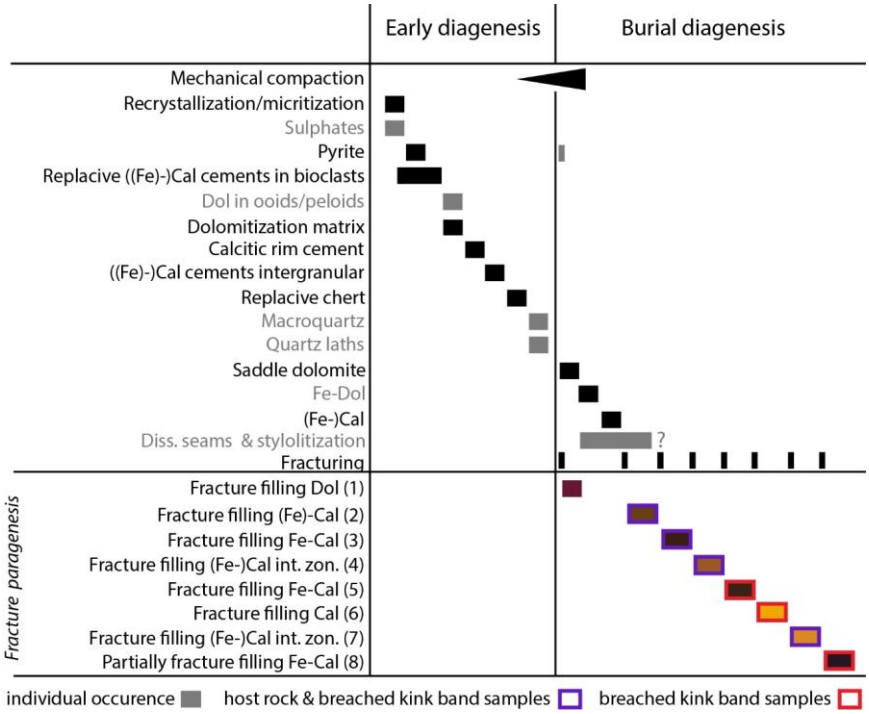

Figure 3.19 Paragenetic sequence of the studied samples of Lower Keuper and Upper Muschelkalk. Gray boxes correspond to diagenetic products only observed in individual samples. Colored boxes correspond to the observed CL color, no frame means observed only in host rock samples, purple frame means observed in host rock and breached kink band samples, and a red frame means observed only in breached kink band samples.

3.10.3 Structure and fracture correlation to regional stress field

Previous studies on fractures and faults, as well as UAV aerial image assessments in the Knittlingen quarry (Merz et al., 2018; Merz et al., 2019) indicated that the Upper Muschelkalk was subject to normal faulting (Fig. 3.14a, red arrow on the uppermost part). This was followed by later compression, resulting in decameter scale reverse kink bands with locally breached kink band boundaries with associated faults. Slickenlines on mineralized breached kink-band faults indicating both normal strike-slip and reverse faulting.

3.10.3.1 Fracture orientation and history

The fracture sets were analyzed on two walls and additionally along the vertical lithological columns in the quarry (Fig. 3.13). The NNE-SSW striking fractures are parallel to the Upper Rhine Graben boundary, and are, in contrast to Meier et al. (2015), the fracture set with the highest frequency. This may be related to the selection of scanline orientation. Therefore, our study compares two approximately orthogonal scanlines to capture all available fracture orientations. Because age data e.g., from calcite veins is missing, the corresponding fracture strike direction is related to published tectonic phases within Central Europe and the Upper Rhine Graben area (Schumacher, 2002; Kley and Voigt, 2008; Dezayes and Lerouge, 2019) (Fig. 3.2), but remains speculative as cross-cutting and abutting relationships are missing, as no large bedding planes exposing the fracture network were accessible.

The two most prominent fracture sets are NNE-SSW (parallel to the Upper Rhine Graben) and WNW-ESE, with additional sets striking NE-SW, ENE-WSW, NW-SE, W-E and NNW-SSE. Dezayes and Lerouge (2019) described three major sets: N-S, NE-SW/NW-SE and W-E in the sedimentary cover of the Upper Rhine Graben, Hemes (2008) described sets striking NNE-SSW, WNW-ESE, NW-SE, NNW-SSE, ENE-WSW and W-E for the Upper Muschelkalk lithologies on the eastern Graben shoulder approximately 40 km–50 km N to NE of the study location.

W-E striking fractures were related to pre-existing basement structures formed by the collapse of the Variscan range, which were reactivated during the Tertiary (Dezayes and Lerouge, 2019). Fracture sets striking NE-SW may be related to NE-SW directed Early Eocene Pyrenean collision and South Atlantic rifting during the Late Cretaceous until the Early Eocene (Kley and Voigt, 2008). During the Early/Middle Eocene, N-S striking fractures may have formed (Schumacher, 2002; Dezayes and Lerouge, 2019) (Fig. 3.2). NNE-SSW oriented compression during the Late Eocene most likely reactivated earlier faults and fractures (Schumacher, 2002; Meier et al., 2015).

The main rifting phase occurred during the Early Oligocene in an extensional setting (σ_3 oriented W-E to WNW-ESE) forming the normal faults of the Upper Rhine Graben (Schumacher, 2002). Simultaneously the graben shoulders underwent pronounced rift flank uplift as well as erosion (Villemin et al., 1986).

Reactivation of the Upper Rhine Graben faults as dextral strike slip faults probably occurred during the Late Oligocene, where the central Upper Rhine Graben part formed a releasing bend (Schumacher, 2002) forming the Heidelberg pull apart basin (Fig. 3.1a) accumulating more than 3000 m of Tertiary and Quaternary deposits (Edel et al., 2007).

Hemes (2008) relate the occurrence of fractures striking ENE-WSW to Early Miocene changes in stress regime. The NW-SE oriented σ_1 stress direction was active during the Miocene and Pliocene, caused by the Alpine orogeny, also leading to a left lateral strike-slip phase of the graben-bounding faults (Ziegler, 1992; Schumacher, 2002; Dezayes and Lerouge, 2019).

3.10.3.2 Fracture clustering and T_d/T_s

Analyzing the fracture clustering using the normalized correlation count (NCC) method, random fracture arrangements could be distinguished from clustered and periodic arrangements. It is shown, that clustering does not only occur in fracture sets striking parallel to strike orientation of the breached kink band (fracture set 110°) (Fig. 3.14) or only in the vicinity of faults, but can also be present in a wall without a fault (Fig. 3.17). This extends previous datasets, which so far only linked higher fracture intensity to the vicinity of faults in the Muschelkalk in the same quarry (Meier et al., 2015).

Our results indicate the potential for elevated fracture intensities (fracture clusters) away from fault zones in the Muschelkalk. Exploration of fracture clusters may reduce the risk associated with drilling into fault zones and induced seismicity (e.g., Kruszewski et al., 2023).

Since the quarry is located on the eastern Upper Rhine Graben shoulder, which experienced approximately 800 to 1200 m uplift with respect to the same lithology in the graben center (Villemin et al., 1986; Schwarz and Henk, 2005), care has to be taken to match observed fracture orientations and intensities to the subsurface. However, for other limestone successions in northern Germany, this correlation could successfully be performed, where a variation of main strike direction is assumed to be caused by e.g., an influence of near-field stress perturbations around faults bounding the reservoir (e.g., Becker et al., 2018). Other studies report lower fracture intensities in outcrops than in the subsurface (Li et al., 2018).

The reported clusters show characteristics of regularly spaced fractal clusters or weak clustering with cluster spacings between 1 and 10 m and cluster widths <1 m and between 3-5 m (Fig. 3.16, 3.17) (cf. Li et al., 2018; Marrett et al., 2018). If subsurface fracture orientations were similar, this analysis may guide horizontal drilling orientations and placements of perforated or open-hole sections in reservoir utilizations.

The normalized correlation count method performed on individual strike orientations with Terzaghi-corrected perpendicular fracture distances, deliver values for fracture intensities in the studied region, and are therefore less liable to artificially inflated fracture intensities if fractures of different strike sets are assessed in one combined dataset. This is essential, as only individual fracture sets are likely contributing to fluid flow in the studied region, based on the evaluation of dilation and slip tendencies. These have also been successfully used to assess the presence of individual hydrocarbon reservoirs in the Upper Rhine Graben, as varying fault strikes show different dilation and slip tendencies (Allgaier et al., 2023a). As mentioned by Li et al. (2018), the spatial arrangement of fracture clusters are important features referred to industry application (Questiaux et al., 2010) and for reservoir models (Panza et al., 2016).

Dilation and slip tendencies of fracture surfaces as a function of present-day stress provide additional insights and quantify the individual reactivation potential of each cluster set (Barton et al., 1995; Morris et al., 1996; Ferrill et al., 1999; Collettini and Trippetta, 2007; Becker et al., 2019a; Ferrill et al., 2020). Slip potential for fracture strike set 110° and 10° are at highest, low to medium T_s is observed for strike set 50°, 70°, 140° using the present-day stress orientation and magnitude from Meixner et al. (2014). The dilation tendency for fracture strike set 140° is high, and medium for sets 110° and 10° under present-day stress. The (strongly) clustered sets striking NNE-SSW (10°), WNW-ESE (110°), and NW-SE (140°) do therefore likely contribute to flow in the subsurface as they are suitably oriented, whereas the other orientations are unlikely to contribute to fluid flow, as they are unsuitably oriented in the present-day stress field.

Fracture roughness classification was not part of this study. However, fractures which are shear displaced may show a misfit between surfaces and therefore shear dilation (Barton et al., 1985). Shear dilation of fractures can cause an enhancement of stress-resistant permanent permeability (e.g., Cheng and Milsch, 2021).

Additional controls on fluid flow in fractures and faults are chemical alterations and the formation of cements. Cements can act as bridges between fracture surfaces and thus preserve fracture porosity (Hilgers et al., 2004; Laubach et al., 2004). Our results indicate that samples containing partially cemented veins do preserve permeability higher than samples containing stylolites or the undisturbed host rock even at 30 MPa confining stress (Fig. 3.11). When the permeability measurements are normalized to the highest measured value

of each sample as 1.0, the partially sealed vein retains 41% of the initial permeability, the stylolite retains 16%, and the undisturbed host rock retains only 11% of the initial permeability if measurements at confining pressures of 1.2 (initial) and 30 MPa (highest) are compared. Partially sealed veins are interpreted to preserve permeability at depths (Gale et al., 2010; Lander and Laubach, 2015). Our laboratory results demonstrate for the first time the predicted permeability increase due to partly open fractures as well as showing that stylolites can increase permeability. The lab measurements therefore confirm the applicability of literature models to reservoir scenarios, and imply the necessity for structural diagenetic assessment of samples from fractured reservoir plays.

Thus, the presence of partially sealed veins in all strike orientations (green dots in Fig. 3.13b) shows that in addition to suitably oriented fracture orientations in the present-day stress field, partial sealing can also preserve fluid pathways in all studied fracture orientations. This highlights that in addition to T_d and T_s evaluations, the study of structural diagenetic properties of partially sealed veins is necessary to fully understand the fluid flow system, because they additionally contribute to the fluid flow network in fractured carbonates irrespective of the current present-day stress.

3.10.3.3 Kink band formation

The reconstructed σ_1-orientation during kink band formation is N-S (Fig. 3.15), matching the Middle Eocene stress field orientation related to the Alpine orogeny (Fig. 3.2). Additionally, reactivation of the kink band could have occurred during the Miocene, where also the releasing bend in Wiesloch ~30 km of the study location in Wiesloch is interpreted to be formed (Pfaff et al., 2010).

Calcite cemented fault planes are exposed along the breached kink band boundary (Fig. 3.9g, h). Microstructures show euhedral crystal facets in contact with fracture porosity, with some fracture porosity locally preserved in the breached kink band. The breached kink band boundaries indicate thrust, normal, and strike slip movement, the latter likely related to fault reactivation, e.g., synchronous with the Miocene MVT Pb-Zn impregnation near Wiesloch (Fig. 3.1a, Pfaff et al., 2010) and the subsidence of the pull-apart basins near Heidelberg and Rastatt (Fig. 3.1a, Gabriel et al., 2013; Böcker et al., 2017). Normal fault reactivation by younger reverse faults was also reported from the eastern graben fault (Ziegler, 1992).

3.10.4 Reservoir quality controls

The matrix reservoir quality of the Upper Muschelkalk and Lower Keuper limestones is influenced by small grain size (micrite to microspar), early and burial diagenetic

cementation with mostly (Fe-)calcite and dolomite/saddle dolomite (Fig. 3.19). Both result in low porosity (0.13%–10.87%) and low permeability (<0.0001–9.7 mD) of the host rock. Permeability is only enhanced where open or partially sealed fractures are present (9.7 mD) and porosity is enhanced where druses are present (10.9 %). Samples containing partially sealed veins, measured under higher confining pressures (up to 30 MPa) indicate that permeability is preserved, as the permeability measurement using 1.2 MPa confining stress do not represent the stresses in the subsurface at depths. This assessment is also supported by lower pressure sensitivity coefficient of permeability γ in the sample containing partially sealed vein, indicating a lower stress sensitivity of permeability than in samples containing a stylolite or of the undisturbed host rock. While permeability in a reservoir is not controlled by the permeability of an individual fracture, the fracture network (fracture lengths and connectivity) requires further analyses in the studied region. However, as partially sealed fractures are observed in all strike orientations (green points in Fig. 3.13b), it is likely that they will contribute to reservoir-scale fluid migration.

Rock typing shows that only one sample showed positive correlation with micrite and permeability (Fig. 3.12a), but this is due to higher amount of fracture porosity and vein cements (Fig. 3.12d), overprinting the plug. This means that micrite has no positive effect on porosity or permeability in this study. However, the micrite content can enhance porosity due to microporosity which was shown for Upper Cretaceous limestones (Ölmez et al., 2024). Also, the content of shells (with primary features) and recrystallized shells does not correlate to enhanced porosity or permeability (Fig. 3.12b), whereas the stylolites (Fig. 3.12c), fracture porosity, and partially sealed veins (Fig. 3.12d) appear to positively affect permeability in individual samples. However, stylolite-bearing samples show a more drastic decrease in permeability at higher confining pressures as samples containing partially sealed veins (Fig. 3.11).

Previous studies on Muschelkalk samples highlight, however, that matrix porosity and permeability may be locally enhanced in porous coquinite layers, and peloid or ooid grainstones formed in shoal areas (Koehrer et al., 2010; Petrovic and Aigner, 2017; Warnecke and Aigner, 2019). Thus, the main controls on reservoir quality in the studied samples are fractures, partially sealed veins and, to some extent, stylolites. Furthermore, the porosity-permeability plot does not show a clear correlation. Other studies on less cemented samples from the Upper Muschelkalk in SW Germany show a weak positive correlation (Ruf and Aigner, 2004), which is not similar to this study, and highlights the heterogeneity found in the Muschelkalk in south-western Germany.

The Lower Keuper lithologies with higher amount of claystones and some smaller interbeds of limestones are more prone to act as a seal on top of the fractured Upper Muschelkalk reservoir. This is similar to Upper Muschelkalk reservoirs in NE Netherlands

(Pöppelreiter et al., 2004). Fractured carbonates in Muschelkalk thus may contribute to accessible reservoir volumes in the Upper Rhine Graben.

3.11 Conclusions

Pervasively sealed veins, fine grained mudstones or pervasive early diagenetic pore space cementation have been shown to generally reduce matrix reservoir quality in the presented study. Thus, the reservoir quality in the tight carbonate reservoir is solely related to natural fractures and partially sealed veins, and to some extent stylolites if they are aligned parallel to fluid flow direction.

The measurement of plugs containing partially sealed veins under elevated confining pressure of 30 MPa show permeabilities of 0.13 mD, upon normalizing the permeability measurements to the maximum recorded value of each sample, this sample retains c. 41% of the initial permeability as opposed to only 11% of retained permeability in an undisturbed host rock sample.

Decameter-scale reverse kink-bands form reverse faults along breached kink band boundaries and indicate a N-S compressional tectonic phase during formation. They thus formed by Alpine far-field stress during the Eocene in the studied region, which were not documented so far. Kink-related reverse and thrust faults were locally reactivated by strike slip and may be synchronous with Miocene shear along the NNE striking Rhine graben fault, associated with pull apart basins and MVT-mineralization in the region.

Fracture clusters striking 10°, 110° and 140° occur in the undisturbed host rock, indicating, that fracture clusters are not necessarily restricted to faults or their damage zone. Integrating shear and dilation tendency analyses with clustering analyses highlight that likely only fracture clusters striking NNE-SSW, WNW-ESE, and NW-SE are potential fluid conduits and thus of importance for geoenergy application, if these fracture sets are also developed in the subsurface.

4 Reservoir characterization and well production proxy analyses on drill cuttings: Case study from the Flysch play in the Vienna Basin (NE Austria)

4.1 Abstract

Drill cuttings, though rarely used, are crucial subsurface samples to understand petrographic properties affecting reservoir quality. Unlike core material, cuttings are continuously available along the wellbore and can be used during drilling to monitor progress. Therefore, cuttings may allow a semi-quantitative, statistical calibration of rock properties from the subsurface, but they are often underutilized. Although fracture and vein orientations cannot be reconstructed from drill cuttings, the presence of veins and their internal textures (open, partially sealed or sealed) in specific formation sections and depths can be identified and analyzed using e.g., transmitted light microscopy and cathodoluminescence to supplement characterization at the well site and subsequently assess production behavior. Borehole gamma ray logs in combination with handheld portable X-ray fluorescence (pXRF) analyses on cleaned and dried drill cuttings can be used to further improve the depth accuracy of the cutting samples and to geochemically fingerprint the samples, based on the Si/Al ratio, as a proxy for sandstone-rich and mudrock-rich sections of the well. In this study, eighty-three sandstone cutting samples from two wells, covering ~400 m of stratigraphy targeting the Paleocene-Eocene Greifenstein Fm. equivalent (Glauconite Sandstone, GLS) in the Vienna Basin (Austria), were studied. They also cover parts of three different reservoir sections (1. to 3. GLS). The Flysch play in the Vienna Basin hosts several sandstone-mudrock interbeds and is composed of several nappes, forming complex reservoir compartments. The glauconite contents vary between different sections of the GLS, where the highest is observed in the 3. GLS. The sandstones are predominantly cemented by ferroan calcite, resulting in low optical porosity (<5 %) in both wells, with only individually elevated porosity, related to partially dissolved K-feldspar grains. A paragenetic sequence solely based on cuttings further highlights that reservoir quality in the studied section is independent of sandstone compaction, but is related to lower optical porosity in finer-grained sandstones and higher carbonate vein cement contents. Furthermore, productive intervals are related to lower Fe + Mg contents. The understanding of reservoir

properties, diagenesis, and their influence on fluid flow is crucial for successful exploration and reduction of uncertainty in reservoir production and development. The diagenetic variations from cuttings and the geochemical fingerprint by pXRF are linked to reservoir quality and production performance of individual well perforations. This approach can provide additional information on reservoir quality where core material is unavailable.

4.2 Introduction

Reservoir assessment and a better understanding of reservoir quality variations are critically important for successful exploration, reduction of uncertainties and help to understand the economic viability of natural resources (e.g., Ozkan et al., 2011; Camp et al., 2018; Worden et al., 2018; Ciriaco et al., 2020). Reservoir quality assessment therefore is of importance particularly for exploration and production of hydrocarbons or geothermal water in areas with increasingly challenging conditions.

While drilling a well, drill cuttings are the first opportunity to directly analyze the subsurface rocks on-site, though these are only rock fragments and have undergone damage by the drilling process. Furthermore, drill cuttings are the only geological samples in oil, gas or geothermal wells that are usually continuously taken and can provide direct information on rock properties such as the mineralogy of detrital grains, authigenic cementation, vein composition and optical porosity. Drill cuttings are used to assess formation properties and to improve the drilling performance in an inexpensive way (e.g., Tiainen et al., 2002) and have been integrated with gamma ray and other borehole measurements to better assess reservoir characteristics (e.g., Gulf of Suez Rift, Radwan, 2022). The potential of drill cuttings to better understand the reservoir performance or source potential was assessed e.g., for fields in the Vienna Basin (Rupprecht et al., 2017), the Volga-Ural Basin in Russia (Ibrahem and Morozov, 2024), the Montney tight gas siltstone play in Canada (Sanei et al., 2020), and at onshore blocks in the Sultanate of Oman (Swami et al., 2022).

Geochemical fingerprinting is based on several geochemical techniques as e.g., fluid inclusion techniques, light stable isotope analyses or C-O clumped isotopes to analyze diagenetic or sedimentary features (Worden et al., 2018; Mamdouh et al., 2024). However, mineralogical analyses of core samples or cuttings is often performed using laboratory X-ray diffraction (e.g., Gier et al., 2018), infrared techniques and point counting using a microscope (Worden et al., 2018). Chemical analysis on core or cutting samples is used less, but can be performed using e.g., benchtop X-ray fluorescence and portable X-ray fluorescence (pXRF) devices (Worden et al., 2018). The pXRF analyzer provide low cost, rapidly available data of both cleaned core and cutting material and is used for e.g., chemostratigraphy and detection of trace metal contaminants in aquifers (e.g., Zambito et al., 2022).

Results of pXRF measurements of geothermal drill cuttings have been shown to be comparable in accuracy with laboratory XRF results for many elements, especially elements with atomic numbers >17 (Mauriohooho et al., 2016). Being a non-destructive method, pXRF allows to reuse the cuttings for petrographic analysis. Alternative works utilizing drill cuttings in industry approaches shown by Swami et al. (2022) and by Pandion Energy in Norway (Offshore, 2021) are employing automated mineralogy mapping techniques using a SEM platform. However, sample preparation and analysis is time consuming and ultimately lags behind drilling operations. Therefore, linking pXRF measurements to cuttings on the well site and calibrating the process to standard petrographic workflows may enable the use of pXRF measurements to assess likely producing intervals in future wells. Caja et al. (2019) also described the combination of petrography and geochemistry methods for analyzing cutting material using virtual microscopy, automated mineralogy and digital petrophysics.

In general, the primary composition of sandstones is controlled by factors such as the provenance and plate tectonics (e.g., Dickinson and Suczek, 1979), the depositional system, transport energy, transport distance (e.g., Bjørrlykke, 1998; Lupin and Hampson, 2020) and therefore grain size and sorting, which can affect reservoir properties (e.g., Coskun et al., 1993; Griffiths et al., 2019). However, diagenetic processes such as compaction and cementation or dissolution can overprint primary sedimentary controls on reservoir properties, resulting in either improvement or reduction of given matrix permeability and porosity of the reservoir rock (e.g., Bjørlykke, 1988; Coskun et al., 1993; Dutton and Loucks, 2010; Morad et al., 2010; Busch et al., 2024). Quartz cement can either result in reduction of pore space and therefore the deterioration of reservoir quality (e.g., Bjørlykke and Egeberg, 1993; Morad et al., 2010) or in preservation and stabilizing of the framework and pore space (if not filling the pore space completely), improving the reservoir quality (Molenaar, 1986; Makowitz et al., 2006; Busch et al., 2022a). Furthermore, in tight rocks, natural fractures play an important role for reservoir exploitation as they are the main fluid conduit (besides faults) (e.g., Olson et al., 2009; Bahrami et al., 2012; Khelifa et al., 2014). Whilst all these are established from core, and outcrop analyses our motivation was to test if some of these correlations can be also recognized on drill cuttings.

In the study area, the Upper Cretaceous to Paleocene Flysch play is assessed, as it is interpreted as a fractured reservoir play leading to the fact that exploration and production wells commonly deliver mixed results. As fractures are commonly present in the investigated sections (Möbius et al., 2023), fracture and vein characteristics are likely to influence reservoir quality and productivity. Cores are not continuously available, therefore cuttings were used to better understand the influence of petrographic properties. An in-depth assessment of vein cement textures was undertaken to better assess their influence on reservoir quality. Therefore, the petrography, diagenesis and geochemical fingerprint of

sandstone drill cuttings from reservoir rocks from two wells are presented in this study. Detailed petrographic studies will provide a paragenetic sequence for this reservoir section based on cuttings only.

The Flysch play in the Vienna Basin, Austria, was already discovered to be prolific to produce oil and gas since the beginning of the 20th century. Production volumes peaked in the 1940s, however the area is still actively producing. Furthermore, detailed structural diagenetic assessments on veins and partially sealed fractures will shed light on the effect of fractures in the reservoir section of the lithology. The geochemical fingerprint measured with a portable X-ray fluorescence analyzer (pXRF) is used in combination with petrographic data obtained from thin sections and borehole gamma ray (GR) logs. By comparison with information on producing and non-producing intervals, possible proxies from pXRF data for reservoir quality assessments were derived. Such proxies may be used directly on the wellsite. Using geochemical proxies based on pXRF analyses may close that time-gap from analyses such as SEM-based automated mineralogy mapping techniques, as cuttings can be already washed and dried directly at the wellsite for their description. The presented pXRF approach, if calibrated to standard reservoir quality analyses, may thus enable the assessment of suitable reservoir quality intervals directly on the well site. It can therefore be used to accelerate completion and perforation decisions, influence well continuation and data acquisition needs and thus may reduce total well cost. Furthermore, such a calibration can be similarly applied on historic cuttings of intervals that were not of interest at the time of drilling (e.g., dry holes in the hydrocarbon industry). However, such may meanwhile be of interest for geothermal development or to evaluate the quality of subsurface storage locations.

4.3 Geological setting and tectonic evolution

The Vienna Basin, a major hydrocarbon province in Central Europe (Fig. 4.1a), is a NE-SW trending 200 km long and up to 60 km wide Tertiary thin-skinned intramontane pull-apart basin in Austria, Czech Republic and Slovakia (Ladwein, 1988; Piller et al., 1996; Arzmüller et al., 2006; Strauss et al., 2006; Rupprecht et al., 2017). It is part of the Neogene Paratethys Basin System and forms a structural evolution along the junction of the Eastern Alps in the West, the southeast Pannonian Basin System and the Western Carpathians in the NE (Royden et al., 1985; Wagreich and Schmid, 2002). The basin hosts crystalline basement rocks from the Bohemian Massif, Mesozoic autochthonous sediments and foreland basin deposits from the Cenozoic, and a Neogene clastic basin fill (Fig. 4.1b) (Ladwein, 1988; Rupprecht et al., 2017). During Alpine subduction of the European lithosphere, thrusting occurred and led to the deposition of flysch in the Carpathian foredeep

(Royden et al., 1985). The flysch is composed of submarine sediment-flows to turbidity currents (e.g., Rammel, 1989 and references therein). The basin locally hosts Alpine thrust sheets of Cretaceous to Miocene flysch, as well as subordinate molasse deposits (Fig. 4.1c) (Royden et al., 1985). Neogene sedimentary rocks of the Vienna Basin are sandstones, marls and subordinate carbonates, which can exceed thicknesses up to 5000 m in the depocenters (Ladwein, 1988; Gier et al., 2008). At the base of the Neogene part of the section, Late Burdigalian sediments were deposited in a fluvial to lacustrine environment (Piller et al., 1996; Gier et al., 2008). In the Early Badenian a marine transgression started and evolved to brackish conditions during the Sarmatian (Piller et al., 1996; Gier et al., 2008). The decrease in salinity leads to the deposition of fluvial to lacustrine deposits in the Pannonian (Piller et al., 1996; Gier et al., 2008, and references therein). The Vienna Basin was separated into fault blocks during the pull-apart phase, which may have resulted in local variations in sedimentary evolution (Strauss et al., 2006).

Strike-slip faulting, back-arc extension and retreating subduction led to the formation of Miocene pull-apart basins in the alps such as the Vienna Basin (Royden et al., 1985; Decker, 1996; Decker et al., 2005). The Vienna Basin started to form as a piggy-back basin along a sinistral fault system during the Early Miocene, and continued evolution as a rhombic shaped pull-apart basin until the Late Miocene until W-E compression started, which also led to regional basin inversion (Royden et al., 1985; Decker, 1996). From the Pleistocene to recent time W-E extension started (Decker, 1996).

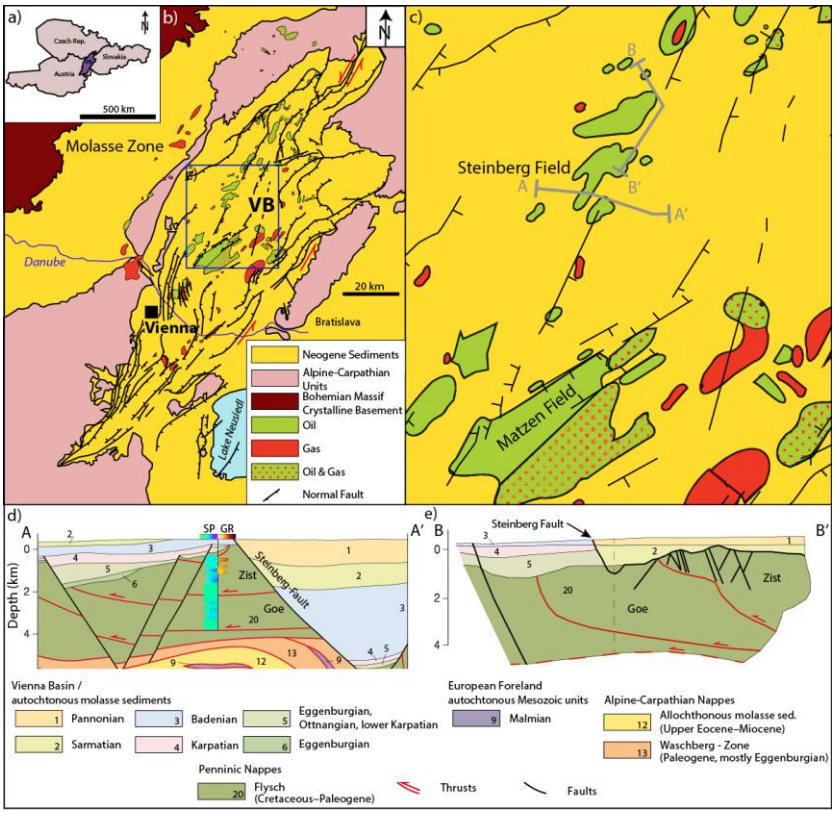

Figure 4.1 Location and profiles of the Vienna Basin. a) Location of the Vienna Basin (VB) in the NE part of Austria, SE part of the Czech Republic and W part of Slovakia redrawn from Rupprecht et al. (2018). b) Overview map of prominent units and the regional geology of the Vienna Basin, redrawn & modified from Rupprecht et al. (2018) and references therein. Vienna is marked with a black rectangle. Oil (green), gas (red) and oil & gas (green with red dots) fields adapted from Arzmüller et al. (2006), the study area is marked with a blue box. c) Magnification of the blue box in b) showing the study area and marked profiles in d) and e). d) Simplified W-E profile along the line A-A' with early thrusts and later normal and strike-slip faults, highlighting the Zistersdorf (Zist) and Gösting (Goe) units (redrawn and modified after Berka, 2015). Spontaneous potential (SP) log (purple low, green high) is available for the whole Zis and Goe units, whereas gamma ray log data (GR) is in historic wells often only available for intervals of particular interest (reference well provided by OMV). e) NW-SE to NE-SW profile along B-B' with interpreted lithological sequence for 3 to 5 (redrawn and modified after Wessely, 2006). The vertical dashed line indicates the change of orientation of the profile (parallel to the Steinberg fault from dashed line to B').

One of the main tectonic units of the flysch in Austria (Wienerwald Flysch, Cretaceous-Eocene) and also the northernmost is the Greifenstein Nappe, containing the Altlengbach Fm. (Upper Cretaceous), Glauconite Sandstone Series (Paleocene-Eocene) and Steinberg Flysch (Eocene) (Götzinger et al., 1954; Rammel, 1989; Mattern and Wang, 2008) (Fig. 4.2a). The Greifenstein Nappe itself is subdivided into the Gösting and Zistersdorf units, separated by internal thrusts, leading to a stacking of Upper Cretaceous to Eocene lithologies (Fig. 4.2b) (Götzinger et al., 1954; Rammel, 1989). This stacking is supported by biostratigraphic studies (Wessely, 2006 and references therein), and the repetition of log responses (two sections of low SP response in Fig. 4.1d, GR in Fig. 4.2b).

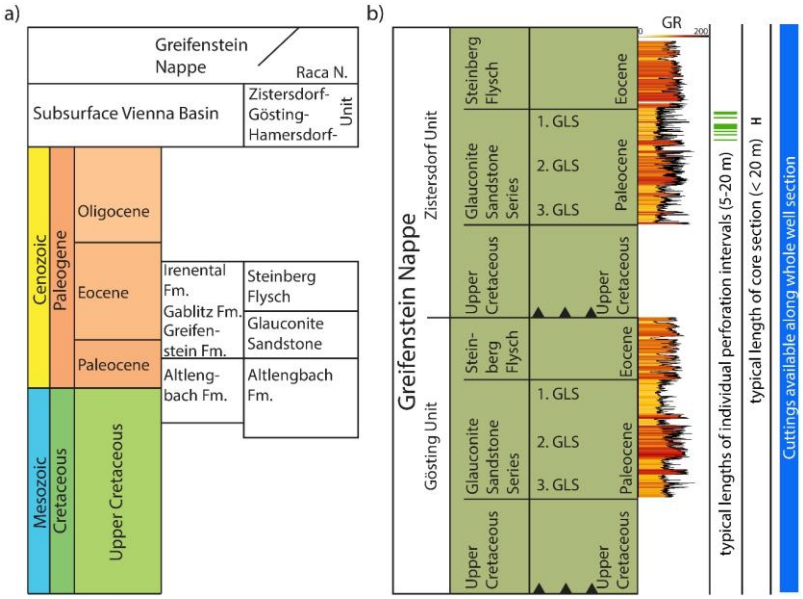

Figure 4.2 Regional stratigraphy. a) Simplified stratigraphy of the Vienna Basin Flysch, modified after Wessely (2006) and references therein, colors are adapted from the international chronostratigraphic table by Cohen et al. (2024). b) Simplified subdivision of the Greifenstein Nappe including 1. to 3. GLS (Glauconite Sandstone), thrusting results in repetition of lithologies, modified after Wessely (2006) and references therein. Colors for the flysch (Cretaceous to Paleogene) are related to the profile in Fig. 4.1d) for Zistersdorf and Gösting unit. GR well log data provided by OMV is given for the studied sections, showing similar log responses. Due to thrusts, layer doubling of sandstone and mudstone units are shown in the GR from reference/example wells, were the Greifenstein equivalent was continuously logged. The typical thickness of single production perforations is between 5 to 20 m, whereas the typical length of a core section is <20 m, but cuttings are available along the whole section (blue field).

4.3.1.1 Reservoir System

Exploration for oil and gas in the Vienna Basin started around 150 years ago and first economically producible discoveries of conventional oil and gas fields in the flysch were made in the early 1930s (Arzmüller et al., 2006; Rupprecht et al., 2017; Möbius et al., 2023). About 6000 wells have been drilled there since the 20th century (Arzmüller et al., 2006) and the Vienna Basin is a well-studied area in terms of the stratigraphic history and depositional settings (see Harzhauser et al., 2020 and references therein). Although the source rock is well known (e.g., Schulz et al., 2010; Rupprecht et al., 2017; Schicker et al., 2021), the reservoir rock properties in sandstone reservoirs in the Flysch play of the Vienna Basin is not fully understood due to the small-scale reservoir compartmentalization and the lack of comprehensive modern data within the flysch. Furthermore, only few studies highlight and focus on the impact of diagenesis on the reservoir quality in other sandstone units of the Vienna Basin (e.g., Gier et al., 2008). The two studied legacy wells captured the Greifenstein Fm. equivalent Glauconite Sandstone (GLS, Zistersdorf unit) in the flysch of the Vienna Basin. Production from the 1. and 2. GLS (Paleogene) and the 3. GLS (Upper Cretaceous) are restricted to the footwall of the Steinberg Fault and hanging wall of the Hochleiten-Pirawarth faults (cf. Sachsenhofer et al., 2025 and references therein). The dominant hydrocarbon source rocks in the Vienna Basin are mudstones from the autochthonous Malmian Mikulov Fm. (e.g., Rupprecht et al., 2017; Sachsenhofer et al., 2025). The marly limestones from the Falkenstein Fm., which show a thickness of more than 1 km and overlie the crystalline rocks of the Bohemian Massif, and the Middle Jurassic Gresten Group additionally show source potential (Piller et al., 1996; Rupprecht, 2017; Rupprecht et al., 2017; Schicker et al., 2021; Sachsenhofer et al., 2025). The flysch reservoir is sealed by interlayering mudstones and overlain by the Miocene reservoir formation (Sachsenhofer et al., 2025). Hydrocarbon migration is interpreted as pre-Miocene to Miocene, and likely follows basal flysch overthrusts (Rupprecht, 2017). The Malmian Mikulov Fm. may also host a significant shale gas/shale oil potential besides the important role for conventional oil and gas (Schulz et al., 2010).

Generally, the flysch in the Vienna Basin represents a sandstone reservoir rock with poor matrix porosities which can only locally reach up to a maximum of 15% porosity and with generally low matrix permeabilities, often below 0.1 mD (Möbius et al., 2023). Reduced permeability values are interpreted due to quartz cementation and glauconitic clay mineral content (Sauer et al., 1992). Predictive and reliable controls on reservoir quality are not established. This leads to a challenge for well planning, as finding high reservoir quality intervals with open or partially sealed fractures, which can only partially be resolved by seismic data, is complex (Möbius et al., 2023). As the reservoir contains stacked producing intervals with thicknesses from 5 to 20 m (Fig. 4.2b) distributed along the wellbore and core runs do not exceed 20 m, they are unlikely to allow the study of reservoir quality

controls. However, as cuttings are continuously sampled along the whole well (Fig. 4.2b), the assessment may unlock a better understanding of the distribution of producing and non-producing intervals.

4.4 Materials and methods

For this study eighty-three cutting samples covering an interval of ~400 m stratigraphy were collected from two wells targeting the Paleocene-Eocene Glauconite Sandstone (GLS, Greifenstein Fm. equivalent) of the Vienna Basin. Well 1 covers 22 samples from the 1. GLS (depth: 1190–1235 m) and 2. GLS (depth: 1275–1295 m) covering a total depth range of 105 m. Well 2 covers 61 samples from the 1. GLS (depth: 930–995 m), 2. GLS (depth: 1035–1095 m), and 3. GLS (depth: 1100–1270 m) covering a total depth range of 340 m. The lateral distance of the two wells is less than 1 km. Cuttings in the present wells were regularly sampled (every 2.5, 5, or 7.5 m), however, the provided cutting samples are not representing a single depth, but likely represent a depth interval. Here, we interpreted the cuttings to represent an average rock composition of the respective 2.5, 5, or 7.5 m interval, (for specific depths, see digital appendix – chapter 4). This accounts for the possible mixing of cutting material happening during the drilling process, therefore the described cuttings are treated as average composition for a well section as also noticed by e.g., Traineau et al. (1991). Furthermore, claystones/mudstones and soft siltstones can be disaggregated and fine sand can be entrained in the drilling mud.

The provided samples of rock chips are between 25 g and 50 g. The samples were placed into a plastic cup, cleaned with tap water, then placed into an ultrasonic bath for maximum durations of 30 s in order to remove residual drilling mud. No disaggregation of cuttings or removal of depositional clay mineral matrix was observed when compared with thin section samples from core material. In addition to remaining drilling mud residue, this step removed metal shavings as well as wood remnants from the wooden storage boxes. As all cutting samples were equally cleaned using this process, petrographic and geochemical data are comparable within this dataset. The cleaned cuttings were dried in a vacuum-oven at 40 °C until for at least three to four days until weight constancy was achieved. Samples are subsequently documented photographically using an Optika SZN-4 binocular microscope with a mounted Jenoptik Progres Gryphax Subra camera (Fig. 4.3).

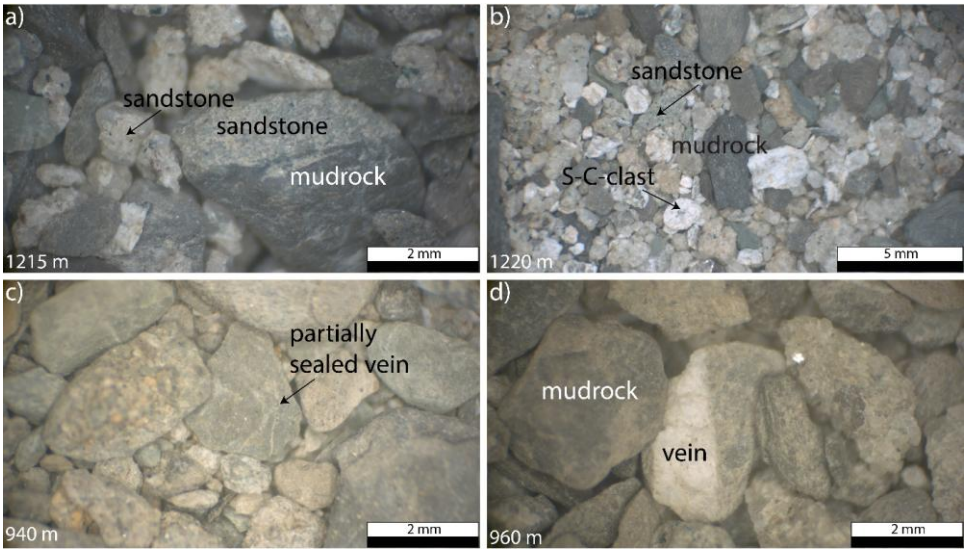

Figure 4.3 Photographs of individual cuttings from well 1 & 2. a) Fine grained sandstone-mudrock transition (well 1, depth 1215 m), b) Sandstone and mudrock cuttings with white ground-up host rock clasts showing S-C-shear structure (S-C-clast) in thin sections (well 1, depth 1220 m). c) Partially sealed vein in mudrock cutting (well 2, depth 940 m). d) Mudrock and sandstone cuttings with a vein penetrating a cutting (well 2, depth 960 m).

4.4.1 Portable X-ray fluorescence (pXRF) and gamma ray (GR) well log

Elemental concentrations of drill cuttings were determined using a Bruker S1Titan800 pXRF operating with an electric power of 4 W, an electric current of max. 200 µA, and a voltage of max. 50 kV in GeoExploration mode, which can measure elements from Mg to U. The device is composed of a Rh-target X-ray tube, an Ultralene window and a Graphene window silicon drift detector. As pXRF measurements are non-destructive, they are preferred for the analyses of small amounts of samples, which should also be studied petrographically. The reproducibility using standards delivered with the pXRF device is shown by Quandt et al. (2024).

The bulk rock geochemistry measurements were performed on 83 rock cutting samples after cleaning and drying but before selecting cuttings for petrographic analyses. The rock chips were placed in a ceramic bowl for measurement. Each sample was measured three times for 20 seconds (cf. Quandt et al., 2024). Concentrations of Si, Al, Fe, Ca, K, S, Ti, Mn, Sr, Zr, Ba, Ni, Cu, Zn, Rb, Y, Nb and Pb were measured in this study. Element

concentrations showing an average for the individual well below 0.01 wt% are classified as trace elements. For comparison with the gamma ray well log trends, the Si/Al ratio is determined from the pXRF measurements (see Craigie, 2018). As the provided cutting samples are mostly taken in a 5 m interval, the provided gamma ray log data provided by the operator was also averaged (arithmetic mean) over 5 m intervals to better compare it to the average rock compositions. Where the gamma ray value is increasing, a decrease in the Si/Al value is expected, and vice versa.

4.4.2 Petrography

Sandstone cuttings were picked from the bulk cutting samples using the binocular microscope for subsequent thin section preparation and further diagenetic studies and the assessment of optical porosity. Different sizes of cuttings were combined to reflect the distribution of each sample bag. In addition, sandstone and mudstone cuttings containing veins and individual vein fragments were preferentially sampled to enable studying the vein paragenesis and fracture porosity of the fractured sandstone reservoir. Fracture porosity is restricted to intragranular fractures, as these are also observed in thin sections from core material. Whereas most uncemented intergranular fractures are interpreted to be induced by drilling, as they are absent in thin sections from core material. The selected drill cuttings were then embedded in blue-dyed epoxy to enable the optical determination of porosity and were prepared to a thickness of 30 µm thickness for thin section analysis. Of total eighthy-three thin sections prepared, sixty-nine were stained with Alizarin Red S and potassium ferricyanide in 0.3% HCl to distinguish different carbonate phases according to Dickson (1965) and covered with a glass cover slip. Therefore, calcite stain pale pink to red, ferroan calcite royal blue to purple or mauve, ferroan dolomite pale to deep turquoise whereas dolomite remain colorless (Dickson, 1965). Additional fourteen further thin sections were polished and analyzed using cold cathode cathodoluminescence (CITL CL8200 Mk5-2 Optical Cathodoluminescence System mounted on a Leica DIALUX 20 ES) (e.g., Monsees et al., 2020) at an acceleration voltage of 10.3 kV and a current of 325 µA. The luminescence of carbonates is influenced by the amount of Mn or Fe (Budd et al., 2000). A bright orange luminescence is mostly related to Mn-enrichment, whereas a darker luminescence may indicate a higher amount of Fe (Budd et al., 2000).

Grain sizes were analyzed on each thin section from sandstone cuttings using thin section microphotographs and ImageJ. Therefore, a grid adjusted to the maximum grain size of each sample was applied to the images and the long axes of at least 100 grains in each sample were measured to obtain area-weighted results (e.g., Busch et al., 2018). The arithmetic mean is given as the grain size per sample. Grain size thresholds are taken from Folk (1980) with size classes after Wentworth (1922). Sorting was calculated according to Folk and Ward (1957). Rock composition was analyzed using a semi-automatic Pelcon point

counting stage installed on a Leica DMLP transmitted light microscope. For each sample, 300 points were counted with a step-length adjusted to the maximum grain sizes (digital appendix – chapter 4) (e.g., Quandt et al., 2024). The point counting only covers the cuttings, whereas the blue dyed epoxy resin and non-sandstone grains in between sandstone cuttings mounted on the same slide are skipped. Point counted categories are based on the Touchstone™ point counting scheme (Busch et al., 2018). The differentiation between glauconite "sensu stricto" and other glauconitic minerals (Odin and Fullagar, 1988) is not possible using transmitted light microscopy. Therefore, the term glauconite to describe most likely detrital green grains showing different shaped pellets, but the same interference color under crossed polarizers is used here. Glauconite can have several origins and the genesis of glauconite is still under debate (e.g., Triplehorn, 1966; Odin and Fullagar, 1988; López-Quirós et al., 2020; Wilmsen et al., 2024). From point counts detrital quartz (Q), feldspar (F) and rock fragments (R) were normalized and plotted in the QFR diagram after Folk (1980). However, as an individual thin section made from cuttings may contain sandstone cuttings of different rock types, the presented QFR compositions may not accurately represent individual beds, but changes along the studied well sections may still be assessed. Optical porosity was obtained from point counting and differentiated in intergranular, intragranular porosity (in K-feldspar, carbonate or undifferentiated rock fragments), and fracture porosity. Microporosity present in e.g., clay minerals and chlorite cannot be point counted using transmitted light microscopy (e.g., Nadeau and Hurst, 1991). The intergranular volume (IGV) was calculated based on point counting results and represents the sum of intergranular pore space ($P_{intergranular}$), depositional clay mineral matrix ($M_{depositional}$), and intergranular cements ($C_{intergranular}$) and indicates the degree of compaction (Paxton et al., 2002). Similar to the QFR composition, derived IGV do not represent individual rock types, but may show variation along the studied well sections.

4.5 Results

4.5.1 pXRF

The main geochemical elements for well 1 and well 2 are Si (avg.: 22.87 wt% and 14.59 wt%), Al (avg.: 4.27 wt% and 2.36 wt%), Ca (1.71 wt% and 2.14 wt%), K (avg.: 0.97 wt% and 0.82 wt%), and Fe (avg.: 1.87 wt% and 1.51 wt%) (Fig. 4.4). Trace elements for both wells are S, Ti, Mn, Sr, Zr, Ba, Ni, Cu, Zn, Rb, Y, Nb, and Pb (digital appendix – chapter 4). Si contents in well 1 are higher than in well 2 (Fig. 4.4a), whereas the other elements do not show any trend within well depth and GLS subdivision. Only within a section from 1160 to 1210 m higher Ca contents are recorded in the 3. GLS of well 2, related to higher contents of carbonate rock fragments and calcitic bioclasts (Fig. 4.4d).

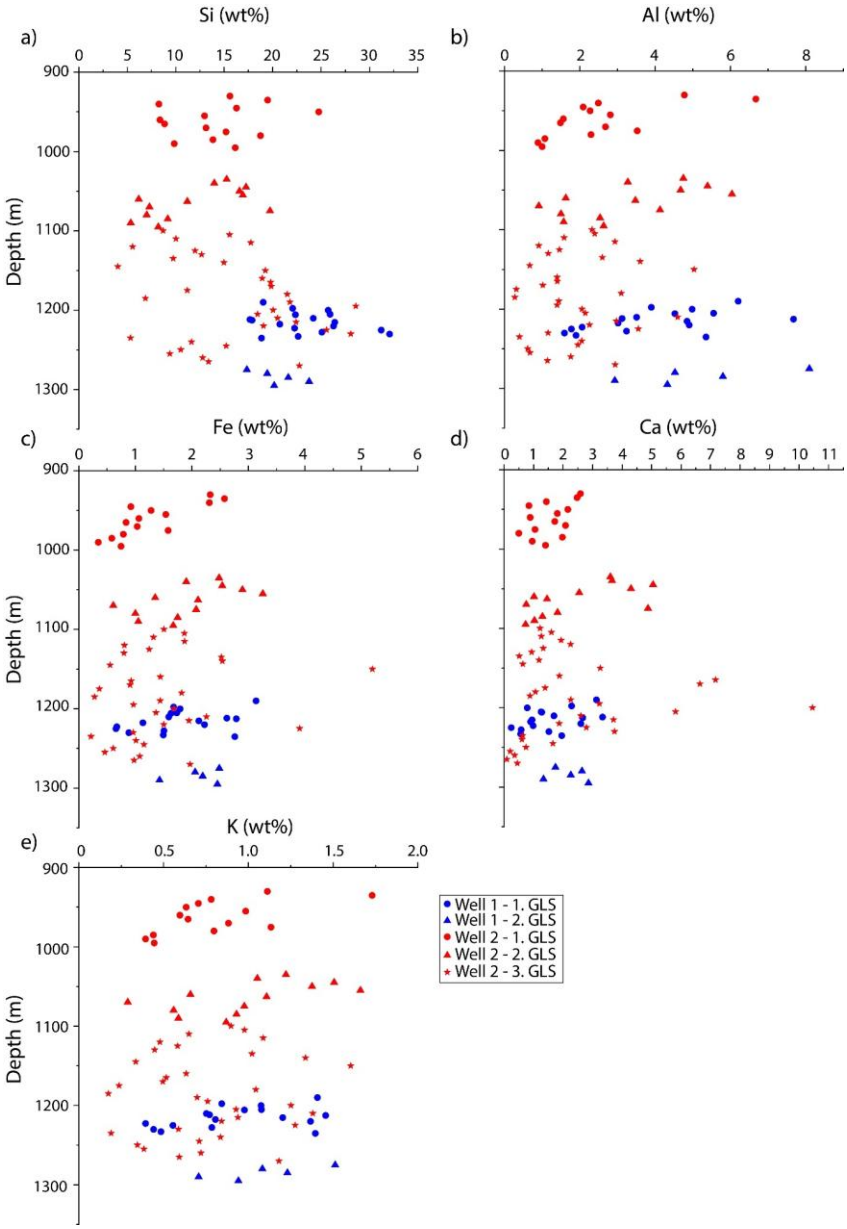

Figure 4.4 The main geochemical components. For well 1 (blue) and well 2 (red) the main geochemical components are a) Si, b) Al, c) Fe, d) Ca, and e) K. The samples cover different GLS, which are shown as circles (1. GLS), triangles (2. GLS) and stars (3. GLS).

4.5.2 Borehole gamma ray data and correlation to Si/Al bulk rock ratio

The provided gamma ray data for well 1 originate from well depth 1185 m–1295 m and range between 42 API to 143 API. The data for well 2 originate from well depth 900 m–1241 m and range between 45 API to 166 API. The 5 m-averages (arithmetic mean) for the gamma ray log from well 1 range from 55 API to 137 API, and for well 2 from 68 API to 138 API. The Si/Al ratio for well 1 vary between 2.1 and 20.1, and for well 2 between 2.8 and 35.3. Both, GR and Si/Al data vary with well depth. On average, higher Si/Al ratios and lower GR values are found in the 1. and 3. GLS and lower Si/Al showing higher GR values in the 2. GLS (Fig. 4.5). Generally, the shape of GR and Si/Al ratio curves are comparable, however, individual sections do not show the same relation between GR and Si/Al ratio.

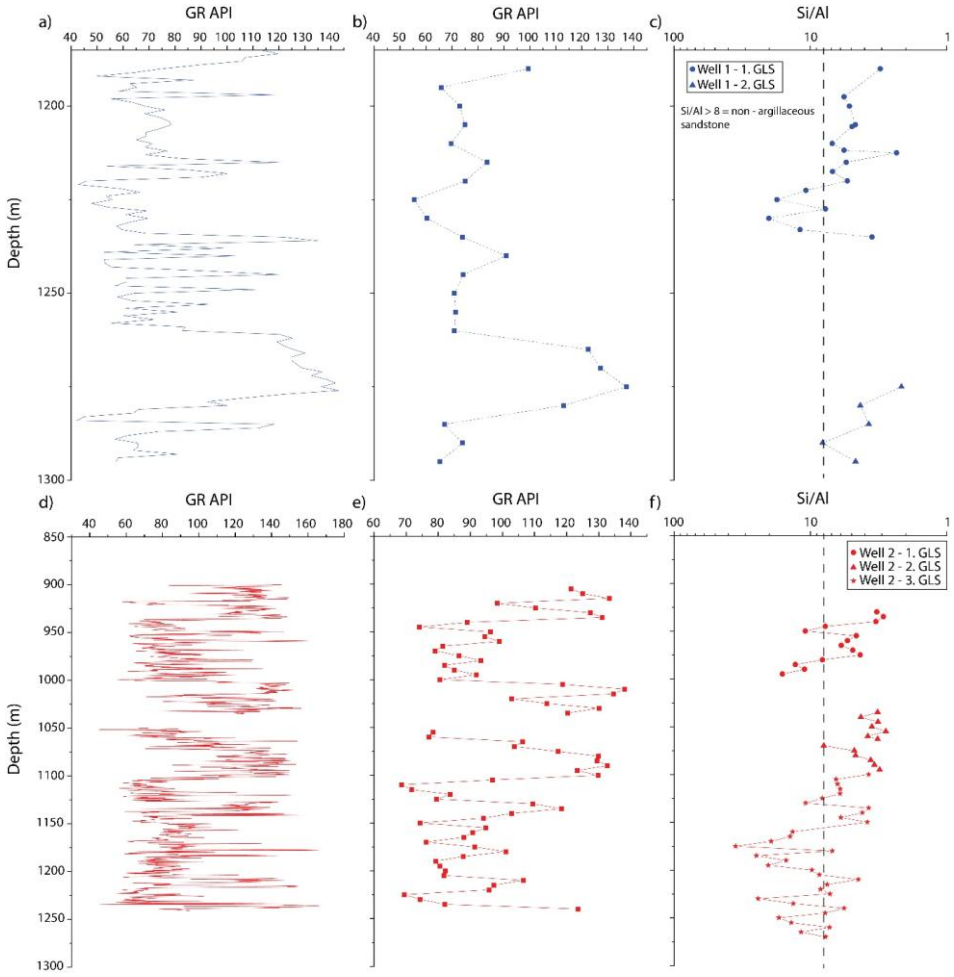

Figure 4.5 Gamma Ray well log and Si/Al ratio. Log GR data in API for well 1 (a) and well 2 (d), arithmetic mean of GR data in API in 5-meter intervals for well 1 (b) and well 2 (e), and Si/Al ratio observed from bulk drill cuttings from well 1 (c) and well 2 (f). Note that the Si/Al axis is inverted to more easily compare trends, circles represent samples from 1. GLS, triangles 2. GLS, and stars 3. GLS. Si/Al values of > 8 in c) and f) are indicative for non-argillaceous sandstones (dashed line as sandstone cut off) after Craigie (2018).

4.5.3 Petrography

4.5.3.1 Grain size and sorting

For well 1, the mean grain size ranges between 0.101 mm and 0.245 mm (very fine to fine sand) and for well 2 from 0.085 mm to 0.233 mm (very fine to fine sand). Whereas no difference is visible between the 1. and 2. GLS for well 1, the 2. GLS in well 2 shows on average finer grain sizes than the 1. and 3. GLS (Fig. 4.6a). Sorting coefficients after Folk and Ward (1957) for well 1 ranges between 0.78 and 1.53 (moderately sorted to poorly sorted), and no difference between the 1. and 2. GLS is seen. Sorting for well 2 ranges between 0.53 and 1.23 (moderately well sorted to poorly sorted), where the 2. GLS show on average a slightly better sorting than the 1. and 3. GLS (Fig. 4.6b). Samples from well 2 also include material from thin intercalated sand bodies in the finer-grained 2. GLS (indicated by higher GR values in Fig. 4.5d), resulting in generally better sorting and finer grain sizes. Samples from the 2. GLS of well 1 are mostly taken in a coarse-grained section below a finer grained interval (indicated by lower GR in Fig. 4.5a).

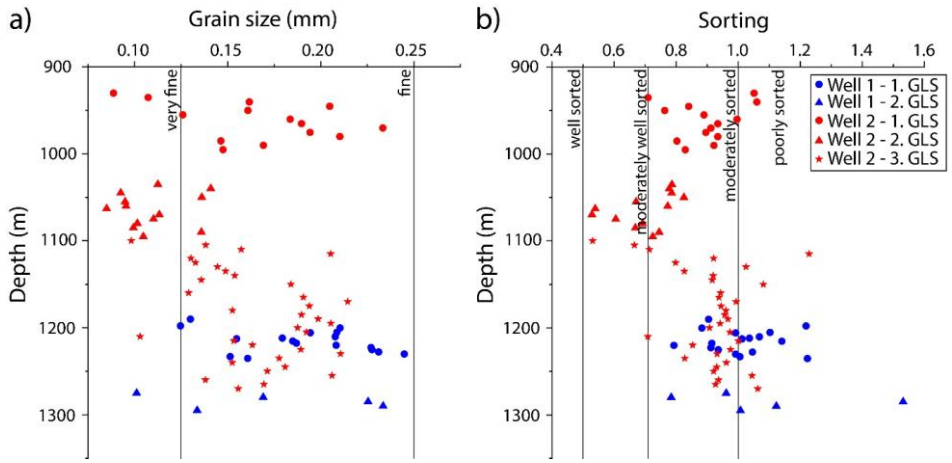

Figure 4.6 Grain size and sorting distribution. Cross plot of a) mean grain size and b) sorting versus well depth for well 1 (blue) and well 2 (red). The 1. GLS is indicated by circles, the 2. GLS by triangles, and the 3. GLS by stars. a) Grain sizes for both wells vary between very fine- and fine-grained sand, whereas the top interval between 930-995 m (1. GLS) and the bottom area (1100–1270 m) (3. GLS) comprises on average larger grain sizes than the middle interval (2. GLS) between 1035 and 1100 m. b) Sorting for both wells vary between moderately well sorted and poorly sorted. The middle (2. GLS) interval for well 2 shows on average the best sorting (1035–1100 m).

4.5.3.2 Detrital Components

Well 1

The main detrital components are quartz grains (47.3%–80.7%), K-feldspar (0.3%–10.0%), and glauconite (0.3%–4.3%) (Fig. 4.7a). Other detrital components are plagioclase (0.0%–0.3%), muscovite (0.0%–3.0%), biotite (0.0%–3.0%), brownish and greenish chlorite flakes (0.3%–2.0%), mudrock fragments (RF) (0.0%–5.3%), siltstone RF (0.0%–2.7%), sandstone RF (0.0%–2.3%), siderite grains (0.0%–1.7%), calcitic RF and foraminifera (0.0%–1.7%), ferroan calcitic RF and foraminifera (0.0%–0.3%), chert (0.0%–3.0%), phyllite (0.0%–0.7%), undifferentiated ductile RF (0.0%–0.7%), metamorphic RF (0.0%–0.7%), and quartzite (0.0%–0.3%). Detrital clay minerals are glauconite rims (0.0%–3.3%), pore-lining illite (0.0%–1.0%), and pore-filling illite (0.0%–0.7%). Accessories are rutile (0.0%–0.7%), zircon (0.0%–1.0%), tourmaline (0.0%–0.3%), phosphate grains (0.0%–0.3%), iron oxide grains (0.0%–0.7%), and undifferentiated opaque phases (0.0%–0.7%).

Well 2

The most abundant detrital components are quartz grains (37.7%–73.3%), K-feldspar (1.3%–8.0%), and glauconite (0.7%–11.7%) (Fig. 4.7b). Other detrital components are plagioclase (0.0%–1.7%), muscovite (0.0%–3.0%) (Fig. 4.7c), biotite (0.0%–2.3%), brownish and greenish chlorite flakes (0.0%–1.3%), mudrock RF (0.0%–15.7%), siltstone RF (0.0%–0.7%), sandstone RF (0.0%–0.7%), siderite grains (0.0%–3.0%) (Fig. 4.7c), calcitic RF and foraminifera (0.0%–3.7%), ferroan calcitic RF and foraminifera (0.0%–3.3%) (Fig. 4.7d), chert (0.0%–2.0%), phyllite (0.0%–3.0%), plutonic RF (0.0%–0.7%), undifferentiated ductile RF (0.0%–1.7%), metamorphic RF (0.0%–2.3%), volcanic RF (0.0%–0.3%), and quartzite (0.0%–2.0%). Detrital clay minerals are mainly chlorite (0.0%–5.7%), glauconite rims (0.0%–3.7%) and pore-lining illite (0.0%–2.7%), and pore-filling illite (0.0%–1.0%). Accessories are rutile (0.0%–1.3%), zircon (0.0%–0.7%), tourmaline (0.0%–0.3%), phosphate grains (0.0%–2.0%), iron oxide grains (0.0%–1.3%), and undifferentiated opaque phases (0.0%–0.7%).

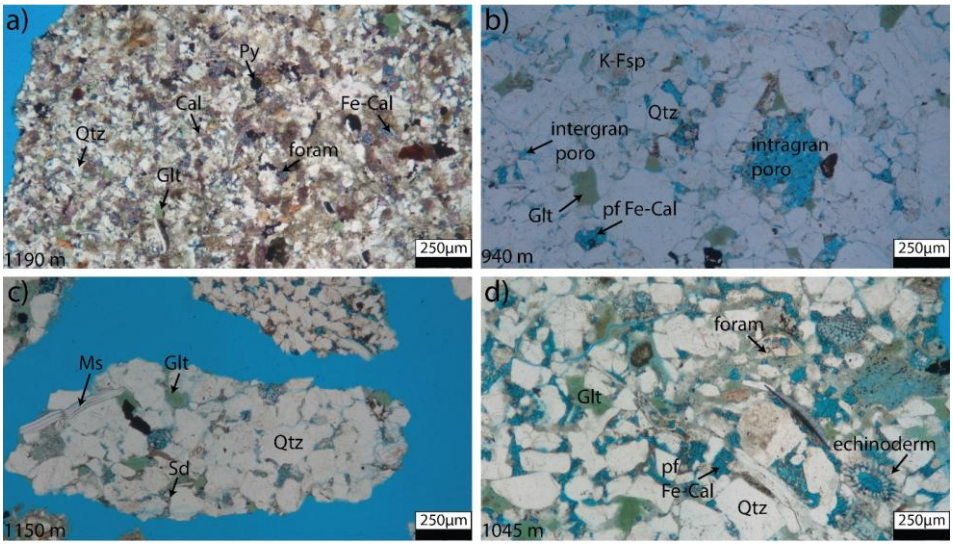

Figure 4.7 Thin section microphotographs of individual cuttings from well 1 and well 2 from different depths. a) Well 1 (depth 1190 m), individual sandstone cuttings show smaller grain sizes and are composed of e.g., detrital quartz (Qtz), foraminifera (foram) with calcitic tests (Cal), glauconite (Glt), and inter- and intragranular ferroan calcite cements (Fe-Cal). b) Well 2 (depth 940 m), intragranular porosity (intragran poro) in former feldspar and intergranular (intergran poro) porosity is visible as optical porosity. Besides detrital quartz, glauconite and feldspar occur, as well as pore-filling (pf) Fe-Cal. c) Well 2 (depth 1150 m), siderite (Sd), quartz grains, glauconite occurs as well as muscovite (Ms). d) Well 2 (depth 1045 m), some individual cuttings are rich in bioclasts, e.g., foraminifera and echinoderm fragments. Ferroan calcite cements (Fe-Cal) fills former pores in bioclasts (e.g., echinoderm fragments).

4.5.3.3 Rock composition

The most prominent rock types for well 1 are sublitharenites and subarkose, and subordinately quartzarenites and lithic arkose (Fig. 4.8). The normalized quartz content varies between 74.3% and 95.3%, feldspar between 0.5% and 13.7% and rock fragments between 0.4% and 15.7%. For well 2 the most prominent rock types are sublitharenites, feldspathic litharenites and subordinately litharenites and subarkose (Fig. 4.8). The normalized quartz content in well 2 varies between 59.8% and 86.7%, feldspar between 2.7% and 15.1% and rock fragments between 5.6% and 30.3%.

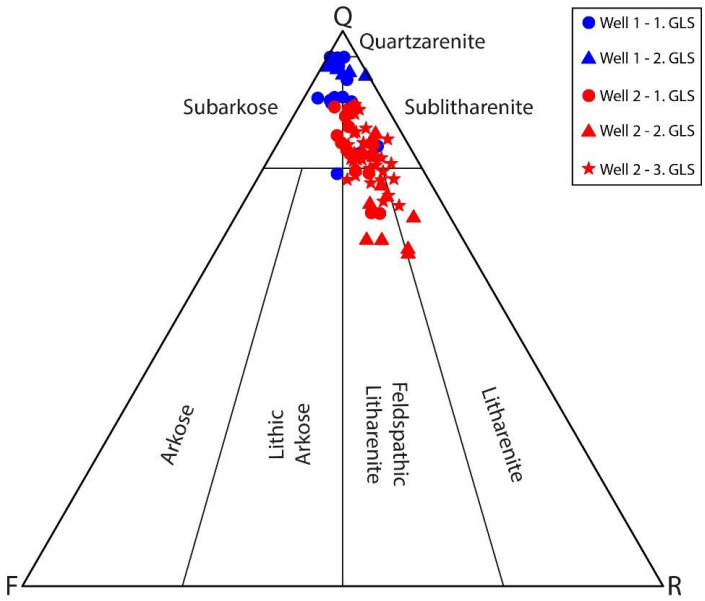

Figure 4.8 Ternary classification for sandstones (Q= quartz, F=feldspar, R=rock fragments, in %) according to Folk (1980) for well 1 (blue) and well 2 (red). Sandstone cuttings are in general quartz rich, showing rock compositions of sublitharenites, subarkose, and subordinate quartzarenites and lithic arkose for well 1, and sublitharenites, feldspathic litharenites and subordinate litharenites and subarkose for well 2.

4.5.3.4 Authigenic phases

Well 1

The most abundant authigenic phases are quartz cement (1.7%–7.0%), blue-stained pore-filling ferroan calcite cement (0.3%–18.3%), and pore-filling siderite cement (0.0%–2.3%). Furthermore, K-feldspar cement (0.0%–0.3%), pore-filling calcite cement (0.0%–2.3%), purple-stained pore-filling ferroan calcite cement (0.0%–1.3%), pore-filling dolomite cement (0.0%–1.0%), pyrite (0.0%–2.0%), kaolinite cement (0.0%–0.7%), and Fe-oxide cement (0.0%–0.3%) occur. Also, partially pore-filling cements as ferroan calcite (0.0%–0.3%), and dolomite (0.0%–0.3%) are present. Vein cements are grouped into calcite veins (0.0%–0.3%), ferroan calcite veins (0.0%–4.7%) and intragranular ferroan calcite veins (0.0%–1.3%). Replacive phases are subdivided into kaolinite replacing muscovite (0.0%–0.3%), kaolinite replacing K-feldspar (0.0%–2.0%), illite replacing kaolinite (0.0%–0.7%), illite replacing K-feldspar (0.0%–1.0%) and Fe-calcite replacing K-feldspar (0.0%–1.3%).

Well 2

Quartz cement is the main authigenic phase (1.3%–11.7%), followed by blue-stained pore-filling ferroan calcite cement (0.3%–24.7%), and pore-filling siderite cement (0.0%–4.3%). Furthermore, K-feldspar cement (0.0%–1.3%), pore-filling calcite cement (0.0%–0.3%), purple-stained pore-filling ferroan calcite cement (0.0%–1.7%), pore-filling dolomite cement (0.0%–1.3%), pyrite (0.0%–1.0%), kaolinite cement (0.0%–1.0%), and Fe-oxide cement (0.0%–1.0%) occur. Also, partially pore-filling cements as purple- and blue-stained ferroan calcite (0.0%–0.7%), partially pore-filling siderite cements (0.0%–1.7%) and dolomite (0.0%–0.3%) are present. Vein cements are calcite veins (0.0%–0.3%), ferroan calcite veins (0.0%–3.3%) and intragranular ferroan calcite veins (0.0%–0.7%). Replacive phases occur as kaolinite replacing muscovite (0.0%–0.7%), kaolinite replacing K-feldspar (0.0%–0.7%), illite replacing kaolinite (0.0%–0.3%), illite replacing K-feldspar (0.0%–1.0%) and Fe-calcite replacing K-feldspar (0.0%–2.0%).

4.5.3.5 Optical porosity

Well 1

Optical porosity is mainly represented by intergranular porosity (0.3%–1.7%) and intragranular porosity (0.0%–1.7%) mainly after K-feldspar dissolution. Additionally, intragranular porosity in undifferentiated RF (0.0%–0.3%), and fracture porosity (0.0%–2.3%) occur.

Well 2

Intergranular porosity (0.0%–2.3%) is the main type of optical porosity (Fig. 4.11d), followed by intragranular porosity in K-feldspar (0.0%–2.3%) (Fig. 4.11g). Additionally, intragranular porosity in carbonate grains (0.0%–0.3%), and in undifferentiated RF (0.0%–1.0%) occurs.

4.5.4 Intergranular volume (IGV)

The IGV for well 1 range from 7.7% to 25.7%, and for well 2 from 9.0% to 31.7%. The IGV shows no correlation to the GLS formation or depth (Fig. 4.9a), and low correlations with detrital quartz and feldspar contents (Fig. 4.9b) for well 1 and 2, showing lower IGV at higher detrital quartz and feldspar contents. A general correlation with sorting (Fig. 4.9c) with well to moderately well sorted samples showing higher median IGV than poorly sorted samples (Fig. 4.9c). Furthermore, a slightly negative correlation between IGV and grain size can be seen in samples from in well 2 (Fig. 4.9d). While only two samples from well 1 fall in the very fine sand category, the overall decrease in IGV with increasing grain

size, based on the median values can still be matched between both wells. The main pore-filling cement types (quartz and carbonates) show different correlations to the IGV. The impact of quartz cement on IGV is only minor (Fig. 4.9e), and more pronounced for pore-filling and partially pore-filling carbonate cements (Fig. 4.9f), especially for well 1 (R^2=0.93).

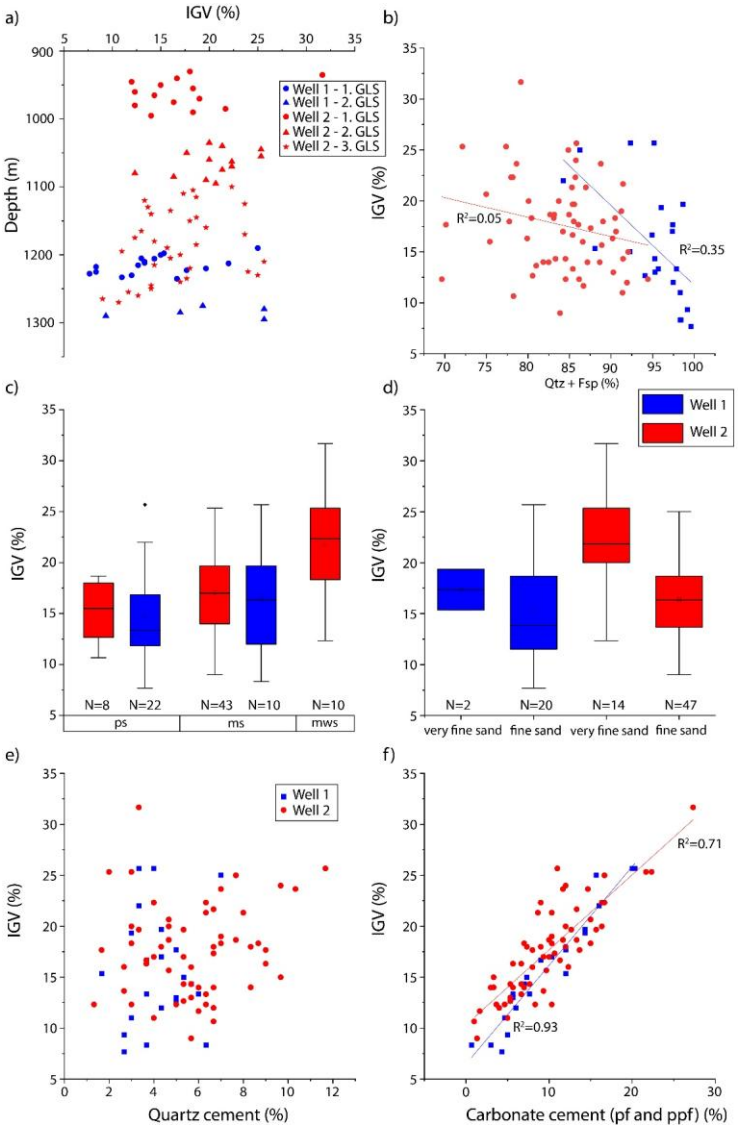

Figure 4.9 (Figure caption on next page)

Figure 4.9 (previous page) IGV cross plots with depth, detrital quartz + feldspar content, sorting, grain size classes, quartz cement and carbonate cements. a) IGV shows no correlation with well depth, nor with the 1., 2. or 3. GLS. b) IGV shows low correlation with detrital quartz and feldspar content for well 1 and 2. c) Overall, better sorting is correlated to higher IGV, whereas moderately well sorted samples from well 2 show highest IGV, ps: poorly sorted, ms: moderately sorted, mws: moderately well sorted. d) Very fine sand grain size class in well 2 shows higher IGV values compared to fine sand. e) IGV shows no correlation with quartz cement. f) IGV versus pore-filling (pf) and partially pore-filling (ppf) carbonate cements with a very high positive correlation for well 1 and a high correlation for well 2.

4.5.5 Correlation of grain size, sorting, and glauconite content

Grain size and sorting show a positive correlation for well 2, but not for well 1 (Fig. 4.10a). The glauconite content varies with well depth and shows a positive correlation for well 2, but no correlation for well 1 (Fig. 4.10b). However, the glauconite content in well 2 is especially elevated in the 3. GLS (stars in Fig. 4.10b), which was not sampled in well 1. The glauconite content in the 1. and 2. GLS of wells 1 and 2 is comparable.

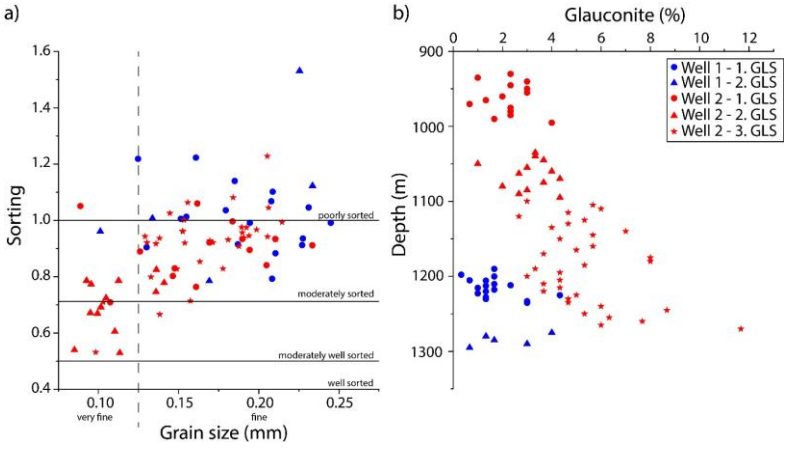

Figure 4.10 Sorting vs. grain size and glauconite content vs. depth cross plots. a) Sorting after Folk and Ward (1957) and grain size after Wentworth (1922) in Folk (1980) show a positive correlation for well 2 (red), whereas well 1 (blue) shows no correlation. The different GLS intervals are given in circles (1. GLS), triangles (2. GLS) and stars (3. GLS). b) The glauconite content obtained from point counting shows elevated glauconite contents in the 3. GLS as opposed to the 1. and 2. GLS in well 2.

4.5.6 Paragenetic relationships

As the paragenesis and mineralogical composition of individual cuttings in the two observed wells show no large difference, the paragenetic relationships are described together for the studied sections of the GLS in the Vienna Basin Flysch play.

Quartz grains display syntaxial quartz overgrowth cements. Glauconite or chlorite rims which are occasionally present outline grains such as quartz or occur between quartz grains and their syntaxial overgrowths (Fig. 4.11a, b). Beside chlorite and glauconite, pore-lining tangential illite is rarely encasing detrital grains such as quartz. Quartz grains and their syntaxial quartz overgrowths are encased by pore-filling Fe-Cal (stained blue, Fig. 4.11a) if present, which also fills former pores in bioclasts (Fig. 4.7d). The Fe-Cal can also occur partially pore-filling in individual cuttings. Besides the blue-stained (partially) pore-filling Fe-Cal, purple-stained Fe-Cal or calcite (red staining, Fig. 4.7a) pore-filling cements show the same paragenetic relationships as Fe-Cal. The partially pore-filling siderite is present as brownish elongated rhombs with a high relief (Fig. 4.7c, 4.11e), either embedded in chloritic matrix or outlining detrital grains, and occasionally encased in quartz cement. Chlorite and glauconite also fill chambers of foraminifera with calcitic tests. Pyrite occurs as framboidal or cubic aggregates in some cuttings (Fig. 4.7a), in rock fragments or filling individual foraminifera tests and is most prominent in samples rich in limestone rock fragments (Fig. 4.11c). Furthermore, pyrite occurs at the host rock-vein interface in one sample (Fig. 4.11j). Intergranular Fe-oxide cements occur only rarely, showing a red color at the rim of opaque grains. In some individual cuttings feldspar grains, feldspar cement and/or intragranular feldspar dissolution can also be observed, the latter resulting in intragranular porosity (Fig, 7b). In some samples the intragranular dissolution pores from K-feldspar (K-Fsp) grains are filled by replacive Fe-Cal cement (Fig. 4.11f), but these uncompacted intragranular pores can locally be filled with kaolinite, showing a vermicular structure (Fig 11g). However, individual open intragranular pores are also noted within K-Fsp and undifferentiated RF. Besides the replacement of K-Fsp, kaolinite replaces muscovite in individual cuttings, and can also occur as cement filling intergranular pores. Illite replaces individual kaolinite particles or K-Fsp grains.

Based on optical evaluations, different fracture and vein generations are identified. In general, the veins are of calcitic or Fe-calcitic composition and can also occur as trans- or intragranular veins (Fig. 4.11c). Some of the Fe-calcitic veins are not only stained blue, but also purple. Additionally, blue-stained partially sealed veins occur (Fig. 4.11i). The veins will be further evaluated in the next section.

Cataclastic shear bands composed of small, angular, and densely packed quartz grain fragments, preserving little to no optical porosity (Fig. 4.12a, b), are found only rarely within individual cutting fragments of both wells, and some of them are crosscut by carbonate

veins (Fig. 4.12c). The shear bands do not show intergranular carbonate cement and are devoid of deformed glauconite grains (Fig. 4.12a, b). In contrary, artificial cataclastic fragments show high optical porosity and parallel fracturing within grains in all studied cutting samples (Fig. 4.12d). They are prominently visible as white cutting fragments (S-C clast in Fig. 4.3b). Here, the cataclastic zone contains ground-up intergranular ferroan calcitic cements and deformed glauconite grains.

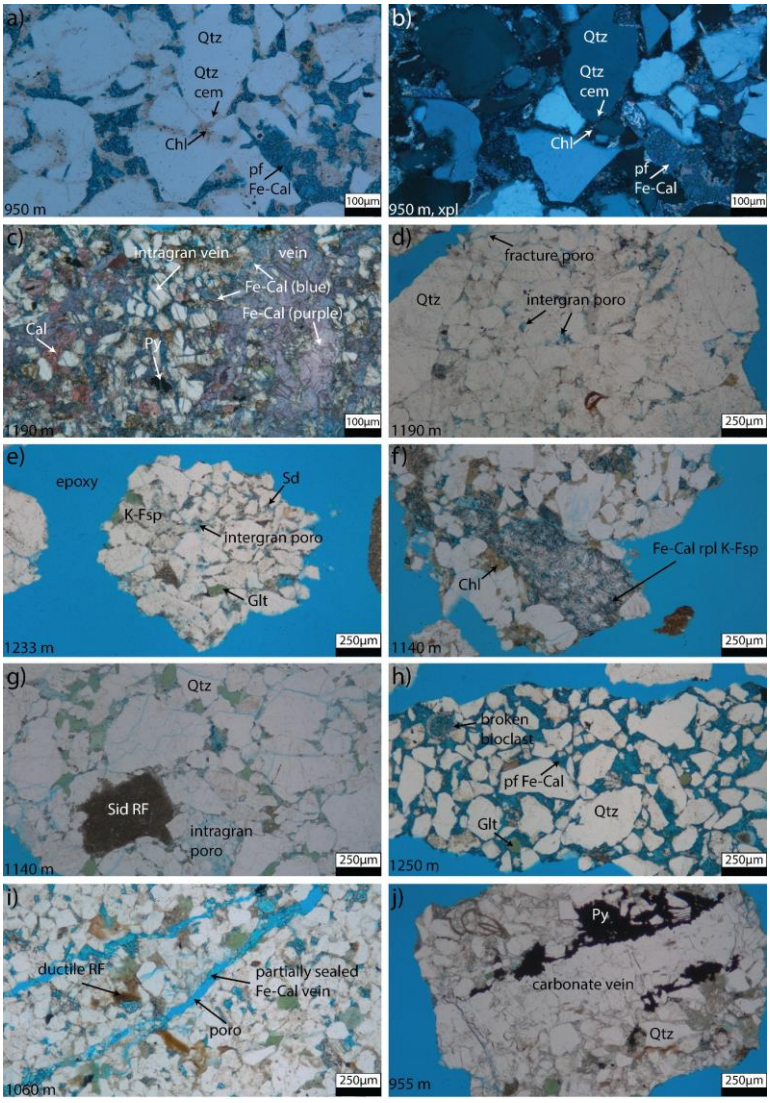

Figure 4.11 (Figure caption on next page)

Figure 4.11 (previous page) Photomicrographs showing mineralogical and structural elements. a) Quartz grains (Qtz) and quartz cement (Qtz cem) with grain lining chlorite (Chl), and crossed-polarized in b) (well 2, 950 m). c) Well 1 (1190 m), individual cuttings, containing calcite grains (Cal, stained red) are cemented by pore-filling ferroan calcite (Fe-Cal, stained blue). Veins are either composed of blue Fe-Cal or purple Fe-Cal. The veins outlining or penetrating grains as well as forming intragranular veins (intragran vein) in detrital grains such as quartz. d) Individual cuttings show carbonate veins with pyrite (Py) at the transition to the host rock (well 2, 955 m). e) Siderite (Sd) occurs as single crystals filling intergranular pores (well 1, 1233 m). f) Detrital quartz is enclosed by brownish chlorite, which is encased by pore-filling Fe-Cal (blue) and also replaces K-feldspar (K-Fsp) (well 2, 1140 m). g) Detrital siderite grain (Sid RF). The dissolution of K-Fsp leads to the formation of intragranular porosity (intragran poro) (well 2, 1140 m). h) Sandstone cutting with detrital quartz grains, pore-filling ferroan calcite cements, glauconite and broken bioclasts (well 1, 1250 m). i) Completely cemented and partially sealed veins with Fe-Cal in cutting fragment containing ductile RF (well 2, 1060 m). j) Individual cuttings contain carbonate veins with pyrite at the transition to the host rock (well 2, 955 m).

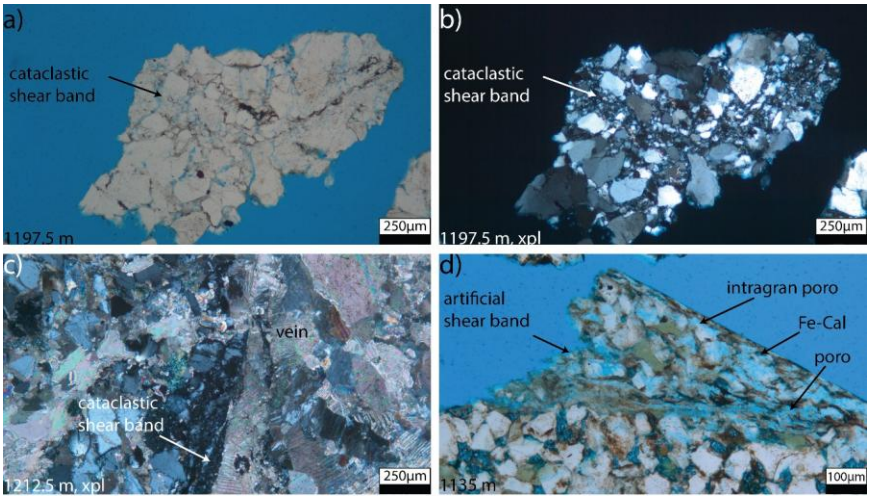

Figure 4.12 Cataclastic shear bands in individual cuttings. Natural cataclastic shear band a), grain rearrangement and angular small grain sizes are more visible under crossed polarizers (b) (well 1, depth 1197.5 m). c) An individual cutting contains a natural cataclastic shear band with angular, densely packed small grains. The shear band is cross cut by a carbonate vein (xpl, well 1, 1212.5 m). d) Artificial shear bands are mostly seen at cutting boundaries, and missing parts of grains (now intragranular porosity, intragran poro), contain ground up Fe-Cal cements, and unsealed, fractured grains around the shear band (well 2, depth 1135 m).

4.5.7 Cold cathodoluminescence

Cathodoluminescence (CL) on polished thin sections show different brightness of luminescence for Fe-Cal cements and Fe-Cal vein generations (Fig. 4.13, 4.14). Furthermore, the luminescence of detrital K-Fsp grains is bright blue, detrital quartz grains show a mostly dark blue luminescence, whereas quartz overgrowth cements are non-luminescent (Fig. 4.13a, d). Siderite shows no luminescence, whereas the interstices are filled with orange luminescent Fe-Cal. Pervasively sealed veins generally show a slightly brighter orange luminescence, whereas the pore-filling cement shows a darker luminescence (Fig. 4.13a), although the differences may be minute (Fig. 4.14). Based on the cross-cutting relationships of the pervasively sealed veins, three generations can be differentiated. The first generation shows a dull luminescence, and is crosscut by the two following generations (Fig. 4.13a, b). The two other generations show a bright and dull luminescence, respectively. The bright luminescing phase is crosscut by the dull luminescing phase in other cutting samples (Fig. 4.14b).

Partially sealed veins show an orange luminescence at the center of rhombic crystals composed of Fe-Cal and a dull rim of Fe-Dol (Fig. 4.13b, c). Intercrystalline porosity is preserved within partially sealed carbonate veins containing euhedral rhombs (Fig. 4.13c). Additionally, some cuttings show formerly fractured quartz grains, which are healed by quartz cement, showing no luminescence (Fig. 4.13d).

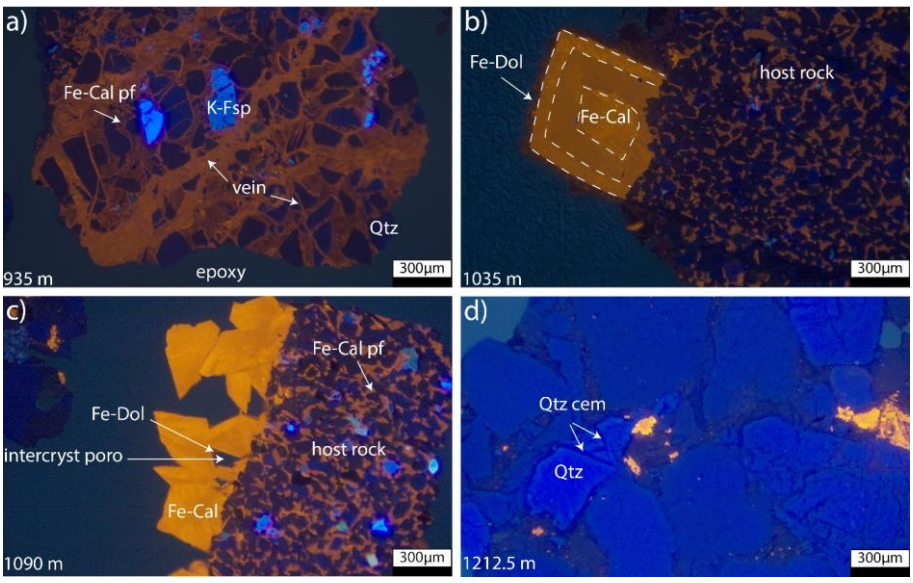

Figure 4.13 (Figure caption on next page)

Figure 4.13 (previous page) Photomicrographs of cold cathodoluminescence showing luminescence properties of detrital and authigenic minerals, and veins for individual drill cuttings from well 1 and well 2. a) Pore-filling (pf) Fe-Cal shows dull luminescence, whereas the veins, penetrating the host rock and individual grains, show a brighter luminescence. Quartz shows a dark blue luminescence and K-feldspar (K-Fsp) bright blue (well 2, depth 935 m). b) Euhedral shaped carbonate crystal with zonation, showing a bright center, followed by a less bright zone, and a dull Fe-Dol rim. The host rock cement luminescence is less bright than the vein. The euhedral crystal shape and absence of pervasive cements indicates a partially sealed vein (well 2, depth 1035 m). c) The partially sealed vein with euhedral crystal facets shows a brighter luminescence than the pore-filling cement in the host rock. Also, the euhedral shape preserves intercrystalline porosity (intercryst poro), and they are encased by a dull Fe-Dol phase (well 2, depth 1090 m). d) Fractured and cemented quartz grains showing no luminescence quartz cement (well 1, depth 1215.5 m).

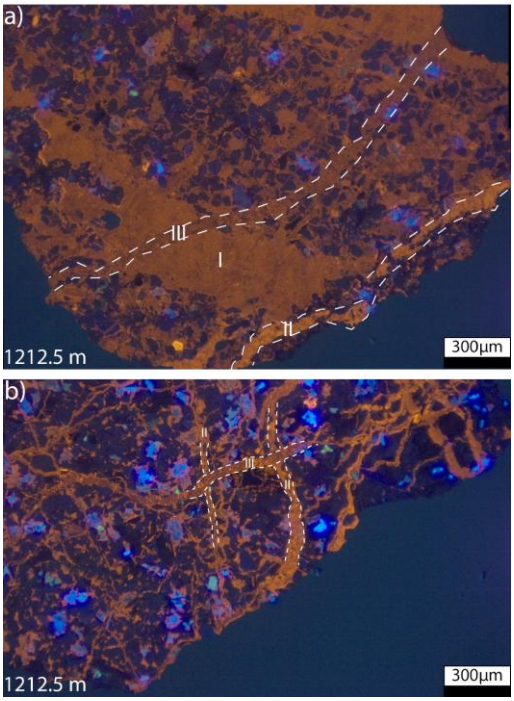

Figure 4.14 CL photomicrograph highlighting vein generations. a), b) CL photomicrograph showing three generations of sealed veins crosscutting each other of an individual cutting (well 1, 1212.5 m). a) The different generations (I, II, III) are distinguished using the CL luminescence color, indicating a slightly change of Mn and Fe-contents. b) Crosscutting relation of vein generation II and III.

4.5.8 Bulk drill cutting pXRF comparison to petrography

Iron and magnesium contents obtained from bulk drill cuttings pXRF may suggest a generally positive relation with the sum of the mostly ferroan calcitic carbonate cements including veins (Fig. 4.15a) and with minerals containing iron (glauconite, Fe-calcite, siderite, pyrite, opaques, Fe-oxides, mudrock RF, biotite, and chlorite) (Fig. 4.15b) obtained from point counting. While R^2 values are moderate to low (R^2 from 0.2–0.4) for the correlation of Fe+Mg contents with both mineral contents, median values of Fe+Mg contents increase with increase in carbonate cement (incl. veins) and Fe-bearing mineral contents.

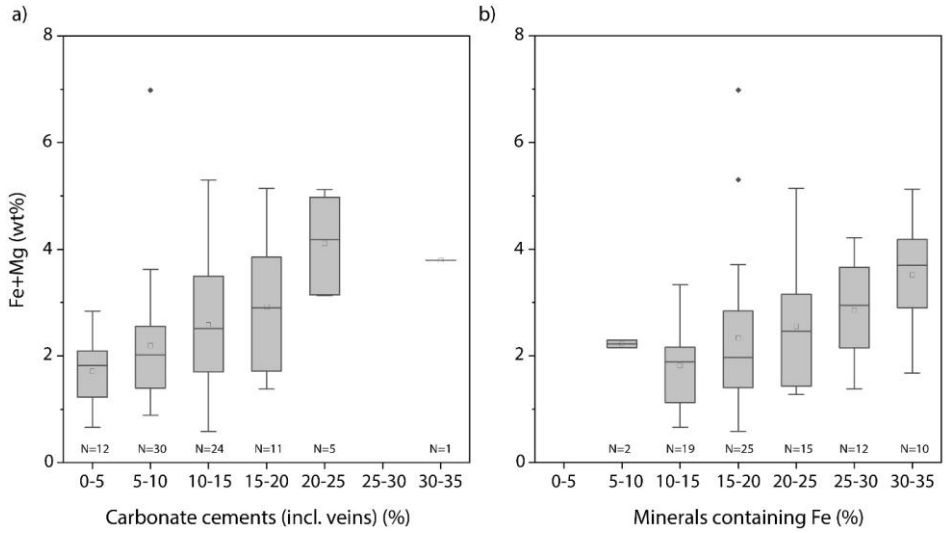

Figure 4.15 Box-and-whisker bars plotted for bulk drill cuttings pXRF and petrographic point-counting results, combined for both wells. Iron (Fe) plus magnesium (Mg) content (wt%) is in general higher in samples with higher amount of a) carbonate cements (incl. veins) and b) minerals containing Fe.

4.5.9 Correlation to production data

To find potential proxies for production intervals from drill cuttings, several properties and results were compared with known producing and non-producing intervals for both wells. Based on the overlap of interquartile ranges (IQR, P25 to P75) we decide between distinctly different and indifferent properties. Therefore, the IQRs of either producing and non-producing intervals should not overlap with each other for more than 25% (50% of the IQR). Producing intervals show lower Fe+Mg ratios, lower optical porosity, and contain more

total vein cements (Fig. 4.16b, e, f). The Si/Al content observed from pXRF, the Ca/Mn, and total carbonate cement content including veins for producing and non-producing intervals are largely overlapping and may therefore not be good criteria to assess the producibility of prospective intervals (Fig. 4.16a, c, d).

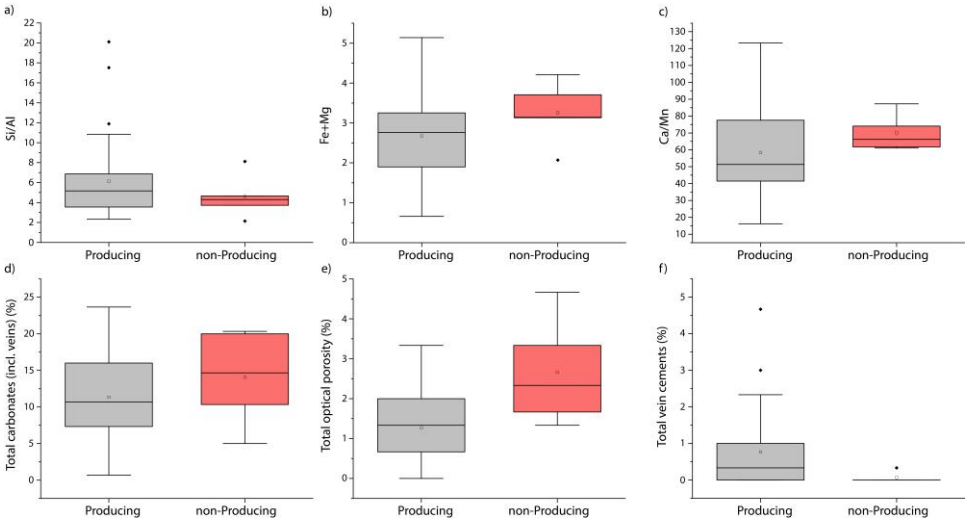

Figure 4.16 Box-and-whisker bars plotted for geochemical data (a-c) derived from pXRF, and petrographic data (d-f) obtained from point counting, and producing (grey)/non-producing (red) intervals for well 1 and well 2 (N=42). The producing interval has on average lower Fe+Mg content (b), lower optical porosity (e), and higher amount of total vein contents (f). But properties like Si/Al (a), Ca/Mn ratio (c), and the total carbonates including veins (d) are overlapping and cannot be used to distinguish between producing and non-producing intervals for the two wells.

4.6 Discussion

4.6.1 GR and pXRF

The 1. to 3. GLS are composed of roughly 70% of massive sandstone beds of proximal turbidites (Rammel, 1989). The comparison between the geochemical fingerprint i.e. lower Si/Al ratio, obtained from pXRF measurements, fits well with higher GR data in areas of higher clay content (Fig. 4.5). Generally, higher Si/Al ratios (>8) and low GR values are indicative for sandstone (e.g., Rider and Kennedy, 2011; Craigie, 2018). However, the mineralogical composition of the studied sandstones contains K-bearing minerals as

feldspar or mica, K-bearing phyllosilicates such as glauconite and illite, and mudrock RF. This may enhance the amount of potassium, thorium and uranium, leading to overall higher GR signals, even in sandstone-rich sections (e.g., Rider, 1990; Johan and Neil, 2001; Rider and Kennedy, 2011).

A minor shift between the depth ranges of peaks in Si/Al and GR plots is observable in some intervals (Fig. 4.5), which might result from averaging GR data over 5 m intervals to match the sample depth ranges. As the provided bulk cutting samples also contain mudrock fragments, it is not excluded that the mudrock content is underrepresented within the samples as mudrocks are more easily ground up especially along the planar lamination of the mudrocks. This may influence the pXRF measurements, but the impact is interpreted as minor, as the Si/Al ratio is comparable to borehole GR data (Fig. 4.5). For an individual section from 1160 to 1210 m, a higher Ca content is measured and is related to higher contents of carbonate rock fragments and bioclasts observed in microscopic analyses. As log trends can be used to assess stratigraphic properties (Milton and Emery, 1996), their comparison to Si/Al trends may thus enable the cross check if the derived cutting depth interval may be linked to log depth and evaluate the representativeness of cutting composition (i.e. relative proportions of sandstone and mudrock cuttings).

Natural fractures play an important role for reservoir exploration, production and well planning, as they may be the main fluid conduit in tight sandstone reservoirs and many carbonate reservoirs (e.g., Olson et al., 2009; Bahrami et al., 2012; Lamarche et al., 2012; Khelifa et al., 2014; Becker et al., 2018). Care has to be taken when assessing fractures as open, uncemented fractures are not well preserved in cuttings. Thus, their intensity (i.e. number of fractures per meter) and aperture cannot be reconstructed from cuttings, but could be deduced from borehole image logs (e.g., resistivity or acoustic image logs) (e.g., Fernández-Ibáñez et al., 2018) or core material. However, partially sealed veins and their composition may not be visible in image logs e.g., due to uncertainties of log interpretation (Fernández-Ibáñez et al., 2018) and the resolution of the measurements. Consequently, cuttings and petrographic analyses are a way to show if a fracture is partially sealed and with which mineral. The assessment of the amount and locations of partially sealed fractures affects the reservoir development e.g., during acidizing in carbonate-bearing lithologies (Knox and Ripley, 1979). However, depending on the well direction, only certain fracture orientations are observed (Terzaghi, 1965). In the absence of orientated core material, the occurrence of veins and partially sealed veins can be identified from cuttings, by using a binocular microscope (Fig. 4.3) (e.g., Tiainen et al., 2002). Cuttings may therefore still preserve information on vein paragenesis to further constrain the amount and temporal succession of several natural fracturing events.

The pXRF-based Fe+Mg measurements were conducted on bulk drill cutting from respective sample depths, composed of different sandstone and mudrock lithotypes. Carbonate cement in pores and veins is reflected by mostly ferroan calcite, dolomite and siderite in sandstone cuttings. With increasing carbonate cement contents (incl. veins) a general increase in median Fe+Mg contents can be observed (Fig. 4.15a). As carbonate cements are the main pore-filling and vein cement phases, this correlation may be used as a first pass RQ assessment if producing intervals are related to elevated vein cement contents (Fig. 4.16f).

4.6.2 Mineralogy and texture

The two studied wells show a similar mineralogic composition using petrographic tools such as point counting, whereas the quartz-content varies slightly within the wells (higher in well 1, Fig. 4.8) and GLS but is largely comparable for the 1. GLS in both wells (avg. 1. GLS well 1: 67.8%, avg. 1. GLS well 2: 59.6%). However, well 1 also shows higher amount of Si measured with pXRF (Fig. 4.4a), which can explain the higher quartz content of well 1 samples in the QFR plot (Fig. 4.8). The overall rock types (sublitharenites, subarkose, quartzarenites, lithic arkose for well 1, sublitharenites, feldspathic litharenites, litharenites, subarkoses for well 2) are in accordance to rock descriptions by Rammel (1989), analyzing the equivalent sediments from the Wienerwald Flysch, where the sandstones are described as mostly quartzarenites, and also sublitharenites and subarkose. Likewise the observed moderate to poor sorting of the cutting samples (Fig. 4.6) is comparable to the core study by Rammel (1989). The distance between the two observed wells is less than 1 km and both samples are covering the same formations (1. to 3. GLS) of a turbidite sequence which is known to be regionally present. This explains the observed similarities of the petrographic results from both wells.

The 3. GLS shows higher glauconite contents than the overlying 1. and 2. GLS. As only well 2 covers all three GLS sections (Fig. 4.10b) this could not be verified in well 1. The average glauconite content for well 1 (1.8%) is lower as described in Sauer et al. (1992) but average glauconite content in well 2 (4.2%) is in general in accordance, as the glauconite content in the Glauconite Sandstone Fm. is given between 5–10%. While generally the glauconite content in sediments increases in transgressive stages at climate optima (Amorosi, 2013; Santanu et al., 2016; Baioumy et al., 2020; Tribovillard et al., 2023), the studied sedimentary rocks of the GLS represent turbidite deposits (Rammel, 1989). Therefore, we interpret the glauconite as redeposited. Nevertheless, the turbidite deposits may still record the changes affecting the “glauconite factory” (sensu Tribovillard et al., 2023) in shallower water depths, prior to redeposition. Although absolute age data for the studied lithologies are not available, the recorded change in glauconite content may be linked to the “Paleocene/Eocene Thermal Maximum, Middle Eocene Climatic Optimum” and

subsequent climatic deterioration and cooling (Sotak, 2010) known to have affected the nearby Pannonian and Carpathian Basins. Higher glauconite contents in the 3. GLS are therefore interpreted to result from higher glauconite production in shallow water depth at higher surface temperatures, whereas a lower glauconite production during the deposition of the 1. and 2. GLS is interpreted to be linked to subsequent climatic cooling (Sotak, 2010).

Individual samples are affected by different grade of carbonate cementation (e.g., pore filling and partially pore filling carbonate cements in well 1: 0.7%–20.3%, and well 2: 1.0%–30.7%). Within the samples, individual cuttings show fully cemented pores by e.g., Fe-Cal (Fig. 4.11h), whereas in others the pores and veins are only partially cemented. Additionally, locally found loose quartz grains within the samples indicate less intensely cemented sections, which were then very likely disaggregated during the drilling process. This is in contrast to Sauer et al. (1992) where quartz cement and glauconitic clay minerals are mentioned as main permeability reducers.

4.6.2.1 Compaction and porosity

The IGV shows no correlation with depth or the GLS subdivision (Fig. 4.9a), and also low correlation with the detrital quartz and feldspar content for well 1 and 2 (Fig. 4.9b). For well 1, the IGV is lower for samples containing higher detrital quartz and feldspar grain contents, while typically the IGV should be higher with increasing detrital quartz and feldspar contents as they act as rigid grains, where mechanical compaction is less severe than in rocks with higher contents of ductile components (Rossi and Alaminos, 2014). Well to moderately well sorted samples show in general higher median IGV than only poorly sorted samples (Fig. 4.9c). Additionally, the IGV show slight negative correlation with grain size in well 2 (Fig. 4.9d), thus, samples with smaller grain sizes show higher IGV (Fig. 4.9d). Theoretically, finer grained and more poorly sorted samples should be characterized by a lower IGV (Beard and Weyl, 1973). Therefore, the observed correlation indicates that finer grained sediments have generally higher IGV, due to higher carbonate cement contents, as pore-filling and partially pore-filling carbonates show a positive correlation with IGV (Fig. 4.9f, well 1 R^2=0.93, well 2 R^2=0.71). Furthermore, the lower degree of compaction in finer grained samples may be due to detrital clay mineral matrix contents.

Low optical porosity is therefore due to both cementation and detrital clay mineral matrix contents (in very fine sand sized samples) and compaction (in fine sand sized samples), as seen in deformation of ductile RF and undifferentiated RF (Fig. 4.11i). However, investigating samples with increasing depth would be difficult to establish on core data as cores are never continuous taken. Our investigation can therefore be used to confirm and refine the (indirect) log interpretation.

4.6.3 Paragenetic sequence

For this study the diagenetic sequence is subdivided into early and burial diagenesis. Furthermore, indicators for telogenesis and thus interaction with meteoric water following burial diagenetic conditions are missing. Though the studied succession is subdivided into three sections (1.–3. GLS) the units in the two observed wells show similar mineralogical characteristics. Therefore, one summarising paragenetic sequence is presented (Fig. 4.17).

4.6.3.1 Early diagenesis

As chlorite and pore-lining illite rim individual grains or are present between grains such as e.g., quartz and their syntaxial overgrowth cement (Fig. 4.11a), a depositional origin before compaction and cement formation is interpreted. This is in agreement with depositional models for turbidite/flysch deposits (Cummins, 1962). Glauconite occurs as individual grains (e.g., Fig. 4.7b) or as rims outlining grains in individual cuttings. Glauconite is described as the earliest stage in the paragenesis, as the differentiation between authigenic and detrital glauconite is not possible since the flysch consists of turbidite layers (Rammel, 1989).

Siderite rhombs are observed embedded in chlorite matrix, outlining detrital grains and encased in quartz cement. Therefore, an early diagenetic origin is interpreted. This is in agreement with interpretations from other marine and deltaic sections which are also occasionally found to be glauconite bearing (Morad et al., 2002; Adamolekun et al., 2022; Greve et al., 2024). Siderite most likely formed in iron reduction zones (Morad, 1998).

Pyrite observed as cubic crystals in intergranular pores, framboids and pore-filling in bioclasts such as foraminifera most likely originate from bacterial sulphate reduction (BSR) processes in shallow burial environments (Berner, 1970; Coleman, 1985; Morad, 1998). Therefore, the pore water needs to be anoxic and a certain amount of dissolved sulphate must be available (Morad, 1998). The BSR leads to an increase in alkalinity, which may enhance the precipitation of carbonate cements (Berner, 1970; Morad, 1998).

4.6.3.2 Burial diagenesis

Mechanical compaction, grain rearrangement and deformation of ductile components such as ductile rock fragments or phyllosilicates, squeezed into pore spaces, reduces porosity and IGV. Compaction is interpreted to initiate during early diagenesis, following the emplacement of the chloritic and illitic matrix, as both minerals are prominently found in between detrital grains (e.g., Busch et al., 2024).

Quartz cements partially encase chlorite and siderite, and all three phases are encased in Fe-Cal. Thus, the formation of Fe-Cal postdates chlorite emplacement, siderite, and quartz

cement formation. Generally, quartz precipitation rates are elevated at temperatures above 70 °C (Walderhaug, 2000; Lander et al., 2008) and is related to burial diagenesis (Morad et al., 2002). Authigenic quartz cements including fracture healing cements in quartz grains (Fig. 4.13d) show dark and non-luminescent areas in CL around or inside detrital quartz as described by Demars et al. (1996). The blue luminescing detrital quartz grains may be indicative of an igneous origin or fast cooled high-grade metamorphic rocks (Götze et al., 2001 and references therein). The healed intragranular fractures in quartz grains (Fig. 4.13d) may indicate grain fracturing during mechanical compaction (Wilson et al., 1994), pre-dating quartz cementation. As chemical compaction with convex-concave and sutured contacts is rarely observed, the main source for quartz cement is interpreted to be from K-Fsp dissolution and clay mineral recrystallization (e.g., Worden and Morad, 2003).

Partially dissolved K-Fsp grains still retain their grain shape, therefore, dissolution of K-Fsp is interpreted as a burial diagenetic process ensuing after compaction, rarely followed by the formation of kaolinite (e.g., Morad et al., 2010). Feldspar dissolution is most likely the result of interaction with acidic formation waters (Worden and Morad, 2003), which is supported by the preservation of kaolinite, the latter is stable at low K^+/H^+ ratios (Lanson et al., 2002). The analyzed samples show a sandstone-mudrock alternation, organic acidic fluid may originate from maturation of organic matter in mudrock layers or associated to source rock maturation (Lanson et al., 2002 and references therein). Thus, kaolinite can form due to acidic fluids and the reaction with feldspar. The distribution of illite/kaolinite or the replacement of kaolinite by illite depends on the availability of potassium. Potassium may be derived from influx of potassium-rich waters or dissolution of potassium-bearing minerals e.g., K-Fsp and temperature (Lanson et al., 2002). Therefore, a low potassium-content and low temperatures inhibit the alteration of kaolinite to illite, as well as low K^+/H^+ ratios, which favors kaolinite formation (Lanson et al., 2002). The formation of illite from kaolinite is often shown in relatively deeply buried sandstones as opposed to precipitation from a kaolinite precursor in relatively shallowly buried sandstones, e.g., on the Norwegian Continental Shelf (Lanson et al., 2002 and references therein). Furthermore, kaolinite replacing mica was observed in individual cuttings. Kaolinite replacing mica is one of the dominant types of diagenetic kaolinite in sandstones (Lanson et al., 2002 and references therein). The other dominant types are vermiform and blocky kaolin, whereas their crystallization conditions are controversial (Lanson et al., 2002). One of the hypotheses is the formation of vermiform and blocky kaolin at shallow burial depth by interaction with fluids of meteoric origin during early diagenesis or after inversion. The other hypothesis is that the mixture of meteoric fluids and organic acid-rich or CO_2-rich fluids might be responsible for feldspar alteration and kaolinite precipitation, with the altering fluids resulting from maturation of organic matter, e.g., from mudrocks (Lanson et al., 2002 and

references therein). As the kaolinite booklets are preserved in uncompacted intragranular pores, the latter formation pathway is interpreted for the studied samples.

Illite is rarely observed to replace K-Fsp and kaolinite, and occurrence of both is possible due to slow reaction rates at lower temperatures (Worden and Morad, 2003 and references therein). Given that illite authigenesis is generally related to temperature (Morad et al., 2002) and common at temperatures >70 °C, a burial diagenetic formation is supported. However, as individual feldspar grains show replacement by Fe-Cal (Fig. 4.11f) but other K-Fsp grains preserve intragranular pores, two phases of K-Fsp dissolution and alteration before and after carbonate cementation are interpreted. As kaolinite and illite replacements are not observed encased in carbonate cement, their formation is interpreted to postdate Fe-Cal cement precipitation. The occurrence of dissolved feldspar and the formation of secondary porosity or replacement by kaolinite or carbonate cement is comparable to the description by Gier et al. (2008) for Miocene sandstones from the Vienna Basin.

The ferroan calcite cements (Fe-Cal) encase quartz cement overgrowths, partially pore-filling siderite, and fill residual porosity remaining in clay mineral matrix-rich sandstone cutting samples, thus the formation of Fe-Cal is interpreted to post-date the formation of all other diagenetic products. The formation of Fe-Cal cements in sandstones can be caused by elemental uptake from claystones as described by Miocic et al. (2020), which would match the interstratified depositional sequence of flysch deposits. A direct relation to marine carbonate cementation is unlikely as Fe-calcite cement postdates most burial diagenetic phases. Similarly, in a different study of Neogene sandstones from the Aderklaa-78 well in the Vienna Basin, the Fe-Cal cement is the most important porosity reducer (Gier et al., 2008). However, the Fe-Cal cements from the Aderklaa-78 well are interpreted to originate from dissolved detrital limestone rock fragments (Gier et al., 2008). In the studied samples the detrital carbonate rock fragments are still intact (Fig. 4.11c), therefore we do not imply a similar source.

4.6.3.3 Structural diagenesis

Natural shear bands, such as deformation bands, are localized deformation structures and characterized by their microstructure and the occurrence of grain rearrangement, cementation and/or cataclasis (Fossen et al., 2007; Ballas et al., 2013) (cf. Fig. 4.12). They often form in poorly consolidated, porous sand(stones) (Antonellini and Aydin, 1995; Fossen, 2010; Ballas et al., 2012; Soliva et al., 2013). As the observed shear bands in the studied wells are characterized by a reduced grain size, porosity reduction, and grains showing an angular shape, the bands can be classified as cataclastic deformation bands. Porosity reduction due to deformation band formation is caused by crushed and small grain fragments which block pores (Antonellini and Aydin, 1994; Ballas et al., 2013), as it is also observed in this study (Fig. 4.12). The crushed grains may further act as precipitation sites for

syntaxial quartz cements, further reducing porosity. However, the lateral continuity, which is important for the interpretation of an influence on fluid flow (Saillet and Wibberley, 2013; Busch et al., 2015), cannot be ascertained by using drill cuttings. While deformation bands may limit flow perpendicular to the deformation band, some studies suggest enhanced permeability in the plane of the deformation band (Fowles and Burley, 1994). The cataclastic deformation bands in this study are interpreted to predate the formation of quartz and carbonate cementation, as no crushed carbonate cements are obtained within the fine grained, angular and densely packed zones in the deformation bands (Fig. 4.12) and intragranular fractures in quartz grains are filled by syntaxial quartz cements (Fig. 4.13d). Furthermore, the cataclastic lenses are encased in Fe-Cal vein cements indicating shear band formation prior to vein formation (Fig. 4.12c). On the other hand, the artificial shear bands, only observed on the outside of cutting fragments and as individual cutting fragments, are most likely related to drilling. However, they can easily be differentiated from natural shear bands in the studied samples by high porosity in the artificial shear band and ground up pore-filling Fe-Cal cements.

Based on the luminescence color from CL analyses and the crosscutting relation of veins (Fig. 4.13, 4.14), three pervasively-sealed vein cementation phases, and three partially-sealed carbonate vein cement generations are observed. Partially-sealed veins show euhedral crystal facets composed of orange luminescence Fe-Cal, which is brighter than the pore-filling Fe-Cal cement (Fig. 4.13b, c). Partially-sealed veins show an outer rim of dull luminescent Fe-Dol in all studied samples, which is interpreted to be the last generation of fracture cements. Additionally, one pervasively sealed vein shows a dissolved Fe-Cal rim. However, interpretation solely based on luminescence colors and texture cannot be considered to account for different fracture orientations as this information is not available from cutting fragments. The most prominent fracture mineralization is Fe-Cal, with minor contents of Fe-Dol forming the dull to non-luminescent outer rim in partially sealed veins (see also Hilgers and Urai, 2002; Greve et al., 2024 for further information on CL color). At the host rock-vein interface, some veins show the occurrence of pyrite (Fig. 4.11j). Pyrite may result from fluid-rock interactions possibly including Fe released from ongoing fluid expulsion from intercalated mudrocks (Miocic et al., 2020; Greve et al., 2024).

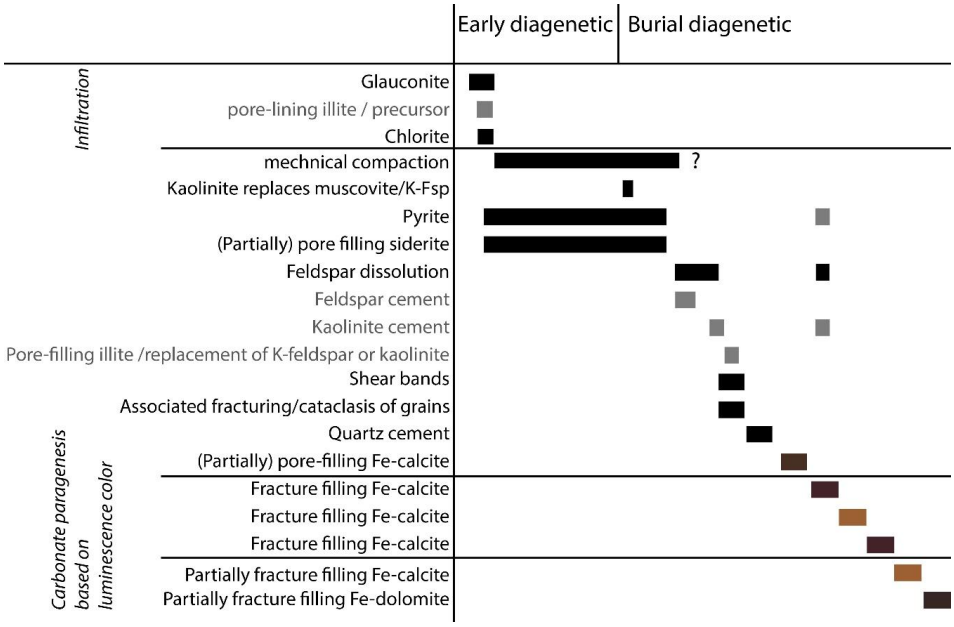

Figure 4.17 Paragenetic sequence for well 1 & well 2 subdivided into relative early and burial diagenesis. The diagenetic sequence is established using transmitted light microscopy and CL analyses to differentiate vein and cement generations based on their luminescence color and texture. Black boxes mean mineral phases are found in almost all samples, grey mineral phases occur in individual samples, and the colors for Fe-calcite cement generation and veins relates to the respective CL luminescence color (non-luminescent, dull, and bright orange).

4.6.4 Reservoir quality controls and application of cutting analyses in reservoir geology

The overall poor matrix porosity of the sandstones within the two studied wells is controlled by compaction and cementation of former pore spaces predominantly by Fe-Cal. While cementation in sandstones can occasionally enhance reservoir quality by inhibiting mechanical compaction (e.g., Busch et al., 2022a), further ongoing cementation reduces reservoir quality (e.g., Houseknecht, 1987; Morad, 1998; Busch et al., 2024).

Intragranular porosity is mostly present in individual K-Fsp grains and/or partially preserved if kaolinite is formed as an alteration product. The intragranular porosity is only up to 2.3% and thus unlikely to improve permeability, as it is mostly not connected in 3D (Pittman, 1979; Kumar et al., 2023). Microporosity e.g., in chlorite, kaolinite, mudrock RF

or illite is not visible in transmitted light microscopy, but could enhance the porosity in total (e.g., Nadeau and Hurst, 1991). Considering the low optical porosity (0–5%), flow is likely restricted to open fractures and partially sealed veins rather than the matrix porosity. This observation is in line with the typical production behavior of this reservoir, which is historically characterized by high initial rates followed by a rapid decline (Möbius et al., 2023). Additionally, Sauer et al. (1992) describes that the reservoir quality of the flysch is depended on open fractures and mylonitized fractures zones (cp. cataclastic deformation bands). The observation of overall higher contents of vein cements in samples from producing intervals as opposed to non-producing intervals (Fig. 4.16) and including the fact that such are often only partially filling the fractures, may be a useful proxy to differentiate productive and non-productive zones. Especially partially sealed veins have been shown to preserve permeability in reservoir sandstones (e.g., Lander and Laubach, 2015 and references therein). In tight reservoirs, the understanding of fracture systems, or partially sealed veins, and their connectivity is crucial to reduce uncertainties in production (e.g., Narr, 1996; Bahrami et al., 2012; Becker et al., 2018). Future work in the Flysch play should include samples of known orientation to assess partially and completely sealed fractures in relation to the present-day stress field (e.g., Allgaier et al., 2024).

Cataclastic deformation has been described in reservoirs from the Vienna Basin (Gier et al., 2008). In the investigated samples, their formation is interpreted to predate the formation of fractures and veins (Fig. 4.12c). Therefore, we interpret, that any compartmentalization due to deformation bands is overcome by fracturing and that production performance is linked to low matrix porosities and fracture-bound fluid flow.

For the two studied wells, producing intervals are characterized by mostly lower Fe+Mg contents (Fig. 4.16b), and a higher content of carbonate vein cements (Fig. 4.16f). As the total carbonate cement content (incl. vein cements) (Fig. 4.16d) is not a suitable criterion to differentiate producing and non-producing intervals, the inclusion of petrographic studies assessing vein cement contents and textures, in addition to pXRF measurements (Fig. 4.16b, f) is needed.

Utilizing a combined petrographic and handheld pXRF approach on cuttings in concert with historical production data may additionally enable future assessments of producing/non-producing intervals in case core material is not available. Reservoir sandstones in general cover a wide range in detrital and authigenic composition and reservoir quality controls which differ from region to region. Thus, case specific calibration of this approach is required.

Although the outlined pXRF analyses are non-destructive and petrographic analyses can still be performed on the same samples, as presented here, some other pXRF approaches

require crushed sample material and calibration with a known standard (e.g., Weedmark et al., 2014). The presented approach, also utilized by Quandt et al. (2024), can be used directly on cutting and core samples, and can be checked during measurements against a known standard to allow deployment at the well site in parallel to standard optical cutting analyses.

Although fracture and vein orientations cannot be reconstructed by analyzing drill cuttings, the presence of partially sealed veins and their occurrence in specific formation intervals can be identified and used for reservoir quality assessments. While porosities may be estimated based on thin sections of cuttings or standard lab measurements, direct measurements of permeability or mechanical properties are difficult using cutting material for reservoir quality assessment, a gap may be bridged by utilizing digital rocks (Monsees et al., 2020). The inability to accurately re-orient cuttings to gain information on sediment structures and vein/fracture orientations, however, requires core- and logging data and a structural model. Especially partially sealed veins, which may preserve open fracture porosity in the present day stress field (Laubach et al., 2004), may need to be further evaluated in these naturally fractured reservoir lithologies, and knowledge about their orientation is essential for dilation- and shear-tendency evaluations (Allgaier et al., 2023b).

In cases where core material is unavailable, drill cutting analysis using petrography, pXRF, and geophysical log measurements can be a powerful tool to bridge knowledge gaps and enhance the utilization of reservoir systems worldwide.

4.7 Conclusions

A detailed petrographic study of sandstone drill cuttings from the Glauconite Sandstone (GLS) in the Vienna Basin highlights low optical porosity (<5 %) in samples from both wells due to cementation with mostly Fe-Cal. This study enables the assessment that fracture formation is postdating the formation of deformation bands, which enhances reservoir properties. The reservoir quality in the studied section is independent of compaction of the sandstones and is only related to fractures and partially sealed veins in sandstones with lower optical porosity, higher carbonate vein contents, and lower Fe + Mg contents from pXRF analyses.

Further geochemical data obtained from pXRF as e.g., the Si/Alratio to distinguish between mudrock-rich and sandstone-rich intervals, can additionally be used to cross-check formation depths of cuttings to relate them to log-derived gamma ray measurements and other well-log data. As µm-wide partially sealed veins are not visible in image logs, cuttings can additionally inform about microstructures that may influence reservoir-scale fluid migration. Furthermore, cutting examination highlights that the glauconite content in the 1. and

2. GLS is lower than that in the 3. GLS. Cuttings can thus be used to derive meaningful paragenetic sequences, assess reservoir quality controls, and deliver information about changes in the detrital mineralogy.

Due to the observed low pore volume the most critical factor contributing to reservoir quality are open fractures or partially sealed veins. Partially sealed veins preserved in cuttings, derived from petrographic analyses and pXRF measurements may thus indicate producing reservoir intervals in the low porosity reservoirs studied. This may support log-derived petrophysical interpretations in particular in the absence of core material e.g., when working on historic data sets.

5 Effects of the Russia-Ukraine conflict on the supply of selected raw materials

5.1 Abstract

The Russia-Ukraine conflict resulted in the occupation of the eastern Ukraine, and disrupted supply chains of raw materials such as oil, gas and metals since 2022. Russia is one of the most resource-rich countries in the world with long-standing economic ties to Germany and was an important exporter of raw materials to the EU and Germany. While Russia has a large global share in the extraction of nickel and vanadium ores through mining and refining into metals, bauxite/alumina and titanium are imported to Russia as ore and primary products and refined and exported using the available and inexpensive energy. In 2022, Australia banned exports of aluminium ores as bauxite, and alumina to Russia as part of its sanctions, while the Ukraine banned exports of titanium ore to Russia. In addition, the Ukrainian export of the noble gas neon for semiconductor production with a global market share of around 50% came to an halt. If existing stockpiling and infrastructure construction at existing steelworks are present, shortages can be counterbalanced, e.g., in case of South Korea's steel industry. To reduce reliance on third nations, increasing mining awareness among EU countries and signing strategic agreements with countries with unexplored mining potential are suggested actions. Recycling of critical raw materials is crucial, but cannot meet the increasing future demand. The raw materials market is adapting through alternative sources of supply and, where possible, production is being increased in countries such as China, as in the example of titanium sponge. Procedures have been proposed by the EU to ensure a resilient supply of critical and strategic raw materials within the EU, possibly accelerated by the Russia-Ukraine conflict. To realize the benchmarks of the Critical Raw Materials Act, 47 projects on strategic raw materials in different EU27 member states are adopted. Diversified supply chains from processed ores to semi-finished products, stock piling, smelting and refining of carrier metals and critical raw materials, as well as existing heavy industry with new plants for the extraction of scarce raw materials could increase the availability and security of raw materials in the event of disruptive events. Stockpiling of critical raw materials, diversification and increased production of other mines, smelters and refineries, and the presence of associated industries ensure the supply of raw materials and counterbalance shortages.

5.2 Introduction

Global demand for raw materials both from mines (primary raw materials) and recycling (secondary raw materials) continues to increase (OECD, 2019). Increasing technical developments such as digitalization and the energy and mobility transition of several countries are leading to a further global increase in demand for raw materials. The International Energy Agency (IEA) estimates that the demand for critical metals and industrial metals will triple by 2050 for the “net zero scenario” (IEA, 2023). The worldwide demand for metallic raw materials is predicted to double from 9 Gt in 2017 to 20 Gt in 2060, as a result of digitalization, technological advancements, e-mobility, and the "Green Deal" reorganization towards renewable energies (OECD, 2019; Lutter et al., 2022). For an industrialized country such as Germany, it is vital to secure access to raw materials to maintain international competitiveness. Risks related to pricing and supply threaten competitiveness and the integrity of the value chain, as seen during the Covid-19 pandemic, or due to closed land-based supply routes like those from Asia to Germany via the Russian Federation (Russia). Simultaneously, the worldwide need for raw materials will keep increasing in the coming decades.

Despite essential recycling procedures, the growing global demand and technological constraints mean that recycling and the use of secondary raw materials alone will not be sufficient to meet this growth in metals and other essential raw materials in the future (Lutter et al., 2022). For some specific metal (e.g., tantalum), there are currently no defined recycling structures (Deutscher Bundestag Fraktion der CDU/CSU, 2022).

In addition to the extraction of primary raw materials from mining, secondary raw materials are obtained from recycling of new and old scrap. However, not all metals can be recycled w.r.t. to metallurgy from End-of-life goods (e.g., Tercero Espinoza, 2012; UNEP, 2013; Reuter et al., 2019). In some cases, recycling does not make sense from an economic and ecological point of view, such as efficient large tonnage high volume copper mining versus copper from building waste (Schmidt et al., 2020) or the required quality of the metal cannot be achieved with recycled scrap.

Furthermore, some critical elements like tellurium and indium can only be produced through smelting as by-products from other carrier metals sing. Hence, without energy-intensive smelting process, neither such critical by-products can be produced nor can metals be smelted from ore or scrap (cf. Hilgers et al., 2021).

The Russia-Ukraine conflict has disrupted trade between the EU with Russia and the Ukraine, affecting raw material supply. EU sanctions against Russia have halted the import of specific raw materials, such as steel imports (Europäischer Rat/Rat der Europäischen Union, 2025b). According to Article 3g) of Regulation (EU) No. 833/2014, certain iron-

and steel-related products are subject to federal oversight requirements (European Union, 2025). Additionally, pipeline-bound natural gas imports from Russia to Germany have substantially decreased as a result of the attack on three of the four Northstream pipelines 1 and 2 in the Baltic Sea on September 26, 2022, and related cascading effects in the raw materials sector.

The 16th sanctions package of the EU against Russia went into effect on February 25, 2025 (Europäischer Rat/Rat der Europäischen Union, 2025b). This entails further trade restrictions and sanctions, as e.g., export of some products that are assumed to be used for the Russian military industry is prohibited. Chemical precursors, chrome, predetermined machine parts, and devices such as video game controllers that may be used to control combat drones are among them (Europäischer Rat/Rat der Europäischen Union, 2025b). The EU's trade sanctions include a ban on the import of steel, iron, copper, and primary aluminium, copper and aluminium alloys, rebar and foil, bitumen and asphalt, helium and other chemicals, diamonds and gold (including jewelry), and other goods that were assessed to potentially strengthen Russia's industrial capabilities (Europäischer Rat/Rat der Europäischen Union, 2025b). Chrome is used as a corrosion inhibitor on the inside of protective tubes as for artillery weapons refurbishment of old artillery weapons (Krumbeck, 2025). However, Russian metals continued to account for a significant portion of Germany's overall imports, such as nickel and titanium, at 25% in the first quarter of 2023.

To ensure a supply of raw materials, the EU and Germany will need to diversify and form alliances with resource-rich non-EU nations, even though the domestic recycling potential needs to be increased (BGR, 2024; Ölmez and Hilgers, 2024b, a). However, from several imported commodities it is difficult to determine with certainty whether a product is of Russian origin. China became a global leader in the domestic and global mining of large volumes of numerous raw materials such as rare earths, lithium, copper, among others, and a global leader in refining production, importing ores and valuable scrap globally and aims to become the global leader (DERA, 2019).

In this article, we provide selected information on the development of critical and strategic raw materials. We summarize and expand aspects from Ölmez & Hilgers (2023) and revise some of the information. We outline for selected raw materials, how or if supply chains adapted to the disruption caused by the Russia-Ukraine conflict. This analysis focusses on selected raw materials from Russia and Ukraine (bauxite and alumina, titanium, lithium, noble gases, nickel, palladium and platinum, vanadium), developments and effects of the Russia-Ukraine conflict for the EU and Germany.

5.3 Analysis of raw material supply disruptions and resulting adaptations

In Ukraine, Russia controls 63% of the coal reserves, 11% of the oil reserves, 20% of the natural gas reserves, as well as 42% of the metals and 33% of the rare earths, additional critical minerals, and potential lithium deposits, according to the Washington Post (as of 08/2022) (Faiola and Bennett, 2022; Schulze, 2023). Due to the ongoing conflict, mining operators in the regions of Donetsk and Luhansk have halted their extraction activities, and there is a lack of investment in reconstruction or the development of new deposits (Schulze, 2023).

Ukraine has one of Europe's largest lithium deposits, however it is currently producing no lithium (Ukrainian Geological Survey, 2023). Furthermore, Ukraine's lithium resources are currently difficult to evaluate in an international comparison, as exploration rate is low (Blum et al., 2023). Two early-stage lithium projects in Ukraine intended to utilize hard rock reserves. The larger ones include Shevchenkivskyi in Donetsk (one of the districts claimed by Russia), as well as Polokhivske, Kruta Balka (district Zaporischschia) and Dobra (district Kirowohrad) deposits in central Ukraine (Blum et al., 2023; Devitt and Osterman, 2025). Petalite and spodumene occur in the Dobra Block, as well as lithium phosphates, with lithium contents ranging from 0.25 to 2.23% LiO_2 (Blum et al., 2023). So far, lithium is mainly mined in Australia, Chile, China, and Zimbabwe, but also Argentina and other countries (Fig. 5.1).

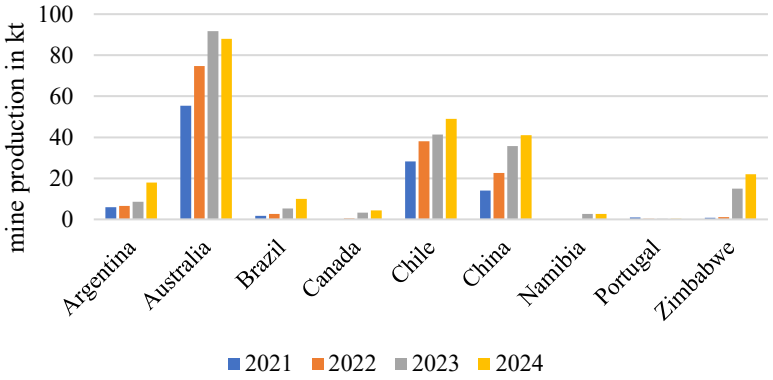

Figure 5.1 Lithium mine production in kilotons (kt) of contained lithium from USGS mineral commodities. Data for 2024 is estimated, furthermore, some values between 2021 and 2023 are estimated (USGS, 2023, 2024, 2025).

5.3.1 Bauxite and alumina

Source

Ukraine is a large producer of aluminium oxide (Al_2O_3, also called alumina) in 2021 (among the world's ten as of USGS data) with 1.7 Mt (USGS, 2023) from imported bauxite, since it lacks larger bauxite mines or resources (USGS, 2023). The Ukraine is reported to have only few known bauxite deposits (Bashniak et al., 2022). Previously, bauxite had been imported by the Ukraine from countries as Turkey, China, Brazil, Guinea and more (UN Cometrade, 2025). Main bauxite producer are Guinea (estimated 130 Mt in 2024), Australia (estimated 100 Mt in 2024) and China (estimated 93 Mt in 2024), but also other countries in recent years (Fig. 5.2). To produce 2 tons of alumina the USGS states that 4 tons of dried bauxite is required, and two tons of alumina can be used to produce 1 ton of aluminium as a general assumption (USGS, 2025). Due to the Russia-Ukraine conflict, the alumina refinery in Ukraine which produced 1.7 Mt/a had to be closed (USGS, 2025). The production of 1.77 Mt (dry weight) of alumina in 2021 in Ukraine were reduced to first expected 740 kt (dry weight) in 2022 (USGS, 2023), but were reported as 300 kt alumina for 2022 (Fig. 5.3) (USGS, 2024). Imports of HS2606 - aluminum ores and concentrates (includes bauxite) to Ukraine are reduced from reported 5.2 Mt in 2020 to 50.5 kt in 2024 (using UN Comtrade with Ukraine as reporter and partners "world") (UN Cometrade, 2025).

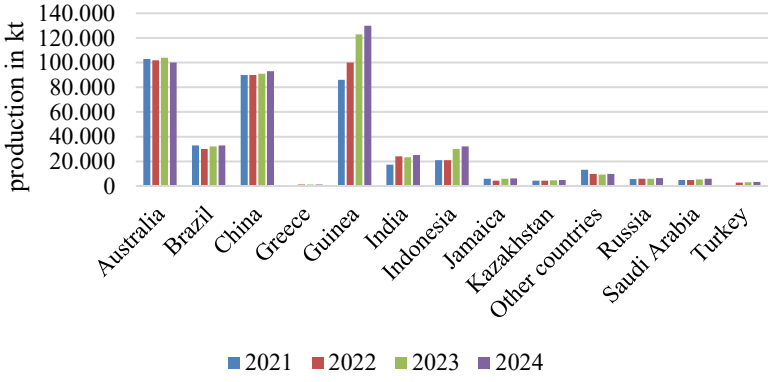

Figure 5.2 Bauxite mine production, data in kilotons (kt) dry tons from USGS mineral commodities. Data for 2024 is estimated, furthermore, some values between 2021 and 2023 are estimated. To avoid disclosing company proprietary data United States values are withheld (USGS, 2023, 2024, 2025).

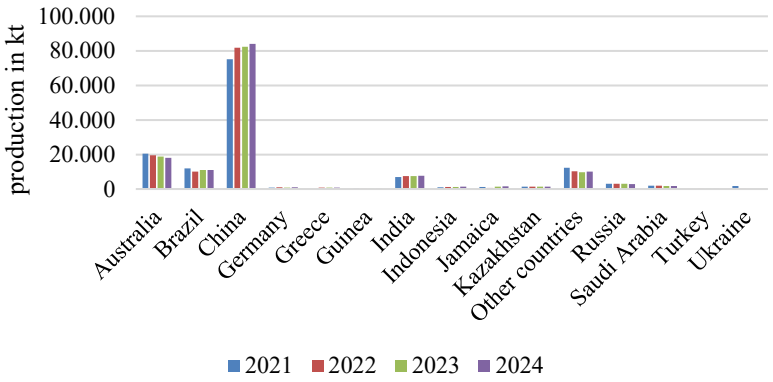

Figure 5.3 Alumina refinery production ("calcined equivalent weights") data in kilotons (kt) dry tons from USGS mineral commodities. Data for 2024 is estimated, furthermore, some values between 2021 and 2023 are estimated (USGS, 2023, 2024, 2025).

Adaptation

In 2021, Australia and Ukraine accounted for more than half of Russia's bauxite imports, but since March 20, 2022, Australia has stopped supplying alumina to Russia (Barich and Chen, 2022). Australia's export prohibition in 2022, and due to a shortage of alumina supplies from Ukraine, Russia transferred its alumina supply chains to other countries. Russia instead imported aluminium ores and concentrates (HS2606) from China and other countries such as Turkey (UN Cometrade, 2023a). Russia's aluminium smelting production is expected to be 3.8 Mt in 2024, ranking third among countries after China (43 Mt) and India (4.2 Mt) (USGS, 2025). Although importing bauxite from China to Russia is more expensive than from Ukraine and Australia, Russia became the main importer of bauxite from China in 2022 (Devitt et al., 2023). Rusal, the world's second-largest aluminium producer after China, further diversified its supply by bauxite imports from India and Kazakhstan (Devitt et al., 2023). The bauxite mining in Russia increased by less than 2% from 2021 to 2024 to expected 6.3 Mt, alumina refinery decreased by 4.9% to expected 2.9 Mt (USGS, 2023, 2025).

The Ukrainian Mykolaiv (Nikolaev) Alumina Refinery imported bauxite from different countries and exported alumina to e.g., Rusal in Russia (Devitt and Osterman, 2025), but was forced to stop production in 2022. Guinea, on the other hand is the greatest producer of bauxite in 2024. Guinea produced 130 Mt (dry tons) bauxite in 2024, accounting for about 28.9% of the predicted worldwide production of 450 Mt (excluding the United States) (USGS, 2025). Thus, Guinea increased the bauxite production from 86 Mt to 130

Mt within three years (c. 51% increase). For comparison, in 2011, Guinea only produced 17.6 Mt bauxite (USGS, 2013).

Within the 47 strategic raw materials projects supported by the EU, one aims for on an integrated approach for extraction and processing for bauxite/alumina/aluminium and gallium (Promoter: Metlen Energy and Metals and European Bauxites, Metlen BAUX-EU, GALLANT, LEADER), project start is estimated for 2028 (European Commission (DG GROW), 2025b).

5.3.2 Titanium

Sources

In 2021, Ukraine was one of the top ten mining countries in the world for the titanium minerals rutile and ilmenite (USGS, 2023), which were mainly exported to Russia for further processing. In 2021, Ukraine produced 316 kt ilmenite and and 95 kt rutile (USGS, 2023). For 2024, it is estimated that Ukraine produced 120 kt ilmenite and 10 kt rutile (Fig. 5.4) (USGS, 2025). Russia imported titanium ore concentrate and processed it to titanium sponge and metal, with around 5% supplied from Ukraine in 2022 (UN Cometrade, 2023b). Since 2022, ilmenite is subject to an export ban from Ukraine to Russia (Schulze, 2022).

The Russian company VSMPO-Avisma is the world's largest producer of titanium from titanium sponge, which is an important metal e.g., for air and space travel (Stock, 2022). VSMPO-Avisma's contract partners include the American Boeing and the European Airbus; previously, VSMPO-Avisma covered 35% of the titanium needs of Boeing and 50% of Airbus (Schulze, 2022). Back in 2021, Ukraine produced 6.1 kt of titanium sponge and 1 kt in 2022 (USGS, 2023, 2024), which likely came to a halt, as no data for 2023 and 2024 is reported in USGS mineral commodities (USGS, 2025). Russia, produced 27 kt titanium sponge in 2021 and 20 kt in 2024 (USGS 2025).

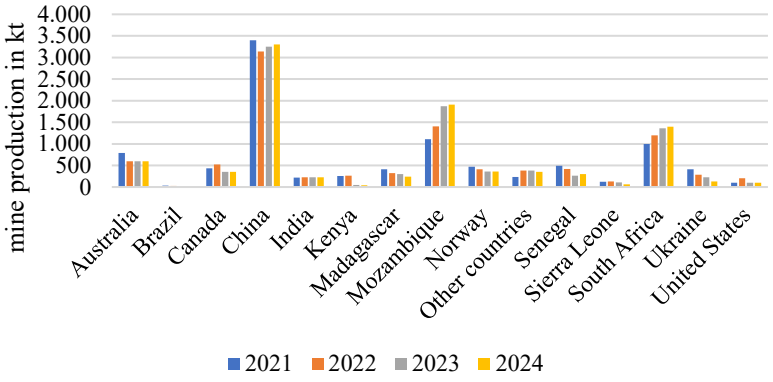

Figure 5.4 Combined values of mine production for rutile and ilmenite, data in kilotons (kt) of contained titanium dioxide (TiO_2) from USGS mineral commodities. Data for 2024 is estimated, furthermore, some values between 2021 and 2023 are estimated (USGS, 2023, 2024, 2025).

Adaptation

There were no global shortages of titanium sponge (Europäische Kommission, 2022d). The amount of produced titanium sponge increased globally by 33% from 2021 to 2023 (Fig. 5.5), highlighting an increasing demand, which is mostly supplied by China. Production capacity in Japan and Kazakhstan, as well as increased production in Saudi Arabia, offsets the loss of Russian and Ukrainian imports (Europäische Kommission, 2022d). Titanium sponge was produced in 2024 primarily in China (estimated 220 kt), Japan (55 kt), Russia (20 kt), Saudi Arabia (15 kt) and Kazakhstan (14 kt) (USGS, 2025). Short supply shortages in the aircraft industry were covered by stock levels and no new demand of stock is foreseen (Europäische Kommission, 2022d). China increased titanium sponge production between 2021 and 2024 by a factor of 1.6 (USGS, 2023, 2024, 2025). Japan increased production by 12% from 2021 to 2024 and Russia reduced production by 26%.

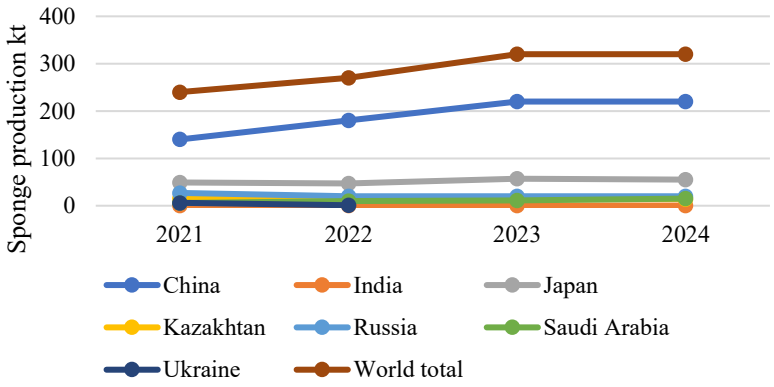

Figure 5.5 Sponge metal production in kilotons (kt), data from USGS mineral commodities. Sponge production globally increased by 33.3% from 2023 (240 kt) to estimated values for 2024 (320 kt). United Stated production is withheld. Data for 2024 is estimated, furthermore, some values between 2021 and 2023 are estimated (USGS, 2023, 2024, 2025).

Titanium is not covered among the EU's 47 strategic projects, but titan metal is listed as strategic within the EU's CRMA list (European Commission, 2025). Titanium sponge production is energy intensive and is refined in countries using sufficient, readily available and affordable energy, such as Russia, allowing titanium sponge and titanium to be produced (Europäische Kommission, 2022d).

5.3.3 Noble gases

Sources

Noble gases krypton, neon, and xenon are used in the production of semiconductors, for example, in the automotive and aerospace industries (Europäische Kommission, 2022c). Ukraine supplied about 50% of the global neon in 2021/2020 and other noble gases (Alper, 2022). About 30,000 m³/month were delivered from Ukraine to China, Germany, the USA, Taiwan, and South Korea (Alper, 2022). The extraction of noble gases as a by-product in steel production, which was based in Mariupol (Ingas) and Odessa (Cryoin), had to be halted. Additionally, Russia ended the export of noble gases Ne, Kr, Xe to "unfriendly" countries, further increasing global scarcity (Baron, 2022). In 2021, 47% of the total imports of noble gases into the EU came from Russia and Ukraine (Europäische Kommission, 2022c). Germany is the largest importer of noble gases in the EU by value and imported noble gases with an average value of € 4.3 mio. between 2019 and 2021, with 39% coming from Russia and 23% from Ukraine (Europäische Kommission, 2022c). For 2021, Russia

accounted to 22% of the EU imports for neon, krypton and xenon, while China accounted for 30% and the Ukraine for 25% (Fig. 5.6) (Europäische Kommission, 2022c).

The noble gases helium, neon, krypton, and xenon are obtained as by-products in the extraction of oxygen for the steel industry. Large steelworks with a demand of more than 1,000 t of oxygen per day can produce 1 m³ of Xe (5.9 kg) from 10 Mm³ (12,920 t) of air through the cryogenic distillation of large quantities of liquefied air, given the low concentrations of the inert noble gases in the air: 0.9% Ar, 0.0018% Ne, 0.00011% Kr, and 0.000009% Xe. Plants are designed for the extraction of Kr and Xe, or the extraction of He and Ne as by-products for technical reasons (Europäische Kommission, 2022c).

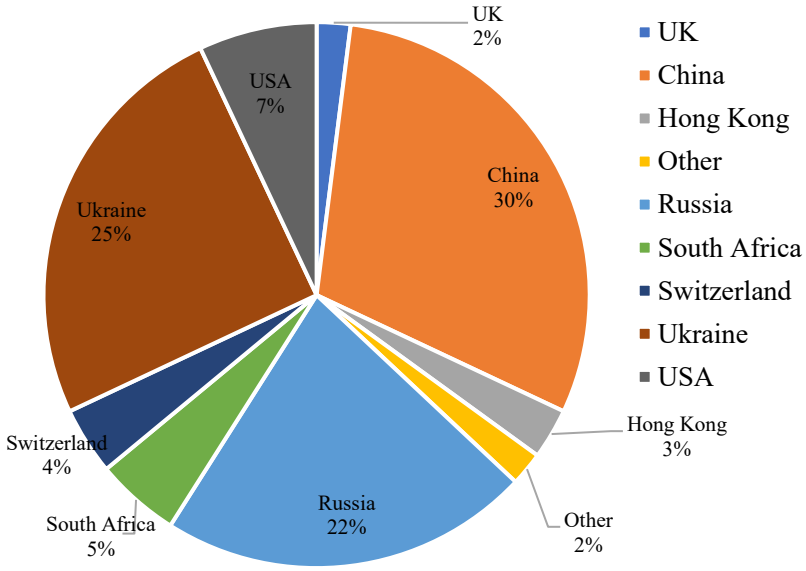

Figure 5.6 EU import values of rare gases by countries in 2021 for neon, krypton and xenon crude and purified gases (CN 28042990) (data adapted from Europäische Kommission, 2022c and references therein).

Adaptation

The two main producers of high-purity neon in Mariupol and Odessa (Cryoin and Ingas in 2020), which accounted for 50% of the global production market share (as of 2020), had to ceased neon production (Wittmann, 2022; Schulze, 2023). The start of the Russia-Ukraine conflict resulted in supply chain problems and price increases due to the need to fill warehouses with large amounts of neon. POSCO Holding, a South Korean steel company, and South Korean TEMC Co., a gas manufacturer, are two examples of adapting to

a lack of noble gas supplies (Baron, 2022). POSCO is the world's seven largest steel producer, with 38.4 Mt in 2023, compared to Thyssenkrupp, the largest German producer, produces 10.3 Mt (in 2023, ranked 41) (Worldsteel, 2023). The largest steel producer in 2023 was China Baowu Group with 130.8 Mt (Worldsteel, 2023). Neon production at POSCO began in April 2022 and is expected to cover 100% of the neon demand (now at 40%) for the South Korean chipmaker SK Hynix Inc. by 2024 (Korea Bizwire, 2022). Cryoin Engineering, a Ukrainian neon manufacturer, intends to establish a joint venture in South Korea with the Korean JI Tech (a supplier of semiconductor raw materials), which could result in a transfer of production technologies to South Korea. SK Hynix Inc. and TEMC Co. have developed the industry's first neon gas recycling technology for chip manufacturing in 2024, thus the dependence on imported neon will be further reduced (SKHynix, 2024).

5.3.4 Nickel

Source

Russia mines the third-largest volume of nickel after Indonesia and the Philippines (Fig. 5.7), with an estimated 210 kt (nickel content) in 2024 (USGS, 2025). Russia supplies approximately 20% of the high-grade nickel required for battery construction worldwide (Sullivan, 2022). Of the approximately 100 kt of Russian nickel-grade-1 exports (January-November 2021), around 53 kt were sent to the Netherlands and Germany (Erickson, 2022).

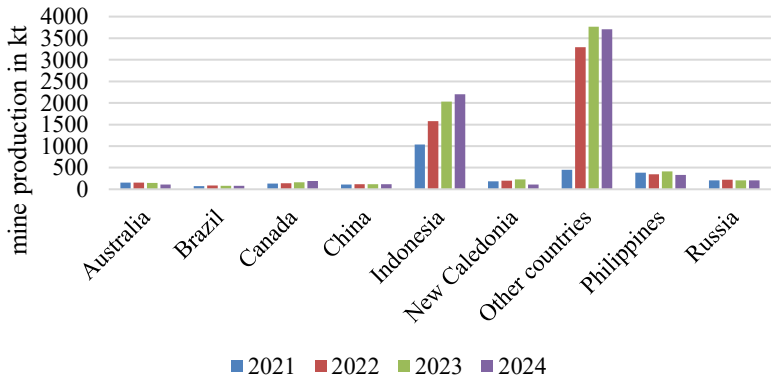

Figure 5.7 Nickel mine production given in kilotons (kt) of contained nickel from USGS mineral commodities. Data for 2024 and some values between 2021 and 2023 are estimated (USGS, 2023, 2024, 2025).

Adaptation

In the first quarter of 2021, Germany imported 6,500 tons of raw nickel from Russia; in the first quarter of 2023, 3,300 tons; during the same year, raw titanium imports fell from 270 to 150 tons (DERA, 2023). Russian Nornickel, the world's largest palladium producer and a key producer of high-grade nickel, saw a profit drop of 37% in 2024 due sanctions and low metal prices (MiningTechnology, 2025).

For nickel, there are currently 11 projects supported by the EU from extraction, to processing and recycling, as well as one integrated approach on extraction and processing. However, these projects do not only cover nickel, but also other raw materials as cobalt, PGMs and more (Tab. 5.1). Values of estimated production for nickel are not available in the project sheets, but are questionable to cover the future EU’s demand.

Tab. 5.1 Projects among the 47 announced by the EU supported projects for strategic raw materials which cover nickel and nickel in battery grade in form of extraction, recycling, processing.

Country	Strategic raw material	Type	Promoter	Project name	Estimated production	Reference
Finland	Ni (battery grade), Co	Extraction	Terrafame Ltd	Kolmisoppi	09/2028	(European Commission (DG GROW), 2025f)
Spain	Co, PGMs, Ni (battery grade), Cu	Extraction	RIO NARCEA RECURSOS S.A.	Aguablanca Project	2026	(European Commission (DG GROW), 2025a)
Finland	Co, PGMs, Cu, Ni (battery grade)	Integrated: Extraction, processing	Anglo American Services (UK) Ltd.	Sakatti Project	2030	(European Commission (DG GROW), 2025k)
France	Ni (battery grade), Co (battery grade), Li (battery grade), Graphite (battery grade), Mn (battery grade), Cu	Processing	SIBANYE-STILLWATER SANDOUVILLE REFINERY	GALLICAM	2027	(European Commission (DG GROW), 2025d)
Finland	Li (battery grade), Co, Ni (battery grade), Cu	Recycling	Fortum Battery Recycling Oy	Project Fortum Hydromet	2029	(European Commission (DG GROW), 2025i)
France	Li (battery grade), Co, Ni (battery grade), Mn, Graphite (battery grade)	Recycling	ORANO Batteries	Hydrometallurgy	2030	(European Commission (DG GROW), 2025e)
Italy	Cu, Ni (battery grade), PGMs	Recycling	Circular Materials s.r.l.	RECOVER-IT	2026	(European Commission (DG GROW), 2025j)
Italy	Li (battery grade), Ni, Co, Cu	Recycling	Portovesme srl	Portovesme CRM Hub	2029	(European Commission (DG GROW), 2025h)
Poland	Ni (battery grade), Cu, Co, Li (battery grade), PGMs, Mn (battery grade)	Recycling	Elemental Strategic Metals Sp. z o.o.	POLVOLT	2029	(European Commission (DG GROW), 2025g)
Spain	Cu, PGMs, Ni	Recycling	Atlantic Copper SLU	CirCular	2026	(European Commission (DG GROW), 2025c)
Sweden	Mn (battery grade), Li (battery grade), Graphite (battery grade), Ni (battery grade), Co	Recycling	Northvolt Revolt AB	NorthCYCLE	No Data	(Europäische Kommission, 2025)

5.3.5 Palladium and platinum

Source

Russia is the world's largest producer of palladium, with an estimated 75,000 kg in 2024 for palladium (Fig. 5.8), followed by South Africa (72,000 kg), and third largest producer for platinum (Fig. 5.9) with estimated 18,000 kg in 2024 (USGS, 2023), but Canada and Zimbabwe are also noteworthy producers of platinum and palladium (USGS, 2025). Russia is also a player in the global export of refined palladium, accounting for 30% in 2020 (Europäische Kommission, 2022a). Furthermore, Russia's share of the platinum exports was 7% in 2020 (Europäische Kommission, 2022b).

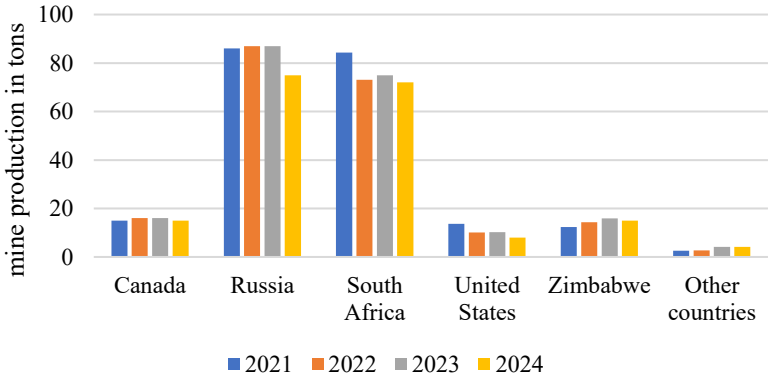

Figure 5.8 Mine production for palladium in tons of contained palladium from USGS mineral commodities. Data for Russia and 2024 are estimated (based on Government report) (USGS, 2023, 2024, 2025).

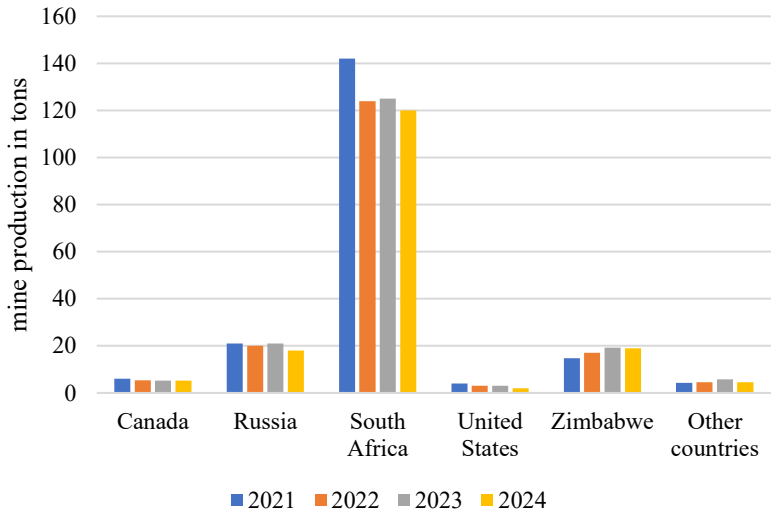

Figure 5.9 Mine production for platinum in tons of contained platinum from USGS mineral commodities. Data for Russia and 2024 are estimated (based on Government report) (USGS, 2023, 2024, 2025).

Adaptation

Imports of refined palladium can be diversified through current production in South Africa and Zimbabwe (Europäische Kommission, 2022a). It is expected that the global platinum market would be in deficit until 2030, making diversification of platinum producers more difficult. Nornickel, the world's largest producer of palladium and grade-1 nickel with headquarters in Russia, is now unaffected by the sanctions, therefore there are no restrictions in place (Europäische Kommission, 2022a).

For PGMs, currently six projects supported by the EU from extraction, and recycling, as well as one integrated approach on extraction and processing. These projects do not only cover PGMs, but also other raw materials as cobalt, copper, nickel and more (Tab. 5.2). The estimated production numbers for palladium and platinum are not available, but are unlikely to cover the future EU’s demand.

Tab. 5.2 Projects among the 47 announced by the EU supported projects for strategic raw materials which cover PGMs in form of extraction, recycling, processing. As these projects also cover nickel and nickel in battery grade, the same are shown in table 1.

Country	Strategic raw material	Type	Promoter	Project name	Estimated production	Reference
Spain	Co, PGMs, Ni (battery grade), Cu	Extraction	RIO NARCEA RECURSOS S.A.	Aguablanca Project	2026	(European Commission (DG GROW), 2025a)
Finland	Co, PGMs, Cu, Ni (battery grade)	Integrated: Extraction, processing	Anglo American Services (UK) Ltd.	Sakatti Project	2030	(European Commission (DG GROW), 2025k)
Italy	Cu, Ni (battery grade), PGMs	Recycling	Circular Materials s.r.l.	RECOVER-IT	2026	(European Commission (DG GROW), 2025j)
Italy	Li (battery grade), Ni, Co, Cu	Recycling	Portovesme srl	Portovesme CRM Hub	2029	(European Commission (DG GROW), 2025h)
Poland	Ni (battery grade), Cu, Co, Li (battery grade), PGMs, Mn (battery grade)	Recycling	Elemental Strategic Metals Sp. z o.o.	POLVOLT	2029	(European Commission (DG GROW), 2025g)
Spain	Cu, PGMs, Ni	Recycling	Atlantic Copper SLU	CirCular	2026	(European Commission (DG GROW), 2025c)

5.3.6 Vanadium

Source

Vanadium is an important metal in the production of highly toughened steels and superalloys, as well as vanadium redox flow batteries (Neitzel, 2022). In 2019, the EU mostly sourced refined vanadium from Austria (52%), followed by Russia (32%) (Neitzel, 2022). In the same year, China supplied 80% of Germany's vanadium oxide/hydroxide (total import value $6.28 mio. USD), but in 2021 80% of the German imports origin from Netherlands (OEC, 2023). The Netherlands, in turn, obtained vanadium concentrates from South Africa (80% in 2019, 41% in 2021) (OEC, 2023). Russia has the world's second-largest mining production of vanadium after China (estimated 70 kt), with an estimated 21 kt of vanadium content (as of 2024) (Fig. 5.10) (USGS, 2025).

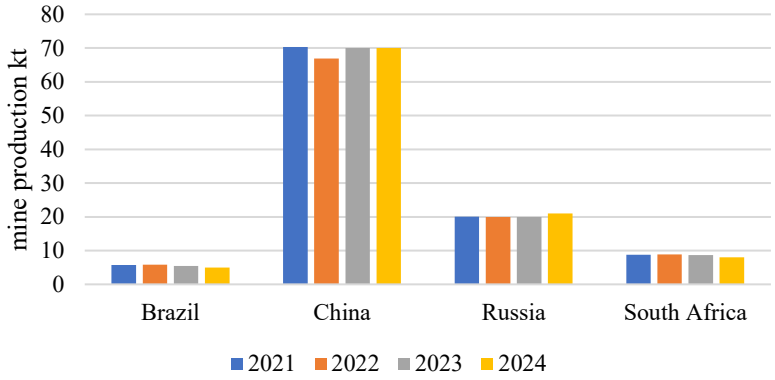

Figure 5.10 Vanadium mine production in kilotons (kt) of contained vanadium content with data from USGS mineral commodities. Data for 2024 and individual values between 2021 and 2023 are estimated (USGS, 2023, 2024, 2025).

Adaptation

There are no specific import bans on vanadium in the EU's sanctions packages against Russia (Europäischer Rat/Rat der Europäischen Union, 2025b). The EU, including Germany, is completely dependent on imports for vanadium. Production in China, Russia, South Africa and Brazil has remained relatively constant since 2021, as has global production (2021: 105 kt, 2024: est. 100 kt) (USGS, 2023, 2025).

Vanadium is classified as critical but not as strategic raw material, thus none of the 47 projects on strategic raw materials cover vanadium.

5.4 Discussion

5.4.1 The EU strategic sectors

The EU defined five relevant sectors “renewables, e-mobility, energy industry, ITC (information technology and communication), and aerospace and defense”, being most relevant for the economy in the EU (European Commission, 2023). This has been linked to the supply risk of raw materials (European Commission, 2023). However, the products listed for some industrial sectors such as PV, wind power, ITC, batteries, drones, among others, are produced in China with competitive technology and price benefit, and imported to Europe.

In December 2024, NATO drew up a list of 12 defense-critical raw materials: aluminium, beryllium, cobalt, gallium, germanium, graphite, lithium, manganese, platinum, rare earth elements, titanium, tungsten (NATO, 2024). Interruptions or failures in supply chains with these raw materials could therefore jeopardize the production of defense systems, for example, if there is no stockpiling that could ensure a short or medium-term supply.

5.4.2 Raw material strategy of the EU

Diversifying EU imports, reducing market concentrations, and fortifying the European value chain for strategic and critical raw materials are the objectives of the European regulation on critical raw materials (Europäische Kommission, 2023b). Due to the EU's inability to supply these raw materials entirely from domestic resources, foreign trade will remain necessary (Europäische Kommission, 2023b). The EU is supporting bilateral agreements with third countries and local supply chains to reduce reliance on market concentrations, which calls for both short and long-term actions (Europäische Kommission, 2023c). The European "Critical Raw Materials Act (CRMA)" aims to ensure the EU's future supply of critical and strategic raw materials (Europäische Kommission, 2023d). The CRMA aims to increase the EU independence in strategic and critical raw materials, and set benchmarks for 2030, as 10% of the EU need of strategic raw materials has to be produced within the EU member states, 40% of the annual EU consumption of strategic raw materials has to be processed within the EU and 25% to be covered by recycling. Additionally, the EU aims to limit 65% of an individual strategic raw material import origins from a single third country, accelerate approval procedures, and expand refining and processing facilities (Europäischer Rat/Rat der Europäischen Union, 2025a). Although such benchmarks are good and important, they are unlikely to be achieved in the given timeframe (Hilgers and Busch, 2024).

5.4.3 EU strategic raw material projects

In an effort to diversify supply chains, the EU is supporting 47 (as of April 2025) projects throughout Europe with anticipated capital investments of € 22.5 bio. for strategic raw materials, four of which are located in Germany (Europäische Kommission, 2025). The projects include various stages, such as recycling (e.g., Elemental Strategic Metals Sp. z o.o., for nickel in battery quality, copper, cobalt, lithium in battery quality, PGM, manganese in battery quality), processing (e.g., graphite in battery quality at the NGC Battery Materials GmbH in Germany), substitution (e.g., PCC Thorian GmbH in Germany for graphite in battery quality), extraction for copper in Romania (Euro Sun Mining Inc.), or an integrated approach to extraction and processing (e.g., lithium in batterie quality from Eramet in France) (Europäische Kommission, 2025; European Commission, 2025).

However, the EU Commission also received proposals for projects from countries outside EU. The decision about the potential selection of such projects will be considered at a later time (Europäische Kommission, 2025). These might potentially cover the three strategic raw materials titanium, silicon, and bismuth, for which there are currently no funded projects.

5.4.4 Importance of the Russia-China strategic alliance for the economy

The European Union's sanctions on Russia also have an impact on the Chinese economy. Previous trade routes for Chinese commodities through Russia to Europe, and hence to Germany, no longer exist; an alternative route across the Caspian Sea allows for just three to five percent of the trade volume that used to move through Russian routes to Europe (Grosser, 2022). In the future, trade processes will be streamlined and accelerated by a joint venture between Azerbaijan, Kazakhstan, Turkey, and Georgia. This is aimed to diversify commercial routes via Central Asia.

5.4.5 USA – Ukraine raw material deal

On April 31, 2025, the formation of a reconstruction fund for Ukraine was settled between the USA and the Ukraine (Spiegel Ausland, 2025; ZDF, 2025). While the infrastructure in Ukraine is to be rebuilt, the USA thus secures access to raw materials such as oil, gas, and minerals. For this, 50% of the revenue from future extraction licenses or raw material sales from Ukraine should be paid into the fund. From the Ukrainian side, it was suggested that the USA fulfil its share with money, but also with new arms deliveries – for example, with air defense systems (Spiegel Ausland, 2025). The USA seems particularly interested in rare earths, but as of now, the agreement is that Ukraine should retain all ownership rights over its mineral resources.

5.4.6 EU – Ukraine raw material deal

On July 13, 2021 the EU and Ukraine signed a MoU “Memorandum of Understanding between the European Union and Ukraine on a Strategic Partnership on Raw Materials”, according to the Directorate-General for Internal Market, Industry, Entrepreneurship and SMEs (European Commission, 2021b, a). This is based on the high potential in lithium and titanium deposits (Schulze, 2023). This strategic partnership covers primary, secondary raw materials and batteries (European Commission, 2021b). Therefore, geological and mining exploration, raw material extraction, processing/refining and transport and monitoring, but also urban waste treatment, and recycling will be part (European Commission,

2021b). However, no official announced projects between EU member states and the Ukraine are published so far (as of 26.05.2025).

5.4.7 Recycling, substitution and circular economy

Recycling requires smelters, which in turn require sufficient, reliant and affordable energy. Not all metals can be recycled or substituted, and product-specific analyses show that recycling is not always more cost-effective or environmentally friendly than mining (Schmidt et al., 2020). Furthermore, an increasing demand on metallic raw materials is expected due to growing world population, increasing prosperity and technological innovation (Hilgers et al., 2021; Hilgers et al., 2023).

The recycling share is denoted as the End-of-Life Recycling Input Rate (EoL-RIR), which is a raw material indicator that is calculated based on a number of factors, including raw material demand and the amount of materials in end-of-life scrap (EoL) that can be recycled (Eurostat, 2022). The indicator thus measures how much input of a raw material in the production system comes from recycling of end-of-life scrap (Recycling Input Rates, RIR), where the origin of the scrap is may unknown, such as through import into the EU (Eurostat, 2022). Scrap from manufacturing processes ("process or new scrap") is not considered in this context because its composition is more homogeneous and known (Eurostat, 2022). Recycling is more cost effective for process or new scrap (Eurostat, 2022). End-of-life scrap, on the other hand, is made up of a variety of materials and alloys, making recycling secondary raw materials more difficult (Eurostat, 2022).

For **aluminium** the demand is expected to rise from 90 Mt in 2020 to 150 Mt by 2040, but recycling rates in 2022 in the EU are at 32% EoL-RIR and 50% in Germany (Kinch, 2020; Eurostat, 2022; DERA and acatech, 2023: 21). Substitutions for aluminium in lightweight construction are unlikely, and scrap availability will initially increase slowly due to market growth (DERA and acatech, 2023: 30).

The EU's recycling rate for **nickel** is 16% EoL-RIR in 2022 (Eurostat, 2022). Secondary **nickel** can be obtained through processing stainless steel scrap or recovering nickel from lithium-ion batteries (USGS, 2023). The global demand is expected to rise from 3.1 Mt in 2023 to 6.4 Mt by 2040 with “clean energy” scenario from IEA (IEA, 2024).

In 2022, approximately 110 t of **palladium** and **platinum** were recovered worldwide from scrap, with autocatalyst recovery accounting for a significant portion of this (USGS, 2023). Global demand for platinum is expected to increase by 2040 to up to 230–800 t in 2040 for platinum (Drobe, 2022) or 66–810 t, which would be up to 426% of mining production in

2018 after DERA (2021). Platinum recycling rates in the EU are 11% EoL-RIR and 10% for palladium in 2022 (Eurostat, 2022).

Titanium dioxide, titanium metal, and welding wire coatings are made from minerals like ilmenite, rutile, leucoxene, slag, and synthetic rutile (USGS, 2023). Global demand for titanium could increase to up to 55% of 2018 production by 2040, and for titanium sponge to up to 72%, which would be a need of 142.120 t (DERA, 2021). The EU's titanium recycling rate is in 2022 at 1% EoL-RIR (Eurostat, 2022).

Lithium

The global lithium demand is expected to rise from 165 kt t in 2023 to 1,326 kt in 2040 with the “clean energy” scenario from IEA [64]. The EoL-RIR for lithium in the EU is 0% in 2022 (Eurostat, 2022).

Noble gases

For noble gases, recycling, re-use or substitution in industrial application is common, where technically feasible (Elsner, 2018; Europäische Kommission, 2022c). For krypton, the interest in recycling is only limited due to global oversupply (Elsner, 2018). Data about recent changing demands, as e.g., the neon demand increased by globally 6.3% per year between 2000 and 2015, and by 9.0% between 2012 and 2017, the global demand for neon is expected to increase by 6.7% annually between 2017–2022 (Elsner, 2018 and references therein).

Vanadium

The vanadium demand is estimated by up to 77% of primary mine production by 2040 as of 2018 (DERA, 2021). The total global demand on Vanadium was 320 t in 2018 (0.4% of mining production) and could be between 60,770 t and 69,430 t in 2040, regard assumed future technology options of DERA (DERA, 2021). The EoL-RIR for Vanadium within the EU is currently 1% (as of 2022) (Eurostat, 2022).

Given values for demand of individual raw materials is, however, always dependent on current technology and future innovations. Therefore, the values can change within time and e.g., new technologies or substitution.

5.4.8 New mines, recycling and processing in Europe

The European "Critical Raw Materials Act (CRMA)" came into force on 23.05.2024 and aims to ensure the EU's future supply of critical and strategic raw materials (Fig. 5.11) (Europäische Kommission, 2023d).

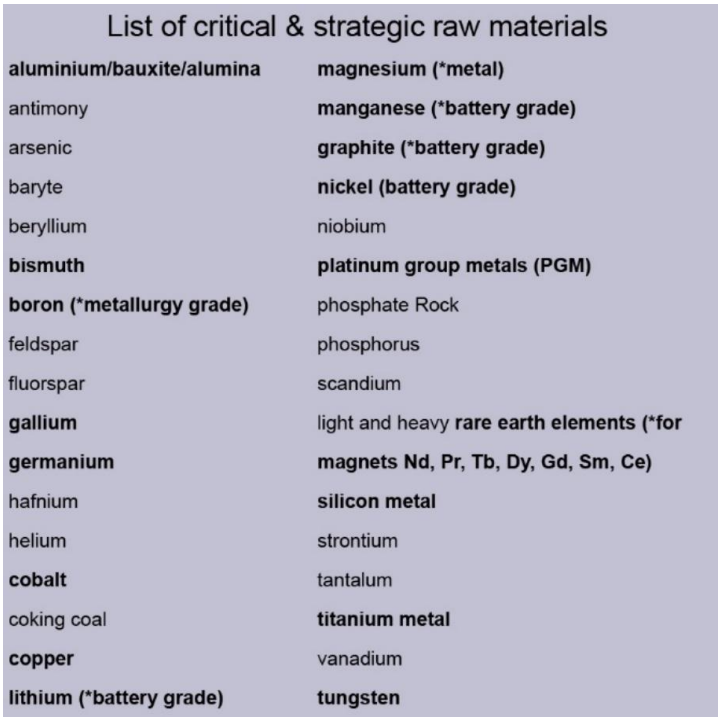

Figure 5.11 List of critical and strategic (bold) raw materials for the EU as of 11. April 2024 (European Union, 2024), modified after Ölmez and Hilgers (2023). Copper and nickel do not meet the thresholds of the Critical Raw Materials Act, but are classified as strategic raw materials. For some strategic raw materials, only certain classifications (e.g., battery quality) are significant and are marked with an asterisk.

For all metals, reliance on imports will persist, with recycling capacity from smelting and refining contributing to primary raw materials. As a result, the EU's political signal through the CRMA objectives is vital, with the benchmark of achieving a 10% share through domestic EU mining and a 40% share through domestic processing of strategic raw materials by 2030. Although the need of a reliable raw material supply is increasingly recognized, lengthy licensing procedures frequently result in the early termination of mining operations. Additionally, the average time from discovery to mine operation is 18 years (Manalo,

2024), and it is thus unlikely the benchmarks are achieved in the given time frame (cf. Hilgers and Busch, 2024).

Although the EU is expanding the availability of raw materials within the EU countries with the projects currently being funded, no estimates are yet available on the proportion of future coverage on the EU demand of the individual raw materials nor are all strategic raw materials covered so far. Projects with countries outside the EU have been submitted, but there are no funded projects yet (Europäische Kommission, 2025).

The strategic projects benefit from streamlined approval regulations, as approval procedures for extraction projects should not take longer than 27 months and for other projects no longer than 15 months, otherwise, approval procedures in the EU could take five to ten years (Europäische Kommission, 2025). However, if supply chains suddenly cease to exist, for example due to disrupted trade routes because of war, rapid actions are not possible and thus the supply of strategic raw materials which may be also of importance for the national and civil security are not guaranteed.

5.4.9 New collaboration with countries outside EU

African countries, as e.g., Botswana, have undeveloped mining potential despite its relatively stable political and social environment (Ölmez and Hilgers, 2024b, a). Botswana is rich in raw minerals such as e.g., copper and nickel. Previous investments in the country have primarily come from China. The expansion of strategic agreements, as well as investment in mining and local processing (as e.g., copper refining), helps to create value in resource-rich countries, secures local jobs and training opportunities, and ensures Germany's secure access to raw materials. The EU's political signal to diversify, through the CRMA's target requirements, is critical when the EU relies on more than 65% imports of strategic raw materials from a third country.

5.5 Conclusions

The CRMA and the first currently funded 47 strategic projects are an important step towards diversification, but the CRMA benchmarks are unlikely to be achieved in the given time frame. Import from third countries remain essential and demand cannot be supplied by recycling and circular economy alone.

An energy-intensive smelting and refining industry is required, as well as sufficient amounts primary raw materials and recyclable materials from high-quality waste, to ensure the supply of raw materials. Countries like China were able to significantly increase their

titanium sponge production in three years by a factor of c. 1.6. In the same time Japan increased production by 12% and Russia reduced production by 26%.

The presence of heavy industry in the country can be evident for raw material supply. Countries like South Korea demonstrate the importance of heavy industry, as the production capacities of domestic steel mills were able to establish the production of the missing noble gases required for semiconductor production.

None of the raw materials considered ran short in supply due to adaptation strategies. These included the stockpiling of critical raw materials, diversification and increased production of other mines, smelters and refineries, and the presence of associated industries.

6 Resilient supply of critical and strategic raw materials for Germany – Potentials in Africa

6.1 Abstract

The global demand for mineral and metallic raw materials is increasing due to the energy and mobility transition, climate protection and general technological progress. A growing world population, rising prosperity and increasing demand for raw materials emphasize the need for responsible mining, as recycling and closed-loop recycling alone cannot meet the demand for raw materials and material quality. While other countries operate globally and invest directly in mining, Germany and other countries in Europe lack major globally operating companies in the field of metallic raw materials extraction. In an increasingly protectionist, multipolar world, economic, geopolitical and security policy measures are needed to ensure a resilient supply of raw materials. This applies not only to the EU's strategic sectors such as electromobility, renewable energies, defense and space, but also to other, currently unknown, technological advances. This article highlights African countries such as Botswana, Morocco, Namibia, and Zimbabwe that offer various opportunities for securing raw materials through mining, processing of mining products and participation in smelters, which are hardly recognized by German investors.

6.2 Introduction

Resilient supply chains for metallic raw materials are essential for Germany as an industrial nation. A secure supply of raw materials and innovative alloys form the basis for the competitiveness of the economy and the prosperity of the population. Domestic raw materials such as industrial rocks and minerals, limestone, rock salt, potash salt, gypsum and anhydrite cover the current demand (BGR, 2023). However, the German economy depends on imports of metallic raw materials. There are currently no large, internationally active mining companies in the metal raw materials sector headquartered in Germany.

Countries with a high share of GDP in manufacturing such as China, Japan, the USA, South Korea and, in Europe, Germany (20.2 % of gross value in 2021 (Destatis, 2022)) require resilient supply chains. Primary mining of metallic raw materials does not currently take place in Germany (BGR, 2023) although domestic deposits are known and it is highly

likely that further new deposits would be found with modern exploration techniques. From a global perspective, Africa plays an important role as a continent rich in raw materials, with around 30% of the currently known global mineral reserves. A large number of different metallic raw materials are produced in Africa, and direct investments in mining projects are largely made by companies and mining firms based, for example, in China, South Africa, the UK, the USA, Canada and Australia (e.g., Ericsson et al., 2020). Smaller projects such as the direct purchase of cobalt from the BMW Group's raw material producer in Morocco, for example, secure a company's supply chains and at the same time increases value creation in the mining country (BMW Group, 2019). In recent decades, large, internationally active companies based in Germany in the mining sector have been transformed into plant manufacturers or travel companies. The deposits of other German industrial groups have been sold off. Due to energy costs, energy volumes, the CO_2 footprint and lower industrial production in Germany, the smelting and refining of primary raw materials from ore and secondary raw materials from scrap is currently being scaled back or relocated outside of Europe. At the same time, issues relating to the necessary expansion of recycling and the circular economy are becoming increasingly important in the media and political arena (BGR, 2021, 2023). However, this alone will not be able to cover the raw material volume of an export-oriented industrialized country in the future and raw material quality cannot be guaranteed (Hilgers and Becker, 2020; Hilgers et al., 2021).

The envisioned industrial transformation caused by the German energy- and mobility transition and general technological progress require resilient supply chains in order to secure the growing demand for raw materials in an increasingly protectionistic environment of a multipolar world. The EU sets goals to be achieved with the Critical Raw Materials Act as an EU law and comprehensive packages of actions. The EU currently defines 34 raw materials as critical and 17 of these as strategic (Europäische Kommission, 2023a). In addition to the construction of energy converters for renewable energy, the EU has identified energy storage for battery mobility and defence and space as strategic sectors (European Commission, 2020). The BMWK's raw materials fund in Germany is also set to provide a total of € 1 billion by 2028, as already exists in France and Italy, for example, with € 2 billion each (Zapf, 2024). This article examines aspects of Germany's supply of metallic raw materials. In order to meet the increasing demand for raw materials and maintain the competitiveness of Germany as an industrialized country, raw material sources need to be diversified. However, it can take well over ten years from exploration to production of metallic raw materials.

The African continent is presented as a major producer of raw materials. The African countries of Botswana, Morocco, Namibia, and Zimbabwe are analyzed as examples, but other African countries of note are also included.

6.3 Germany's demand for metallic raw materials

In 2022, around 27.4% of raw material imports to Germany in terms of volume came from EU member states and 9.2% from Africa (for more see Fig. 6.1, 6.2) (BGR, 2023). Around 40% of metallic raw materials excluding recycled raw materials came from the EU-27 (BGR, 2023). 20.2% of supplies of ores, concentrates and refined metals originated from Africa (BGR, 2023). In 2021, the share of ores, concentrates and refined metals from Africa was 17.6% (BGR, 2022). Recycled raw materials imported to Germany from Africa were only 1.1 % in 2022, around 82.8 % were imported from the EU-27 (BGR, 2023).

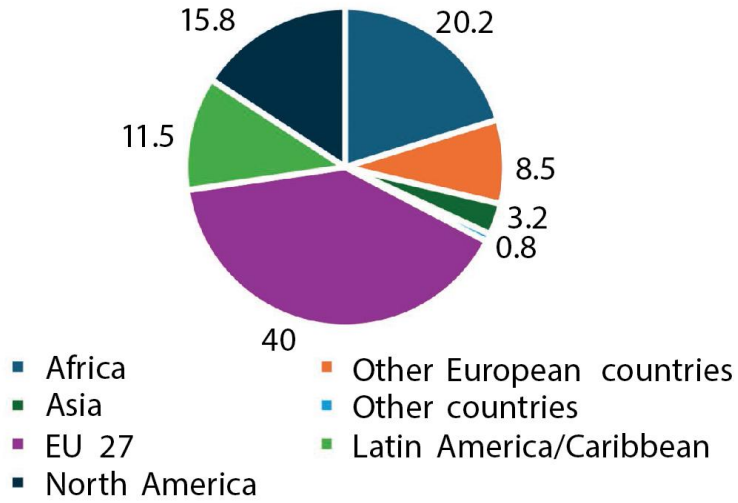

Figure 6.1 Raw material imports of metallic raw materials (ores, concentrates and refined metals, excluding recycled raw materials) to Germany in 2022 (percentage share by volume). In terms of volume, most imports came from Europe and Africa, data from BGR (2023).

In terms of value, the import and export total of raw materials (energy, metals excluding recycled raw materials, metallic recycled raw materials and non-metals) increased from 2020 to 2021, but the total import and export quantities of these raw materials decreased. Imports of raw materials to Germany equaled € 139.7 bn in 2020 and € 310.6 bn in 2022, while exports amounted to € 81.3 bn in 2020 and € 134.5 bn in 2022 (BGR, 2023). The import volume of raw materials decreased from 386.1 Mt in 2020 to 342.5 Mt in 2022, while the export volume was 157.5 Mt in 2020 and 130.3 Mt in 2022 (BGR, 2023). The increased prices are due to higher commodity prices for metals and energy raw materials (BGR, 2023). South Africa is Germany's most important trading partner for metallic raw

materials in Africa (Monnerjahn, 2023). Here, Germany imported raw materials such as titanium (Ti), iron (Fe), chromium (Cr, ores and concentrates), aluminium (Al, refined metal), ferro-manganese alloys and ferro-vanadium alloys (FeMn and FeV) in 2022 (Fig. 6.2) (BGR, 2023). Other imports came from Guinea (Al), Morocco (Pb), Sierra Leone (Ti) and Burkina Faso (Zn).

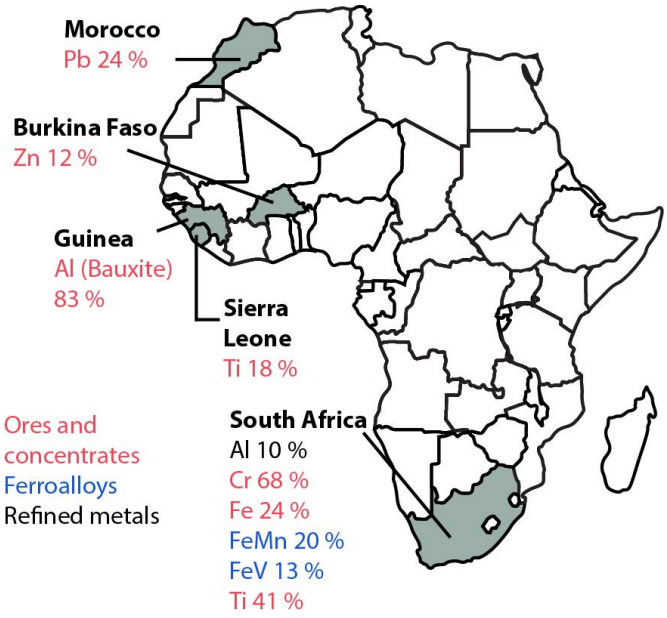

Figure 6.2 Share of German imports (quantitatively) of industrial metals (ores and concentrates, refined metals) and metal alloys in 2022 from Africa with an import share of over 10%, quantitative data from BGR (2023). Imports of ore and concentrates are mainly from South Africa (Cr, Ti, Fe) and Guinea (bauxite). Al: aluminium, Cr: chromium, Fe: iron, FeMn: ferro-manganese alloy, FeV: ferro-vanadium alloy, Pb: Lead, Ti: Titanium, Zn: Zinc.

6.4 Exemplary market concentrations and geographical locations

Some primary raw materials show significant market concentrations. For example, in terms of global production volumes, more than 70% of cobalt is mined in the Democratic Republic of the Congo (DRC), around 89% of iridium and 70% of platinum is produced in South Africa, 60% of natural graphite and 50% of dysprosium is produced in China (Deutscher

Bundestag, 2023). Approximately 47% of lithium is mined in Australia and 30% in Chile (Deutscher Bundestag, 2023). The processing of raw materials is also concentrated. China plays a major role in this context. 100% of natural graphite and dysprosium are processed there; in addition, 70% of cobalt, 60% of lithium and, for example, 90% of manganese are processed in China (Deutscher Bundestag, 2023). However, African countries such as South Africa also have a significant position in the processing of primary raw materials. 90% of iridium is processed in South Africa and 8% in Zimbabwe, while around 71% of platinum is processed in South Africa and around 8.6% in Zimbabwe (IRENA, 2023).

6.5 Exemplary critical raw materials from Africa

Around 30% of global mineral reserves are located on the African continent (African Business Guide, 2023). Guinea is a globally requested supplier of bauxite, the Democratic Republic of the Congo (DRC) is a global leader in the export of cobalt and Rwanda is known for its tin, coltan (and extracted elements), and tungsten resources (African Business Guide, 2024). Estimated cobalt production in the DRC for 2023 is 170,000 t with estimated reserves of 6 Mt, around 54.5 % of estimated global reserves (USGS, 2024).

6.5.1 Botswana

The Republic of Botswana has been a democracy since 1966 with a population of 2.63 million and a GDP of USD 7738 per capita in 2022 (Destatis, 2024a). The Human Development Index (HDI) in 2021 is 0.693 (low 0, high 1) (UNDP, 2022). Various mineral resources are mined in Botswana, including diamonds, iron ore, coal, copper, nickel, salt, silver and potash (Schill, 2022). Botswana is one of the world's largest producers of diamonds and is estimated to have produced 7 million ct of industrial diamonds and 17 million ct of gem-quality diamonds in 2023 (USGS, 2024). Furthermore, 943 kg of gold and 34,000 kg of silver were produced in Botswana in 2019 (Yager, 2023). Mining in Botswana is regulated by the Mines and Minerals Act of 1999 (Yager, 2022). Copper and nickel were mined and smelted in the "Bamangwato Concessions Limited (BCL)" Phoenix and Selebi-Phikew mines until 2016 (production of 14,273 t of Ni and 11,348 t of Cu, 248 t of Co in 2016) (Yager, 2022). Mining of palladium, silver and platinum was discontinued in 2015 (Yager, 2022). Mining and smelting operations were stopped at the end of 2017 due to high energy and processing costs and falling copper prices (Yager, 2022). Although the production of copper and silver was resumed in 2019 (Khoemacau mine), there is a lack of investment to resume the production of cobalt and nickel (Yager, 2022). A memorandum of understanding was signed between Botswana and Premium Nickel Resources Corp (Canada) to resume work on the mines for copper and nickel (Knupp, 2021). The Kalahari Belt, for

example, which is currently not fully explored, could potentially be suitable for exploration and diversification efforts (Prof. Dr. Thierry Olivier Bineli Betsi, 2023, personal communication).

6.5.2 Morocco

Morocco is a constitutional monarchy and a population of 37.458 million, the GDP in 2022 was USD 3570 per capita (Destatis, 2024b). The Human Development Index (HDI) was 0.683 in 2021 (UNDP, 2022). Some mineral and metallic raw materials are mined in Morocco. In 2023, for example, an estimated 1.2 Mt of barite (14.1% of global mine production), an estimated 35 Mt of phosphate rock (15.9% of global mine production) and an estimated 2300 t of cobalt (1.2% of global production) were mined in 2022 (USGS, 2023, 2024). However, copper, lead, gold, cobalt, zinc, iron ore, manganese, silver and tungsten are also produced in Morocco (e.g., Managem Group). Morocco's mining industry is to be further diversified in the future, creating opportunities for foreign investors. Mining is particularly important for the Moroccan economy and accounts for around 26% of the country's export revenue; according to the Fédération de l'industrie Minérale, around 85 companies and 450 individual entrepreneurs are active in mining (Umann, 2023). However, Morocco is dependent on imports of machinery for the mining industry; the most important supplier country in 2023 was China (€ 280 million), including drilling equipment and systems for processing and safety technology (Umann, 2023). Imports from Germany (€ 180 million) ranked in second place (Umann, 2023).

6.5.3 Namibia

Namibia is a democratic republic and has 2.567 million citizens in 2022. The GDP is USD 4854 per inhabitant per year (Destatis, 2024c). The Human Development Index (HDI) in 2021 was 0.593 (UNDP, 2022). The country's most important raw materials are diamonds and uranium. Mining (and industry) makes a significant contribution to GDP at 26.4% (2019) (GIZ, 2021). In addition to diamonds and uranium, gold, zinc and lead, tin, salt and other raw materials are also mined, and copper concentrates from Zambia are processed and reexported in the country (GIZ, 2021). Exploration is taking place for rare earths, cobalt and copper, and also for graphite and lithium. Further projects are expected for the exploration of zinc, tin and iron ore (GIZ, 2021). Namibia also has large phosphate deposits, the mining of which is considered environmentally controversial (GIZ, 2021). Low market prices (e.g., for diamonds) and problems with the power supply partially restrict mining (GIZ, 2021).

6.5.4 Zimbabwe

The Republic of Zimbabwe has 16.321 million inhabitants in 2022, with a GDP of USD 1991 per capita (Destatis, 2024d). The Human Development Index (HDI) in 2021 is 0.593 (UNDP, 2022). In 2023, Zimbabwe had an estimated 1.9 % of the global reserves of platinum group metals and produced about 1.9 % of the globally estimated lithium output (USGS, 2024). Zimbabwe also has deposits of almost 40 mineral commodities, including chromium, diamonds, iron ore, gold, cobalt, copper, manganese, nickel and rare earth elements (Najjar, 2024). The Great Dyke in particular offers potential for mining platinum group metals (Najjar, 2024). Zimbabwe also has significant potential for the extraction and processing of lithium; it currently has the sixth largest known lithium reserves in the world (Schmidt, 2023). Lithium is mined, for example, in hard rock projects from pegmatites in the Mutare greenstone belt (Tempest Minerals LTD, 2019) extracted from spodumene and petalite. Tempest Minerals (Australia) acquired further licences for lithium extraction in 2019. Other pegmatites for potential lithium extraction are the Bikita, Arcadia, Kavativi and Zulu pegmatites (Knupp, 2023). From November 2021 to February 2022, a large number of Chinese companies, e.g., Chengxin Lithium Group and Zhejian Huayou, were involved in lithium exploration and are also looking to invest in lithium processing projects (Knupp, 2023). The Great Dyke also offers potential for the extraction of platinum, palladium and rhodium as an example (Schmidt, 2015).

6.5.5 Investments in mining in Africa

Investments in mining depend on a variety of factors. These include the energy supply, infrastructure, social and political situations or unrest in the country and factors that are summarized as the World Governance Indicator (WGI) of the World Bank. These include “control of corruption”, “regulatory quality”, “voice and accountability”, “government effectiveness” and “rule of law” and “political stability and absence of violence and terror” of a country (The World Bank, 2023). Botswana, for example, is an African country that has a particularly good WGI. Botswana is also one of the wealthiest countries in Africa (GDP USD 20 billion in 2022) (Destatis, 2024a). Other countries, such as Zimbabwe, have low WGIs compared to Botswana (cf. Ölmez and Hilgers, 2024b). Zimbabwe also deals with hyperinflation with an annual consumer price inflation rate of around 193.4 % in 2022, which was around 98.5% in 2021 (IMF, 2024). To counter inflation, Zimbabwe introduced a new currency “Zimbabwe Gold” (ZiG) on 5 April 2024, which is pegged to the price of gold (Reserve Bank of Zimbabwe, 2024). The Worldwide Governance Indicator (WGI) from the World Bank shows that some resourcerich African countries demonstrate general conditions and would be interesting partners for the expansion of a commodity partnership (Fig. 6.3).

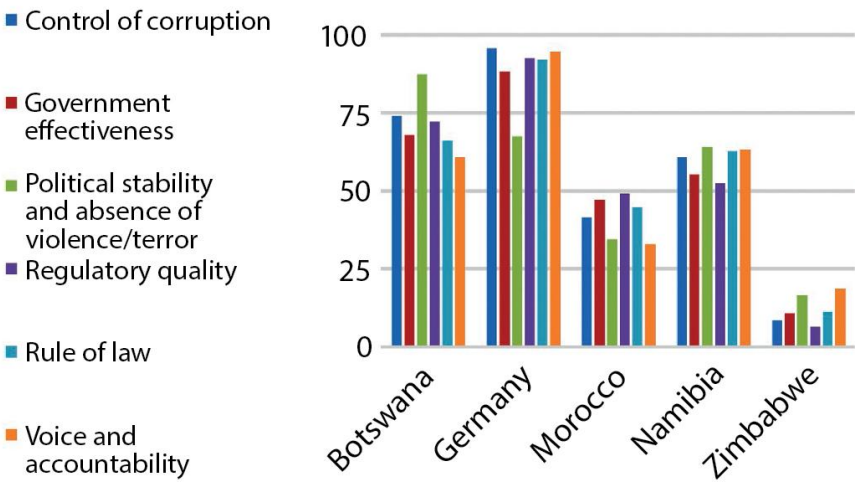

Figure 6.3 World Bank "Worldwide Governance Indicator" (WGI) data for Botswana, Germany, Morocco, Namibia and Zimbabwe in 2022, data from The World Bank (2023).

Direct investments in large-scale mining, smelting and refining, such as those carried out by China in African countries, are not currently known from German companies. Projects for responsible raw materials management by OEMs (original equipment manufacturers) (e.g., BMW Group, 2019; Volkswagen AG, 2023; BMW Group, 2024) are ensured through supply contracts and quality controls. Such opportunities remain excluded from German SMEs. The required increase in transparency in the extractive sector is to be implemented as part of the African Mining Vision (African Union, 2009). The Extractives Industries Transparency Initiative (EITI) is intended to contribute to increasing transparency. Currently, more than 50 countries are members, including, Germany and the DRC (African Union, 2009; EITI, 2023). The African Mining Vision, for example, supports small-scale mining (African Union, 2009). Due to the increasing global demand for transparency and safety, environmental and health standards, internationally recognized “Environmental, Social and Corporate Governance Standards” (ESG) are also being implemented by globally operating companies (Najjar, 2024). Countries as Zimbabwe are pursuing the goal of encouraging domestic economic value chains. On 6 January 2023, the government in Zimbabwe banned the export of unprocessed lithium (Base Minerals Export Control Order 2023), extracted lithium shall primarily be processed in the country and the export of raw lithium ore requires a special authorization (Knupp, 2023; Najjar, 2024). As a result of the export ban, Chinese companies have been investing in the processing of lithium ore (Najjar, 2024). In 2023, more than USD 1 bn was invested by Chinese companies in the development and acquisition of lithium projects in Zimbabwe (Najjar, 2024). According to USGS (2024) an estimated 3400 t of lithium were produced in Zimbabwe in 2023, around 1.9 %

of the estimated global production in 2023. In contrast to German and other European companies, Chinese investors continue to purchase smelting operations. In 2024, the Canadian company Dundee Precious Metals Inc. sold its shares in the smelter in Tsumeb, Namibia, for USD 49 million to the Chinese Sinomine Resources Group, which was founded in 1999 and now operates globally (Dou, 2024). Thus, another opportunity for German or other European investment in one of the few smelters for processing arsenic-rich ores (Dou, 2024) and the germanium- and gallium-rich slags (Ettler et al., 2022) has passed.

6.5.6 Raw material wealth alone is not enough

The extraction and export of raw materials is a key component of economic development for African countries (Fig. 6.4) (e.g., Hartlieb-Wallthor and Marbler, 2017). The export of raw materials depends on global demand, global market prices and fluctuating market cycles. This is associated with the fluctuation of local employment. The responsible extraction of raw materials is subject to occupational health and safety and environmental protection requirements. It is now increasingly recognized by the politicians that the desired decarbonization of Germany and Europe cannot go hand in hand with mining, smelting and refining in African countries that do not comply with certain occupational health and safety and environmental protection standards (Pickels, 2023). Even though mining, smelting and refining creates jobs in many African countries, it only provides work for part of the population (Kaube, 2023). International investment often fails to materialize due to inadequate energy supplies and a lack of or poorly developed infrastructure. In addition, social and political instability increases investment risks (KfW et al., 2020). At the same time, the extraction of raw materials can increase the depth of value added in the country. The potential of mineral resources in many African countries is also unknown. Insufficiently explored areas and a lack of investment prevent an accurate awareness of possible extraction areas (see African Business Guide, 2023). Due to the increasing global demand for raw materials, more and more African countries that were previously not a focus of investment are becoming potential centers of raw material production (African Business Guide, 2023). At the same time, African countries such as Botswana are urging for investment in mining (Knupp, 2021). The government in Botswana, for example, is seeking to promote further investment in exploration and production (mineral and metallic resources) in order to broaden the country's investment base and enable the diversification of mining alongside the production of high-quality diamonds (Mining Indaba, 2022). However, the proceeds from mining, smelting and refining should reach the country and its population and may not solely be concentrated in the investment countries, otherwise the raw material blessing can also turn out to be a "raw material curse" (e.g., DW, 2023). In order to support the population and the country, the profits from the mining projects should return in form of infrastructure such as roads, clinics and schools (DW, 2023). The mineral resources that

have not yet been extracted are seen as “natural capital” for the future of the country and its people (DW, 2023).

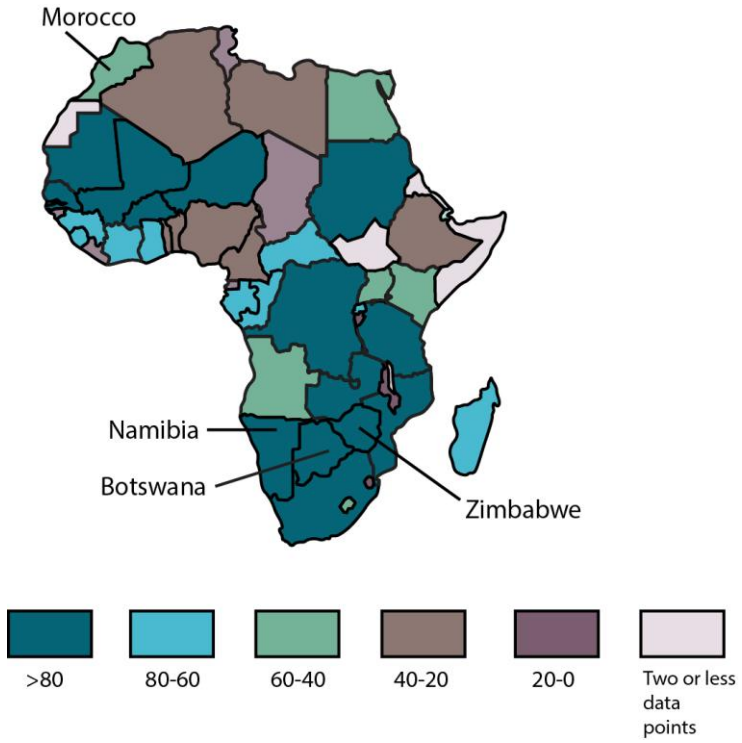

Figure 6.4 "Mining Contribution Index map" (MCI) for 2020 with data from ICMM (2022). The MCI is a measure of the relative importance of the mining sector for the country's economy.

6.6 Discussion

Countries such as China operate and invest directly in mining projects in African countries. Russia is also active in the mining sector in numerous African countries, some of which are accompanied by a military presence (Fig. 6.5) (EPRS, 2024).

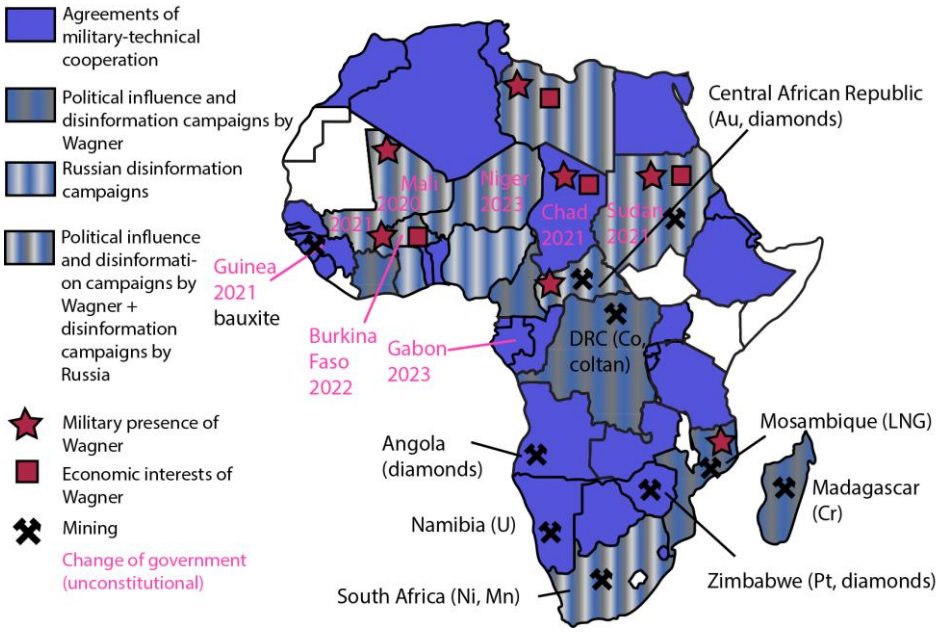

Figure 6.5 Russian influence through military technical cooperation agreements with African countries, political influence through the Wagner military group and disinformation campaign from Russia. The military presence, areas of economic interest and mining cooperation are marked in the countries. Data from 2022 and 2023 from EPRS (2024) and the references listed therein.

Political decision-makers are faced with the challenge of creating framework conditions that enable German/European capital and companies based in Germany/Europe to make a long-term commitment to international raw materials partnerships and to compete with other systems. Social, economic and ecological goals may be achieved through global partnerships. Whether the EU's Green Deal keeps the interests and goals of the raw material partner country in mind should be critically evaluated. Although countries such as Botswana are encouraging direct investment in mining and are providing opportunities for investment in strategic raw materials (e.g., Tsumeb smelter, Namibia or lithium in Zimbabwe), there is no direct investment from Germany or the EU. Fluctuating global prices also affect African countries such as Zimbabwe. The global supply of lithium (battery quality) exceeded demand in 2023, leading to a price collapse of more than 80% (Chingono, 2024). Globally, lithium supply is dominated by Australia, Chile and China (USGS, 2024). Together, they produced around 90% of the raw material in 2023 (USGS, 2024). The consequence of the price drop is a reduction in production, resulting in a market shakeout of less efficient projects. According to a study by S&P Global, the average time from exploration to the start of operations is 16.3 years and for mines from 2020 to 2023 an average of 17.9

years (a) (Manalo, 2024). However, the process depends on the type of deposit and the country in which mining is to take place. Gold deposits have shorter lead times of 15.7 a on average and zinc and nickel the longest (17 and 18.3 a on average) (Manalo, 2024). For example, lead times in Laos (11.3 a), Turkey (12 a) and Africa (DRC, 14 a) are generally shorter than in Canada (18 a) or Indonesia (21 a) and Russia (21.8 a), for example, due to the legal framework (Bastian, 2024; Manalo, 2024). From 2005 to 2009, the average lead time for mines was 12.7 a (Manalo, 2024). The demand for mineral raw materials will continue to rise in the future and will be accompanied by the development of new technologies in the areas of mining and processing (primary raw materials), recycling (secondary raw materials), recycling management and substitution. In order to be able to meet the increasing demand in the future, new deposits must first be explored, identified and developed and then extracted from the ore during smelting and refining and concentrated into a usable metal. Recycling also offers potential to reduce the demand for raw materials from deposits (Hagelüken and Goldmann, 2022), but will not meet demand in the future either. In order to expand supply chains, increase value creation and reduce market concentration, agreements with mining companies and smelters are necessary to enable responsible mining (Najjar, 2024). Mining and recycling go hand in hand with the development of new technologies that are being pushed by the countries involved in exploration, mining technology, processing and metallurgy and thus have direct access to raw materials.

6.7 Conclusions

The African continent holds numerous resources, including some that are still unknown, but could be developed through responsible mining. Unstable supply chains, high (energy)costs and lower demand from industry are leading to an outflow of smelting/refining and expertise from Germany. This limits innovation potential and opportunities for recycling in Germany. Resilient supply chains can diversify investments in mining in African countries. Development times of over 16 years on average until production emphasize the need to invest in exploration projects and develop innovative technologies at an early stage.

7 Conclusions and Outlook

7.1 Conclusions

7.1.1 Reservoir quality assessment

of Upper Cretaceous (Campanian) limestones in the Münsterland Cretaceous Basin, NW Germany

Upper Campanian limestones of the Beckum Member in the Münsterland Cretaceous basin show low porosity (1.0%–18.7%) and permeability (<0.0001 mD–0.2 mD), related to early and burial diagenetic cementation, mechanical compaction and associated formation of compaction bands. Porosity is only enhanced in one sample with faecal pellets, showing dissolution, which does not enhance permeability. Veins showing a preferred NW-SE orientation most likely due to Late Cretaceous inversion and most likely reactivation of older fault systems are partially or pervasively sealed by (ferroan) calcite and additionally by strontianite. Barren fracture surfaces coated by brownish material (e.g., goethite) are most likely the youngest and uplift-related. The occurrence of (ferroan) calcite together with strontianite indicate paleo-fluid pathways. However, the source of strontium to form strontianite remains unknown to date. Host rocks surrounding a fault are not characterized by different petrophysical properties or alteration. The up to 25 m thick Beckum Member lithologies may act as a regional seal, due to low matrix permeability, if not disrupted by faults with associated fractured damage zones. However, this also indicates that geothermal utilization may be limited. Only if open fractures and/or faults are present in the subsurface the fluid pathways could be enhanced.

The newly introduced parameter, the compactable depositional volume (CDV), is derived from petrographic thin section analyses and may be a useful tool to assess timing of cementation in relation to compaction for carbonate rocks, if components as bioclasts with intraparticle porosity are present (in this case calcispheres). Thus, the effect of compactional volume loss on reservoir properties can be assessed. However, the effect of overrepresentation by micrite, resulting in high CDV values, is comparable to the effect of depositional clay minerals forming a matrix on IGV calculations of sandstone samples.

of Middle Triassic limestones at the Upper Muschelkalk-Keuper transition, SW Germany

Middle Triassic Upper Muschelkalk to Lower Keuper limestones on the eastern shoulder of the Upper Rhine Graben in SW Germany show reduced reservoir quality with low matrix porosity (0.13%–10.87%) and low permeability (<0.0001 mD–9.7 mD). The pore space of the rocks is pervasively cemented by early diagenetic (ferroan) calcite. The reservoir quality in the tight limestones is solely related to natural fractures and partially sealed veins.

Plugs measured under elevated confining pressure of 30 MPa show permeabilities of 0.13 mD for a sample containing partially sealed veins parallel to fluid flow direction. Normalizing the permeability measurements to the maximum recorded value of each sample, the partially sealed vein retains c. 41% of the initial permeability as opposed to only 11% of retained permeability in an undisturbed host rock sample. Stylolites also enhance permeability and retain 16% of the initial permeability at 30 MPa.

Fracture clusters for different fracture sets are recorded in the damage zone of a breached kink band. Dominant fracture clusters strike NNE-SSW parallel to the Upper Rhine Graben rift, WNW-ESE, and NW-SE parallel to the current maximum horizontal stress. Furthermore, fracture cluster are not necessarily restricted to faults or their damage zone and may provide additional reservoir opportunities. Fracture clusters striking NNE-SSW, WNW-ESE, and NW-SE may act as potential fluid conduits in the present-day stress field indicated by slip and dilation tendency analyses. Thus, these orientations are of importance for geoenergy application, if the fracture sets are also developed in the subsurface and not pervasively sealed.

Decameter-scale reverse conjugate kink-bands indicate a N-S compressional tectonic phase during formation. They thus likely formed by Alpine far-field stress during the Eocene in the studied region some c. 200 km north of the Alps, which were not documented so far. The kink band boundaries are locally breached and localized reverse and thrust faults, which locally were reactivated by strike slip. The faults planes are partially sealed with calcite. Strike slip movement may be synchronous with Miocene shear along the NNE-striking Rhine graben fault, associated with pull apart basin formation and MVT-mineralization in the region.

of Paleocene-Eocene fractured siliciclastic turbidites in the Vienna Basin, Austria

Drill cuttings from two wells of the 1. to 3. Glauconite Sandstone in the Vienna Basin show low porosity (<5%) controlled by cementation of pore space with mostly ferroan calcite. The IGV obtained from cuttings shows no correlation to the GLS formation or with depth.

This relationship would be difficult to establish on core data, as cores are not continuously taken. The IGV is higher in samples which are moderately well sorted, but show lower IGV at higher detrital quartz and feldspar contents. Furthermore, an overall decrease in IGV with increasing grain size based on median values is noted. The most pronounced influence on IGV are pore-filling and partially pore-filling carbonate cements, while the impact of quartz cement on IGV is minor.

Reservoir quality is independent of compaction of the sandstones and is related to fractures and partially sealed veins, lower optical porosity, higher carbonate vein contents, and lower Fe+Mg contents from pXRF analyses. Fracture formation is postdating the formation of deformation bands, which enhances reservoir properties. The Si/Al-ratio obtained from bulk rock pXRF is used to distinguish between mudrock-rich and sandstone-rich intervals, and can additionally be used to cross-check formation depths of cuttings to relate them to log-derived gamma ray measurements and other well-log data. However, µm-wide partially sealed veins are not visible in image logs. Thus, cuttings can inform about vein occurrence, vein microstructures and textures, that may influence reservoir-scale fluid migration.

Drill cuttings were successfully used to derive a paragenetic sequence, assess reservoir quality controls and changes in the detrital and authigenic mineralogy; the glauconite content is lower in the 1. and 2. Glauconite sandstone (GLS), compared to the 3. GLS. The analysis of drill cuttings supports log-derived petrophysical interpretations in particular in the absence of core material or when working on historic data sets. Drill cuttings can provide the full spectrum of diagenetic reservoir characterization, e.g., assessment of compaction and pore cementation, and allow the identification that partially sealed veins govern reservoir quality.

7.1.2 Raw materials

Analysis of adaptation to the disruption of supply chains during the Russia-Ukraine conflict

The Critical Raw Materials Act (CRMA) and strategic EU-funded projects are a step towards diversification of strategic raw materials. However, the CRMA benchmarks are unlikely to be achieved within the given time frame until 2030. Import of primary raw materials from third countries remain essential, and the future demand cannot be provided by recycling and circular economy alone.

The Russian Federation (Russia) is one of the most resource-rich countries with long-standing economic ties to the EU and Germany. Russia has a large global share in the extraction

of nickel and vanadium ores through mining, but also in refining ores into metals. Therefore, e.g., bauxite/alumina and titanium ore are imported to Russia. There, it is processed using the affordable energy, and exported. Ukraine was a large exporter of steel, titanium, and neon, among others, the latter with a global market share of around 50%, needed for semiconductor production.

The occupation of the eastern Ukraine by Russia disrupted supply chains of raw materials such as oil, gas, and metals to Europe since 2022. None of the raw materials considered (bauxite and alumina, titanium, lithium, noble gases, nickel, palladium and platinum, vanadium) ran short in supply due to adaptation strategies. Stockpiling of critical raw materials, diversification and increased production of other mines, smelters and refineries, and the presence of associated heavy industries counter-balanced bottle necks in supply chains.

For example, South Korea demonstrates that the production capacities of domestic steel mills were able to establish a new facility for the production of noble gases required for South Korean semiconductor production. China was able to increase their titanium sponge production between 2021 and 2024 by a factor of c. 1.6, while Japan increased production by 12% and Russia by 26%.

Analysis of resilient raw material supply from selected countries in Africa: Botswana, Morocco, Namibia, and Zimbabwe

Resilient supply chains can aid in diversification of supply chains, if mining in African countries is considered for investment. Many deposits are unexplored or not further assessed, but could be developed through responsible mining. The countries considered, Botswana, Morocco, Namibia, and Zimbabwe are all rich in raw materials but differ in gross domestic product (GDP), governance indicators, and foreign direct investment (FDI) in mining.

Demanders like companies (and/or governmental initiatives) from China, Russia and other countries compete and offer investments to access raw materials in Africa, while large, internationally operating metal mining companies from the EU27 are missing. However, BMW directly collaborates with a mining company in Morocco to ensure the supply chain of cobalt, high-quality working conditions and sustainability.

Smelters and recycling facilities offer additional local value creation, if affordable and reliable energy can be supplied. In addition, environmental, social and governance criteria are maintained.

7.2 Outlook

7.2.1 Reservoir quality assessment

Model for background fractures

Fracture clusters were recorded not only in the vicinity to a (reverse conjugate) breached kink band, but also as background clusters. No relation between the order of events between fracturing and folding/faulting could be observed in this study, thus, the context of folding/faulting and fracture formation remains unclear. Fracture clustering could be assessed in the vicinity of graben-bounding normal faults and compared with background clustering in outcrops and ideally deviated wells in the URG. Therefore, an understanding of fracture evolution and their relation to e.g., inversion or URG rifting could be addressed. A model on background fracture cluster formation could result in utilizing background fracture clusters away from faults, which would de-risk geothermal operations such as induced seismicity.

Automated analysis of drill cuttings

An automated petrographic approach or automated image classification of cutting photographs using machine learning at the well-site for rock composition could be tested on different cutting sample series. However, care has to be taken in the distinction between a cement phase and detrital grain, or rock fragments, currently limiting the applicability of automated petrographic assessments.

An automated approach of pXRF measurements on cleaned cuttings directly on-site after drilling could be tested for smaller sample intervals of e.g., one meter. If successful, the results could directly be used to monitor drilling progress and to target high reservoir quality intervals.

Temporal evolution of compressive deformation by far field stresses

The reverse conjugate (breached) kink bands may have formed by far field stress influenced by the Alpine orogeny. However, this hypothesis is the first described north of the alpine deformation front. Age dating on vein samples in faults and samples from the mineralized breached kink band using radiometric U-Pb could help to constrain this. Investigating outcrops further north and south of the studied quarry, closer to and further away from the alpine deformation front could help to identify, if compressive structures formed by successive fold propagation or localized above a detachment.

7.2.2 Raw materials

Responsible mining strategies

Mining strategies vary globally, for example Japan, South Korea, the US, the EU, Germany, China, and India adopt different strategies to secure their current needs in raw materials. Developments and actions over the past few years, such as geopolitical tensions and the disruption of supply chains, may influence the introduction and development of these. Better understanding of the reasons for and implementations of raw material strategies and their influence on e.g., the economic stability, could lead to more resilient future strategies.

Without comprehensive approaches to secure the supply of raw materials, including contributions from mining, the competitiveness of industrialized nations such as Germany cannot be maintained and the economic security for the EU cannot be ensured. However, STEEL-PEG (social, technological, economic, environmental, legal, political, ethical, geological) aspects have to be included to reach a holistic view on mining, recycling, and refining.

8 References

Abouelresh, M., Mahmoud, M., 2022. Petrographic charcaterization of microporosity in the organic-rich carbonate Hanifa Formation, Jafurah Basin, Saudi Arabia. 3540–3542, doi: 10.1190/image2022-3745573.1.

Abuamarah, B.A., Nabawy, B.S., 2021. A proposed classification for the reservoir quality assessment of hydrocarbon-bearing sandstone and carbonate reservoirs: A correlative study based on different assessment petrophysical procedures. Journal of Natural Gas Science and Engineering, 88, 103807, doi: 10.1016/j.jngse.2021.103807.

Adamolekun, O., J., Busch, B., Suess, M., P., Molenaar, N., Hilgers, C., 2022. Petrography and reservoir quality controls in shallow transitional marine Cretaceous-Paleogene deposits in the Dahomey Basin, Nigeria. Journal of African Earth Sciences, 186, 104437, doi: 10.1016/j.jafrearsci.2021.104437.

Adams, A., Diamond, L.W., 2019. Facies and depositional environments of the Upper Muschelkalk (Schinznach Formation, Middle Triassic) in northern Switzerland. Swiss Journal of Geosciences, 112, 2, 357–381, doi: 10.1007/s00015-019-00340-7.

African Business Guide, 2023, Branchenprofil, Bergbau und Rohstoffe in Afrika, Hightech braucht afrikanische Bodenschätze https://www.africa-business-guide.de/de/maerkte/bergbau-und-rohstoffe (Accessed: 16.06.2023).

African Business Guide, 2024, Welche Länder in Afrika bieten Potenzial für Investitionen in Bergbau und Rohstoffe?, https://www.africa-business-guide.de/de/praxis/fragen/welche-laender-in-afrika-bieten-potenzial-fuer-investitionen-in-bergbau-und-rohstoffe--950350 (Accessed: 02.04.2024).

African Union, 2009, Africa Mining Vision, https://au.int/sites/default/files/documents/30995-doc-africa_mining_vision_english_1.pdf.

Ager, D., V. , 1974. Storm deposits in the Jurassic of the Moroccan High Atlas. Palaeogeography, Palaeoclimatology, Palaeoecology, 15, 2, 83–93, doi: 10.1016/0031-0182(74)90026-1.

Agosta, F., Alessandroni, M., Antonellini, M., Tondi, E., Giorgioni, M., 2010. From fractures to flow: A field-based quantitative analysis of an outcropping carbonate reservoir. Tectonophysics, 490, 3, 197–213, doi: 10.1016/j.tecto.2010.05.005.

Ahorner, L., 1975. Present-day stress field and seismotectonic block movements along major fault zones in Central Europe. Tectonophysics, 29, 1, 233–249, doi: 10.1016/0040-1951(75)90148-1.

Ahr, M., 2008. Geology of carbonate reservoirs: The identification, description, and characterization of hydrocarbon reservoirs in carbonate rocks, 277; doi: 10.1002/9780470370650.ch3.

Aigner, T., 1985. Storm depositional systems - dynamic stratigraphy in modern and ancient shallow-marine sequences, 1 ed. Springer, Berlin, Heidelberg, 174; doi: 10.1007/BFb0011411.

Aigner, T., 1986. Dynamische Stratigraphie des Hauptmuschelkalks im südwestdeutschen Becken. Jahreshefte der Gesellschaft für Naturkunde in Württemberg, Bd. 141, 1986, 33–55.

Aigner, T., Bachmann, G., H., 1992. Sequence-stratigraphic framework of the German Triassic. Sedimentary Geology, 80, 1, 115–135, doi: 10.1016/0037-0738(92)90035-P.

Alexandersson, T., 1972. Micritization of carbonate particles: processus of precipitation and dissolution in modern shallow-marine sediments, Bull. geol. Instn Univ. Upsal, 201–236.

Allgaier, F., Busch, B., Hilgers, C., 2023a. Fault leakage and reservoir charging in the Upper Rhine Graben, Germany – Assessment of the Leopoldshafen fault bend. Marine and Petroleum Geology, 156, 106428, doi: 10.1016/j.marpetgeo.2023.106428.

Allgaier, F., Busch, B., Niederhuber, T., Quandt, D., Müller, B., Hilgers, C., 2023b. Fracture network characterisation of the naturally fractured Upper Carboniferous sandstones combining outcrop and wellbore data, Ruhr Basin, Germany. Zeitschrift der Deutschen Gesellschaft für Geowissenschaften, 173, 4, 599–623, doi: 10.1127/zdgg/2023/0369.

Allgaier, F., Niederhuber, T., Busch, B., Müller, B., Hilgers, C., 2024. Post-mining related reactivation potential of faults hosted in tight reservoir rocks around flooded coal mines, eastern Ruhr Basin, Germany. Geomechanics for Energy and the Environment, 38, 100560, doi: 10.1016/j.gete.2024.100560.

Almansour, A., Laubach, S.E., Bickel, J.E., Schultz, R.A., 2020. Value-of-Information Analysis of a Fracture Prediction Method. SPE Reservoir Evaluation & Engineering, 23, 3, 0811–0823, doi: 10.2118/198906-pa.

Alper, A., 2022, Exclusive: Russia's attack on Ukraine halts half of world's neon output for chips, https://www.reuters.com/technology/exclusive-ukraine-halts-half-worlds-neon-output-chips-clouding-outlook-2022-03-11/ (Accessed: 05.04.2023).

Amann-Hildenbrand, A., Dietrichs, J.P., Krooss, B.M., 2016. Effective gas permeability of Tight Gas Sandstones as a function of capillary pressure – a non-steady-state approach. Geofluids, 16, 3, 367–383, doi: 10.1111/gfl.12155.

Amorosi, A., 2013. The occurrence of glaucony in the stratigraphic record: Distribution patterns and sequence-stratigraphic significance, Linking Diagenesis to Sequence Stratigraphy, 37–53, doi: 10.1002/9781118485347.ch2.

Amthor, J.E., Mountjoy, E.W., Machel, H.G., 1994. Regional-scale porosity and permeability variations in Upper Devonian Leduc buildups: Implications for reservoir development and prediction in carbonates. AAPG Bulletin, 78, 1541–1559, doi: 10.1306/A25FF215-171B-11D7-8645000102C1865D.

Anders, B., Beccaletto, L., Capar, L., Mermy, D.C., Dezayes, C., Dresmann, H., Elsass, P., Fehn, C., Fischer, G., Franz, M., Haneke, J., Huggenberger, P., Kärcher, T., Krzyzanowski, J., Nitsch, E., Oliviero, G., Prestel, R., Rodat, C., Rupf, I., Schuff, J., Siemon, S., Sokol, G., Storz, R., Tesch, J., Urban, S., Weidenfeller, M., Wielandt- Schuster, U., Wirsing, G., Zumsprekel, H., 2013. Geopotenziale des tieferen Untergrundes im Oberrheingraben: Fachlich-Technischer Abschlussbericht des INTERREG-Projekts GeORG, Teil 4: Atlas. . LGRB-Informationen, Freiburg i. Br./Mainz/Strasbourg/Basel.

Anselmetti, F., Eberli, G., 1999. The Velocity-Deviation Log: A tool to predict pore type and permeability trends in carbonate drill holes from sonic and porosity or density logs, AAPG Bulletin, 450–466.

Anselmetti, F.S., Eberli, G.P., 1993. Controls on sonic velocity in carbonates. Pure and Applied Geophysics, 141, 2, 287–323, doi: 10.1007/BF00998333.

Antonellini, M., Aydin, A., 1994. Effect of faulting on fluid flow in porous sandstones: Petrophysical properties 1. AAPG Bulletin, 78, 3, 355–377, doi: 10.1306/bdff90aa-1718-11d7-8645000102c1865d.

Antonellini, M., Aydin, A., 1995. Effect of faulting on fluid flow in porous sandstones: Geometry and spatial distribution. American Association of Petroleum Geologists Bulletin, 79, 642–671, doi: 10.1306/8D2B1B60-171E-11D7-8645000102C1865D.

Armitage, P.J., Worden, R.H., Faulkner, D.R., Aplin, A.C., Butcher, A.R., Espie, A.A., 2013. Mercia Mudstone Formation caprock to carbon capture and storage sites: petrology and petrophysical characteristics. Journal of the Geological Society, 170, 1, 119–132, doi: 10.1144/jgs2012-049.

Arnold, H., Bode, H., Wortmann, H., Karrenberg, H., Teichmüller, R., 1960. Erläuterungen zu Blatt Münster C 4310, Übersichtskarte von Nordrhein-Westfalen 1:100 000. Geologisches Landesamt Nordrhein-Westfalen, Krefeld.

Arzmüller, G., Buchta, Š., Ralbovský, E., Wessely, G., Golonka, J., Picha, F.J., 2006. The Vienna Basin, The Carpathians and their foreland: Geology and hydrocarbon resources. American Association of Petroleum Geologists, 191–204, doi: 10.1306/985608m843068.

Bahrami, H., Rezaee, R., Hossain, M., 2012. Characterizing natural fractures productivity in tight gas reservoirs. Journal of Petroleum Exploration and Production Technology, 2, 2, 107–115, doi: 10.1007/s13202-012-0026-x.

Baioumy, H., Farouk, S., Al-Kahtany, K., 2020. Paleogeographic, paleoclimatic and sea-level implications of glauconite deposits in Egypt: A review. Journal of African Earth Sciences, 171, 103944, doi: 10.1016/j.jafrearsci.2020.103944.

Ballas, G., Soliva, R., Sizun, J.-P., Benedicto, A., Cavailhes, T., Raynaud, S., 2012. The importance of the degree of cataclasis in shear bands for fluid flow in porous sandstone, Provence, France. AAPG Bulletin, 96, 11, 2167–2186, doi: 10.1306/04051211097.

Ballas, G., Soliva, R., Sizun, J.-P., Fossen, H., Benedicto, A., Skurtveit, E., 2013. Shear-enhanced compaction bands formed at shallow burial conditions; implications for fluid flow (Provence, France). Journal of Structural Geology, 47, 3–15, doi: 10.1016/j.jsg.2012.11.008.

Barich, A., Chen, A., 2022, Australian ban of alumina exports to Russia to leave Rusal scrambling https://www.spglobal.com/marketintelligence/en/news-insights/latest-news-headlines/australian-ban-of-alumina-exports-to-russia-to-leave-rusal-scrambling-69503392 (Accessed: 06.06.2023).

Baron, J., 2022, Will the War in Ukraine Impact Noble Gas Supplies?, https://topics.amcham.com.tw/2022/11/will-the-war-in-ukraine-impact-noble-gas-supplies/ (Accessed: 05.06.2023).

Barton, C.A., Zoback, M.D., Moos, D., 1995. Fluid flow along potentially active faults in crystalline rock. Geology, 23, 8, 683–686, doi: 10.1130/0091-7613(1995)023<0683:Ffapaf>2.3.Co;2.

Barton, N., Bandis, S., Bakhtar, K., 1985. Strength, deformation and conductivity coupling of rock joints. International Journal of Rock Mechanics and Mining Sciences & Geomechanics Abstracts, 22, 3, 121–140, doi: 10.1016/0148-9062(85)93227-9.

Bashniak, H., Hamkens, T., Maksymov, M., Ozeran, O., 2022, Main Barriers and Perceived Risks for Investment in the Ukrainian Raw Materials Resources Sector, https://brdo.com.ua/wp-content/uploads/2022/11/CRM-Report-2022-Ukraine.pdf.

Bastian, D., 2024, Studie: Entwicklungszeit für neue Bergbau-Lagerstätten immer länger, https://www.vdi-nachrichten.com/wirtschaft/rohstoffe/studie-entwicklungszeit-fuer-neue-bergbau-lagerstaetten-immer-laenger/ (Accessed: 02.04.2024).

Bathurst, R.G.C., 1966. Boring algae, micrite envelopes and lithification of molluscan biosparites. Geological Journal, 5, 1, 15–32, doi: 10.1002/gj.3350050104.

Bathurst, R.G.C., 1970. Problems of lithification in carbonate muds. Proceedings of the Geologists' Association, 81, 3, 429–440, doi: 10.1016/S0016-7878(70)80005-0.

Bathurst, R.G.C., 1975. Carbonate sediments and their diagenesis, Developments in sedimentology, 658.

Bauch, E., Hecht, C., Lempp, C., Wrede, V., 2003. Transpressive Tektonik im Campan von Beckum, Zentrales Münsterland, Nordrhein-Westfalen, scriptum - Arbeitsergebnisse aus dem Geologischen Dienst Nordrhein-Westfalen, 5–17.

Baud, P., Meredith, P., Townend, E., 2012. Permeability evolution during triaxial compaction of an anisotropic porous sandstone. Journal of Geophysical Research: Solid Earth, 117, B5, B05203, doi: 10.1029/2012JB009176.

Beard, D.C., Weyl, P.K., 1973. Influence of texture on porosity and permeability of unconsolidated sand 1. AAPG Bulletin, 57, 2, 349–369, doi: 10.1306/819a4272-16c5-11d7-8645000102c1865d.

Becker, I., Birgit, M., Koehrer, B., Jelinek, W., Hilgers, C., 2019a. Present-day stress control on fluid migration pathways: Case study of the Zechstein fractured carbonates, NW-Germany. Marine and Petroleum Geology, 103, 320–330, doi: 10.1016/j.marpetgeo.2019.03.002.

Becker, I., Koehrer, B., Hilgers, C., 2019b. Correlating three Upper Permian Zechstein-2-Carbonate outcrops across the Eichsfeld-Altmark Swell - Facies, reservoir properties, and outcrop analogue potential. Zeitschrift der Deutschen Gesellschaft für Geowissenschaften, 169, 4, 517–531, doi: 10.1127/zdgg/2019/0167.

Becker, I., Koehrer, B., Waldvogel, M., Jelinek, W., Hilgers, C., 2018. Comparing fracture statistics from outcrop and reservoir data using conventional manual and t-LiDAR derived scanlines in Ca2 carbonates from the Southern Permian Basin, Germany. Marine and Petroleum Geology, 95, 228–245, doi: 10.1016/j.marpetgeo.2018.04.021.

Becker, I., Wüstefeld, P., Koehrer, B., Felder, M., Hilgers, C., 2017. Porosity and permeability variations in a tight gas sandstone reservoir analog, Westphalian D, Lower Saxony Basin, NW Germany: Influence of depositional setting and diagenesis. Journal of Petroleum Geology, 40, 4, 363–389, doi: 10.1111/jpg.12685.

Berka, R., 2015. Zur Geologie der großen Beckengebiete des Ostalpenraumes. Abhandlungen der Geologischen Bundesanstalt, 64, 71–141.

Berner, R.A., 1970. Sedimentary pyrite formation. American Journal of Science, 268, 1, 1–23, doi: 10.2475/ajs.268.1.1.

BGR, 2021, Deutschland – Rohstoffsituation 2020, https://www.bgr.bund.de/DE/Themen/Min_rohstoffe/Downloads/rohsit-2020.pdf?__blob=publicationFile&v=4.

BGR, 2022, Deutschland – Rohstoffsituation 2021, https://www.bgr.bund.de/DE/Themen/Min_rohstoffe/Downloads/rohsit-2021.pdf?__blob=publicationFile&v=4.

BGR, 2023, Deutschland – Rohstoffsituation 2022, doi: 10.25928/dero-si22.

BGR, 2024, Deutschland – Rohstoffsituation 2023, doi: 10.25928/dero-si23.

Biehl, B.C., Reuning, L., Schoenherr, J., Lüders, V., Kukla, P.A., 2016. Impacts of hydrothermal dolomitization and thermochemical sulfate reduction on secondary porosity creation in deeply buried carbonates: A case study from the Lower Saxony Basin, northwest Germany. AAPG Bulletin, 100, 4, 597–621, doi: 10.1306/01141615055.

Bing maps, 2025, Bing maps Knittlingen quarry (Germany), https://www.bing.com/maps?cp=49.028437%7E8.735134&lvl=17.4&style=h (Accessed: 13.05.2025).

Bjørlykke, K., 1988. Chapter 2 sandstone diagenesis in relation to preservation, destruction and creation of porosity, in: Chilingarian, G.V., Wolf, K.H. (Eds.), Diagenesis, I. Elsevier, 555–588, doi: 10.1016/S0070-4571(08)70180-8.

Bjørlykke, K., Egeberg, P.K., 1993. Quartz cementation in sedimentary basins 1. AAPG Bulletin, 77, 9, 1538–1548, doi: 10.1306/bdff8ee8-1718-11d7-8645000102c1865d.

Bjørrlykke, K., 1998. Clay mineral diagenesis in sedimentary basins; a key to the prediction of rock properties; examples from the North Sea Basin, Clay Minerals, 15–34.

Blum, U., Borg, G., Kropp, N., Liventseva, H., Rozhkova, I., 2023. Die Rohstoffe der Ukraine und ihre strategische Bedeutung – eine geopolitische Analyse. SIRIUS – Zeitschrift für Strategische Analysen, 7, 3, 257–276, doi: doi:10.1515/sirius-2023-3006.

BMW Group, 2019, Nachhaltigkeit im Einkauf und Lieferantennetzwerk: Wahrnehmung der unternehmerischen Sorgpfaltspflicht (Due Diligence) bei der Lieferantenauswahl, https://www.bmwgroup.com/content/dam/grpw/websites/bmwgroup_com/responsibility/downloads/de/2019/BMW%20Group%20Sorgfaltspflicht%20bei%20der%20Lieferantenauswahl_DE.pdf (Accessed: 15.06.2023).

BMW Group, 2024, Umwelt- und Sozialstandards, https://www.bmwgroup.com/de/nachhaltigkeit/umwelt-und-sozialstandards.html (Accessed: 11.04.2024).

BMWi, 2021, Rohstoffe - Bergbau, Recycling, Ressourceneffizienz - wichtig für Wohlstand und Arbeitsplätze, https://www.bmwk.de/Redaktion/DE/Publikationen/Industrie/rohstoffe-bergbau-recycling-ressourceneffizienz.pdf?__blob=publicationFile&v=1.

Böcker, J., Littke, R., Forster, A., 2017. An overview on source rocks and the petroleum system of the central Upper Rhine Graben. International Journal of Earth Sciences, 106, 2, 707–742, doi: 10.1007/s00531-016-1330-3.

Böcker, J.J., 2015. Petroleum system and thermal history of the Upper Rhine Graben - Implications from organic geochemical analyses, oil-source rock correlations and

numerical modelling. Rheinisch-Westfälische Technische Hochschule Aachen, Aachen, Dissertation, 168.

Boles, J.R., Franks, S.G., 1979. Clay diagenesis in Wilcox sandstones of Southwest Texas; implications of smectite diagenesis on sandstone cementation. Journal of Sedimentary Research, 49, 1, 55–70, doi: 10.1306/212f76bc-2b24-11d7-8648000102c1865d.

Bonnet, E., Bour, O., Odling, N.E., Davy, P., Main, I., Cowie, P., Berkowitz, B., 2001. Scaling of fracture systems in geological media. Reviews of Geophysics, 39, 3, 347–383, doi: 10.1029/1999RG000074.

Börnchen, M., 2007, Der Strontianitbergbau im Münsterland https://www.westfalen-regional.de/de/strontianitbergbau/#anker-16256215 (Accessed: 01.10.2023).

Bossennec, C., Géraud, Y., Böcker, J., Klug, B., Mattioni, L., Sizun, J.-P., Sudo, M., Moretti, I., 2021. Evolution of diagenetic conditions and burial history in Buntsandstein Gp. fractured sandstones (Upper Rhine Graben) from in-situ δ18O of quartz and 40Ar/39Ar geochronology of K-feldspar overgrowths. International Journal of Earth Sciences, 110, 8, 2779–2802, doi: 10.1007/s00531-021-02080-2.

Bouma, A.H., 1964. Turbidites, in: Bouma, A.H., Brouwer, A. (Eds.), Developments in Sedimentology. Elsevier, London, 247–256, doi: 10.1016/S0070-4571(08)70967-1.

Bouma, A.H., 2004. Key controls on the characteristics of turbidite systems. Geological Society, London, Special Publications, 222, 1, 9–22, doi: 10.1144/GSL.SP.2004.222.01.02.

Brüderlin, M., 1970. Beiträge zur Lithostratigraphie und Sedimentpetrographie des Oberen Muschelkalks im südwestlichen Baden-Württemberg. Teil II: Sedimentpetrographie. Jahresberichte und Mitteilungen des Oberrheinischen Geologischen Vereins, 52, 175–209, doi: 10.1127/jmogv/52/1970/175.

Brunner, H., Simon, T., 1985. Lithologische Gliederung von Profilen aus dem Oberen Muschelkalk im nördlichen Baden-Württemberg anhand der natürlichen Gamma-Strahlungsintensität der Gesteine. Jahresberichte und Mitteilungen des Oberrheinischen Geologischen Vereins, 67, 289–299, doi: 10.1127/jmogv/67/1985/289.

Buchbinder, B., Friedman, G.M., 1970. Selective dolomitization of micritic envelopes; a possible clue to original mineralogy. Journal of Sedimentary Research, 40, 1, 514–517, doi: 10.1306/74d71faa-2b21-11d7-8648000102c1865d.

Budd, D.A., 1997. Cenozoic dolomites of carbonate islands: their attributes and origin. Earth-Science Reviews, 42, 1, 1–47, doi: 10.1016/S0012-8252(96)00051-7.

Budd, D.A., Hammes, U., Ward, W.B., 2000. Cathodoluminescence in calcite cements new insights on Pb and Zn sensitizing, Mn activation, and Fe quenching at low trace-element concentrations. Journal of Sedimentary Research, 70, 217–226, doi: 10.1306/2DC4090C-0E47-11D7-8643000102C1865D.

Bundesanstalt für Geowissenschaften und Rohstoffe (BGR), 2025, Geoportal der Bundesanstalt für Geowissenschaften und Rohstoffe, https://geoportal.bgr.de/mapapps/resources/apps/geoportal/index.html?lang=de#/geoviewer (Accessed: 05.06.2025).

Burchette, T., Britton, S., 1985. Carbonate facies analysis in the exploration for hydrocarbons: a case-study from the Cretaceous of the Middle East. Geological

Society, London, Special Publications, 18, 311–338, doi: 10.1144/GSL.SP.1985.018.01.13.

Burchette, T.P., 2012. Carbonate rocks and petroleum reservoirs: a geological perspective from the industry. Geological Society, London, Special Publications, 370, 1, 17–37, doi: 10.1144/SP370.14.

Burgess, D.T., Kettler, R.M., Loope, D.B., 2016. The Geologic Context of Wonderstone: A Complex, Outcrop-Scaled Pattern of Iron-Oxide Cement. Journal of Sedimentary Research, 86, 498–511, doi: 10.2110/jsr.2016.35.

Busch, B., Adelmann, D., Herrmann, R., Hilgers, C., 2022a. Controls on compactional behavior and reservoir quality in a Triassic Buntsandstein reservoir, Upper Rhine Graben, SW Germany. Marine and Petroleum Geology, 136, 105437, doi: 10.1016/j.marpetgeo.2021.105437.

Busch, B., Becker, I., Koehrer, B., Adelmann, D., Hilgers, C., 2019. Porosity evolution of two Upper Carboniferous tight-gas-fluvial sandstone reservoirs: Impact of fractures and total cement volumes on reservoir quality. Marine and Petroleum Geology, 100, 376–390, doi: 10.1016/j.marpetgeo.2018.10.051.

Busch, B., Böcker, J., Hilgers, C., 2024. Improved reservoir quality assessment by evaluating illite grain coatings, quartz cementation, and compaction – Case study from the Buntsandstein, Upper Rhine Graben, Germany. Geoenergy Science and Engineering, 241, 213141, doi: 10.1016/j.geoen.2024.213141.

Busch, B., Hilgers, C., Lander, R.H., Bonnell, L.M., Adelmann, D., 2018. Reservoir quality and burial model evaluation by kinetic quartz and illite cementation modeling: Case study of Rotliegendes, north Germany. AAPG Bulletin, 102, 02, 293–307, doi: 10.1306/0503171605217075.

Busch, B., Spitzner, A.-D., Adelmann, D., Hilgers, C., 2022b. The significance of outcrop analog data for reservoir quality assessment: A comparative case study of Lower Triassic Buntsandstein sandstones in the Upper Rhine Graben. Marine and Petroleum Geology, 141, 105701, doi: 10.1016/j.marpetgeo.2022.105701.

Busch, B., Winkler, R., Osivandi, K., Nover, G., Amann, A., Hilgers, C., 2015. Evolution of small-scale flow barriers in German Rotliegend siliciclastics. Geological Society London Special Publications, 435, 141–160, doi: 10.1144/SP435.3.

Caja, M.A., Santos, C., García, L., Fernandez, P.R., Pérez, J.L., Peña, A., Canal, J., Blázquez, V., González, H., Sánchez, V., García, A.J., 2019. Characterizing Algeria tight reservoir cutting samples with virtual microscopy, petrography, mineralogy and digital petrophysics, EAGE/ALNAFT Geoscience Workshop 2019. EAGE, Algiers, Africa.

Camp, E., R. , Jordan, T., E., Hornbach, M., J., Whealton, C., A. , 2018. A probabilistic application of oil and gas data for exploration stage geothermal reservoir assessment in the Appalachian Basin. Geothermics, 71, 187–199, doi: 10.1016/j.geothermics.2017.09.001.

Cander, H.S., 1994. An example of mixing-zone dolomite, middle Eocene Avon Park Formation, Floridan Aquifer system. Journal of Sedimentary Research, 64, 3a, 615–629, doi: 10.1306/d4267e24-2b26-11d7-8648000102c1865d.

Carlos de Dios, J., Delgado, M., A., Martínez, C., Ramos, A., Álvarez, I., Marín, J., A. , Salvador, I., 2017. Hydraulic characterization of fractured carbonates for CO2 geological storage: Experiences and lessons learned in Hontomín Technology

Development Plant. International Journal of Greenhouse Gas Control, 58, 185–200, doi: 10.1016/j.ijggc.2017.01.008.

Cawood, A., J. , Bond, C., E. , Howell, J., A. , Butler, R., W. H. , Totake, Y., 2017. LiDAR, UAV or compass-clinometer? Accuracy, coverage and the effects on structural models. Journal of Structural Geology, 98, 67–82, doi: 10.1016/j.jsg.2017.04.004.

Chafetz, H.S., 1986. Marine peloids: A product of bacterially induced precipitation of calcite. Journal of Sedimentary Research, 56, 6, 812–817, doi: 10.1306/212f8a58-2b24-11d7-8648000102c1865d.

Cheng, C., Milsch, H., 2021. Hydromechanical investigations on the self-propping potential of fractures in tight sandstones. Rock Mechanics and Rock Engineering, 54, 10, 5407–5432, doi: 10.1007/s00603-021-02500-4.

Chingono, N., 2024, Zimbabwe wants lithium miners to plan new capacity despite price dive, https://www.reuters.com/markets/commodities/zimbabwe-wants-lithium-miners-plan-new-capacity-despite-price-dive-2024-02-23/ (Accessed: 01.03.2024).

Choquette, P.W., Pray, L.C., 1970. Geologic Nomenclature and Classification of Porosity in Sedimentary Carbonates. AAPG Bulletin, 54, 2, 207–250, doi: 10.1306/5d25c98b-16c1-11d7-8645000102c1865d.

Chowns, T.M., Elkins, J.E., 1974. The origin of quartz geodes and cauliflower cherts through the silicification of anhydrite nodules. Journal of Sedimentary Research, 44, 3, 885–903, doi: 10.1306/212f6bd1-2b24-11d7-8648000102c1865d.

Ciriaco, A., E, Zarrouk, S., J, Zakeri, G., 2020. Geothermal resource and reserve assessment methodology: Overview, analysis and future directions. Renewable and Sustainable Energy Reviews, 119, 109515, doi: 10.1016/j.rser.2019.109515.

Clauser, C., Villinger, H., 1990. Analysis of conductive and convective heat transfer in a sedimentary basin, demonstrated for the Rheingraben. Geophysical Journal International, 100, 3, 393–414, doi: 10.1111/j.1365-246X.1990.tb00693.x.

Coffa, A.A., O'Mara, M.J., McLaren, C., Thompson, D.L., Karakatsanis, J., Hall, M., Stilwell, J., 2015. Enhancing oil and gas production in carbonate turbidite fields by the study of high-resolution biostratigraphy, facies and fracture variability: An example from the NW Palawan Basin of the Philippines. SEG Global Meeting Abstracts, 247.

Cohen, K.M., Harper, D.A.T., Gibbard, P.L., 2024. ICS International Chronostratigraphic Chart 2024/12. International Commission on Stratigraphy IUGS.

Coldewey, W.G., Wesche, D., 2017. Hydrogeologische und gesteinsphysikalische Eigenschaften der Emscher-Formation im Hinblick auf den Steinkohlenbergbau des Ruhrgebietes. Grundwasser, 22, 3, 175–183, doi: 10.1007/s00767-017-0365-0.

Coleman, M.L., 1985. Geochemistry of diagenetic, non-silicate minerals: Kinetic considerations. Philosophical Transactions of the Royal Society of London. Series A, Mathematical and Physical Sciences, 315, 39–56, doi: 10.1098/rsta.1985.0028.

Collettini, C., Trippetta, F., 2007. A slip tendency analysis to test mechanical and structural control on aftershock rupture planes. Earth and Planetary Science Letters, 255, 3, 402–413, doi: 10.1016/j.epsl.2007.01.001.

Coskun, S.B., Wardlaw, N.C., Haverslew, B., 1993. Effects of composition, texture and diagenesis on porosity, permeability and oil recovery in a sandstone reservoir. Journal of Petroleum Science and Engineering, 8, 4, 279–292, doi: 10.1016/0920-4105(93)90005-Y.

Craigie, N., 2018. Principles of elemental chemostratigraphy - A practical user guide. Springer Cham, 189; doi: 10.1007/978-3-319-71216-1.

Croizé, D., Renard, F., Gratier, J.-P., 2013. Compaction and porosity reduction in carbonates: A review of observations, theory, and experiments. Advances in Geophysics, 54, 181–238, doi: 10.1016/B978-0-12-380940-7.00003-2.

Cummins, W.A., 1962. The greywacke problem. Geological Journal, 3, 1, 51–72, doi: 10.1002/gj.3350030105.

David, C., Menendez, B., Zhu, W., Wong, T.F., 2001. Mechanical compaction, microstructures and permeability evolution in sandstones. Physics and Chemistry of the Earth, Part A: Solid Earth and Geodesy, 26, 1, 45–51, doi: 10.1016/S1464-1895(01)00021-7.

David, C., Wong, T.-F., Zhu, W., Zhang, J., 1994. Laboratory measurement of compaction-induced permeability change in porous rocks: Implications for the generation and maintenance of pore pressure excess in the crust. pure and applied geophysics, 143, 1, 425–456, doi: 10.1007/BF00874337.

Decker, K., 1996. Miocene tectonics at the Alpine-Carpathian junction and the evolution of the Vienna Basin, Mitt Ges Geol Bergbaustud Österr, 33–44.

Decker, K., Peresson, H., Hinsch, R., 2005. Active tectonics and Quaternary basin formation along the Vienna Basin transform fault. Quaternary Science Reviews, 24, 3, 305–320, doi: 10.1016/j.quascirev.2004.04.012.

Deik, H., Reuning, L., Petrick, B., Takayanagi, H., 2019. Hardened faecal pellets as a significant component in deep water, subtropical marine environments. The Depositional Record, 5, 2, 348–361, doi: 10.1002/dep2.64.

Demars, C., Pagel, M., Deloule, E., Blanc, P., 1996. Cathodoluminescence of quartz from sandstones: Interpretation of the UV range by determination of trace element distributions and fluid-inclusion P-T-X properties in authigenic quartz. American Mineralogist, 81, 7-8, 891–901, doi: 10.2138/am-1996-7-812.

DERA, 2019, Einblicke in die chinesische Rohstoffwirtschaft, https://www.deutsche-rohstoffagentur.de/DE/Gemeinsames/Produkte/Downloads/DERA_Rohstoffinformationen/rohstoffinformationen-41.pdf?__blob=publicationFile&v=2.

DERA, 2021, Rohstoffe für Zukunftstechnologien 2021, https://www.deutsche-rohstoffagentur.de/DE/Gemeinsames/Produkte/Downloads/DERA_Rohstoffinformationen/rohstoffinformationen-50.pdf?__blob=publicationFile&v=4.

DERA, 2023, DERA untersucht deutsche Metallimporte aus Russland, 13.06.2023, www.bgr.bund.de/DE/Gemeinsames/Nachrichten/Aktuelles/2023/2023-06-13_dera-untersucht-deutsche-metallimporte-aus-russland.de (Accessed: 27. November 2023).

DERA, acatech, 2023, Abschlussbericht Dialogplattform Recyclingrohstoffe – Handlungsoptionen zur Stärkung des Beitrags von Recyclingrohstoffen für die Versorgungssicherheit mit Metallen und Industriemineralen, https://www.acatech.de/publikation/abschlussbericht-dialogplattform-recyclingrohstoffe/.

Destatis, 2022, Verarbeitendes Gewerbe 2021, Anteil an der Bruttowertschöpfung in Prozent, https://www.destatis.de/Europa/DE/Thema/Industrie-Handel-Dienstleistungen/Industrie.html (Accessed: 16.04.2024).

Destatis, 2024a, Botsuana-Statistisches Länderprofil, https://www.destatis.de/DE/Themen/Laender-Regionen/Internationales/Laenderprofile/botsuana.pdf?__blob=publicationFile.

Destatis, 2024b, Marokko-Statistisches Länderprofil, https://www.destatis.de/DE/Themen/Laender-Regionen/Internationales/Laenderprofile/marokko.pdf?__blob=publicationFile.

Destatis, 2024c, Namibia-Statistisches Länderprofil, https://www.destatis.de/DE/Themen/Laender-Regionen/Internationales/Laenderprofile/namibia.pdf?__blob=publicationFile.

Destatis, 2024d, Simbabwe-Statistisches Länderprofil, https://www.destatis.de/DE/Themen/Laender-Regionen/Internationales/Laenderprofile/simbabwe.pdf?__blob=publicationFile.

Deutscher Bundestag, 2023, Kritische Rohstoffe aus Afrika für die Energiewende in Deutschland, WD 5 - 3000 – 091/23, https://www.bundestag.de/resource/blob/980430/beb9c012f88df6a653a6ab0c46575157/WD-5-091-23-pdf.pdf.

Deutscher Bundestag Fraktion der CDU/CSU, 2022, Heimischer Rohstoffabbau, internationaler Rohstoffbezug und Auswirkungen auf die Ausbauziele der erneuerbaren Energien - Drucksache 20/2958 und Drucksache 20/3243 https://dserver.bundestag.de/btd/20/032/2003243.pdf.

Deville de Periere, M., Durlet, C., Vennin, E., Lambert, L., Bourillot, R., Caline, B., Poli, E., 2011. Morphometry of micrite particles in cretaceous microporous limestones of the Middle East: Influence on reservoir properties. Marine and Petroleum Geology, 28, 9, 1727–1750, doi: 10.1016/j.marpetgeo.2011.05.002.

Devitt, P., Jadhav, R., Lui, S., 2023, Analysis: To cut reliance on China, Russia turns to India for aluminium feedstock https://www.reuters.com/markets/commodities/cut-reliance-china-russia-turns-india-aluminium-feedstock-2023-09-14/ (Accessed: 25.10.2023).

Devitt, P., Osterman, C., 2025, Ukraine's metals production, development projects and resources, https://www.reuters.com/markets/commodities/ukraines-metals-production-development-projects-resources-2025-05-01/ (Accessed: 15.05.2025).

Dewey, J.F., 1965. Nature and origin of kink-bands. Tectonophysics, 1, 6, 459–494, doi: 10.1016/0040-1951(65)90019-3.

Dezayes, C., Lerouge, C., 2019. Reconstructing paleofluid circulation at the Hercynian basement/Mesozoic sedimentary cover interface in the Upper Rhine Graben. Geofluids, 2019, 1, 4849860, doi: 10.1155/2019/4849860.

Dickinson, W.R., Suczek, C.A., 1979. Plate tectonics and sandstone compositions 1. AAPG Bulletin, 63, 12, 2164–2182, doi: 10.1306/2f9188fb-16ce-11d7-8645000102c1865d.

Dickson, J.A.D., 1965. A modified staining technique for carbonates in thin section. Nature, 205, 4971, 587, doi: 10.1038/205587a0.

Dölling, B., Dölling, M., Hiss, M., Berensmeier, M., Püttmann, T., 2017. Upper Cretaceous shallow-marine deposits of the southwestern Münsterland (northwest Germany) influenced by synsedimentary tectonics. Cretaceous Research, 87, 261–276, doi: 10.1016/j.cretres.2017.05.002.

Dölling, M., Juch, D., 2009. Strukturgeologische Modellvorstellungen zum Kreide-Deckgebirge im zentralen Münsterland in: Zwei Beiträge zur Geologie des zentralen und des südlichen Münsterlandes. scriptum online - Geowissenschaftliche Arbeitsergebnisse aus Nordrhein-Westfalen, 18, 5–27.

Dott, R.H., 1963. Dynamics of Subaqueous Gravity Depositional Processes. AAPG Bulletin, 47, 1, 104–128, doi: 10.1306/bc743973-16be-11d7-8645000102c1865d.

Dou, S., 2024, China`s Sinomine to Buy African Copper Smelter for USD 49 Million, https://www.yicaiglobal.com/news/chinas-sinomine-to-buy-african-copper-smelter-for-usd49-million (Accessed: 10.03.2024).

Drobe, M., 2022, Platingruppenmetalle - Information zur Nachhaltigkeit, https://www.bgr.bund.de/SharedDocs/Produkte/Downloads/Informationen_Nachhaltigkeit/PGM.pdf?__blob=publicationFile&v=1.

Drozdzewski, G., 1988. Die Wurzel der Osning-Überschiebung und der Mechanismus herzynischer Inversionsstörungen in Mitteleuropa Geologische Rundschau, 77, 1, 127–141, doi: 10.1007/BF01848680.

Drozdzewski, G., Dölling, M., 2018. Elemente der Osning-Störungszone (NW-Deutschland) - Leitstrukturen einer Blattverschiebungszone. scriptum online - Geowissenschaftliche Arbeitsergebnisse aus Nordrhein-Westfalen, 7, 5–9.

Dunham, R.J., 1962. Classification of carbonate rocks according to depositional texture, in: Ham, W.E. (Ed.), Classification of Carbonate Rocks - A Symposium. AAPG, 108–121.

Durst, H., 1991. Aspects of exploration history and structural style in the Rhine graben area. Generation, accumulation, and production of Europe's hydrocarbons, 247–261.

Dutton, S., P., Loucks, R., G. , 2010. Diagenetic controls on evolution of porosity and permeability in lower Tertiary Wilcox sandstones from shallow to ultradeep (200–6700m) burial, Gulf of Mexico Basin, U.S.A. Marine and Petroleum Geology, 27, 1, 69–81, doi: 10.1016/j.marpetgeo.2009.08.008.

DW, 2023, Lithium-Abbau in Afrika: Die Schattenseite grüner Energie, https://www.dw.com/de/lithium-mine-in-afrika-zeigt-schattenseite-gr%C3%BCner-energie-auf/a-67459734 (Accessed: 02.04.2024).

Edel, J.B., Schulmann, K., Rotstein, Y., 2007. The Variscan tectonic inheritance of the Upper Rhine Graben: evidence of reactivations in the Lias, Late Eocene–Oligocene up to the recent. International Journal of Earth Sciences, 96, 2, 305–325, doi: 10.1007/s00531-006-0092-8.

Ehrenberg, S.N., 2006. Porosity destruction in carbonate platforms Journal of Petroleum Geology, 29, 1, 41–52, doi: 10.1111/j.1747-5457.2006.00041.x.

Ehrenberg, S.N., Eberli, G.P., Keramati, M., Moallemi, S.A., 2006. Porosity-permeability relationships in interlayered limestone-dolostone reservoirs. AAPG Bulletin, 90, 1, 91–114, doi: 10.1306/08100505087.

Ehrenberg, S.N., Nadeau, P.H., 2005. Sandstone vs. carbonate petroleum reservoirs: A global perspective on porosity-depth and porosity-permeability relationships. AAPG Bulletin, 89, 4, 435–445, doi: 10.1306/11230404071.

EITI, 2023, EITI Countries, https://eiti.org/countries (Accessed: 15.06.2023).

Elliott, S.J., Forstner, S.R., Wang, Q., Corrêa, R., Shakiba, M., Fulcher, S.A., Hebel, N.J., Lee, B.T., Tirmizi, S.T., Hooker, J.N., Fall, A., Olson, J.E., Laubach, S.E., 2025.

Diagenesis is key to unlocking outcrop fracture data suitable for quantitative extrapolation to geothermal targets. Frontiers in Earth Science, 13, 1–38, doi: 10.3389/feart.2025.1545052.

Elsner, H., 2018, Edelgase – Versorgung wirklich kritisch?, https://www.deutsche-rohstoffagentur.de/DE/Gemeinsames/Produkte/Downloads/DERA_Rohstoffinformationen/rohstoffinformationen-39.pdf;jsessionid=A575169B0783CFD5FD81752FD5CAF811.internet962?__blob=publicationFile&v=3.

EPRS, 2024, Russia in Africa: An atlas, https://www.europarl.europa.eu/RegData/etudes/BRIE/2024/757654/EPRS_BRI(2024)757654_EN.pdf.

Erbacher, J., Bornemann, A., Petrizzo, M.R., Huck, S., 2020. Chemostratigraphy and stratigraphic distribution of keeled planktonic foraminifera in the Cenomanian of the North German Basin. Zeitschrift der Deutschen Gesellschaft für Geowissenschaften, 171, 149–161, doi: 10.1127/zdgg/2020/0211.

Erickson, C., 2022, Nickel price spike during Russia-Ukraine conflict could drive up EV costs, https://www.spglobal.com/marketintelligence/en/news-insights/latest-news-headlines/nickel-price-spike-during-russia-ukraine-conflict-could-drive-up-ev-costs-69130867 (Accessed: 06.06.2023).

Ericsson, M., Löf, O., Löf, A., 2020. Chinese control over African and global mining-past, present and future. Mineral Economics, 33, 1, 153–181, doi: 10.1007/s13563-020-00233-4.

Ettler, V., Mihaljevič, M., Strnad, L., Kříbek, B., Hrstka, T., Kamona, F., Mapani, B., 2022. Gallium and germanium extraction and potential recovery from metallurgical slags. Journal of Cleaner Production, 379, 134677, doi: 10.1016/j.jclepro.2022.134677.

Etzold, A., Franz, M., 2005. Ein Referenzprofil des Keupers im Kraichgau - zusammengesetzt aus mehreren Kernbohrungen auf Blatt 6718 Wiesloch (Baden-Württemberg), LGRB-Informationen 17, 25–124.

Europäische Kommission, 2021, Kritische Rohstoffe und ihre Bedeutung für die Zukunft Europas https://cor.europa.eu/de/news/Pages/critical-raw-materials-role-future-of-europe.aspx.

Europäische Kommission, 2022a, Palladium: Impact assessment for supply security, https://rmis.jrc.ec.europa.eu/uploads/jrc133117_briefing_palladium_final.pdf.

Europäische Kommission, 2022b, Platinum: Impact assessment for supply security, https://rmis.jrc.ec.europa.eu/uploads/jrc133245_briefing_platinum_final.pdf.

Europäische Kommission, 2022c, Rare Gases (Krypton, Neon, Xenon): Impact assessment for supply security, https://rmis.jrc.ec.europa.eu/uploads/JRC130349_01_rare_gases.pdf.

Europäische Kommission, 2022d, Titanium metal: Impact assessment for supply security, https://rmis.jrc.ec.europa.eu/uploads/220616_Briefing_Titanium.pdf.

Europäische Kommission, 2023a, Anhänge des Vorschlags für eine Verordnung des Europäischen Parlaments und des Rates zur Schaffung eines Rahmens zur Gewährleistung einer sicheren und nachhaltigen Versorgung mit kritischen Rohstoffen und zur Änderung der Verordnungen (EU) 168/2013, (EU) 2018/858, (EU) 2018/1724 und (EU) 2019/1020, https://eur-

lex.europa.eu/resource.html?uri=cellar:903d35cc-c4a2-11ed-a05c-01aa75ed71a1.0003.02/DOC_2&format=PDF.

Europäische Kommission, 2023b, Fragen und Antworten zur europäischen Verordnung zu kritischen Rohstoffen, https://ec.europa.eu/commission/presscorner/detail/de/qanda_23_1662 (Accessed: 31.03.2023).

Europäische Kommission, 2023c, Kommissions-Vorschlag für eine sichere und nachhaltige Versorgung der EU mit kritischen Rohstoffen, https://germany.representation.ec.europa.eu/news/kommissions-vorschlag-fur-eine-sichere-und-nachhaltige-versorgung-der-eu-mit-kritischen-rohstoffen-2023-03-16_de (Accessed: 31.03.2023).

Europäische Kommission, 2023d, Kritische Rohstoffe: Sichere und nachhaltige Lieferketten für die grüne und die digitale Zukunft der EU gewährleisten, https://ec.europa.eu/commission/presscorner/detail/de/ip_23_1661 (Accessed: 05.04.2023).

Europäische Kommission, 2025, 47 strategische Projekte ausgewählt: Zugang zu kritischen Rohstoffen sichern und diversifizieren, https://germany.representation.ec.europa.eu/news/47-strategische-projekte-ausgewahlt-zugang-zu-kritischen-rohstoffen-sichern-und-diversifizieren-2025-03-25_de (Accessed: 02.04.2025).

Europäischer Rat/Rat der Europäischen Union, 2025a, Infografik – Ein EU-Gesetz zu kritischen Rohstoffen für die Zukunft der EU-Lieferketten https://www.consilium.europa.eu/de/infographics/critical-raw-materials/ (Accessed: 17.01.2025).

Europäischer Rat/Rat der Europäischen Union, 2025b, Sanktionen der EU gegen Russland, https://www.consilium.europa.eu/de/policies/sanctions-against-russia/ (Accessed: 05.05.2025).

European Commission, 2020, Critical Raw Materials for Strategic Technologies and Sectors in the EU - A Forsight Study, https://op.europa.eu/en/publication-detail/-/publication/8e167f11-077c-11eb-a511-01aa75ed71a1/language-en.

European Commission, 2021a, EU and Ukraine kick-start strategic partnership on raw materials, https://single-market-economy.ec.europa.eu/news/eu-and-ukraine-kick-start-strategic-partnership-raw-materials-2021-07-13_en (Accessed: 01.06.2023).

European Commission, 2021b, Memorandum of Understanding between the European Union and Ukraine on a Strategic Partnership on Raw Materials https://ec.europa.eu/docsroom/documents/46300/attachments/1/translations/en/renditions/native.

European Commission, 2023, RMIS - Strategic sectors and technologies value chains and CRM demand, https://rmis.jrc.ec.europa.eu/crms-in-strategic-sectors-and-technologies-e8c632 (Accessed: 30.05.2025).

European Commission, 2025, Selected strategic projects, https://single-market-economy.ec.europa.eu/sectors/raw-materials/areas-specific-interest/critical-raw-materials/strategic-projects-under-crma/selected-projects_en (Accessed: 30.05.2025).

European Commission (DG GROW), 2025a. Strategic project: Aguablanca Project. doi: 10.2873/2541236.

European Commission (DG GROW), 2025b. Strategic project: BAUX-EU/GALLANT/LEADER. doi: 10.2873/2802718.
European Commission (DG GROW), 2025c. Strategic project: CirCular. doi: 10.2873/9921521.
European Commission (DG GROW), 2025d. Strategic project: GALLICAM. doi: 10.2873/2800646.
European Commission (DG GROW), 2025e. Strategic project: Hydro-battery. doi: 10.2873/6786071.
European Commission (DG GROW), 2025f. Strategic project: Kolmisoppi. doi: 10.2873/6463657.
European Commission (DG GROW), 2025g. Strategic project: POLVOLT. doi: 10.2873/0073175.
European Commission (DG GROW), 2025h. Strategic project: Portovesme CRM Hub. doi: 10.2873/1138639.
European Commission (DG GROW), 2025i. Strategic project: Project Fortum Hydromet. doi: 10.2873/3111036.
European Commission (DG GROW), 2025j. Strategic project: RECOVER-IT-Resources recycling extraction and circular optimization via effluent recovery. doi: 10.2873/5473521.
European Commission (DG GROW), 2025k. Strategic project: Sakatti project. doi: 10.2873/0013595.
European Union, 2024. Regulation (EU) 2024/1252 of the European Parliament and of the Council: establishing a framework for ensuring a secure and sustainable supply of critical raw materials and amending Regulations (EU) No 168/2013, (EU) 2018/858, (EU) 2018/1724 and (EU) 2019/1020.
European Union, 2025. Council Regulation (EU) No 833/2014 of 31 July 2014 concerning restrictive measures in view of Russia's actions destabilising the situation in Ukraine - 02014R0833 — EN — 25.02.2025 — 027.002.
Eurostat, 2022, Contribution of recycled materials to raw materials demand - end-of-life recycling input rates (EOL-RIR) (cei_srm010), https://ec.europa.eu/eurostat/databrowser/view/CEI_SRM010__custom_3026831/default/table?lang=en (Accessed: 17.01.2025).
Faiola, A., Bennett, A., 2022, In the Ukraine war, a battle for the nation’s mineral and energy wealth, https://www.washingtonpost.com/world/2022/08/10/ukraine-russia-energy-mineral-wealth/ (Accessed: 05.04.2023).
Fernández-Ibáñez, F., DeGraff, J.M., Ibrayev, F., 2018. Integrating borehole image logs with core: A method to enhance subsurface fracture characterization. AAPG Bulletin, 102, 6, 1067–1090, doi: 10.1306/0726171609317002.
Ferrill, D.A., Smart, K.J., Morris, A.P., 2020. Fault failure modes, deformation mechanisms, dilation tendency, slip tendency, and conduits v. seals, in: Ogilvie, S.R., Dee, S.J., Wilson, R.W., Bailey, W.R. (Eds.), Integrated Fault Seal Analysis. Geological Society of London, doi: 10.1144/sp496-2019-7.
Ferrill, D.A., Winterle, J., Wittmeyer, G.W., Sims, D., Colton, S.L., Armstrong, A., 1999, Stressed Rock Strains Groundwater at Yucca Mountain, Nevada, https://rock.geosociety.org/net/gsatoday/archive/9/5/pdf/i1052-5173-9-5-1.pdf.

Finkbeiner, T., Barton, C.A., Zoback, M.D., 1997. Relationships Among In-Situ Stress, Fractures and Faults, and Fluid Flow: Monterey Formation, Santa Maria Basin, California1. AAPG Bulletin, 81, 12, 1975–1999, doi: 10.1306/3b05c6fe-172a-11d7-8645000102c1865d.

Folk, R.L., 1959. Practical petrographic classification of limestones 1. AAPG Bulletin, 43, 1, 1–38, doi: 10.1306/0bda5c36-16bd-11d7-8645000102c1865d.

Folk, R.L., 1974. The natural history of crystalline calcium carbonate; effect of magnesium content and salinity. Journal of Sedimentary Research, 44, 1, 40–53, doi: 10.1306/74d72973-2b21-11d7-8648000102c1865d.

Folk, R.L., 1980. Petrology of sedimentary rocks. Hemphill publishing company, Austin, Texas.

Folk, R.L., Ward, W.C., 1957. Brazos River bar (Texas): A study in the significance of grain size parameters. Journal of Sedimentary Research, 27, 1, 3–26, doi: 10.1306/74d70646-2b21-11d7-8648000102c1865d.

Fossen, H., 2010. Deformation bands formed during soft-sediment deformation: Observations from SE Utah. Marine and Petroleum Geology, 27, 1, 215–222, doi: 10.1016/j.marpetgeo.2009.06.005.

Fossen, H., Schultz, R., Shipton, Z., Mair, K., 2007. Deformation bands in sandstone: A review. Journal of the Geological Society, 164, doi: 10.1144/0016-76492006-036.

Fowles, J., Burley, S., 1994. Textural and permeability characteristics of faulted, high porosity sandstones. Marine and Petroleum Geology, 11, 5, 608–623, doi: 10.1016/0264-8172(94)90071-X.

Franz, M., Kaiser, S.I., Fischer, J., Heunisch, C., Kustatscher, E., Luppold, F.W., Berner, U., Röhling, H.G., 2015. Eustatic and climatic control on the Upper Muschelkalk Sea (late Anisian/Ladinian) in the Central European Basin. Global and Planetary Change, 135, 1–27, doi: 10.1016/j.gloplacha.2015.09.014.

Frey, M., Bär, K., Stober, I., Reinecker, J., van der Vaart, J., Sass, I., 2022. Assessment of deep geothermal research and development in the Upper Rhine Graben. Geothermal Energy, 10, 1, 18, doi: 10.1186/s40517-022-00226-2.

Friedman, G.M., Shukla, V., 1980. Significance of authigenic quartz euhedra after sulfates; example from the Lockport Formation (Middle Silurian) of New York. Journal of Sedimentary Research, 50, 4, 1299–1304, doi: 10.1306/212f7bda-2b24-11d7-8648000102c1865d.

Friis, H., 1995. The role of faecal pellets in deposition of marine muddy sediments - examples from the Danish Tertiary. Bulletin of the Geological Society of Denmark, 42, 68–73, doi: 10.37570/bgsd-1995-42-07.

Fry, N., 1979. Random point distributions and strain measurement in rocks. Tectonophysics, 60, 1, 89–105, doi: 10.1016/0040-1951(79)90135-5.

Gabriel, G., Ellwanger, D., Hoselmann, C., Weidenfeller, M., Wielandt-Schuster, U., 2013. The Heidelberg Basin, Upper Rhine Graben (Germany): A unique archive of Quaternary sediments in Central Europe. Quaternary International, 292, 43–58, doi: 10.1016/j.quaint.2012.10.044.

Gale, J., F. W. , Lander, R., H. , Reed, R., M. , Laubach, S., E. , 2010. Modeling fracture porosity evolution in dolostone. Journal of Structural Geology, 32, 9, 1201–1211, doi: 10.1016/j.jsg.2009.04.018.

Garland, J., Neilson, J., Laubach, S.E., Whidden, K.J., 2012. Advances in carbonate exploration and reservoir analysis. Geological Society, London, Special Publications, 370, 1, 1–15, doi: doi:10.1144/SP370.15.

Gaswirth, S.B., Budd, D.A., Lang Farmer, G., 2007. The role and impact of freshwater–seawater mixing zones in the maturation of regional dolomite bodies within the proto Floridan Aquifer, USA. Sedimentology, 54, 5, 1065–1092, doi: 10.1111/j.1365-3091.2007.00872.x.

Geng, A., 1996. Diagenesis of the Middle Triassic Muschelkalk, Southwestern Germany. Heidelberg University, Dissertation, 86.

Geng, A., Zeeh, S., 1995. Diagenesis of Middle Triassic Muschelkalk carbonate rocks of the Rhine graben and adjacent areas (southwest Germany). Zeitschrift der Deutschen Geologischen Gesellschaft, 146, 2, 372–385, doi: 10.1127/zdgg/146/1995/372.

Geng, Y., Sarkis, J., Bleischwitz, R., 2023. How to build a circular economy for rare-earth elements. Nature, 619, 7969, 248–251, doi: 10.1038/d41586-023-02153-z.

Geologischer Dienst NRW, 2020, Grubenwasser – Geodaten für den Nachbergbau https://www.gd.nrw.de/gw_be_grundwasserschutz-nachbergbau.htm (Accessed: 20.01.2024).

Gier, S., Worden, R., H., Johns, W., D., Kurzweil, H., 2008. Diagenesis and reservoir quality of Miocene sandstones in the Vienna Basin, Austria. Marine and Petroleum Geology, 25, 8, 681–695, doi: 10.1016/j.marpetgeo.2008.06.001.

Gier, S., Worden, R.H., Krois, P., 2018. Comparing clay mineral diagenesis in interbedded sandstones and mudstones, Vienna Basin, Austria. Geological Society, London, Special Publications, 435, 1, 389–403, doi: 10.1144/SP435.9.

Giers, R., 1958. Die Mukronatenkreide im östlichen Münsterland: Fazies, Stratigraphie und Lagerung. Beihefte zum Geologischen Jahrbuch, Heft 34, Hannover.

Girardeau-Montaut, D., 2017. CloudCompare (version 2.10alpha).

GIZ, 2021, Ein Wegweiser für deutsche Unternehmen, Namibia, https://www.giz.de/en/downloads/neue-maerkte-neue-chancen_namibia_web_mit%20coronahinweis_neu.pdf.

Goldhammer, R.K., 1997. Compaction and decompaction algorithms for sedimentary carbonates. Journal of Sedimentary Research, 67, 1, 26–35, doi: 10.1306/d42684e1-2b26-11d7-8648000102c1865d.

Gomez-Rivas, E., Martín-Martín, J.D., Bons, P., D., Koehn, D., Griera, A., Travé, A., Llorens, M.-G., Humphrey, E., Neilson, J., 2022. Stylolites and stylolite networks as primary controls on the geometry and distribution of carbonate diagenetic alterations. Marine and Petroleum Geology, 136, 105444, doi: 10.1016/j.marpetgeo.2021.105444.

Götze, J., 2012. Application of cathodoluminescence microscopy and spectroscopy in geosciences. Microscopy and Microanalysis, 18, 6, 1270–1284, doi: 10.1017/S1431927612001122.

Götze, J., Plötze, M., Habermann, D., 2001. Origin, spectral characteristics and practical applications of the cathodoluminescence (CL) of quartz – a review. Mineralogy and Petrology, 71, 3, 225–250, doi: 10.1007/s007100170040.

Götzinger, H.G., Grill, R., Küpper, H., Lichtenberger, E., Rosenberg, G., 1954. Erläuterungen zur geologischen Karte der Umgebung von Wien 1:75.000. Geologische Bundesanstalt Wien, Wien.

Greve, J., Busch, B., Quandt, D., Knaak, M., Hilgers, C., 2024. The influence of sedimentary facies, mineralogy, and diagenesis on reservoir properties of the coal-bearing Upper Carboniferous of NW Germany. Petroleum Geoscience, 30, 1, petgeo2023-2020, doi: doi:10.1144/petgeo2023-020.

Griffiths, J., Worden, R.H., Wooldridge, L.J., Utley, J.E.P., Duller, R.A., 2019. Compositional variation in modern estuarine sands: Predicting major controls on sandstone reservoir quality. AAPG Bulletin, 103, 4, 797–833, doi: 10.1306/09181818025.

Grobe, M., Machel, H.G., 2002. Saline groundwater in the Münsterland Cretaceous Basin, Germany: clues to its origin and evolution. Marine and Petroleum Geology, 19, 307–322, doi: 10.1016/S0264-8172(02)00019-3.

Grohmann, C.H., Campanha, G.A.C., 2010. OpenStereo: open source, cross-platform software for structural geology analysis.

Grosser, T., 2022, Russland-Sanktionen: Chinas Suche nach Auswegen https://www.freiheit.org/de/deutschland/russland-sanktionen-chinas-suche-nach-auswegen-0 (Accessed: 05.04.2023).

Gutteridge, P., ten Veen, J., Dewit, J., Garland, J., Riva, A., Mozafari, M., Jaarsma, B., van Melle, T., 2025. Regional assessment of the ultra-deep geothermal (UDG) reservoir quality and potential of the Dinantian Zeeland Formation, the Netherlands. Geological Society, London, Special Publications, 548, 1, SP548-2023-2106, doi: doi:10.1144/SP548-2023-106.

Győri, O., Haas, J., Hips, K., Lukoczki, G., Budai, T., Demény, A., Szőcs, E., 2020. Dolomitization of shallow-water, mixed siliciclastic-carbonate sequences: The Lower Triassic ramp succession of the Transdanubian Range, Hungary. Sedimentary Geology, 395, 105549, doi: 10.1016/j.sedgeo.2019.105549.

Hagdorn, H., Simon, T., 2021. Der Muschelkalk im nördlichen Baden-Württemberg, in: Hagdorn, H., Simon, T. (Eds.), Stratigraphie von Deutschland XIII-Muschelkalk. Deutsche Stratigraphische Kommission, Subkommission Perm-Trias, Berlin, 962–1006.

Hagelüken, C., Goldmann, D., 2022. Recycling and circular economy—towards a closed loop for metals in emerging clean technologies. Mineral Economics, 35, 3, 539–562, doi: 10.1007/s13563-022-00319-1.

Halley, R.B., Schmoker, J.W., 1983. High porosity Cenozoic carbonate rocks of south Florida: Progressive loss of porosity with depth. American Association of Petroleum Geologists Bulletin, 67.

Harbaugh, J.W., 1967. Chapter 7 - Carbonate oil reservoir rocks, in: George, V.C., Harold, J.B., Rhodes, W.F. (Eds.), Carbonate Rocks Origin, Occurrence and Classification. Elsevier, 349–398, doi: 10.1016/S0070-4571(08)71115-4.

Harder, H., 1964. Geochemische Untersuchungen zur Genese der Strontianitlagerstätten des Münsterlandes. Beiträge zur Mineralogie und Petrographie, 10, 2, 198–215, doi: 10.1007/BF02652615.

Harlé, P., Kushnir, A.R.L., Aichholzer, C., Heap, M.J., Hehn, R., Maurer, V., Baud, P., Richard, A., Genter, A., Duringer, P., 2019. Heat flow density estimates in the

Upper Rhine Graben using laboratory measurements of thermal conductivity on sedimentary rocks. Geothermal Energy, 7, 1, 38, doi: 10.1186/s40517-019-0154-3.

Hartlieb-Wallthor, Marbler, H., 2017, Rohstoffe Subsahara, https://www.deutsche-rohstoffagentur.de/DERA/DE/Downloads/rohstoffstudie-subsahara.pdf?__blob=publicationFile&v=2.

Harzhauser, M., Kranner, M., Mandic, O., Strauss, P., Siedl, W., Piller, W., 2020. Miocene lithostratigraphy of the northern and central Vienna Basin (Austria). Austrian Journal of Earth Sciences, 113, 169–199, doi: 10.17738/ajes.2020.0011.

Healy, D., 2023, FracTend, https://github.com/DaveHealy-github/FracTend (Accessed: 01.04.2025).

Healy, D., Rizzo, R.E., Cornwell, D.G., Farrell, N.J.C., Watkins, H., Timms, N.E., Gomez-Rivas, E., Smith, M., 2017. FracPaQ: A MATLAB™ toolbox for the quantification of fracture patterns. Journal of Structural Geology, 95, 1–16, doi: 10.1016/j.jsg.2016.12.003.

Heap, M.J., Kushnir, A.R.L., Gilg, H.A., Violay, M.E.S., Harlé, P., Baud, P., 2019. Petrophysical properties of the Muschelkalk from the Soultz-sous-Forêts geothermal site (France), an important lithostratigraphic unit for geothermal exploitation in the Upper Rhine Graben. Geothermal Energy, 7, 1, 27, doi: 10.1186/s40517-019-0145-4.

Hemes, S., 2008. Strukturgeologische Kartierung des Muschelkalkausstrichs zwischen Wiesloch und Eschelbronn, im nördlichen Kraichgau (Baden-Württemberg). Georg-August-Universität, Göttingen, Diploma, 89.

Hilgers, C., Becker, I., 2020. Local availability of raw materials and increasing global demand – aspects of resilient resource strategies, World of Mining - Surface & Underground, 5 ed. GDMB Verlag GmbH, 254–263.

Hilgers, C., Busch, B., 2024. Rohstoffbewusstsein und geostrategische Rohstoffsicherung, Sitzungsberichte der Leibniz-Sozietät. Haßler, Gerda, Berlin, 21–55, doi: 10.53201/SITZUNGSBERICHTE163.

Hilgers, C., Busch, B., Ölmez, J.A., 2023. Klima, Rohstoffverfügbarkeit und Energiewende - Deutschland in der Krise?, Sitzungsberichte der Leibniz-Sozietät. Gerda Haßler, Berlin, 21–69.

Hilgers, C., Dilg-Gruschinski, K., Urai, J.L., 2004. Microstructural evolution of syntaxial veins formed by advective flow. Geology, 32, 3, 261–264, doi: 10.1130/g20024.1.

Hilgers, C., Kolb, J., Becker, I., 2021, Ist die deutsche Ressourcenstrategie resilient? Bergbau – Verhüttung – Recycling https://www.thinktank-irs.de/wp-content/uploads/2021/05/RZ_THINKTANK_Broschuere_Bergbau_Verhuettung_Recycling_DE_Web_Einzelseiten_NEU.pdf.

Hilgers, C., Urai, J.L., 2002. Microstructural observations on natural syntectonic fibrous veins: implications for the growth process. Tectonophysics, 352, 3-4, 257-274, doi: 10.1016/S0040-1951(02)00185-3.

Hiss, M., 1995. Kreide, Geologie im Münsterland. Drozdzewski, G., Krefeld, 41–65.

Hiss, M., Mutterlose, J., 2010. Field trip E6: Cretaceous geosites of the eastern Ruhr Area and the southern Münsterland. Schriftenreihe der Deutschen Gesellschaft für Geowissenschaften, 66, 168–183, doi: 10.1127/sdgg/66/2010/168.

Honjo, S., Fischer, A.G., Garrison, R., 1965. Geopetal pyrite in fine-grained limestones. Journal of Sedimentary Research, 35, 2, 480–488, doi: 10.1306/74d712b2-2b21-11d7-8648000102c1865d.

Houseknecht, D.W., 1987. Assessing the relative importance of compaction processes and cementation to reduction of porosity in sandstones 1. AAPG Bulletin, 71, 6, 633–642, doi: 10.1306/9488787f-1704-11d7-8645000102c1865d.

Huggett, J.M., 2013. Minerals: Glauconites and green clays, Reference Module in Earth Systems and Environmental Sciences. Elsevier.

Humphrey, E., Gomez-Rivas, E., Koehn, D., Bons, P.D., Neilson, J., Martín-Martín, J.D., Schoenherr, J., 2019. Stylolite-controlled diagenesis of a mudstone carbonate reservoir: A case study from the Zechstein-2-Carbonate (Central European Basin, NW Germany). Marine and Petroleum Geology, 109, 88–107, doi: 10.1016/j.marpetgeo.2019.05.040.

Ibrahem, Y., Morozov, V.P., 2024. Exploring the potential of drill cuttings for reservoir characterization: A case study from the Volga-Ural basin, Russia. Petroleum Research, doi: 10.1016/j.ptlrs.2024.01.012.

ICMM, 2022, Role of mining in national economies: Mining Contribution Index (6th Edition), https://www.icmm.com/en-gb/research/social-performance/2022/role-of-mining-in-national-economies (Accessed: 20.06.2023).

IEA, 2023, Critical Minerals Market Review 2023, https://iea.blob.core.windows.net/assets/afc35261-41b2-47d4-86d6-d5d77fc259be/CriticalMineralsMarketReview2023.pdf.

IEA, 2024, Global Critical Minerals Outlook 2024, https://www.iea.org/reports/global-critical-minerals-outlook-2024.

IMF, 2024, World Economic Outlook Database https://www.imf.org/en/Publications/WEO/weo-database/2023/October/weo-report?c=698,&s=PCPI,PCPIPCH,&sy=2021&ey=2028&ssm=0&scsm=1&scc=0&ssd=1&ssc=0&sic=0&sort=country&ds=.&br=1 (Accessed: 03.04.2024).

Immenhauser, A., 2022. On the delimitation of the carbonate burial realm. The Depositional Record, 8, 2, 524–574, doi: 10.1002/dep2.173.

IRENA, 2023, Geopolitics of the energy transition: Critical materials, https://mc-cd8320d4-36a1-40ac-83cc-3389-cdn-endpoint.azureedge.net/-/media/Files/IRENA/Agency/Publication/2023/Jul/IRENA_Geopolitics_energy_transition_critical_materials_2023.pdf?rev=420aeb58d2e745d79f1b564ea89ef9f8.

Janetschke, N., Wilmsen, M., 2013. Magnetische Suszeptibilität als stratigraphisches Werkzeug – eine unterstützende Methode zur klassischen Profilaufnahme (Fallstudie: norddeutsche Oberkreide von Halle/Westfalen), Geologica Saxonica - Journal of Central European Geology, 149–163.

Johan, B.S., Neil, R.H., 2001. Comparison between outcrop-spectral gamma ray logging and whole rock geochemistry: Implications for quantitative reservoir characterisation in continental sequences. Marine and Petroleum Geology, 18, 6, 657–670, doi: 10.1016/S0264-8172(01)00022-8.

Johnsson, M.J., 1993. The system controlling the composition of clastic sediments, in: Johnsson, M.J., Basu, A. (Eds.), Processes Controlling the Composition of Clastic Sediments. Geological Society of America, 1–21, doi: 10.1130/SPE284-p1.

Kaminskaite-Baranauskiene, I., Wang, H., Liu, Z., Li, H., 2023. Geothermal carbonate reservoirs and their sustainability: what can natural hydrothermal systems tell us? Geothermics, 114, 102798, doi: 10.1016/j.geothermics.2023.102798.

Kaplan, U., 2004. Neue Beobachtungen zu den Stromberg-Schichten, Untercampan, Oberkreide, südöstliches Münsterland. Geologie und Paläontologie in Westfalen, 62, 71–110.

Kaplan, U., Kennedy, W., Ernst, G., 1996. Stratigraphie und Ammonitenfaunen des Campan im südöstlichen Münsterland. Geologie und Paläontologie in Westfalen, 43.

Kappel, J., 2002. Ichnofossilien im Campanium des südöstlichen Münsterlandes. Westfälische Wilhelms-Universität Münster, Münster, Dissertation, 236.

Käßner, A., Tichomirowa, M., Rößler, R., Görz, I., 2024. Zircon U–Pb CA–ID–TIMS constraints on the chronology of the Late Carboniferous–Early Permian continental Döhlen Basin and its correlation with the Thuringian Forest Basin (Central and Eastern Germany). International Journal of Earth Sciences, 113, 7, 1599–1618, doi: 10.1007/s00531-024-02464-0.

Kaube, J., 2023, Der Fluch des Rohstoffreichtums, https://www.faz.net/aktuell/wirtschaft/wirtschaftswissen/der-hollaendische-fluch-des-rohstoffreichtums-18739195.html?GEPC=s9&premium=0xdf25eb6d03e2657f175c3f8ad6263571f783df3c02860fea9e27602e21bc503d (Accessed: 15.06.2023).

Kayser, A., 2006. Herkunft, Auftreten und Visualisierung von Permeabilitätsbarrieren in einer Gaslagerstätte in Sandsteinen des Rotliegenden (Südliches Permbecken, Deutschland): Bedeutung für Diagenese, Fluidfluß und Produktion. Philipps-Universität Marburg, Dissertation, 206.

Kazmierczak, J., Coleman, M., Gruszczynski, M., Kempe, S., 1996. Cyanobacterial key to the genesis of micritic and peloidal limestones in ancient seas. Acta Palaeontologica Polonica, 41, 319–338.

Kenter, J.A.M., Braaksma, H., Verwer, K., van Lanen, X.M.T., 2007. Acoustic behavior of sedimentary rocks: Geologic properties versus Poisson's ratios. The Leading Edge, 26, 4, 436–444, doi: 10.1190/1.2723206.

KfW, GIZ, IRENA, 2020, Energiewende Afrika, Mehr Dynamik für Energiezugang, Resilienz und Wohlstand, https://www.giz.de/de/downloads/Studie_Renewable%20Energy%20Transition%20Africa_DE.pdf.

Khelifa, C., Zeddouri, A., Djabes, F., 2014. Influence of natural fractures on oil production of unconventional reservoirs. Energy Procedia, 50, 360–367, doi: 10.1016/j.egypro.2014.06.043.

Kinch, D., 2020, Global aluminum demand to drop 5.4% this year; output rising: IAI secretary general https://www.spglobal.com/commodityinsights/en/market-insights/latest-news/metals/071720-global-aluminum-demand-to-drop-54-this-year-output-rising-iai-secretary-general (Accessed: 26.06.2023).

Kley, J., Voigt, T., 2008. Late Cretaceous intraplate thrusting in central Europe: Effect of Africa-Iberia-Europe convergence, not Alpine collision. Geology, 36, 11, doi: 10.1130/g24930a.1.

Klinkenberg, L.J., 1941. The permeability of porous media to liquids and gases. Drilling and Production Practice: American Petroleum Institute, 200–213.

Knauth, L.P., 1979. A model for the origin of chert in limestone. Geology, 7, 6, 274–277, doi: 10.1130/0091-7613(1979)7<274:Amftoo>2.0.Co;2.

Knox, J.A., Ripley, H.E., 1979. Fracture acidizing in carbonate rock. Journal of Canadian Petroleum Technology, 18, 04, doi: 10.2118/79-04-07.

Knupp, M., 2021, Neue Vielfalt im Bergbau, https://www.gtai.de/de/trade/botsuana/branchen/neue-vielfalt-im-bergbau--717114 (Accessed: 16.06.2023).

Knupp, M., 2023, Simbabwe unterbindet Lithiumexport, https://www.gtai.de/de/trade/simbabwe/branchen/simbabwe-unterbindet-lithiumexport-955750 (Accessed: 15.06.2023).

Koehrer, B., Aigner, T., Forke, H., Pöppelreiter, M., 2012. Middle to Upper Khuff (Sequences KS1 to KS4) outcrop-equivalents in the Oman Mountains:Grainstone architecture on a subregional scale. GeoArabia, 17, 4, 59–104, doi: 10.2113/geoarabia170459.

Koehrer, B.S., Heymann, C., Prousa, F., Aigner, T., 2010. Multiple-scale facies and reservoir quality variations within a dolomite body – Outcrop analog study from the Middle Triassic, SW German Basin. Marine and Petroleum Geology, 27, 2, 386–411, doi: 10.1016/j.marpetgeo.2009.09.009.

Korea Bizwire, 2022, SK hynix Expands Use of Domestically-produced Neon Gas, http://koreabizwire.com/sk-hynix-expands-use-of-domestically-produced-neon-gas/230369 (Accessed: 06.06.2023).

Kosari, E., Kadkhodaie, A., Bahroudi, A., Chehrazi, A., Talebian, M., 2017. An integrated approach to study the impact of fractures distribution on the Ilam-Sarvak carbonate reservoirs: A case study from the Strait of Hormuz, the Persian Gulf. Journal of Petroleum Science and Engineering, 152, 104–115, doi: 10.1016/j.petrol.2017.03.001.

Kostic, B., Aigner, T., 2004. Sedimentary and poroperm anatomy of shoal-water carbonates (Muschelkalk, South-German Basin): an outcrop-analogue study of inter-well spacing scale. Facies, 50, 1, 113–131, doi: 10.1007/s10347-004-0003-z.

Kramm, U., 1985. Sr-Isotopenuntersuchungen zur Genese der Strontianitlagerstätte Münsterland/Westfalen. Fortschr. Miner., 63, 124.

Krumbeck, V., 2025, Kriegsentscheidendes Material für Putin stammte aus Bayern: Export nach Russland, https://www.merkur.de/wirtschaft/kriegsmaterial-fuer-putin-aus-bayern-export-nach-russland-zr-93691584.html (Accessed: 12.05.2025).

Kruszewski, M., Montegrossi, G., Saenger, E.H., 2023. The risk of fluid-injection-induced fault reactivation in carbonate reservoirs: an investigation of a geothermal system in the Ruhr region (Germany). Geomechanics and Geophysics for Geo-Energy and Geo-Resources, 9, 1, 38, doi: 10.1007/s40948-023-00573-9.

Kumar, A., Prajapati, N., Späth, M., Busch, B., Schneider, D., Hilgers, C., Nestler, B., 2023. Qualitative dissolution modeling of etch-pit formation on the K-feldspar surface through phase-field approach. Journal of Geophysical Research: Solid Earth, 128, 4, e2022JB025749, doi: 10.1029/2022JB025749.

Kummerow, J., 2006. The Influence of Intergranular, Supercritical Water on the Elastic Properties of Rocks. Freie Universität Berlin, Dissertation, 96.

Kushnir, A.R.L., Heap, M.J., Baud, P., Gilg, H.A., Reuschlé, T., Lerouge, C., Dezayes, C., Duringer, P., 2018. Characterizing the physical properties of rocks from the Paleozoic to Permo-Triassic transition in the Upper Rhine Graben. Geothermal Energy, 6, 1, 16, doi: 10.1186/s40517-018-0103-6.

La Bruna, V., Lamarche, J., Agosta, F., Rustichelli, A., Giuffrida, A., Salardon, R., Marié, L., 2020. Structural diagenesis of shallow platform carbonates: Role of early embrittlement on fracture setting and distribution, case study of Monte Alpi (Southern Apennines, Italy). Journal of Structural Geology, 131, 103940, doi: 10.1016/j.jsg.2019.103940.

Ladwein, H.W., 1988. Organic geochemistry of Vienna Basin: Model for hydrocarbon generation in overthrust belts 1. AAPG Bulletin, 72, 5, 586–599, doi: 10.1306/703c8ed4-1707-11d7-8645000102c1865d.

Lamarche, J., Lavenu, A., P. C. , Gauthier, B., D. M. , Guglielmi, Y., Jayet, O., 2012. Relationships between fracture patterns, geodynamics and mechanical stratigraphy in carbonates (South-East Basin, France). Tectonophysics, 581, 231–245, doi: 10.1016/j.tecto.2012.06.042.

Lander, R.H., Larese, R.E., Bonnell, L.M., 2008. Toward more accurate quartz cement models: The importance of euhedral versus noneuhedral growth rates. AAPG Bulletin, 92, 11, 1537–1563, doi: 10.1306/07160808037.

Lander, R.H., Laubach, S.E., 2015. Insights into rates of fracture growth and sealing from a model for quartz cementation in fractured sandstones. GSA Bulletin, 127, 3-4, 516–538, doi: 10.1130/b31092.1.

Lanson, B., Beaufort, D., Berger, G., Bauer, A., Cassagnabère, A., Meunier, A., 2002. Authigenic kaolin and illitic minerals during burial diagenesis of sandstones: A review. Clay Minerals, 37, 1, 1–22, doi: 10.1180/0009855023710014.

Laubach, S., E. , Olson, J., E., Gale, J., F. W., 2004. Are open fractures necessarily aligned with maximum horizontal stress? Earth and Planetary Science Letters, 222, 1, 191–195, doi: 10.1016/j.epsl.2004.02.019.

Lavenu, A.P.C., Lamarche, J., Gallois, A., Gauthier, B.D.M., 2013. Tectonic versus diagenetic origin of fractures in a naturally fractured carbonate reservoir analog (Nerthe anticline, southeastern France). AAPG Bulletin, 97, 12, 2207–2232, doi: 10.1306/04041312225.

LBEG, 2023. Underground Gas Storage in Germany. EEK, 139, 41–49, doi: 10.19225/231103.

Lee, E.Y., Kominz, M., Reuning, L., Gallagher, S., Takayanagi, H., Ishiwa, T., Knierzinger, W., Wagreich, M., 2021. Quantitative compaction trends of Miocene to Holocene carbonates off the west coast of Australia. Australian Journal of Earth Sciences, 68, 1149–1161, doi: 10.1080/08120099.2021.1915867.

Leuthold, J., Gerolymatou, E., Vergara, M.R., Triantafyllidis, T., 2021. Effect of Compaction Banding on the Hydraulic Properties of Porous Rock: Part I—Experimental Investigation. Rock Mechanics and Rock Engineering, 54, 6, 2671–2683, doi: 10.1007/s00603-021-02427-w.

LGRB, 2022, L 6918-8 - Karte der mineralischen Rohstoffe 1 : 50 000 - Rohstoffvorkommen, https://media.lgrb-bw.de/link/ol/ol6918a008.pdf.

Li, J.Z., Laubach, S.E., Gale, J.F.W., Marrett, R.A., 2018. Quantifying opening-mode fracture spatial organization in horizontal wellbore image logs, core and outcrop:

Application to Upper Cretaceous Frontier Formation tight gas sandstones, USA. Journal of Structural Geology, 108, 137–156, doi: 10.1016/j.jsg.2017.07.005.

Longman, M.W., 1980. Carbonate diagenetic textures from nearsurface diagenetic environments 1. AAPG Bulletin, 64, 4, 461–487, doi: 10.1306/2f918a63-16ce-11d7-8645000102c1865d.

López-Quirós, A., Sánchez-Navas, A., Nieto, F., Escutia, C., 2020. New insights into the nature of glauconite. American Mineralogist, 105, 674–686, doi: 10.2138/am-2020-7341.

Lowe, D.R., Guy, M., 2000. Slurry-flow deposits in the Britannia Formation (Lower Cretaceous), North Sea: a new perspective on the turbidity current and debris flow problem. Sedimentology, 47, 1, 31–70, doi: 10.1046/j.1365-3091.2000.00276.x.

Lucia, F.J., Kerans, C., Jennings, J.W., Jr., 2003. Carbonate reservoir characterization. Journal of Petroleum Technology, 55, 06, 70–72, doi: 10.2118/82071-jpt.

Lupin, J.H., Hampson, G.J., 2020. Sediment-routing controls on sandstone bulk petrographic composition and texture across an ancient shelf: Example from Cretaceous Western Interior Basin, Utah and Colorado, U.S.A. Journal of Sedimentary Research, 90, 10, 1389–1409, doi: 10.2110/jsr.2020.044.

Lutter, S., Kreimel, J., Giljum, S., Dittrich, M., Limberger, S., Ewers, B., Schoer, K., Manstein, C., 2022, Die Nutzung natürlicher Ressourcen - Ressourcenbericht für Deutschland 2022 - Spezial: Rohstoffnutzung der Zukunft, http://www.umweltbundesamt.de/ressourcenbericht2022.

Machel, H., 2005. Investigation of burial diagenesis in carbonate hydrocarbon reservoir rocks. Geoscience Canada, 32, 103–128.

Machel, H.G., Grobe, M., 2001. Bacterial and thermochemical sulfate reduction in diagenetic settings — old and new insights. Sedimentary Geology, 140, 1, 143–175, doi: 10.1016/S0037-0738(00)00176-7.

Macintyre, I.G., 1985. Submarine cements—The peloidal question, in: Schneidermann, N., Harris, P.M. (Eds.), Carbonate Cements: Based on a symposium sponsored by the Society of Economic Paleontologists and Mineralogists. SEPM Society for Sedimentary Geology, doi: 10.2110/pec.85.36.0109.

Makowitz, A., Lander, R., Milliken, K., 2006. Diagenetic modeling to assess the relative timing of quartz cementation and brittle grain processes during compaction. Aapg Bulletin - AAPG BULL, 90, 873–885, doi: 10.1306/12190505044.

Mamdouh, M., Reda, M., Raef, A., El Din, M.Y.Z., Abdelhafeez, T.H., Al-Hashim, M.H., 2024. Reservoir quality, lithotype assessment, and geochemical source rock analysis: insights from well logs and pyrolysis data, Karama Field, North-Western Desert, Egypt. Geofluids, 2024, 1, 1235792, doi: 10.1155/2024/1235792.

Manalo, P., 2024, Average lead time almost 18 years for mines started in 2020–23 https://www.spglobal.com/marketintelligence/en/news-insights/research/average-lead-time-almost-18-years-for-mines-started-in-2020-23 (Accessed: 11.04.2024).

Marrett, R., Gale, J., F. W. , Gómez, L., A. , Laubach, S., E. , 2018. Correlation analysis of fracture arrangement in space. Journal of Structural Geology, 108, 16–33, doi: 10.1016/j.jsg.2017.06.012.

Masters, B.A., Scott, R.W., 1979. Calcispheres and Nannoconids. In: Paleontology. Encyclopedia of Earth Science. Springer Berlin Heidelberg, Berlin, Heidelberg, 167–170.

Mattern, F., Wang, P.J., 2008. Out-of-sequence thrusts and paleogeography of the Rhenodanubian Flysch Belt (Eastern Alps) revisited. International Journal of Earth Sciences, 97, 4, 821–833, doi: 10.1007/s00531-007-0200-4.

Mattila, J., Tammisto, E., 2012. Stress-controlled fluid flow in fractures at the site of a potential nuclear waste repository, Finland. Geology, 40, 4, 299–302, doi: 10.1130/g32832.1.

Mauriohooho, K., Barker, S., L. L., Rae, A., 2016. Mapping lithology and hydrothermal alteration in geothermal systems using portable X-ray fluorescence (pXRF): A case study from the Tauhara geothermal system, Taupo Volcanic Zone. Geothermics, 64, 125–134, doi: 10.1016/j.geothermics.2016.03.005.

Mazur, S., Scheck-Wenderoth, M., 2005. Constraints on the tectonic evolution of the Central European Basin System revealed by seismic reflection profiles from Northern Germany. Netherlands Journal of Geosciences, 84, 4, 389–401, doi: 10.1017/S001677460002120X.

McKee, E.D., Gutschick, R.C., 1969. History of the Redwall Limestone of Northern Arizona. Geological Society of Americadoi: 10.1130/mem114.

Medici, G., Smeraglia, L., Torabi, A., Botter, C., 2021. Review of modeling approaches to groundwater flow in deformed carbonate aquifers. Groundwater, 59, 3, 334–351, doi: 10.1111/gwat.13069.

Mehl, J., 1982. Die Tempestit-Fazies im Oberen Muschelkalk Südbadens. Jahreshefte des Geologischen Landesamtes Baden-Württemberg, 24, 91–109.

Meier, S., Bauer, J., F. , Philipp, S., L. , 2015. Fault zone characteristics, fracture systems and permeability implications of Middle Triassic Muschelkalk in Southwest Germany. Journal of Structural Geology, 70, 170–189, doi: 10.1016/j.jsg.2014.12.005.

Meixner, J., Schill, E., Gaucher, E., Kohl, T., 2014. Inferring the in situ stress regime in deep sediments: an example from the Bruchsal geothermal site. Geothermal Energy, 2, 1, 7, doi: 10.1186/s40517-014-0007-z.

Merz, L., Bauer, U., Hilgers, C., 2019. Faults and fracture networks in Upper Muschelkalk outcrop analogues detected by photogrammetry, Upper Rhine Graben (URG), Germany. Poster präsentiert auf DGMK/ÖGEW Frühjahrstagung "Shaping the Energy Transitionwith Upstream and Storage Technologies" (2019), Celle, Deutschland, 25.–26. April 2019.

Merz, L., Manss, Y., Hilgers, C., 2018. Automated fracture analysis in Middle Triassic Muschelkalk, Upper Rhine Graben. Poster präsentiert auf DGMK/ÖGEW Frühjahrstagung "Shaping the Energy Transition with Upstream and Storage Technologies" (2018), Celle, Deutschland, 18.–19. April 2018.

Miller, K.G., Kominz, M.A., Browning, J.V., Wright, J.D., Mountain, G.S., Katz, M.E., Sugarman, P.J., Cramer, B.S., Christie-Blick, N., Pekar, S.F., 2005. The Phanerozoic Record of Global Sea-Level Change. Science, 310, 5752, 1293–1298, doi: doi:10.1126/science.1116412.

Milliken, K.L., 1979. The silicified evaporite syndrome; two aspects of silicification history of former evaporite nodules from southern Kentucky and northern Tennessee. Journal of Sedimentary Research, 49, 1, 245–256, doi: 10.1306/212f7707-2b24-11d7-8648000102c1865d.

Milton, N.J., Emery, D., 1996. Outcrop and well data, in: Emery, D., Myers, K.J. (Eds.), Sequence stratigraphy. BP Exploration, Stockley Park, Uxbridge, London, 61-79.

Mining Indaba, 2022, Botswana at investing in African Mining Indaba, https://www.brandbotswana.co.bw/wp-content/uploads/2022/04/Mining-Indaba-Booklet-1.pdf.

MiningTechnology, 2025, Nornickel's 2024 profit drops 37% to $1.8bn amid sanctions, weak prices, https://www.mining-technology.com/news/nornickels-2024-profit-drops/?cf-view (Accessed: 26.05.2025).

Miocic, J.M., Girard, J.-P., Schöner, R., Gaupp, R., 2020. Mudstone/sandstone ratio control on carbonate cementation and reservoir quality in Upper Permian Rotliegend sandstones, offshore the Netherlands. Marine and Petroleum Geology, 115, doi: 10.1016/j.marpetgeo.2020.104293.

Möbius, R., Gauer, A., Tosoratti, F., 2023. Exploring for unlocked subsurface potential by integration of historic and modern data: The case of a forgotten Flysch reservoir within the Vienna Basin (Austria) discovered almost a century ago, DGMK/ÖGEW Frühjahrstagung 2023, Celle (Germany), 157–160.

Mohrdieck, P., 1996. Ergebnisse geologisch-hydrogeologischer Untersuchungen bei der Herstellung eines Injektionssohle in Mergelgesteinen der Oberkreide. RWTH Aachen, Aachen, Dissertation, 231.

Molenaar, N., 1986. The interrelation between clay infiltration, quartz cementation, and compaction in lower Givetian terrestrial sandstones, northern Ardennes, Belgium. Journal of Sedimentary Research, 56, 3, 359–369, doi: 10.1306/212f8913-2b24-11d7-8648000102c1865d.

Monnerjahn, M., 2023, Deutscher Außenhandel mit Afrika wächst, https://www.gtai.de/de/trade/afrika/wirtschaftsumfeld/deutscher-aussenhandel-mit-afrika-waechst-1031252 (Accessed: 02.04.2024).

Monsees, A.C., Busch, B., Hilgers, C., 2021. Compaction control on diagenesis and reservoir quality development in red bed sandstones: a case study of Permian Rotliegend sandstones. International Journal of Earth Sciences, 110, 5, 1683–1711, doi: 10.1007/s00531-021-02036-6.

Monsees, A.C., Busch, B., Schöner, N., Hilgers, C., 2020. Rock typing of diagenetically induced heterogeneities – A case study from a deeply-buried clastic Rotliegend reservoir of the Northern German Basin. Marine and Petroleum Geology, 113, 104163, doi: 10.1016/j.marpetgeo.2019.104163.

Moore, C., H. , Wade, W., J. , 2013. Chapter 11 - Natural fracturing in carbonate reservoirs, in: Moore, C., H. , Wade, W., J. (Eds.), Carbonate Reservoirs. Elsevier, 285–300, doi: 10.1016/B978-0-444-53831-4.00011-2.

Morad, S., 1998. Carbonate cementation in sandstones: Distribution patterns and geochemical evolution. 1–26.

Morad, S., Al-Ramadan, K., Ketzer, J.M., De Ros, L.F., 2010. The impact of diagenesis on the heterogeneity of sandstone reservoirs: A review of the role of depositional facies and sequence stratigraphy. AAPG Bulletin, 94, 8, 1267–1309, doi: 10.1306/04211009178.

Morad, S., Al Suwaidi, M., Mansurbeg, H., Morad, D., Ceriani, A., Paganoni, M., Al-Aasm, I., 2019. Diagenesis of a limestone reservoir (Lower Cretaceous), Abu

Dhabi, United Arab Emirates: Comparison between the anticline crest and flanks. Sedimentary Geology, 380, 127–142, doi: 10.1016/j.sedgeo.2018.12.004.

Morad, S., Ketzer, M., De Ros, L., 2002. Spatial and temporal distribution of diagenetic alterations in siliclastic rocks: Implications for mass transfer in sedimentary basins. Sedimentology, 47, 95–120, doi: 10.1046/j.1365-3091.2000.00007.x.

Morris, A., Ferrill, D.A., Henderson, D.B., 1996. Slip-tendency analysis and fault reactivation. Geology, 24, 3, 275–278, doi: 10.1130/0091-7613(1996)024<0275:Staafr>2.3.Co;2.

Moshier, S.O., 1989. Microporosity in micritic limestones: a review. Sedimentary Geology, 63, 3, 191–213, doi: 10.1016/0037-0738(89)90132-2.

Munnecke, A., Wright, V.P., Nohl, T., 2023. The origins and transformation of carbonate mud during early marine burial diagenesis and the fate of aragonite: A stratigraphic sedimentological perspective. Earth-Science Reviews, 239, 104366, doi: 10.1016/j.earscirev.2023.104366.

Nadeau, P.H., Hurst, A., 1991. Application of back-scattered electron microscopy to the quantification of clay mineral microporosity in sandstones. Journal of Sedimentary Research, 61, 6, 921–925, doi: 10.1306/d4267807-2b26-11d7-8648000102c1865d.

Najjar, F., 2024, Simbabwe: Lithiumboom an einem schwierigen Sourcing-Standort, https://www.gtai.de/de/trade/simbabwe/specials/rohstoffe-1062570.

Narr, W., 1996. Estimating average fracture spacing in subsurface rock 1. AAPG Bulletin, 80, 10, 1565–1585, doi: 10.1306/64eda0b4-1724-11d7-8645000102c1865d.

NATO, 2024, Defence-Critical Supply Chain Security Roadmap, https://www.nato.int/nato_static_fl2014/assets/pdf/2024/7/pdf/240712-Factsheet-Defence-Supply-Chain-Ro.pdf.

Neitzel, D., 2022, Knapp und teuer: Diese Rohstoffe kommen aus Russland, https://www.technik-einkauf.de/rohstoffe/kritische-rohstoffe/diese-rohstoffe-kommen-aus-russland-215.html (Accessed: 08.06.2023).

Odin, G., 1990. Clay mineral formation at the continent-ocean boundary: The verdine facies. Clay Minerals, 25(4), 477–483, doi: 10.1180/claymin.1990.025.4.06.

Odin, G.S., Fullagar, P.D., 1988. Chapter C4 Geological significance of the glaucony facies, Green Marine Clays. Elsevier, 295–332, doi: 10.1016/S0070-4571(08)70069-4.

OEC, 2023, Niobium, Tantalum, Vanadium and Zirconium Ore in Netherlands, https://oec.world/en/profile/bilateral-product/niobium-tantalum-vanadium-and-zirconium-ore/reporter/nld?yearExportSelector=exportYear1 (Accessed: 15.06.2023).

OECD, 2019, Global Material Resources Outlook to 2060, https://www.oecd-ilibrary.org/content/publication/9789264307452-en.

Offshore, 2021, Norwegian trio develop drill cuttings digital visualization tool, https://www.offshore-mag.com/geosciences/article/14206534/norwegian-trio-develop-drill-cuttings-digital-visualization-tool (Accessed: 15.08.2025).

Ölmez, J.A., Busch, B., Hilgers, C., 2024. Reservoir quality of Upper Cretaceous limestones (Ahlen-Fm., Beckum Member, Münsterland Cretaceous Basin): effects of cementation and compaction on the compactable depositional volume. International Journal of Earth Sciences, doi: 10.1007/s00531-024-02411-z.

Ölmez, J.A., Hilgers, C., 2023. Rohstoffe für Deutschland und Auswirkungen des Russland-Ukraine Konflikts. Thinktank IRS, 55.

Ölmez, J.A., Hilgers, C., 2024a. Resilient Supply of Critical and Strategic Raw Materials for Germany – Potentials in Africa. World of Metallurgy – ERZMETALL (GDMB), 77 2, 113–120.

Ölmez, J.A., Hilgers, C., 2024b. Resiliente Rohstoffversorgung Deutschlands – Bergbaupotentiale in ausgewählten Ländern Afrikas und die Rolle Chinas. Thinktank IRS, 49.

Olson, J.E., Laubach, S.E., Lander, R.H., 2009. Natural fracture characterization in tight gas sandstones: Integrating mechanics and diagenesis. AAPG Bulletin, 93, 11, 1535–1549, doi: 10.1306/08110909100.

Ozkan, A., Cumella, S.P., Milliken, K.L., Laubach, S.E., 2011. Prediction of lithofacies and reservoir quality using well logs, Late Cretaceous Williams Fork Formation, Mamm Creek field, Piceance Basin, Colorado. AAPG Bulletin, 95, 10, 1699–1723, doi: 10.1306/01191109143.

Panza, E., Agosta, F., Rustichelli, A., Zambrano, M., Tondi, E., Prosser, G., Giorgioni, M., Janiseck, J.M., 2016. Fracture stratigraphy and fluid flow properties of shallow-water, tight carbonates: The case study of the Murge Plateau (southern Italy). Marine and Petroleum Geology, 73, 350–370, doi: 10.1016/j.marpetgeo.2016.03.022.

Parrish, W., C. , 1978. Paleoenvironmental analysis of a Lower Permian bonebed and adjacent sediments, Wichita County, Texas. Palaeogeography, Palaeoclimatology, Palaeoecology, 24, 3, 209–237, doi: 10.1016/0031-0182(78)90043-3.

Paxton, S.T., Szabo, J.O., Ajdukiewicz, J.M., Klimentidis, R.E., 2002. Construction of an intergranular volume compaction curve for evaluating and predicting compaction and porosity loss in rigid-grain sandstone reservoirs. AAPG Bulletin, 86, 12, 2047–2067, doi: 10.1306/61eeddfa-173e-11d7-8645000102c1865d.

Petrash, D.A., Bialik, O.M., Bontognali, T.R.R., Vasconcelos, C., Roberts, J.A., McKenzie, J.A., Konhauser, K.O., 2017. Microbially catalyzed dolomite formation: From near-surface to burial. Earth-Science Reviews, 171, 558–582, doi: 10.1016/j.earscirev.2017.06.015.

Petrovic, A., Aigner, T., 2017. Are shoal reservoirs discrete bodies? A coquina shoal outcrop analogue from the Mid-Triassic Upper Muschelkalk, SW Germany. Journal of Petroleum Geology, 40, 249–275, doi: 10.1111/jpg.12675.

Pfaff, K., Hildebrandt, L.H., Leach, D.L., Jacob, D.E., Markl, G., 2010. Formation of the Wiesloch Mississippi Valley-type Zn-Pb-Ag deposit in the extensional setting of the Upper Rhinegraben, SW Germany. Mineralium Deposita, 45, 7, 647–666, doi: 10.1007/s00126-010-0296-5.

Pickels, S., 2023. Value addition in the context of mineral processing.

Pierson, B., 2006. The control of cathodoluminescence in dolomite by iron and manganese. Sedimentology, 28, 601–610, doi: 10.1111/j.1365-3091.1981.tb01924.x.

Piller, W.E., Decker, K., Haas, M., 1996, Sedimentologie und Beckendynamik des Wiener Beckens, https://opac.geologie.ac.at/ais312/dokumente/Berichte_GBA_033.pdf.

Pittman, E.D., 1979. Porosity, diagenesis and productive capability of sandstone reservoirs, in: Scholle, P.A., Schluger, P.R. (Eds.), Aspects of Diagenesis. SEPM Society for Sedimentary Geology, 159–173, doi: 10.2110/pec.79.26.0159.

Playà, E., Travé, A., Caja, M.A., Salas, R., Martín-Martín, J.D., 2010. Diagenesis of the Amposta offshore oil reservoir (Amposta Marino C2 well, Lower Cretaceous, Valencia Trough, Spain). Geofluids, 10, 3, 314–333, doi: 10.1111/j.1468-8123.2009.00266.x.

Pöppelreiter, M., Simone, A., Hoetz, G., 2004. Reservoir characteristics of intercontinental carbonate ramp deposits-Upper Muschelkalk, Middle Triassic, NE Netherlands. Netherlands Journal of Geosciences/Geologie en Mijnbouw, 83, doi: 10.1017/S0016774600020424.

Pribnow, D., Schellschmidt, R., 2000. Thermal tracking of upper crustal fluid flow in the Rhine graben. Geophysical Research Letters, 27, 13, 1957–1960, doi: 10.1029/2000GL008494.

Prof. Dr. Thierry Olivier Bineli Betsi, 2023. Personal Communication.

Püttmann, T., Mutterlose, J., 2021. Paleoecology of Late Cretaceous coccolithophores: Insights from the shallow-marine record. Paleoceanography and Paleoclimatology, 36, doi: 10.1029/2020PA004161.

Quandt, D., Busch, B., Greve, J., Hilgers, C., 2024. Rock characteristics and reservoir properties of Upper Carboniferous (Stephanian A–B) tight siliciclastic rocks from the Saar–Nahe basin (SW Germany). International Journal of Earth Sciences, doi: 10.1007/s00531-024-02394-x.

Quandt, D., Busch, B., Schmidt, C., Hilgers, C., 2022. Diagenesis and controls on reservoir quality of Lower Triassic red bed sandstones (Buntsandstein) from a marginal basin facies, southwest Germany. Marine and Petroleum Geology, 142, 105744, doi: 10.1016/j.marpetgeo.2022.105744.

Questiaux, J.-M., Couples, G.D., Ruby, N., 2010. Fractured reservoirs with fracture corridors. Geophysical Prospecting, 58, 2, 279–295, doi: 10.1111/j.1365-2478.2009.00810.x.

Radwan, A.E., 2022. Provenance, depositional facies, and diagenesis controls on reservoir characteristics of the middle Miocene Tidal sandstones, Gulf of Suez Rift Basin: integration of petrographic analysis and gamma-ray log patterns. Environmental Earth Sciences, 81, 15, doi: 10.1007/s12665-022-10502-w.

Rameil, N., 2008. Early diagenetic dolomitization and dedolomitization of Late Jurassic and earliest Cretaceous platform carbonates: A case study from the Jura Mountains (NW Switzerland, E France). Sedimentary Geology, 212, 1, 70–85, doi: 10.1016/j.sedgeo.2008.10.004.

Rammel, M., 1989. Zur Kenntnis der Flyschzone im Untergrund des Wiener Beckens - Die Glaukonitsandsteinserie. Universität Wien, Wien, Dissertation, 152.

Rashid, F., Glover, P.W.J., Lorinczi, P., Hussein, D., Lawrence, J.A., 2017. Microstructural controls on reservoir quality in tight oil carbonate reservoir rocks. Journal of Petroleum Science and Engineering, 156, 814–826, doi: 10.1016/j.petrol.2017.06.056.

Rashid, F., Hussein, D., Lorinczi, P., Glover, P.W.J., 2023. The effect of fracturing on permeability in carbonate reservoir rocks. Marine and Petroleum Geology, 152, 106240, doi: 10.1016/j.marpetgeo.2023.106240.

Read, J.F., Antun, H., Michael, C., Clayton, W.L., Božo, P., 2016. Climate controlled, fabric destructive, reflux dolomitization and stabilization via marine- and synorogenic mixed fluids: An example from a large Mesozoic, calcite-sea platform,

Croatia. Palaeogeography, Palaeoclimatology, Palaeoecology, 449, 108–126, doi: 10.1016/j.palaeo.2016.02.015.

Regnet, J.B., Robion, P., David, C., Fortin, J., Brigaud, B., Yven, B., 2015. Acoustic and reservoir properties of microporous carbonate rocks: Implication of micrite particle size and morphology. Journal of Geophysical Research: Solid Earth, 120, 2, 790–811, doi: 10.1002/2014jb011313.

Reif, W.E., 1982. Muschelkalk/Keuper bone-beds (Middle Triassic, SW-Germany) - storm condensation in a regressive cycle, in: Einsele, G., Seilacher, A. (Eds.), Cyclic and Event Stratification. Springer Berlin Heidelberg, Berlin, Heidelberg, 299–325.

Reinhold, C., Schwarz, M., Bruss, D., Heesbeen, B., Perner, M., Suana, M., 2016. The northern Upper Rhine Graben–re-dawn of a mature petroleum province? Swiss Bulletin, 21, 35–56.

Reserve Bank of Zimbabwe, 2024, Monetary Policy Statement, https://www.rbz.co.zw/documents/mps/2024/2024_Monetary_Policy_Statement.pdf.

Reuning, L., Deik, H., Petrick, B., Auer, G., Takayanagi, H., Iryu, Y., Courtillat, M., Bassetti, M.-A., 2022. Contrasting intensity of aragonite dissolution and dolomite cementation in glacial versus interglacial intervals of a subtropical carbonate succession. Sedimentology, 69, 5, 2131–2150, doi: 10.1111/sed.12985.

Reuning, L., Reijmer, J., Mattioli, E., 2006. Aragonite cycles: Diagenesis caught in the act. Sedimentology, 53, 849–866, doi: 10.1111/j.1365-3091.2006.00799.x.

Reuter, M., Schaik, A., Gutzmer, J., Bartie, N., Abadias Llamas, A., 2019. Challenges of the circular economy: A material, metallurgical, and product design perspective. Annual Review of Materials Research, 49, doi: 10.1146/annurev-matsci-070218-010057.

Rider, M., Kennedy, M., 2011. The geological interpretation of well logs, 3 ed. Rider-French Consulting Ltd., Scotland, 432.

Rider, M.H., 1990. Gamma-ray log shape used as a facies indicator: Critical analysis of an oversimplified methodology. Geological Society Special Publication, 48, 27–37, doi: 10.1144/GSL.SP.1990.048.01.04.

Rieckmann, M., 1970. Untersuchung von Turbulenzerscheinungen beim Fließen von Gasen durch Speichergesteine unter Berücksichtigung der Gleitströmung. Erdöl-Erdgas-Zeitschrift, Heft 2, 86, 36–51.

Rossi, C., Alaminos, A., 2014. Evaluating the mechanical compaction of quartzarenites: The importance of sorting (Llanos foreland basin, Colombia). Marine and Petroleum Geology, 56, 222–238, doi: 10.1016/j.marpetgeo.2014.04.012.

Rotstein, Y., Schaming, M., 2011. The Upper Rhine Graben (URG) revisited: Miocene transtension and transpression account for the observed first-order structures. Tectonics, 30, 3, doi: 10.1029/2010TC002767.

Royden, L.H., Biddle, K.T., Christie-Blick, N., 1985. The Vienna Basin: A thin-skinned pull-apart basin, Strike-Slip Deformation, Basin Formation, and Sedimentation. SEPM Society for Sedimentary Geology, 319–338, doi: 10.2110/pec.85.37.0303.

Rudolph, T., Melchers, C., Minke, A., Coldewey, W.G., 2010. Gas seepages in Germany: Revisited subsurface permeabilities in the German mining district. AAPG Bulletin, 94, 6, 847–867, doi: 10.1306/10210909074.

Ruf, M., Aigner, T., 2004. Facies and poroperm characteristics of a carbonate shoal (Muschelkalk, South German Basin): a reservoir analogue investigation. Journal of Petroleum Geology, 27, 3, 215–239, doi: 10.1111/j.1747-5457.2004.tb00056.x.

Rupprecht, B.J., 2017. Hydrocarbon generation and alteration in the Vienna Basin. Montanuniversität Leoben, Leoben, Dissertation, 295.

Rupprecht, B.J., Sachsenhofer, R.F., Gawlick, H.J., Kallanxhi, M.E., Kucher, F., 2017. Jurassic source rocks in the Vienna Basin (Austria): Assessment of conventional and unconventional petroleum potential. Marine and Petroleum Geology, 86, 1327–1356, doi: 10.1016/j.marpetgeo.2017.07.026.

Rupprecht, B.J., Sachsenhofer, R.F., Zach, C., Bechtel, A., Gratzer, R., Kucher, F., 2018. Oil and gas in the Vienna Basin: Hydrocarbon generation and alteration in a classical hydrocarbon province. Petroleum Geoscience, 25, 1, 3–29, doi: 10.1144/petgeo2017-056.

Ryan, P.C., Hillier, S., 2002. Berthierine/chamosite, corrensite, and discrete chlorite from evolved verdine and evaporite-associated facies in the Jurassic Sundance Formation, Wyoming. American Mineralogist, 87, 11-12, 1607–1615, doi: 10.2138/am-2002-11-1210.

Sachsenhofer, R.F., Misch, D., Rainer, T., Rupprecht, B.J., Siedl, W., 2025. The Vienna Basin: petroleum systems, storage and geothermal potential. Geological Society, London, Special Publications, 555, 1, SP555-2023-2205, doi: 10.1144/SP555-2023-205.

Saillet, E., Wibberley, C., 2013. Permeability and flow impact of faults and deformation bands in high-porosity sand reservoirs: Southeast Basin, France, analog. AAPG Bulletin, 97, 437–464, doi: 10.1306/09071211191.

Sanei, H., Ardakani, O.H., Akai, T., Akihisa, K., Jiang, C., Wood, J.M., 2020. Core versus cuttings samples for geochemical and petrophysical analysis of unconventional reservoir rocks. Scientific Reports, 10, 1, 7920, doi: 10.1038/s41598-020-64936-y.

Santanu, B., Udita, B., Anup, 2016. A review on palaeogeographic implications and temporal variation in glaucony composition. Journal of Palaeogeography, 5, 1, 43–71, doi: 10.1016/j.jop.2015.12.001.

Sauer, R., Seifert, P., Wessely, G., 1992. Outline of sedimentation, tectonic framework and hydrocarbon occurrence in Eastern Lower Austria (Guidebook). Mitteilungen der Österreichischen Geologischen Gesellschaft, 5–264.

Savarese, M., Dodd, J., Lane, N., 2007. Taphonomic and sedimentologic implications of crinoid intraskeletal porosity. Lethaia, 29, 141–156, doi: 10.1111/j.1502-3931.1996.tb01870.x.

Scheck-Wenderoth, M., Krzywiec, P., Zühlke, R., Maystrenko, Y., Froitzheim, N., 2008. Permian to Cretaceous tectonics, in: McCann, T. (Ed.), The Geology of Central Europe Volume 2: Mesozoic and Cenozoic. Geological Society Publishing House, London, 999–1030, doi: 10.1144/CEV2P

Scheck, M., Bayer, U., 1999. Evolution of the Northeast German Basin — inferences from a 3D structural model and subsidence analysis. Tectonophysics, 313, 1, 145–169, doi: 10.1016/S0040-1951(99)00194-8.

Schicker, A., Gier, S., Schieber, J., Krois, P., 2021. Diagenesis of the Malmian Mikulov Formation source rock, Vienna Basin: Focus on matrix and pores. Marine and Petroleum Geology, 129, 105082, doi: 10.1016/j.marpetgeo.2021.105082.

Schill, T., 2022, Wirtschaftsdaten kompakt, Botswana, https://www.gtai.de/resource/blob/585286/cea7b7bd-329c5dd0cfbeebfdb056a433/gtai-wirtschaftsdaten-no-vember-2021-botsuana-data.pdf (Accessed: 16.06.2023).

Schmidt, C., Busch, B., Hilgers, C., 2021. Lateral variations of detrital, authigenic and petrophysical properties in an outcrop analog of the fluvial Plattensandstein, Lower Triassic, Central S-Germany. Zeitschrift der Deutschen Gesellschaft für Geowissenschaften 172, Heft 4, 541–564, doi: 10.1127/zdgg/2020/0234.

Schmidt, M., 2015, Rohstoffrisikobewertung – Platingruppenmetalle, https://www.deutsche-rohstoffagentur.de/DERA/DE/Downloads/studie_Platin_2015.pdf?__blob=publicationFile&v=2.

Schmidt, M., 2023, Rohstoffrisikobewertung – Lithium, https://www.deutsche-rohstoffagentur.de/DE/Gemeinsames/Produkte/Downloads/DERA_Rohstoffinformationen/rohstoffinformationen-54.pdf;jsessionid=F99C2BCAE7E13A2435581E10C2DED73A.internet962?__blob=publicationFile&v=4.

Schmidt, M., Schäfer, P., Rötzer, N., 2020. Primär-und Sekundärmetalle und ihre Klimarelevanz, Berliner Recycling- und Sekundärrohstoffkonferenz.

Schoenherr, J., Reuning, L., Hallenberger, M., Lüders, V., Lemmens, L., Biehl, B., C., Lewin, A., Leupold, M., Wimmers, K., Strohmenger, C., J., 2018. Dedolomitization: review and case study of uncommon mesogenetic formation conditions. Earth-Science Reviews, 185, 780–805, doi: 10.1016/j.earscirev.2018.07.005.

Schulz, H.-M., Horsfield, B., Sachsenhofer, R.F., 2010. Shale gas in Europe: A regional overview and current research activities. Geological Society, London, Petroleum Geology Conference Series, 7, 1, 1079–1085, doi: doi:10.1144/0071079.

Schulze, G., 2022, Westliche Flugzeugindustrie spürt die Kriegsfolgen, https://www.gtai.de/de/trade/russland/branchen/westliche-flugzeugindustrie-spuert-die-kriegsfolgen-833408 (Accessed: 16.05.2023).

Schulze, G., 2023, Rohstoffreichtum der Ukraine in Gefahr, https://www.gtai.de/de/trade/ukraine/branchen/rohstoffreichtum-der-ukraine-in-gefahr-941166 (Accessed: 02.05.2025).

Schumacher, M.E., 2002. Upper Rhine Graben: Role of preexisting structures during rift evolution. Tectonics, 21, 1, 6-1–6-17, doi: 10.1029/2001TC900022.

Schwarz, M., Henk, A., 2005. Evolution and structure of the Upper Rhine Graben: insights from three-dimensional thermomechanical modelling. International Journal of Earth Sciences, 94, 4, 732–750, doi: 10.1007/s00531-004-0451-2.

Seufert, G., 1984. Lithostratigraphische Profile aus dem Trochitenkalk (Oberer Muschelkalk, mo1) des Kraichgaus und angrenzender Gebiete. Jahresberichte und Mitteilungen des Oberrheinischen Geologischen Vereins, 66, 209–248, doi: 10.1127/jmogv/66/1984/209.

Seufert, G., Schweizer, V., 1985. Stratigraphische und mikrofazielle Untersuchungen im Trochitenkalk (Unterer Hauptmuschelkalk, mo 1) des Kraichgaues und angrenzender Gebiete. Jahresberichte und Mitteilungen des Oberrheinischen Geologischen Vereins, 67, 129–171, doi: 10.1127/jmogv/67/1985/129.

Shinn, E.A., Halley, R.B., Hudson, J.H., Lidz, B.H., 1977. Limestone compaction: An enigma. Geology, 5, 1, 21–24, doi: 10.1130/0091-7613(1977)5<21:Lcae>2.0.Co;2.

SKHynix, 2024, SK hynix teams up with local partners to develop pioneering neon gas recycling tech, https://news.skhynix.com/sk-hynix-teams-up-with-local-partners-to-develop-pioneering-neon-gas-recycling-tech/ (Accessed: 03.05.2025).

Smodej, J., Reuning, L., Becker, S., Kukla, P., A. , 2019. Micro- and nano-pores in intrasalt, microbialite-dominated carbonate reservoirs, Ara Group, South-Oman salt basin. Marine and Petroleum Geology, 104, 389–403, doi: 10.1016/j.marpetgeo.2019.03.036.

Soliva, R., Schultz, R., A., Ballas, G., Taboada, A., Wibberley, C., Saillet, E., Benedicto, A., 2013. A model of strain localization in porous sandstone as a function of tectonic setting, burial and material properties; new insight from Provence (southern France). Journal of Structural Geology, 49, 50–63, doi: 10.1016/j.jsg.2012.11.011.

Sotak, J., 2010. Paleoenvironmental changes across the Eocene-Oligocene boundary: Insights from the Central-Carpathian Paleogene Basin. Geologica Carpathica, 61, 393–418, doi: 10.2478/v10096-010-0024-1.

Spiegel Ausland, 2025, Was der Rohstoffdeal für die Ukraine bedeutet, https://www.spiegel.de/ausland/ukraine-was-der-rohstoffdeal-mit-den-usa-fuer-kyjiw-bedeutet-a-2d8710ad-2833-43fa-aabd-90639736a0b8 (Accessed: 06.05.2025).

Srivastava, D., C. , Lisle, R., J. , Imran, M., Kandpal, R., 1998. The kink-band triangle: a triangular plot for paleostress analysis from kink-bands. Journal of Structural Geology, 20, 11, 1579–1586, doi: 10.1016/S0191-8141(98)00051-0.

Stanchits, S., Fortin, J., Gueguen, Y., Dresen, G., 2009. Initiation and Propagation of Compaction Bands in Dry and Wet Bentheim Sandstone. Pure Appl. Geophys., 166, 843–868, doi: 10.1007/s00024-009-0478-1.

STD, 2016. Stratigraphische Tabelle von Deutschland 2016. Deutsche Stratigraphische Kommission, Hrsg.; Redaktion, Koordination und Gestaltung: Menning, M., Hendrich, A. - Potsdam (GeoForschungsZentrum).

Stober, I., Bucher, K., 2015. Hydraulic and hydrochemical properties of deep sedimentary reservoirs of the Upper Rhine Graben, Europe. Geofluids, 15, 3, 464–482, doi: 10.1111/gfl.12122.

Stock, O., 2022, Boeing boykottiert Titan aus Russland - Airbus kann sich das nicht leisten, https://www.focus.de/politik/ausland/ukraine-krise/boeing-setzt-kauf-von-titan-aus-russland-aus_id_72463482.html (Accessed: 12.04.2023).

Strauss, P., Harzhauser, M., Hinsch, R., Wagreich, M., 2006. Sequence-stratigraphy in a classic pull-apart basin (Neogene, Vienna Basin). A 3D seismic based integrated approach, Geologica Carpathica, 185–197.

Sullivan, A., 2022, Nickel: Germany's other big Russian import, https://www.dw.com/en/russian-nickel-palladium-chromium-exports-a-headache-for-germany/a-61429132 (Accessed: 06.06.2023).

Suski, B., Ladner, F., Baron, L., Vuataz, F.D., Philippossian, F., Holliger, K., 2008. Detection and characterization of hydraulically active fractures in a carbonate aquifer: results from self-potential, temperature and fluid electrical conductivity logging in the Combioula hydrothermal system in the southwestern Swiss Alps. Hydrogeology Journal, 16, 7, 1319–1328, doi: 10.1007/s10040-008-0302-5.

Swami, V., Didenko, A., Allo, F., Rogers, G., Cowgill, M., Rahbi, K., Harthi, R., Verma, S.K., Zonjee, P., 2022. New insights into wellbore stability analysis with integration of petrophysics, rock physics, geology, geomechanics and drilling, 1–5.

Tavakoli, V., 2020. 4 Macroscopic Heterogeneity - 4.2 Fractures, Carbonate Reservoir Heterogeneity - Overcoming the Challenges. Springer Cham, 73–76, doi: 10.1007/978-3-030-34773-4.

Tempest Minerals LTD, 2019, New licenses granted in Zimbabwe, https://tempestminerals.com/asx-announcements/new-licenses-granted-in-zimbabwe/ (Accessed: 15.06.2023).

Tercero Espinoza, L.A., 2012. The contribution of recycling to the supply of metals and minerals, Polinares working paper n. 20. Fraunhofer ISI.

Terzaghi, R.D., 1965. Sources of error in joint surveys. Géotechnique, 15, 3, 287–304, doi: 10.1680/geot.1965.15.3.287.

The World Bank, 2023, Worldwide Governance Indicators, https://databank.worldbank.org/source/worldwide-governance-indicators (Accessed: 15.06.2023).

Tiainen, S., King, H., Cubitt, C., Karalaus, E., Prater, T., Willis, B., 2002. Drill cuttings analysis & a new approach to reservoir description and characterisation; Examples from the Cooper Basin, Australia. The APPEA Journal, 42, 1, 495–509, doi: 10.1071/AJ01027.

Toffolo, M.B., Ricci, G., Caneve, L., Kaplan-Ashiri, I., 2019. Luminescence reveals variations in local structural order of calcium carbonate polymorphs formed by different mechanisms. Scientific Reports, 9, 1, 16170, doi: 10.1038/s41598-019-52587-7.

Toussaint, R., Aharonov, E., Koehn, D., Gratier, J.P., Ebner, M., Baud, P., Rolland, A., Renard, F., 2018. Stylolites: A review. Journal of Structural Geology, 114, 163–195, doi: 10.1016/j.jsg.2018.05.003.

Traineau, H., Genter, A., Jp, C., H, F., P, C., 1991. Petrography of the granite massif from drill cutting analysis and well log interpretation in the HDR borehole GPK1 (Soultz, Alsace, France), Geothermal Science and Technology, 1–29.

Tribovillard, N., Bout-Roumazeilles, V., Abraham, R., Ventalon, S., Delattre, M., Baudin, F., 2023. The contrasting origins of glauconite in the shallow marine environment highlight this mineral as a marker of paleoenvironmental conditions. Comptes Rendus. Géoscience, 355, S2, 1–16, doi: 10.5802/crgeos.170.

Triplehorn, D.M., 1966. Morphology, internal structure, and origin of glauconite pellets. Sedimentology, 6, 4, 247–266, doi: 10.1111/j.1365-3091.1966.tb01894.x.

Uffmann, A.K., 2014. Paleozoic petroleum systems of northern Germany and adjacent areas: A 3D modeling study. Aachen, Techn. Hochsch., Aachen, Dissertation, 174.

Ukrainian Geological Survey, 2023, Presentation - Investment Opportunities in Exploration & Production, https://www.geo.gov.ua/wp-content/uploads/presentations/en/investment-opportunities-in-exploration-production-strategic-and-critical-minerals.pdf (Accessed: 20.03.2023).

Umann, U., 2023, Marokkos Bergwerke ordern umweltfreundliche Maschinen und Anlagen https://www.gtai.de/de/trade/marokko/branchen/marokkos-bergwerke-ordern-umweltfreundliche-maschinen-und-anlagen-1057640 (Accessed: 12.04.2024).

UN Cometrade, 2023a, Database, Trade Data - HS2606, https://comtradeplus.un.org/TradeFlow?Frequency=A&Flows=M&CommodityCodes=2606&Partners=0&Reporters=804&period=all&AggregateBy=none&BreakdownMode=plus (Accessed: 06.06.2023).

UN Cometrade, 2023b, Database, Trade Data - HS2614, https://comtradeplus.un.org/TradeFlow?Frequency=A&Flows=M&CommodityCodes=2614&Partners=0&Reporters=804&period=all&AggregateBy=none&BreakdownMode=plus (Accessed: 05.06.2023).

UN Cometrade, 2025, Database, Trade Data - HS2606, https://comtradeplus.un.org/TradeFlow?Frequency=A&Flows=M&CommodityCodes=280429&Partners=492&Reporters=all&period=2024&AggregateBy=none&BreakdownMode=plus (Accessed: 27.05.2025).

UNDP, 2022, Latest human development composite indices tables, table 1, https://hdr.undp.org/data-center/documentation-and-downloads (Accessed: 16.06.2023).

UNEP, 2013, Metal Recycling: Opportunities, Limits, Infrastructure, A Report of the Working Group on the Global Metal Flows to the International Resource Pane, https://www.wrforum.org/wp-content/uploads/2015/03/Metal-Recycling-Opportunities-Limits-Infrastructure-2013Metal_recycling.pdf.

USGS, 2013, Mineral commodity summaries 2013, https://pubs.usgs.gov/publication/mineral2013.

USGS, 2023, Mineral commodity summaries 2023, https://pubs.usgs.gov/periodicals/mcs2023/mcs2023.pdf.

USGS, 2024, Mineral commodity summaries 2024, https://pubs.usgs.gov/publication/mcs2024.

USGS, 2025, Mineral commodity summaries 2025, https://pubs.usgs.gov/publication/mcs2025.

Vejbæk, O.V., Andersen, C., Dusar, M., Herngreen, G.F.W., Krabbe, H., Leszczyński, K., Lott, G.K., Mutterlose, J., Van der Molen, A.S., 2010. Cretaceous, in: Doornenbal, J.C., Stevenson, A.G. (Eds.), Petroleum Geological Atlas of the Southern Permian Basin Area. EAGE Publications b.v, Houten, Netherlands, 195–209.

Versteegh, G.J.M., Servais, T., Streng, M., Munnecke, A., Vachard, D., 2009. A Discussion and Proposal concerning the use of the therm calcispheres. Palaeontology, 52, 2, 343–348, doi: 10.1111/j.1475-4983.2009.00854.x.

Vidal, J., Genter, A., 2018. Overview of naturally permeable fractured reservoirs in the central and southern Upper Rhine Graben: Insights from geothermal wells. Geothermics, 74, 57–73, doi: 10.1016/j.geothermics.2018.02.003.

Vidal, J., Genter, A., Schmittbuhl, J., 2015. How do permeable fractures in the Triassic sediments of Northern Alsace characterize the top of hydrothermal convective cells? Evidence from Soultz geothermal boreholes (France). Geothermal Energy, 3, 1, 8, doi: 10.1186/s40517-015-0026-4.

Villemin, T., Alvarez, F., Angelier, J., 1986. The Rhinegraben: Extension, subsidence and shoulder uplift. Tectonophysics, 128, 1, 47–59, doi: 10.1016/0040-1951(86)90307-0.

Vodrazkova, S., Munnecke, A., 2010. Calcispheres as a source of lime mud and peloids evidence from the early Middle Devonian of the Prague Basin, the Czech Republic. Bulletin of Geosciences, 85, 585–602, doi: 10.3140/bull.geosci.1206.

Voigt, E., Häntzschel, W., 1964. Gradierte Schichtung in der Oberkreide Westfalens, Fortschr. Geol. Rheinland Westfalen 495–548.

Voigt, T., Kley, J., Voigt, S., 2021. Dawn and dusk of Late Cretaceous basin inversion in central Europe. Solid Earth, 12, 6, 1443–1471, doi: 10.5194/se-12-1443-2021.

Volery, C., Davaud, E., Durlet, C., Clavel, B., Charollais, J., Caline, B., 2010. Microporous and tight limestones in the Urgonian Formation (late Hauterivian to early Aptian) of the French Jura Mountains: Focus on the factors controlling the formation of microporous facies. Sedimentary Geology, 230, 1-2, 21–34, doi: 10.1016/j.sedgeo.2010.06.017.

Volkswagen AG, 2023, Responsible War Materials Report 2022, https://uploads.vw-mms.de/system/production/files/cws/039/420/file/7e79c83ac8f242e289c83f2674edd77fa61c0ec5/VW_Responsible_Raw_Materials_Report_2023.pdf?1689341355.

Vollrath, A., 1938. Zur Stratigraphie und Bildung des Oberen Hauptmuschelkalkes in Mittel- und Westwürttemberg. Jahresberichte und Mitteilungen des Oberrheinischen Geologischen Vereins, 27, 69–80, doi: 10.1127/jmogv/27/1938/69.

Vulcan Energy, 2025, Vulcan Energy erhält Status als „Strategisches Projekt“ von der Europäischen Kommission, https://v-er.eu/de/blog/vulcan-energy-erhaelt-status-als-strategisches-projekt-von-der-europaeischen-kommission/ (Accessed: 04.05.2025).

Wagner Moreira, L., Tuany Younis Abdul, F., Maria Cordeiro do, C., Antonio Fernando Menezes, F., Luiz Antonio Pierantoni, G., 2023. Controls of fracturing on porosity in pre-salt carbonate reservoirs. Energy Geoscience, 4, 2, 100146, doi: 10.1016/j.engeos.2022.100146.

Wagreich, M., Schmid, H.P., 2002. Backstripping dip-slip fault histories: Apparent slip rates for the Miocene of the Vienna Basin. Terra Nova, 14, 3, 163–168, doi: 10.1046/j.1365-3121.2002.00404.x.

Walderhaug, O., 2000. Modeling quartz cementation and porosity in Middle Jurassic Brent Group sandstones of the Kvitebjørn Field, Northern North Sea. AAPG Bulletin, 84, doi: 10.1306/A9673E96-1738-11D7-8645000102C1865D.

Wang, Q., Laubach, S.E., Gale, J.F.W., Ramos, M.J., 2019. Quantified fracture (joint) clustering in Archean basement, Wyoming: application of the normalized correlation count method. Petroleum Geoscience, 25, 4, 415–428, doi: 10.1144/petgeo2018-146.

Warnecke, M., Aigner, T., 2019. Asymmetry of an epicontinental basin—facies, cycles, tectonics and hydrodynamics: The Triassic Upper Muschelkalk, South Germanic Basin. The Depositional Record, 5, 1, 147–187, doi: 10.1002/dep2.59.

Warren, J., 2000. Dolomite: Occurrence, evolution and economically important associations. Earth-science Reviews, 52, 1–81, doi: 10.1016/S0012-8252(00)00022-2.

Weedmark, T.C., Spencer, R.J., Juss, D.P., Marecha, F., 2014. Applications of portable XRF, chemical stratigraphy and SEM in the Horn River Basin, Adapted from extended abstract prepared in conjunction with presentation at CSPG/CSEG/CWLS

GeoConvention 2012, (Vision) Calgary TELUS Convention Centre & ERCB Core Research Centre, Calgary, AB, Canada, 14-18 May 2012. AAPG.

Weger, R.J., Eberli, G.P., Baechle, G.T., Massaferro, J.L., Sun, Y.-F., 2009. Quantification of pore structure and its effect on sonic velocity and permeability in carbonates. AAPG Bulletin, 93, 10, 1297–1317, doi: 10.1306/05270909001.

Wendler, J., Willems, H., 2004. Pithonelloid wall-type of the Late Cretaceous calcareous dinoflagellate cyst genus Tetratropis. Review of Palaeobotany and Palynology, 129, 3, 133–140, doi: 10.1016/j.revpalbo.2003.12.011.

Wendler, J.E., Bown, P., 2013. Exceptionally well-preserved Cretaceous microfossils reveal new biomineralization styles. Nature Communications, 4, 1, 2052, doi: 10.1038/ncomms3052.

Wentworth, C.K., 1922. A scale of grade and class terms for clastic sediments. The Journal of Geology, 30, 5, 377–392.

Wessely, G., 2006. Niederösterreich, Geologie der Österreichischen Bundesländer. Geologische Bundesanstalt, Wien, 89–94.

Westphal, H., Munnecke, A., 1997. Mechanical compaction versus early cementation in fine-grained limestones: differentiation by the preservation of organic microfossils. Sedimentary Geology, 112, 1, 33–42, doi: 10.1016/S0037-0738(97)00033-X.

Wiese, F., Wood, C., Kaplan, U., 2004. 20 years of event stratigraphy in NW Germany: Advances and open questions, Acta geologica Polonica, 639–656.

Wilmsen, M., Bansal, U., Metzner, N., Böning, P., 2024. Geochemical and depositional environment of an Upper Cretaceous greensand giant (Münsterland Cretaceous Basin, Germany). Chemical Geology, 661, 122168, doi: 10.1016/j.chemgeo.2024.122168.

Wilmsen, M., Dölling, B., Hiss, M., Niebuhr, B., 2019. The lower Upper Cretaceous of the south-eastern Münsterland Cretaceous Basin, Germany: facies, integrated stratigraphy and inter-basinal correlation. Facies, 65, 2, doi: 10.1007/s10347-018-0552-1.

Wilson, J.L., 1975. Carbonate facies in geologic history, 1 ed. Springer, New York, 471; doi: 10.1007/978-1-4612-6383-8.

Wilson, M.D., Stanton, P.T., Wilson, M.D., 1994. Diagenetic mechanisms of porosity and permeability reduction and enhancement, Reservoir Quality Assessment and Prediction in Clastic Rocks. SEPM Society for Sedimentary Geology, doi: 10.2110/scn.94.30.0059.

Wirges, J., Dodenhoff, P., 2019, Visualizing spatio-temporal data as an animation vs. as static maps: black coal mine shafts in the ruhr region, https://www.dataviz-jwirges.de/visualizing-spatio-temporal-data-as-an-animation-vs-as-static-maps/ (Accessed: 20.01.2024).

Wittmann, H.-J., 2022, Ukrainekrieg: Engpass für Rohstoffe und globale Lieferketten, https://www.gtai.de/de/trade/russland/branchen/ukraine-krieg-rohstoffe-globale-lieferketten-engpass-832784 (Accessed: 29.05.2023).

Wolf, E.O., 1995. Sedimentologie, Paläogeographie und Faziesentwicklung der Allochthonite des Campan von Beckum/Zentrales Münsterland, Berliner geowiss. Abh., 305–333.

Wolf, K.H., 1965. Gradational Sedimentary Products of Calcareous Algae. Sedimentology, 5, 1, 1–37, doi: 10.1111/j.1365-3091.1965.tb01556.x.

Worden, R., Armitage, P., Butcher, A., Churchill, J., Csoma, A., Hollis, C., Lander, R., Omma, J., 2018. Petroleum reservoir quality prediction: Overview and contrasting approaches from sandstone and carbonate communities. Geological Society, London, Special Publications, 435, 1–31, doi: 10.1144/SP435.21.

Worden, R., Morad, S., 2003. Clay minerals in sandstones: Controls on formation, distribution and evolution, 1–41; doi: 10.1002/9781444304336.ch1.

Worldsteel, 2023, Top steel-producing companies 2023/2022, https://worldsteel.org/data/top-producers/ (Accessed: 02.04.2025).

Wulff, L., Kaplan, U., Mutterlose, J., 2017. Zur spätkretazischen Hebungsgeschichte des Raumes Halle (Westfalen): die Biostratigraphie der Rutschmassen des Hesseltals, Geologie und Palaeontologie in Westfalen, 5–19.

Wyrick, G.G., Borchers, J.W., 1981. Hydrologic effects of stress-relief fracturing in an Appalachian Valley, Geological Survey Water-Supply Paper 2177. U.S. Government Printing Office, Washington, 12–13.

Xi, K., Yingchang, C., Jahren, J., Zhu, R., Bjørlykke, K., Haile, B., Lijing, Z., Hellevang, H., 2015. Diagenesis and reservoir quality of the Lower Cretaceous Quantou Formation tight sandstones in the southern Songliao Basin, China. Sedimentary Geology, 330, 90–107, doi: 10.1016/j.sedgeo.2015.10.007.

Yager, T.R., 2022, Minerals Yearbook, Botswana 2017-2018, https://pubs.usgs.gov/myb/vol3/2017-18/myb3-2017-18-botswana.pdf.

Yager, T.R., 2023, The Mineral Industry of Botswana in 2019, https://pubs.usgs.gov/myb/vol3/2019/myb3-2019-botswana.pdf.

Zambito, J., J, Haas, L., D., Parsen, M., J. , 2022. A portable x-ray fluorescence (pXRF) elemental dataset collected from Cambrian-age sandstone aquifer material, Wisconsin, U.S.A. Data in Brief, 43, 108411, doi: 10.1016/j.dib.2022.108411.

Zapf, M., 2024, Wie Deutschland sich Rohstoffe mit einem Staatsfonds sichern will, https://www.capital.de/wirtschaft-politik/wie-deutschland-sich-rohstoffe-mit-einem-staatsfonds-sichern-will-34459304.html (Accessed: 11.04.2024).

ZDF, 2025, USA und Ukraine: Was das Abkommen bedeutet, https://www.zdf.de/nachrichten/politik/ausland/rohstoffabkommen-usa-trump-ukraine-krieg-russland-100.html (Accessed: 06.05.2025).

Zeeh, S., Geng, A., 2001. Origin and diagenesis of dolomite from the Muschelkalk Group (Middle Triassic) of SW Germany. Neues Jahrbuch fur Geologie und Palaontologie - Abhandlungen, 221, 359–395, doi: 10.1127/njgpa/221/2001/359.

Zhang, S., Lu, P., 2019. Effect of micrite content on calcite cementation in an Upper Jurassic carbonate reservoir, Eastern Saudi Arabia. Journal of Petroleum Geology, 42, 1, 79–89, doi: 10.1111/jpg.12725.

Ziegler, P., A., 1982. Geological Atlas of Western and Central Europe Shell Internationale Petroleum Maatschapij B.V., The Hague, 239.

Ziegler, P., A. , 1992. European Cenozoic rift system. Tectonophysics, 208, 1, 91–111, doi: 10.1016/0040-1951(92)90338-7.

Appendix

Research data can be accessed using the provided Digital Object Identifier (DOI): 10.35097/rxk3rf43m1mft0un